High-fidelity simulation of conjugate heat transfer between a turbulent flow and a duct geometry

Rodrigo Vicente Cruz

THÈSE

Pour l'obtention du Grade de

DOCTEUR DE L'UNIVERSITÉ DE POITIERS
Faculté des Sciences Fondamentales et Appliquées
Diplôme National - Arrêté du 25 mai 2016

École Doctorale : École Doctorale Sciences et Ingénierie des Matériaux, Mécanique, Énergétique (ED 609)

Secteur de Recherche : Mécanique des milieux fluides

Présentée par

Rodrigo VICENTE CRUZ

HIGH-FIDELITY SIMULATION OF CONJUGATE HEAT TRANSFER BETWEEN A TURBULENT FLOW AND A DUCT GEOMETRY

Directeur de Thèse : Eric LAMBALLAIS

Soutenue publiquement le 10 décembre 2021

— JURY —

H. I. ANDERSSON	Professeur, NTNU, Norvège	Rapporteur
G. BALARAC	Professeur, Grenoble INP, Grenoble	Rapporteur
P. CINNELLA	Professeur, Sorbonne Université, Paris	Examinateur
S. DECK	Directeur de recherche, ONERA, Meudon	Examinateur
F. DUCHAINE	Chercheur, CERFACS, Toulouse	Examinateur
C. FLAGEUL	Maître de conférences, Université de Poitiers, Poitiers	Examinateur
E. LAMBALLAIS	Professeur, Université de Poitiers, Poitiers	Directeur de thèse

High-Fidelity Simulation of Conjugate Heat Transfer Between a Turbulent Flow and a Duct Geometry

Abstract This study concerns the development of a new numerical technique for the simulation of Conjugate Heat Transfer (CHT) in turbulent pipe flow configuration. The method is progressively developed in order to ultimately grow into the desired high-fidelity technique. All numerical developments and simulations are carried out within the massively parallel open-source code *Incompact3d/Xcompact3d*. In a first phase, the capabilities of the present numerical strategy are expanded and assessed. By means of Direct and Implicit Large-Eddy Simulation (DNS/ILES), its advantageous combination of numerical features are explored, among which we may highlight the Immersed Boundary Method (IBM) based on Lagrange polynomial interpolations, the original Viscous Filtering technique for DNS/ILES and the implicit wall-layer modelling feature intrinsic to the use of high-order numerical dissipation as an ersatz of the subgrid-scale (SGS) contribution. The second part is focused on the introduction of an original strategy for the simulation of heat-transfer in wall turbulence. For that purpose, the IBM is subjected to extensive developments for the correct imposition of boundary conditions on the thermal field. The numerical techniques are validated with DNS of heat transfer in turbulent pipe flow with Isoflux (IF) and Mixed-type Boundary Conditions (MBC). Special attention is given to IF, as an original methodology based on IBM is developed for the imposition of Neumann boundary conditions. The strategy is then used to introduce a versatile method for the numerical simulation of CHT in pipe configuration. It is shown that this technique is capable of providing an accurate description of the thermal interaction between fluid and solid media, which may be valuable, for instance, to improve RANS/LES modelling in industrial applications where fluctuating thermal stresses are a concern. The pipe geometry is considered here as a prototype of complex geometry to investigate, in further work, conjugate heat transfer in more complex geometries such as solar power plants and T-junction flow.

Keywords Direct Numerical Simulation, Large-Eddy Simulation, High Performance Computing, turbulent pipe flow, conjugate heat transfer, thermal boundary conditions, complex geometry, immersed boundary method

---

Simulation haute-fidelité du transfert thermique conjugué entre un fluide turbulent et le corps d'une conduite hydraulique

Résumé Cette étude est consacrée au développement d'une nouvelle technique numérique pour la simulation du transfert thermique conjugué avec une application pour la reproduction de l'écoulement turbulent dans une conduite. La méthode est construite progressivement pour atteindre la haute-fidélité souhaitée. Tous les développements numériques et simulations sont effectués sur la base du code libre et massivement parallèle *Incompact3d*/*Xcompact3d*. Dans une première phase, le potentiel de la stratégie numérique choisie est étendu puis évalué par simulation directe et implicite à grande échelle pour mieux cerner la façon de combiner avantageusement ses caractéristiques. Parmi ces dernières, on peut mentionner la méthode des frontières immergées basée sur des interpolations polynomiales de Lagrange, la technique originale de filtrage visqueux et la modélisation implicite de turbulence pariétale par utilisation d'une dissipation numérique d'ordre élevé comme ersatz de la contribution sous-maille. La deuxième partie est consacrée à l'introduction d'une stratégie originale pour la simulation du transfert thermique turbulent pariétal. Dans ce but, la méthode des frontières immergées est adaptée pour permettre l'imposition de conditions aux limites thermiques spécifiques. L'approche est validée par simulation numérique directe du transfert de chaleur en turbulence de conduite avec des conditions aux limites de type Isoflux ou mixte. Une attention particulière est accordée au cas Isoflux qui nécessite des développements pour permettre l'imposition d'une condition aux limites de type Neumann. Cette stratégie est ensuite mise à profit pour mettre au point une méthode polyvalente qui permet la reproduction d'un phénomène de transfert thermique conjugué entre un fluide turbulent et le corps de la conduite qui le contient. Il est démontré que cette technique de couplage est capable de fournir une description précise de l'interaction thermique entre les milieux fluide et solide, ce qui peut être utile, par exemple, pour améliorer la modélisation RANS/LES dans les applications industrielles pour lesquelles les contraintes thermiques fluctuantes sont une préoccupation. La conduite cylindrique considérée ici, sans lien avec la nature Cartésienne du maillage, peut être vue comme un prototype de géométrie complexe, ceci ouvrant la voie à la réalisation de simulations haute-fidélité en géométrie réaliste telle que celle d'un Té de mélange avec plus largement des applications dans le cadre des centrales nucléaires ou solaires.

Mots-Clés Simulation Numérique Directe, Simulation à Grande Echelle, Calcul Haute Performance, écoulement turbulent dans les conduites, transfert thermique conjugué, conditions aux limites thermiques, géométrie complexe, méthode des frontières immergées

---

Acknowledgements

First and foremost, I would like to thank You, Jesus, for this thesis. You have not only opened the door for this experience but You have also provided and sustained me in every way imaginable throughout these years. It has been an incredible journey of growth by Your side. What a privilege it is to explore more in depth the work of Your hands Lord, thank You for Your faithfulness and may this title glorify Your name. I deeply thank my beloved wife Alessandra, I can't even imagine how this path would be without you by my side, thank you for sharing this dream and for building it together with me.

A very special thank you to the person without whom the results presented in this thesis could not have been achieved, my thesis supervisor, Prof Eric LAMBALLAIS. You have truly inspired me with your passion for science. Besides being a remarkable researcher, you are an admirable person. Thank you for the constructive advice, for all the fruitful discussions and for your dedication, it has been a real pleasure to go through these three years with you. I would also like to thank Dr Rodolphe PERRIN for the insightful exchanges on the subject during these years.

I sincerely thank Prof Helge ANDERSSON and Prof Guillaume BALARAC for having accepted the role of rapporteur for this thesis. I also thank the other members of the jury - Prof Paola CINNELLA, Dr Sebastien DECK, Dr Florent DUCHAINE and Dr Cédric Flageul - for having accepted to judge the scientific quality of this work and for bringing your valuable experience when doing so, this resulted in very interesting discussions during the defence.

During this thesis, I was also introduced to the beautiful world of teaching. Thank you Dr Veronique FORTUNE for welcoming me so warmly into the team and thank you Dr Florent MARGNAT for sharing with me, once again, your experience. Working under your supervision during my master internship certainly played a major role in my decision of diving into the world of scientific research.

I have also had the pleasure of working in international collaboration with high-level PhD candidates over these years. Thank you Athanasios GIANNENAS and Kay SCHAFER, the exchanges with you have been very enriching and have encouraged me to think outside the box. Your scientific rigour leaves me in no doubt that you have a brilliant career ahead of you.

Last but not least, I thank my family - both in Brazil and in Italy - for all the supportive gestures and words during these years. A more than special thank you to my parents - Rosângela and Nildomar - and my good friend and brother - Nildomar Junior - for supporting my decision of leaving our beloved country. Whether in person for a few days during the holidays or through video calls, the moments spent with all of you have always given me renewed energy to continue the journey, thank you for always being there for me.

Contents

List of Figures

List of Tables

Chapter 1

Introduction

Pipes are the most widely used fluid transport system in the world, being found in nearly every engineering design: from pipelines to water supply systems, integrating different components in an airplane, everywhere in our cars, in our houses, etc. In heat transfer applications, fluids in movement inside ducts are commonly employed for thermal regulation, as exemplified in Figure 1.1, with the cooling systems of a turbine blade (left) and a nuclear power plant (right). In order to extract the best performance out of these systems, their design must take into account heat exchange characteristics that are intrinsically related to the geometry of the flow. Many simplified theoretical and empirical tools may be used to globally predict heat transfer in hydraulic systems but they are unable to provide reliable information for every possible scenario, specially when thermal fatigue phenomena are involved or complex geometries must be considered.

Furthermore, when considering heat exchange in confined flows, not only the fluid is concerned but also its thermal interaction with the solid pipe body. The terminology *Conjugate Heat Transfer* (*CHT*) refers to this thermal interaction between fluid and solid media by exchanging thermal energy at the interfaces between them. The classic example of the kettle in Figure 1.2-left illustrates well the principle. Here, we can identify the three basic ways in which heat transfer take place - namely conduction, convection and radiation - but we may focus only on conduction and convection. In solid bodies, heat is transferred by conduction, whereas in fluids, convection often dominates over conduction. This way, the load of heat received at the base of the kettle in direct contact with the fire is transported throughout its thickness by conduction. This heat is then transferred by convection to the fluid recirculating inside.

This same reasoning can be projected to the pipe configuration represented in Figure 1.2-right, the load of heat received at its outer surface is conducted throughout the solid thickness and then conveyed by the fluid in movement inside. Therefore, to investigate a CHT problem means considering different physical processes occurring in distinct media. The complexity of this scenario can be further increased if the confined flow is in turbulent state - which is the case in the vast majority of real life industrial applications - adding a multi-scale and random nature to the problem.

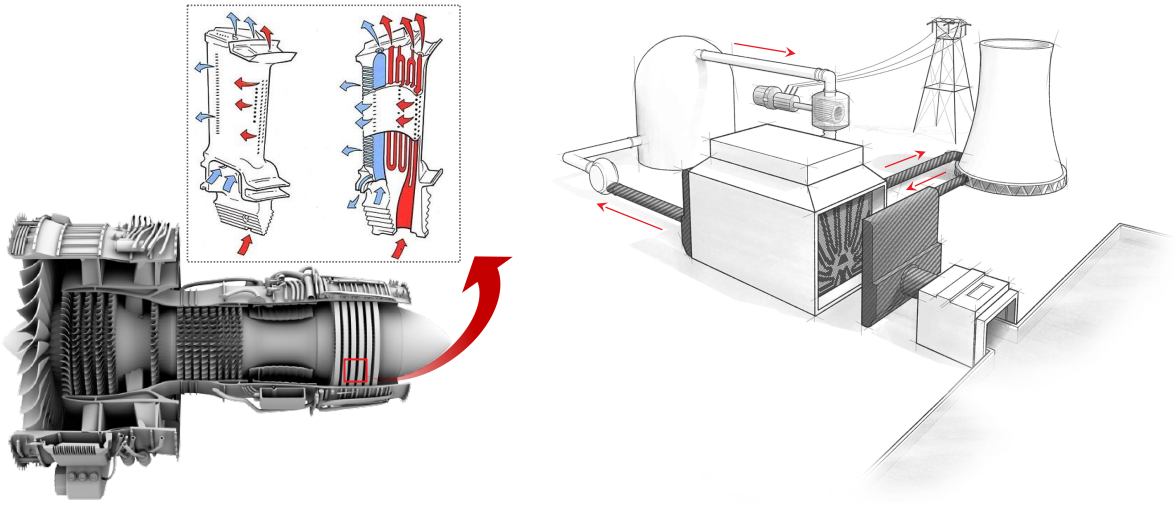

Figure 1.1: Examples of cooling systems based on pipe flow. (Left) Micro-channels through which air flows to cool down the turbine blades of an aeronautical engine. (Right) Pipes are present all over nuclear power plants connecting components and transporting the cooling fluid. Images adapted from [1, 2, 3].

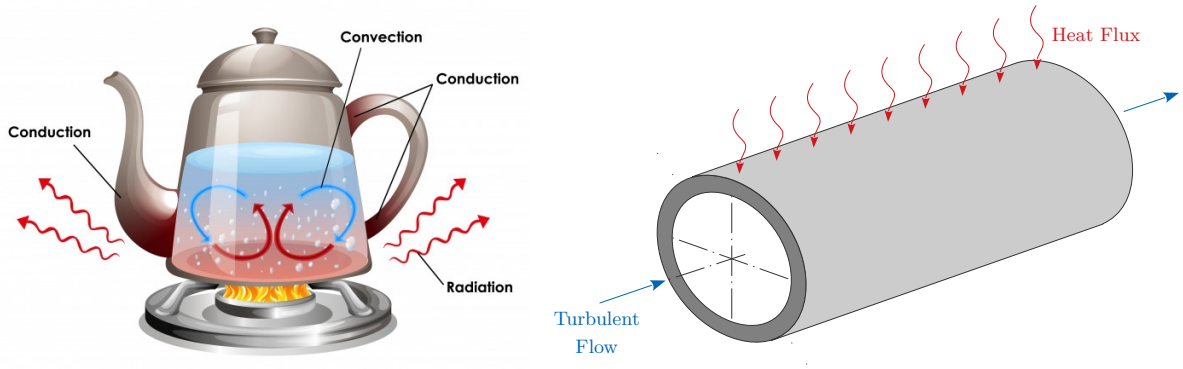

Figure 1.2: (Left) Illustration of the three basic ways in which heat can be transferred: conduction, convection and radiation. (Right) Schematic representation of the Conjugate Heat Transfer problem in the present pipe flow configuration.

Thanks to the progressive development of High Performance Computing (HPC), the investigation of these thermal phenomena are no longer limited only to experimental studies, as numerical simulations in much more demanding configurations are nowadays possible. This is our field of action here, the ultimate goal of the present work is to introduce a numerical technique for the high-fidelity simulation of the conjugate heat transfer in turbulent pipe flow configuration. To do so, in the course of the last three years, various numerical features have been developed and progressively embedded in the open-source code Incompact3d/Xcompact3d [7, 11, 12]. This massively parallel code has been in continuous development since its creation in Pprime Institute and counts today with a relatively large (and still growing) community of international developers [12].

In this chapter, fundamentals of wall-bounded turbulence and heat transfer in turbulent flows, relevant to this work, are briefly presented. Then, the numerical developments brought to the code as well as its main features are progressively described and validated throughout chapters 2 through 4. Chapters 5 and 6 are then dedicated to the numerical treatment of heat transfer in pipe flow.

1.1 Fundamentals of wall-bounded turbulence

As a matter of fact, most turbulent flows present in engineering applications are bounded by solid surfaces and the turbulent pipe flow, together with channel and boundary layer flows, are canonical examples with a wide spectrum of industrial applications. The presence of a solid body exerts strong influence on the behaviour of a viscous flow since viscous effects will govern the physics of the flow near the wall surface. Statistically speaking, the presence of a wall introduces inhomogeneity and anisotropy in the wall-normal direction, further increasing the complexity of the turbulent flow. Nonetheless, wall-bounded turbulent flows are of major relevance to the industry as ducts of different sizes and shapes are present in nearly every engineering design, hence the interest in thoroughly investigating, understanding and modelling wall effects in turbulence research.

In this section, main aspects of wall-bounded turbulence are briefly recalled using the pipe flow as a guideline. The flow configuration treated in this work is presented as well as the flow governing equations and relevant physical/statistical definitions. Then, the transport of temperature as a passive scalar is also addressed.

1.1.1 Turbulent pipe flow

Flow geometry We consider here the turbulent flow in a long, straight, circular pipe with uniform inner radius R and outer radius R_o, as illustrated in Figure 1.3. Because a regular Cartesian mesh is used in the present work, a Cartesian system of coordinates (x, y, z) is represented together with the cylindrical one (r, ϕ, z) associated to the wall geometry. They are both centred at the pipe axis and

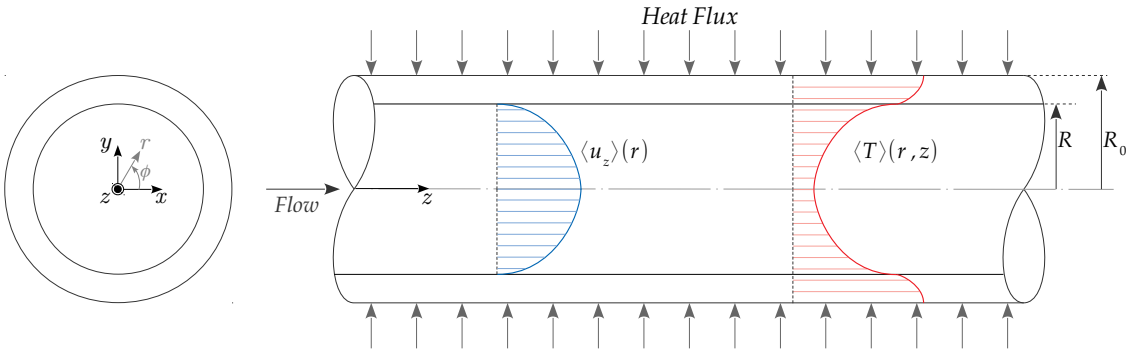

Figure 1.3: Sketch of the pipe flow geometry subjected to a heat flux at its outer surface $r = R_o$. Typical shapes of the the mean axial velocity and mean temperature are represented in blue and red respectively.

relate to each other according to

$$\begin{aligned} r &= \sqrt{x^2+y^2} \\ \phi &= \arctan(y/x) \\ z &= z \ . \end{aligned} \tag{1.1}$$

Governing equations The flow is governed by the incompressible Navier-Stokes (N-S) equations for a Newtonian fluid

$$\frac{\partial u_i}{\partial x_i} = 0 \tag{1.2}$$

$$\frac{\partial u_i}{\partial t} + \frac{1}{2}\left(u_j \frac{\partial u_i}{\partial x_j} + \frac{\partial u_i u_j}{\partial x_j} \right) = -\frac{1}{\rho}\frac{\partial p}{\partial x_i} + \nu \frac{\partial^2 u_i}{\partial x_j \partial x_j} + f_i \tag{1.3}$$

where repeated indices imply summation over the three Cartesian components $(x_1, x_2, x_3) = (x, y, z)$, this convention is kept in the rest of this monograph, unless indicated otherwise. The fluid density ρ and kinematic viscosity ν are assumed constant. The fluid velocity field is a function of time and space $u_i(x_i, t) = (u_x, u_y, u_z)$, as well as the pressure field $p(x_i, t)$ which is defined so that the incompressibility constraint (1.2) is satisfied. The convective term on the left-hand side (lhs) of eq.(1.3) is presented in skew-symmetric form, as it is numerically treated [7]. Here, the forcing term f_i corresponds only to the pressure gradient forcing

$$f_i = -\frac{1}{\rho}\frac{\partial \langle p \rangle}{\partial x_i}, \tag{1.4}$$

that compensates friction losses along the pipe in order to ensure a constant flow rate.

Reynolds number The Reynolds number translates the competition between inertial and viscous forces within a flow

$$Re = \frac{\textit{inertial forces}}{\textit{viscous forces}} = \frac{U_b D}{\nu}. \tag{1.5}$$

It is defined here with the pipe diameter D, the kinematic viscosity of the fluid ν and the bulk velocity U_b, which, for a duct of uniform diameter, corresponds to the average velocity through the cross-sectional area A_c

$$U_b = \frac{1}{A_c}\int_{A_c} \langle u_z \rangle dA_c \quad . \tag{1.6}$$

Evenly, the bulk velocity can be also defined by means of a volumetric average operator embedding the average operator $\langle\cdot\rangle$ (as it is numerically computed in the present work):

$$U_b = \frac{1}{\Omega_f}\int_{\Omega_f} u_z d\Omega_f \quad , \tag{1.7}$$

where Ω_f is the fluid inner volume of the pipe

$$\Omega_f = \{(r,\phi,z) \;\mid\; r \in [0, R[, \;\; \phi \in [0, \;\; 2\pi], z \in [0, L_z]\} \quad . \tag{1.8}$$

When viscous forces are predominant (i.e., at lower Reynolds number) the viscous term $\nu\nabla^2\boldsymbol{u}$ in eq.(1.3) tends to damp perturbations in the flow, preventing a turbulent wake from developing and the flow is therefore laminar. Contrarily, when inertial forces are dominant (higher Reynolds number), the non-linear convective term in eq.(1.3) overcomes the stabilizing effect of the viscous forces and small perturbations are amplified triggering transition towards a full turbulent state. Transition has a well established theoretical base nowadays and unlike the other canonical wall-bounded configurations, the laminar profile of a pipe flow is linearly stable for all Reynolds numbers [13], therefore, in order to trigger transition, two ingredients must be combined: a sufficiently fast flow and a sufficiently strong perturbation [14]. For this reason, the precise value of Re to trigger turbulent effects in a pipe flow is difficult to define, still, if a sufficiently strong perturbation is considered, as in the original experimentation of Osborne Reynolds in 1883 [15], the transitional value $Re \approx 2300$ is generally accepted and presented in theory [16, 17].

Statistical considerations Classically, turbulence has been seen as a random event and therefore investigated by means of statistical approaches [6, 13]. In the last three decades however, a more deterministic view has grown and much contributed to the present understanding of the physics involved in turbulence. In this scenario, randomness is no longer seen as a property but rather as a methodological choice, so that turbulence is treated as a dynamical system that satisfies the Navier-Stokes equations and the attention is turned to the investigation of coherent structures in the flow [18]. Numerically, this type of investigation requires a large amount of computational resources and, in many cases - depending on the desired application and available resources - a statistical approach remains the most suitable one. For instance, industrial engineering analyses are focused, in good part, on the performance of system by predicting certain of the flow characteristics such as stresses on a immersed body or the mixing of transported quantities in a duct [19]. In this case, statistical analyses (as well as the development of efficient models) are of major relevance in turbulence research.

As just mentioned, in a statistical framework, turbulence is studied as a random event and the flow quantities, treated as random functions in both time and space. We introduce therefore the Reynolds decomposition

$$f = \langle f \rangle + f' \ , \tag{1.9}$$

where $f(x_i, t)$ is a given quantity of the flow (such as velocity, pressure or temperature), $\langle f(x_i, t) \rangle$ is its ensemble average and $f'(x_i, t)$ is the fluctuations with zero mean value $\langle f' \rangle = 0$. By taking the ensemble average of the N-S equations (1.2, 1.3) while using (1.9), one obtains the mean-flow equations (not shown for conciseness, the reader is referred to [6] p.86) with its classic closure problem associated to the Reynolds stresses

$$-\rho \langle u_i' u_j' \rangle \ , \tag{1.10}$$

which arises from the non-linearity of the N-S equations. The mean-flow equations are analogous to the N-S ones with this supplementary stress, so that, physically, the mean motion can be interpreted as a real flow motion, smooth in space and time, subjected to *i*) mean pressure gradient, *ii*) mean molecular stresses and *iii*) the extra turbulent Reynolds stresses (1.10) (see [13], p.122).

In the present pipe configuration, homogeneity is assumed for the azimuthal-ϕ direction because of the axial symmetry . Analyses are always carried out in fully developed turbulent state, which allows us to assume a mean flow statistically stationary and independent of the streamwise-z direction. Thus, mean quantities are assumed to depend only on r - the inhomogeneous direction - and the ensemble average is therefore reduced to an average in ϕ, z and over time

$$\langle u_i(x_i, t) \rangle = \langle u_i \rangle (r) \ . \tag{1.11}$$

Mean pressure gradient When simplified with the above considerations, the conservation of wall-normal momentum in the mean flow reveals that the force induced by the mean pressure gradient is unidirectional and constant

$$-\frac{\partial \langle p \rangle}{\partial x_i} = \left(0,\ 0,\ -\frac{d\langle p \rangle}{dz} \right) \ , \ \text{with} \ \ \frac{d\langle p \rangle}{dz} = cst \ , \tag{1.12}$$

which implies a linear drop of the mean pressure $\langle p \rangle (z)$ along the duct. Moreover, the conservation of axial momentum displays an equilibrium between pressure and viscous effects in the mean flow direction

$$\tau_w = -\frac{R}{2} \frac{d\langle p \rangle}{dz} \ , \tag{1.13}$$

where τ_w is the mean wall shear stress given by

$$\tau_w = \rho \nu \left. \frac{d\langle u_z \rangle}{dz} \right|_{r=R} \ . \tag{1.14}$$

The friction losses induced by the wall shear stress are compensated by the forcing term f_i (1.4) - which may represent, for instance, the action of a pump - in order to sustain statistical steady state of the flow.

Friction quantities The predominance of viscous effects close to the wall requires the definition of viscous scales to consistently scale flow quantities. From the wall shear stress τ_w and flow density ρ, we introduce the *friction velocity* defined as

$$u_\tau = \sqrt{\frac{\tau_w}{\rho}} \ , \tag{1.15}$$

and an associated *viscous length scale* δ_ν which must account for the viscous effects in the near-wall region, so that

$$\frac{\delta_\nu u_\tau}{\nu} = 1 \Longrightarrow \delta_\nu = \frac{\nu}{u_\tau} \ . \tag{1.16}$$

And lastly the *viscous time scale*

$$\tau_\nu = \frac{\delta_\nu}{u_\tau} = \frac{\nu}{u_\tau^2} \ . \tag{1.17}$$

When flow quantities are normalized here with viscous scales, they are referred to as in *wall units* and the superscript '$+$' is used, e.g. the normalized distance from the wall $(R-r)/\delta_\nu = (R-r)^+$ and the normalized mean velocity profile $\langle u_z \rangle^+ = \langle u_z \rangle / u_\tau$.

Friction Reynolds number From the viscous scales, the *friction Reynolds number* is defined as

$$Re_\tau = \frac{u_\tau R}{\nu} \tag{1.18}$$

which can be interpreted as [20]

$$Re_\tau = \frac{\delta}{\delta_\nu} = R^+ \ .$$

That is, it translates the separation range between the length scale $\delta = R$, dictated by the geometry of the flow, and the viscous length scale $\delta_\nu = \nu/u_\tau$. Due to the influence of wall-viscous effects into the flow, coherent structures that compose wall-bounded flows are generally stratified in three layers according to their distance from the wall. These different regions influence directly the shape of the mean velocity profile as shown in Figure 1.4. In the *i*) *inner region*, viscous effects have strong influence over the structures and hence it is generally accepted that mean flow quantities scale with u_τ and δ_ν [18, 5]. In the *ii*) *outer region*, far from the wall, viscous effects are mostly negligible (analogously to free-shear flows) and the length scale is the flow thickness delimited by R, in the case of a pipe flow. Thus, Re_τ may be interpreted as a scale separation between inner and outer scales [18]. At higher Re (or Re_τ), this separation extends and a *iii*) *overlap layer* forms between inner and outer regions, where neither the flow thickness nor viscosity are relevant [18]. In statistical terms, this region has been interpreted as a cascade of momentum from the outer towards the inner region, which works as a sink of momentum at the wall, analogously to the turbulent energy cascade from large scales - responsible for the production of turbulent kinetic energy - toward the smallest scales, whose role is to dissipate it [21].

As a matter of fact, the canonical configurations - namely channel, boundary layer and pipe - are very similar in the near-wall and log-layer regions, differing mostly in the outer region because of the influence of the pressure gradient [22, 23].

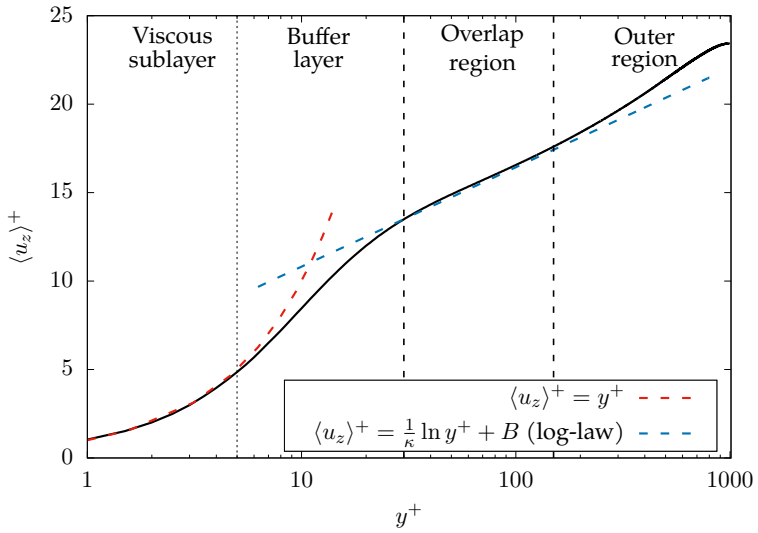

Figure 1.4: Mean velocity profile in wall units $\langle u_z \rangle^+$ from our DNS at $Re_\tau = 1000$. The inner region ($0 \leq y^+ \leq 30$) is usually sub-divided in viscous sublayer and buffer layer. In the former, the mean profile is linear with $\langle u_z \rangle^+ = y^+$ and the latter makes the connection with the overlap layer ($0 \leq y^+ \leq 0.15 Re_\tau$), which is not clearly identified due to the not sufficiently high Re_τ ($Re_\tau > 2000$ would be required [4]). There has been much debate whether this regions follows a logarithmic or power law [5]. Classically, the outer region ($0.15 Re_\tau \leq y^+ \leq Re_\tau$) is also scaled with u_τ and then the mean velocity is presented in terms of a velocity defect, following a defect law, see [6] p.272.

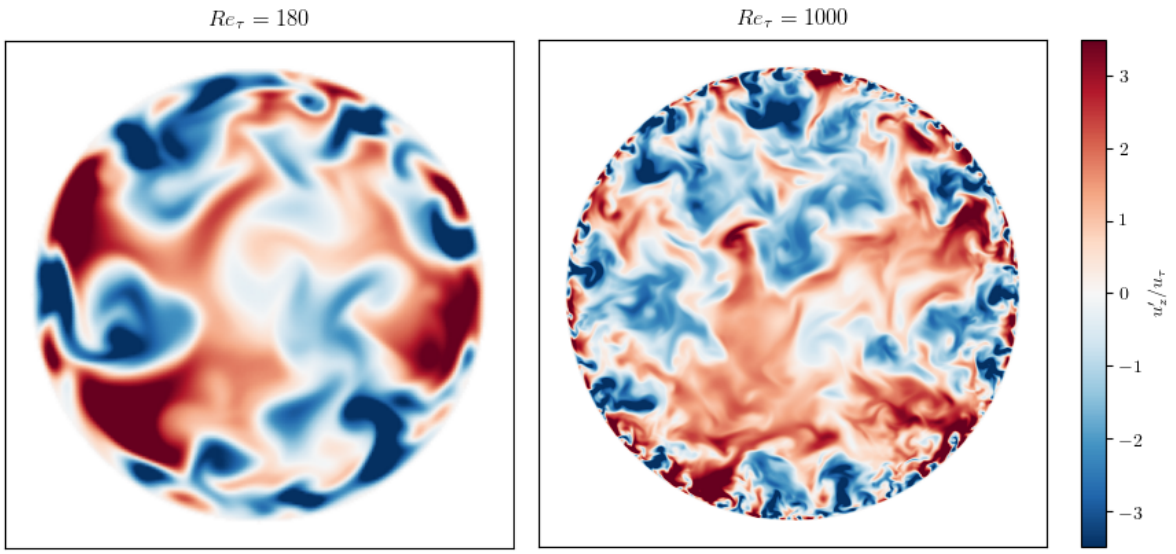

Figure 1.5: Snapshots of the normalized streamwise fluctuation velocity ${u_z'}^+$ at $Re_\tau = 180, 1000$ $(Re = 5300, 37700)$.

In the present work, numerical simulations are carried out at two nominal friction Reynolds numbers $Re_\tau = 180, 1000$; and Figure 1.5 provides two cross-sectional snapshots of the streamwise fluctuation velocity $u_z' = u_z - \langle u_z \rangle$ from our DNS, where the increase in the number of structures that compose the flow can be clearly perceived. Theoretical considerations on the fundamental scaling laws for the mean velocity profile are not presented here, the reader is referred to the good review of [5] which covers the main advancements in the last 50 years and the ongoing discussions on the topic.

1.1.2 Heat transfer in turbulence

In a general turbulent flow context, the flow field induces fluctuations on the scalar field through turbulent convection and, in turn, the fluctuating scalar field impacts the velocity field through mean gradients and density changes caused by the temperature variation [24]. We suppose here that these temperature fluctuations are relatively small which allows us to assume that the thermal field is transported without being affected by these temperature differences (passive scalar), such that, buoyancy effects can be neglected, as well as any temperature dependence of the fluid and solid material properties [24, 25].

In the present work, we consider the conjugate heat transfer context where a fully developed turbulent flow of an incompressible Newtonian fluid in a pipe is subjected to a constant heat flux at its outer surface, as illustrated in Figure 1.3. The load of heat received on the outer surface $r = R_o$ is transported

through the solid subdomain

$$\Omega_s = \{(r, \phi, z) \mid r \in [R, R_o], \ \ \phi \in [0, \ \ 2\pi], z \in [0, L_z]\} \tag{1.19}$$

by conduction only and then conveyed by the turbulent flow in the fluid subdomain Ω_f defined in eq.(1.8). Thus, heat transfer in the fluid medium is governed by the advection-diffusion equation

$$\frac{\partial T}{\partial t} + u_j \frac{\partial T}{\partial x_j} = \alpha \frac{\partial^2 T}{\partial x_j \partial x_j} \qquad \text{in} \quad \Omega_f \tag{1.20}$$

where $T(x_i, t)$ is the temperature field and $\alpha = \lambda / \rho c_p$ is the thermal diffusivity of the fluid with λ its thermal conductivity and c_p its specific heat at constant pressure (which for an incompressible fluid, as in here, is constant and equal to the specific heat at constant volume $c_p = c_v$). In the solid medium, heat transfer is governed by the unsteady heat diffusion equation

$$\frac{\partial T}{\partial t} = \alpha_s \frac{\partial^2 T}{\partial x_j \partial x_j} \qquad \text{in} \quad \Omega_s \tag{1.21}$$

where $\alpha_s = \lambda_s / \rho_s c_{p_s}$ is the thermal diffusivity of the solid with λ_s its thermal conductivity, ρ_s its density and c_{p_s} its specific heat at constant pressure.

As for the hydrodynamic quantities, temperature is decomposed into mean and fluctuating parts

$$T = \langle T \rangle + T' \ . \tag{1.22}$$

The typical shape of mean temperature profile $\langle T \rangle$ is illustrated in Figure 1.3 for the generic case where the wall temperature is higher than the fluid one $T_w > T$ (and fluid/ solid thermal properties $\lambda, \lambda_s, \alpha, \alpha_s$ are comparable), implying that heat transfer would be occurring from the solid towards the fluid.

Bulk temperature When dealing with internal flows, a reference temperature T_b must be defined to represent for the convection heat transfer in the confined flow what T_∞ - the fixed free stream temperature - represents for external flows [17]. The bulk temperature T_b is defined as an average quantity such that its transport in the mean flow (lhs of eq.(1.23)) represents the true rate of thermal energy advection integrated over the cross-sectional area (rhs of eq.(1.23)) [17]

$$\dot{m} c_p T_b = \int_{A_c} \rho c_p \langle u_z \rangle \langle T \rangle dA_c \ , \tag{1.23}$$

where $\dot{m} = \rho U_b A_c$ is the average mass flux. For an incompressible fluid, and from the definition of the bulk velocity U_b in eq.(1.6), the above expression may be rewritten as

$$T_b = \frac{\int_{A_c} \langle u_z \rangle \langle T \rangle dA_c}{\int_{A_c} \langle u_z \rangle dA_c} \ . \tag{1.24}$$

Note that T_b plays for the temperature field the same role that U_b plays for the velocity field and, when expressed like this, T_b is assumed uniform across the cross-sectional area. So, as it has been done for

the bulk velocity, the cross-sectional integrals may be equivalently replaced by volumetric ones

$$T_b = \frac{\int_{\Omega_f} u_z T d\Omega_f}{\int_{\Omega_f} u_z d\Omega_f} \quad . \tag{1.25}$$

This way, the local wall heat flux can be expressed with Newton's law of cooling as

$$q_w = h\left(T_w - T_b\right) \quad , \tag{1.26}$$

where h is the convection heat transfer coefficient, a parameter of major interest in engineering analysis.

Dimensionless parameters Throughout the years, many dimensionless parameters have been defined to translate important thermal characteristics of fluids and/or flows. We dedicate some words here to the most relevant ones for the present framework, for an extensive presentation of other meaningful quantities, the reader is referred to [17], p.376.

The *Prandtl number*,

$$Pr = \frac{\nu}{\alpha} \quad , \tag{1.27}$$

is a property of the fluid and those characterised by $Pr \ll 1$, such as liquid metals, transport energy (represented by the thermal diffusivity α) much more effectively than momentum (represented by the kinematic viscosity ν), the inverse is true for fluids with $Pr \gg 1$. For ideal gases, whose Prandtl number is near unity, the transport of the two quantities is comparable [17]. A fluid characterised by a Prandtl number higher than unity $Pr > 1$ develops a hydrodynamic boundary layer quicker than the thermal one; the inverse is true when $Pr < 1$ [17]. For the numerical simulations carries out here, two typical Prandtl numbers are considered $Pr = 0.71, 0.025$, representative of air and mercury respectively.

The *Nusselt number* provides a measure of the convection heat transfer occurring at the surface and it is a quantity of major importance in heat transfer analyses, representing for the thermal boundary layer what the friction coefficient represents for the velocity one. It is given by

$$Nu = \frac{hD}{\lambda} \quad , \tag{1.28}$$

or, from Newton's law of cooling eq.(1.26)

$$Nu = \frac{q_w D}{\lambda\left(T_w - T_b\right)} \quad . \tag{1.29}$$

For a fully developed flow of an incompressible fluid, both the heat transfer coefficient h and the thermal conductivity λ are assumed constant, implying $Nu = cst$ as well.

The *Péclet number*

$$Pe = \frac{U_b D}{\alpha} = RePr \quad , \tag{1.30}$$

translates the ratio of advection to conduction heat transfer of a given flow. For sufficiently high values $Pe > 100$, the heat transfer can be interpreted as essentially convective and axial heat conduction can be therefore neglected [26], which is valid for all cases in the present work, where even the most critic combination with $Re = 5300$ and $Pr = 0.025$ still provides $Pe = 132.5$.

Thermal boundary conditions The imposition of proper boundary conditions is a fundamental criteria to obtain realistic representations of real life phenomena. When dealing with the Navier-Stokes equations for instance, the velocity boundary conditions are well-defined from the no-slip condition. On the other hand, defining thermal boundary conditions (TBCs) that fairly represent a real heat transfer phenomena may not be so straightforward [27]. What is commonly done in numerical simulation of heat transfer in wall-bounded configurations is to bypass the heat conduction in the solid (1.21) and solve only the advection-diffusion in the fluid (1.20). In this case, assumptions and simplifications are made concerning the solid-to-fluid transfer of heat, and the physical process in the solid is modelled by a simplified/idealized TBC imposed to eq.(1.20) at the inner interface $r = R$. This approach is referred to as *ideal local imposition* in this monograph and it is the subject of chapter 5. It is widely recognised however that idealized TBCs cannot provide realistic representations of real life heat transfer in every possible scenario [28], since simplifications concerning the behaviour of temperature fluctuations at the wall cannot be avoided as long as the calculations are performed for the fluid side only. Alternatively, in the framework of *Conjugate Heat Transfer* (*CHT*) simulations, the heat conduction occurring in the solid is also solved and coupled to the fluid solution through shared conditions at the fluid-solid interface. This strategy can provide a fine description of the turbulent thermal interaction between fluid and solid media which may be valuable, for instance, to investigate applications where fluctuating thermal stresses are a concern and may even lead to thermal fatigue [28].

As mentioned, in chapter 5, ideal local imposition is addressed as a pathway into developing a numerical methodology for imposing Dirichlet and Neumann boundary conditions to the thermal field in the present computational configuration. This paves the way then to introduce in chapter 6 an original and high-fidelity technique to tackle *CHT* problems in complex geometries[1].

Statistical considerations The temperature field is also considered always in thermally fully developed state and statistical homogeneity is directly assumed for the azimuthal-ϕ direction. Concerning the axial direction however, the basic condition for heat transfer to occur between the solid body and the fluid is the existence of a temperature gradient, that is,

$$\frac{\partial \langle T \rangle}{\partial z} \neq 0 \quad \text{and, consequently,} \quad \frac{dT_b}{dz} \neq 0 \ . \tag{1.31}$$

In other words, the existence of convection heat transfer in the axial direction makes the temperature field statistically non-homogeneous in thermally fully developed conditions. This condition is represented in Figure 1.3 by the dependence of the mean temperature profile $\langle T \rangle$ on the streamwise-z direction, exemplifying the existence of a temperature gradient that triggers heat transfer between fluid and solid media.

Non-dimensional temperature The aforementioned condition (1.31) raises an obstacle for the numerical treatment/discretization of the flow direction. This hindrance can be, nonetheless, bypassed

[1]The term complex geometry refers to a mesh arrangement disconnected from the wall geometry

by working with suitable non-dimensional temperature forms $\Theta\left(T_w, T_b, T\right)$ such that

$$\frac{\partial\langle\Theta\rangle}{\partial z} = 0 \quad \text{and} \quad \Theta_b = cst \ , \tag{1.32}$$

which allows the streamwise direction to be practically treated as statistically homogeneous and thermally stationary [29, 17]. Distinct dimensionless expressions may be used according to their convenience when imposing one or another TBC (appropriate expressions of Θ will be presented in due time for each ideal TBC in chapter 5).

1.2 Computational Fluid Dynamics

The incompressible Navier-Stokes (N-S) equations (1.2, 1.3) are an excellent model to describe fluid motion, being able to provide very good predictions of turbulent flows, describing every details from the largest to the smallest length and time scales [13]. The inherent difficulty however is found in the complexity of this model, our mathematics, up to the present day, only allows for analytical solutions in simplified cases while turbulence is characterised by a "chaotic" organization, with many degree of freedom.

Yet, under the right assumptions, turbulence can be seen as a deterministic phenomenon which evolves in time in a very complicated way [13, 18]. This is the approach followed in numerical simulation of fluid dynamics - to put it better, *Computational Fluid Dynamics* (*CFD*) - where the partial differential equations (N-S) that describe the fluid motion with an infinite space-time continuum of values throughout some domain is approximated by only a finite number of discrete points in time and space [30]. In this process, called *discretization*, the continuous space-time is broken down on a grid of mesh $\Delta x, \Delta t$. Then, the once continuous spatial and temporal partial derivatives in the governing equations are now represented by analogous operators, that can be treated independently for space and time, and rely on appropriate algorithms (spectral, finite-difference, finite volume, finite elements, ...) to provide approximations of real life phenomena modelled by the N-S equations [31]. Moreover, given the just mentioned reliability of the N-S equations to describe fluid motion, from a given initial state and a set of boundary conditions, a deterministic/discrete time evolution of the flow can be calculated [13].

As highlighted by [5], it was in 1987 that the scientific community was convinced about the capability of numerical simulations to realistically reproduce turbulent flows, after the visualizations of [32] which successfully mimicked the experimental hydrogen bubble visualization of [33]. This work was recognised worldwide as a validated database and even used later to improve and validate new measurement techniques [23]. Since then, CFD has much evolved and numerical results have contributed to remarkable advancements in turbulence research. Furthermore, with an accurate and validated method, numerical simulations aim to work alongside with experimental research for the common goal: to improve theoretical understanding of turbulence [13]. For instance, for certain flow configurations - such as the turbulent confined flow considered here - accurate measurements may be very challenging to perform very near to the wall, under high-velocity and with an intrusive equipment. Another aspect is its versatility, e.g. vorticity fields can be easily and accurately calculated from numerical simulations [13].

If the spatial discretization Δx is fine enough to capture all the energetic scales that compose the flow (from the smallest, which dissipate energy as heat, to the largest which inject energy in the system), we refer to *Direct Numerical Simulation* (*DNS*) since all relevant information contained in the flow is explicitly (directly) computed and, therefore, does not require additional modelling. Despite the ongoing computational development, this approach is still limited to moderate Reynolds numbers lest it becomes too costly [13]. Alternatively, higher Reynolds number may be investigated by *Large-Eddy simulation* (*LES*)[2], where a not-so-fine mesh Δx is employed so that only the largest scales of the flow can be accurately computed. The smallest scales are filtered out (subgrid scales, SGS) and their effect is represented by a SGS model. LES contain some errors which are commonly associated to the numerical methods, or, as stated by [13], due to our current ignorance *vis-à-vis* the smallest scales, and to the lack of detail concerning the initial and boundary conditions. Throughout a simulation, these errors will be amplified by the non-linear behaviour of the equations and after a period of time the predicted field will differ significantly from the actual field [13]. This helps understand how, even for a deterministic system, unpredictability and randomness are still evoked [13]. Yet, as stressed by [13], LES remain extremely useful, since it can decently predict the shape (but not the phase and/or precise position) of the large vortices existing in the flow. Also, very often, it can suitably provide the statistical information needed by the engineer. Both DNS and LES of turbulent pipe flow are performed in this work with an inexpensive and accurate numerical methodology detailed in chapters 2 through 4.

1.2.1 Spatial discretization

As briefly mentioned above, the partial differential equations express the continuous solution of the dependent variables of the problem throughout the physical domain. Numerical solutions, on the other hand, provide results only at discrete points - that is *grid points* - in this domain [30]. In the process of spatial discretization of the governing equations (1.2, 1.3, 1.20, 1.21), first and second partial spatial derivatives, defined in the infinite continuum, are replaced by finite approximations provided by algebraic operators. The first step is to discretize the solution domain. This consists of inserting discrete locations into the geometrical domain where the problem is to be solved, that is, we define a *numerical grid*. Distinct types of grids may be used according to the shape of the body, complexity of the problem or numerical method used. In Figure 1.6 we illustrate the principle with a section of the discrete structured (regular) grid used for the present pipe geometry, each intersection between grid lines composes a grid point. The terms structured and regular refer to the consistent geometrical regularity based on a Cartesian organization of the grid with uniform spacing (grid size) in all three Cartesian-xyz directions

$$\Delta x = cst\ , \quad \Delta y = cst\ , \quad \Delta z = cst\ . \tag{1.33}$$

Furthermore, in here, for the transverse-xy directions we have always

$$\Delta x = \Delta y\ . \tag{1.34}$$

Following the definition of the numerical grid, a *method of discretization* must be chosen. There are many but we may focus only on *finite-difference* here as it is the method used in this work.

[2]For the sake of pertinence, we shall not consider Reynolds-Averaged Navier-Stokes (RANS) simulations here, the reader is referred to the comprehensive book of [6]

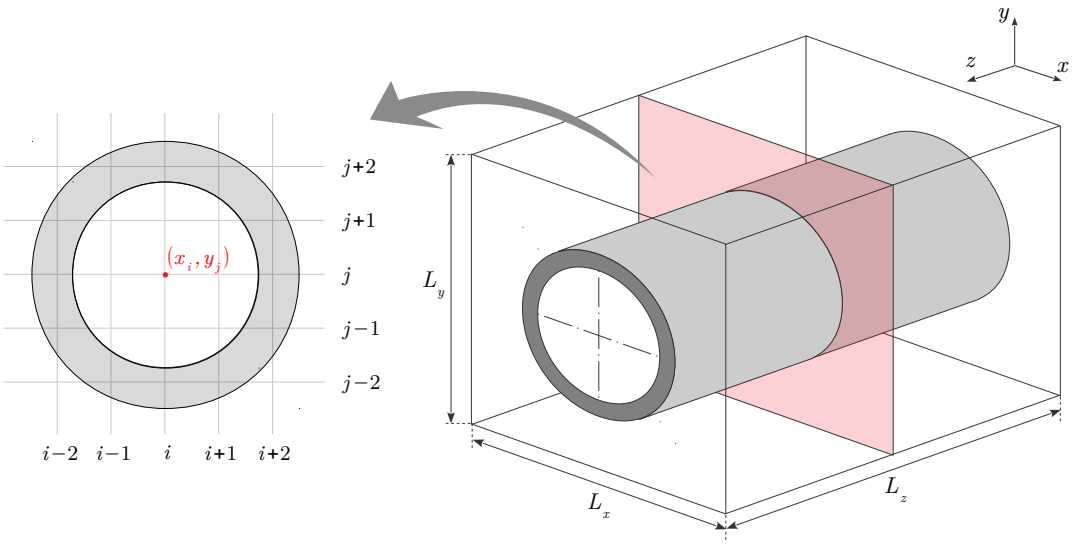

Figure 1.6: Illustration of the structured (regular) Cartesian grid used to discretize the present pipe geometry.

As stressed by [23], finite-difference is the simplest method to solve partial differential equations in regions bounded by simple as well as by complex geometries. In the finite-difference framework, the spatial differential operators are substituted by algebraic ones which are obtained from Taylor series expansions. More precisely, these algebraic operators are defined in terms of the neighboring discrete grid points and provide approximations of the partial spatial derivatives with a certain *order of accuracy* which corresponds to the truncation error of the Taylor series. The order of accuracy dictates how quick the discretized solution converges towards the exact one as the number of grid points goes to infinity (or, equivalently, the grid size goes to zero). Different types and orders of accuracy may be used for the finite approximations of the spatial derivatives which defines the *numerical schemes* for the spatial discretization. The choice of the finite approximation is crucial for the reliability of a numerical method, as it defines its *numerical properties* (consistency, stability, convergence, conservation, accuracy, etc). As stressed by [31], when defining a numerical method, a compromise between simplicity, ease of implementation, accuracy and computational efficiency has to be made.

In the present context where a regular grid is used, the numerical implementation of finite-difference is straightforward and higher-order schemes can be easily defined. The complete description of the spatial discretization is given in the next chapter, section 2.6. Although greater accuracy can be obtained from the association of regular Cartesian grid and finite-difference discretization, note that it results in a mesh arrangement disconnected from the wall geometry, as it can be seen in Figure 1.6. In cases like this, what is commonly done to conciliate grid and body geometry is to use an Immersed Boundary Method.

1.2.2 Immersed boundary methods

In the previous sections, we have highlighted in different occasions the importance of prescribing consistent boundary conditions (BC) to the partial differential equations in order to fairly represent real life phenomena. Likewise, in CFD, the proper choice and imposition of BC is a crucial factor to obtain reliable physical representations out of numerical results. To do so, traditional methods employ *body-fitted meshes* which consists of design the grid (either structured or unstructured) to follow the shape of the object immersed in the flow, see representation in Figure 1.7-(b). This approach causes the grid point to coincide with the boundary of the object, making the imposition of the desired BC straightforward. Another advantage is the possibility of locally refining the grid near the body (as also illustrated in Figure 1.7-(b)) in order to satisfy the requirements of normal mesh resolution to properly capture the viscous effects in wall-bounded turbulent flows [19, 34, 23]. However, this strategy has also its drawbacks, for instance, if a finite-difference method is to be used with a structured mesh, the governing equations must be transformed onto a curvilinear system of coordinates [31]. In addition, for more complex geometries, the generation of a proper grid can be very demanding in terms of computational resources (in particular for simulations with moving bodies for which a remeshing is needed every time step) and user input. All these factors can make the simulation much more costly and lead to loss of accuracy due to grid distortion [35].

Alternatively, an *Immersed Boundary Method* (*IBM*) may be used. In this scenario, a structured grid is generated without taking into account the solid boundaries as illustrated in Figure 1.7-(c). This naturally allows the treatment of more complex geometries with the presence of the body being generally modelled through a modification of the governing equations. This modification can be done in many different ways, reason why - since the method was designed in the 70's to simulate the flow around heart valves [36, 37] - many variations and novel approaches have been developed, especially in the last 20 years [38, 39, 40, 41, 42, 43, 44, 45, 46, 47]. Because the structured (usually Cartesian) mesh can be kept even when the flow around complex-shaped bodies is concerned, efficient numerical schemes such as fast Fourier transform algorithm and high-order compact schemes can be straightforwardly used [7]. Fundamentally, the introduction of the forcing term that reproduces the effect of the body can be done in two different ways, which allows us to roughly divide the many existing strategies in two groups: *continuous* and *discrete* forcing approaches.

Continuous forcing approach The forcing function is implemented on the continuous (not discretized) governing equations and hence can be applied everywhere in the computational domain. The action of the body is represented through a model - for instance, in the original work of [36], the heart valves have been modelled as an elastic solid body following Hooke's law - and a smooth delta Dirac function is used to administer its effect on the target surrounding nodes. Since its first implementation, this method has been mostly used for biological applications and multiphase flows where elastic boundaries are widely considered. For rigid bodies, such a representation is more challenging but can still be used by modelling the elastic body on the rigid limit, however, it may raise accuracy and stability problems [35].

Discrete forcing approach Here, the effect of the boundary is modelled directly on the discretized equations. A numerical procedure is defined to apply the effect of the body on the cells near to the boundary, resulting, usually, in a modified system of equations [35]. Within this category, the methods can be still be subdivided in *indirect* [48, 41] or *direct* forcing [49, 40, 44].

Among the disadvantages of IBM, one may cite the loss of accuracy condensed in the near-wall region depending on the quality of the forcing technique. Also, the consequences of the boundary treatment on the conservation properties of the numerical scheme are not so easy to determine and, since it is normally used in the context of a non-body fitted meshes, it may be tricky to precisely define the grid resolution in the vicinity of the body. However, these methods are attractive for their many advantages such as simplicity (even when complex geometries are considered), favourable computational cost (especially when simulating moving bodies) and accuracy - notably when high-order finite difference schemes are used [35, 50].

Nowadays, the use of immersed boundary methods is not only an alternative for the treatment of complex geometries but beyond that, in many cases, more sophisticated IBM are used as a methodological choice, providing efficient answers to real requirements of industrial applications. For instance, Strandenes *et. al* [51] represented the solid geometry through an IBM (based on least square interpolation for direct forcing of first fluid nodes [42]) while using a Cartesian grid with local refinement by zones, which enabled the proper resolution of the boundary layer and wake behind the cylinder. Another example is the Immersed Boundary Conditions (IBC) approach [46, 52], where the immersed boundaries are handled in a *quasi* body-fitted mesh enabling the treatment of complex industrial configurations. For instance, the Zonal Immersed Boundary Conditions (ZIBC) methodology has been used by Weiss and Deck [46] for the simulation of the Ariane 5 space launcher.

The goal of this section is not to provide a comprehensive description of the different IBM strategies developed in the last 50 years of research in the domain. For that purpose, the reader is referred to the complete review article of [35] and more recently [53]. We aim here rather to present the fundamentals in general lines in order to described later on, in section 2.5, the customised IBM developed over the last 10 years in the framework of Incompact3d/ Xcompact3d.

1.2.3 Time integration

The time discretization, or *time grid*, may be regarded in the same fashion as the spatial discretization with finite-difference, that is, as discrete points in time, spaced by a time-step Δt. Still, differently from the computation of the spatial derivatives of the incompressible N-S equations (which has an elliptic behaviour), the time solution has a parabolic-like behaviour, meaning that a forcing in time at a certain moment can only affect future values of a the quantity concerned [31]. In this sense, to be consistent with the physical nature of time, from a given initial condition, the numerical solution is advanced (integrated) in time step-by-step. As pointed-out by [54], some requirements must be met by a time-integration method: *accuracy, efficiency, flexibility and physical consistency* (see p.98 of [54]). Nonetheless, it is generally not possible to equally comply all of them and a balance must be sought. Furthermore, the author stresses that there is little use for an extremely accurate method if it is not

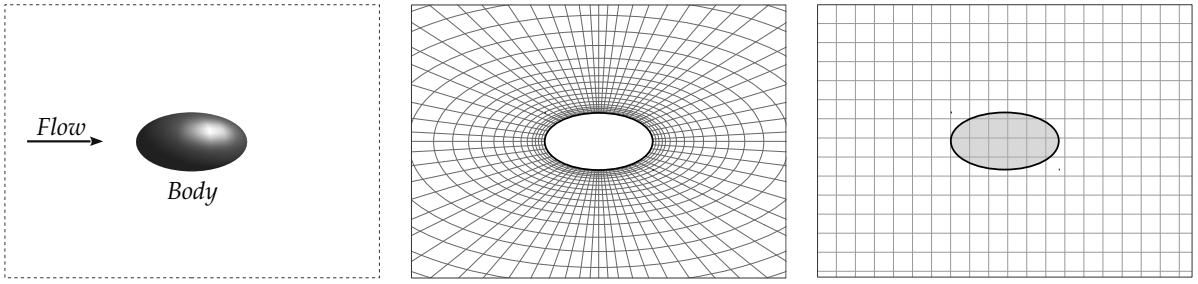

(a) Physical representation (b) Structured body-fitted grid (c) Regular Cartesian grid (non-body fitted)

Figure 1.7: Illustration of a (a) structured body-fitted mesh and a (b) regular Cartesian mesh which does not conform to the body geometry. In the Cartesian grid representation, blue points designate fluid domain and the red ones solid domain.

efficient or capable of treating the flow complexities in a particular application of interest.

As for the spatial discretization, time-integration methods are to provide consistent solutions with small time steps Δt. However, as highlighted by [31], the behaviour of methods for a large step size is important because in problems with widely varying time scales (such as the present turbulent flow in wall-bounded configuration), the goal is often to compute the slow, long term behaviour of the solution and the short time scales are merely a nuisance. This discussion raises the issue of *stability*, for which a time-integration method may be defined as stable if it produces a bounded solution [31], this aspect is further explored in chapter 4.

Time-integration schemes are either *explicit* or *implicit*, the former requires only information from previous time steps $(n, n-1, n-2, ...)$ to predict the new value $n+1$ of a certain quantity of the flow, while the latter uses also information on time level $n+1$ and therefore requires an iterative solution to obtain the new values for the quantities. Explicit schemes has the disadvantage of being unstable for larger time steps, yet, they are relatively easy to use and program and, since they require one single evaluation of the time derivative per time step, they are also relatively cheap [30]. Conversely, implicit schemes are generally more stable but usually are more costly (longer time per time step) and require more computer memory [31]. Another important aspect of time-integration methods is their formal *order of accuracy*, which can be generally increased by using information at more points in time, in this sense we refer to *multi-points methods* [31].

Conventionally in Incompact3d/Xcompact3d, simulations of turbulent pipe flow have been carried out with a full-explicit time integration of convective and diffusive terms in eqs.(1.3, 1.20, 1.21) with a third-order Adams-Bashforth scheme (AB3). Chapter 4 of this text is dedicated however to a new filtering technique for DNS/LES which - when combined with the explicit time-integration with AB3 - can considerably relax stability constraints related to diffusivity, allowing for the use of significantly larger time steps which ultimately leads to remarkable savings of computational resources.

1.3 General conclusion

Some fundamental aspects of wall-bounded incompressible turbulence while including heat transfer are recalled in section 1.1 and applied to the flow geometry treated in this work. More precisely, fundamental concepts of turbulent pipe flow and fluid-solid thermal interaction in turbulent flows are briefly discussed in sections 1.1.1 and 1.1.2. These are key concepts for the discussions to be developed in the following chapters. Likewise, fundamental principles of Computational Fluid Dynamics (CFD) relevant in the present work - such as Immersed Boundary Method (IBM) and space-time discretization - are subsequently recalled in section 1.2.

Version française

Quelques aspects essentiels de la turbulence pariétale incompressible avec transfert thermique sont rappelés dans la section 1.1 par référence à la configuration d'écoulement traitée dans ce travail. Plus précisément, les concepts fondamentaux reliés à l'écoulement turbulent dans une conduite et les enjeux associés de l'interaction thermique fluide-solide sont brièvement discutés dans les sections 1.1.1 et 1.1.2. Il s'agit des concepts clés pour les discussions qui seront développées dans les chapitres suivants. De même, les éléments essentiels de la stratégie numérique suivie dans ce travail qui relève de la Mécanique des fluides numérique (CFD en sigle anglo-saxon), en particulier la Méthode des frontières immergées (IBM en sigle anglo-saxon) et la discrétisation spatio-temporelle, sont ensuite rappelés dans la section 1.2.

Chapter 2

Numerical Methods

In the present work, DNS and LES of turbulent pipe flow are carried out with the open-source code Incompact3d/ Xcompact3d [7, 11, 12]. Moreover, thanks to its attractive computational efficiency and suitable structure, many numerical tools have been developed, adapted and implemented in the framework of this thesis. This chapter is therefore dedicated to providing a description of the fundamental numerical aspects of the code so that the main numerical developments may be progressively presented in the following chapters. Firstly, an overview of the code and its general features is given, followed by a description of the flow configuration, governing equations, initial conditions and customised immersed boundary technique. Next, the spatial discretization is presented while focusing on the notion of targeted numerical dissipation for regularization, an essential concept for the present numerical framework. Thereafter, the time integration strategy is described followed by the statistical averaging methodology used in the present computational configuration.

2.1 The code Incompact3d/Xcompact3d

Incompact3d is an in-house open-source code developed in a partnership between Pprime Institute and Imperial College London since the mid-90's [7, 11]. This code solves the incompressible Navier-Stokes equations by means of DNS and LES in the context of High Performance Computing (HPC). Among its attractive numerical features to investigate incompressible turbulent flows, we may cite: *i*) the quasi-spectral accuracy; *ii*) the treatment of complex geometries and *iii*) the advantageous computational efficiency. The first one is achieved thanks to the use of high-order compact finite-difference schemes (the subject of section 2.6) combined with a regular Cartesian grid[1]. Despite the use of a simple regular grid, the treatment of complex geometries is done thanks to an efficient immersed boundary method (IBM) adapted to high-order spatial schemes (the subject of section 2.5). Concerning the third

[1] a mesh refinement in one direction is also enabled by the code, but it has not been used in this study

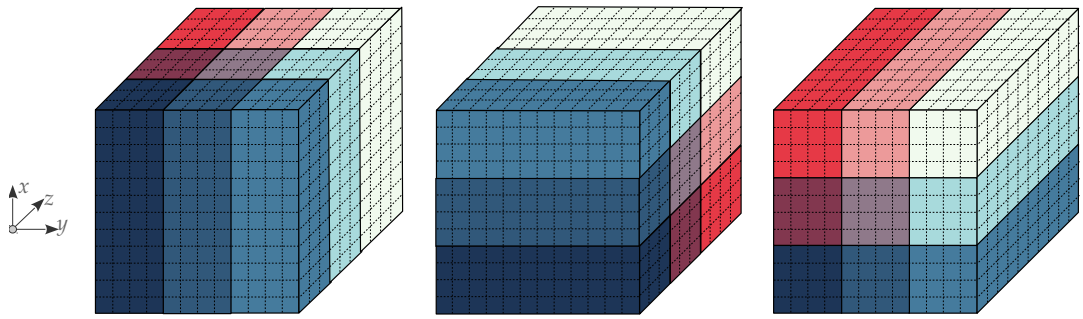

Figure 2.1: Illustration of the 2D decomposition of the computational domain in Incompact3d/Xcompact3d. In this representation, 9 (3×3) MPI processes are used. Different colours mean different MPI processes.

aspect, since 2010, Incompact3d has been rebuilt around the *2D Decomp and FFT library* [55] which introduced a 2D (or *pencil*) decomposition of the computational domain, following an idea initially implemented for spectral codes [11]. Schematic representations of the pencil decomposition are provided in Figure 2.1 for: *a*) *X-Pencils*, *b*) *Y-Pencils* and *c*) *Z-Pencils*. The basic principle is to perform all the finite-difference operations (and Fourier transforms) in only one direction - the *pencil* direction - at time, the domain is partitioned in two Cartesian directions and each MPI process manages the data contained in one block. Thanks to this improvement, issues related to serial processors memory resources (due to the 1D - or *slab* - decomposition previously used) were solved, enabling the code to be executed on massively parallel computing systems. Its scalability has been demonstrated for up to one million MPI processes while keeping its computational efficiency. The implementation and validation of this 2D decomposition method are entirely issued from [11]. Another great feature of Incompact3d is the resolution of the Poisson equation that satisfies the incompressibility condition, which is fully solved in spectral space by applying relevant three-dimensional fast Fourier transforms (*3D FFT*). Through the concept of modified wavenumber (to be discussed also later in this chapter), the divergence-free condition can be ensured up to the machine accuracy.

Throughout the years, many developments have been brought to the code's architecture thanks to the constant growth of the international community of users. As a result, the capabilities of the code have been expanded in terms of flow regime (up to compressible flow regime at low Mach number) and flow geometries. Thus, recently, a new version of the code has been released under the name *Xcompact3d* in which the main developments have been restructured and grouped together in a user-friendly design. Many ready-to-run simulations are available in this new version, for a detailed description the reader is referred to [12]. The implementation of the turbulent pipe flow in Xcompact3d has also been an important part of this thesis.

2.2 Computational configuration

For the description of the numerical methodology provided in this chapter, we consider the standard flow solver approach of Incompact3d/Xcompact3d, where only the DNS and LES solutions of the fluid zone are concerned. The numerical developments brought to the code to deal with the multi-physics Conjugate Heat Transfer (CHT) problem is fully described later on in chapter 6.

A schematic view of the computational configuration is presented in Figure 2.2. The pipe geometry of uniform inner radius R, outer radius R_o and longitudinal length $L_z = 12.5D$ is centred in a computational domain $\Omega = [-L_x/2, L_x/2] \times [-L_y/2, L_y/2] \times [0, L_z]$, with $L_x = L_y$. The domain is then discretized with a regular Cartesian mesh of $n_x \times n_y \times n_z$ nodes regularly distributed with $n_x = n_y$, leading to the uniform grid spacing [2]

$$\Delta x = L_x/n_x \ , \quad \Delta y = L_y/n_y \ , \quad \Delta z = L_z/n_z \ , \tag{2.1}$$

with $\Delta x = \Delta y$. The Cartesian frame of reference is placed on the axis of the pipe and the regular distribution of grid points is given by

$$x_i = (i-1)\Delta x - L_x/2 \tag{2.2}$$
$$y_j = (j-1)\Delta y - L_y/2 \tag{2.3}$$
$$z_k = (k-1)\Delta z \tag{2.4}$$

where the index i runs in the transverse-x direction, the index j runs in the transverse-y direction and the index k runs in the streamwise-z direction. For the sake of convenience, we may use throughout this text both the Cartesian coordinates $(x_1, x_2, x_3) = (x, y, z)$ associated to the computational mesh and the cylindrical coordinates (r, ϕ, z) associated to the pipe geometry where r is the radial distance to the pipe axis, ϕ is the azimuthal angle $\phi = \arctan(y/x)$ and z is the common streamwise direction. The relationship between the two system of coordinates is given by

$$r_{ij} = \sqrt{x_i^2 + y_j^2} \tag{2.5}$$
$$\phi_{ij} = \arctan\left(\frac{y_j}{x_i}\right) \tag{2.6}$$
$$z_k = z_k \ , \tag{2.7}$$

and is illustrated in Figure 2.3. The use of a Cartesian mesh also offers a straightforward solution for the classical difficulty of dealing with the singularity at $r = 0$. As stressed by [23] in chapter 10 of his book, this is one of the major reasons for the scarcity of pipe flow simulations in literature (when compared to channel and boundary-layer flows for instance) as the treatment of the centre condition commonly implies additional programming work, loss of accuracy and/or extra computational cost.

The conciliation between the nodes distribution and the wall geometry is done with the customized IBM also illustrated in Figure 2.2. The technique is based on reconstructions of the solution into the

[2] With periodic boundary conditions at the domain borders

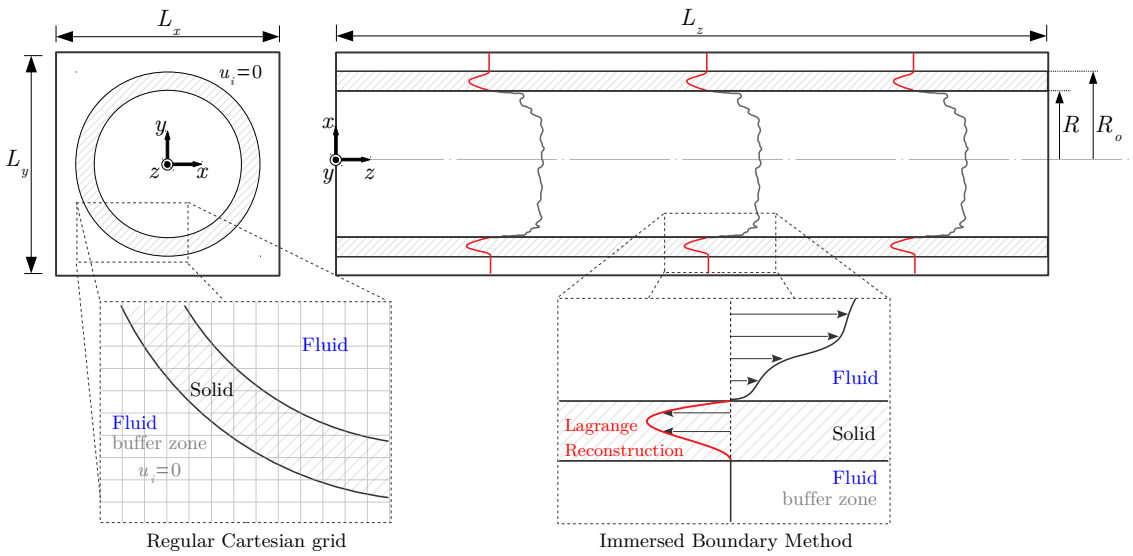

Figure 2.2: Schematic view of the computational configuration. The zoomed views evidence the buffer zone, the regular Cartesian grid and the immersed boundary technique.

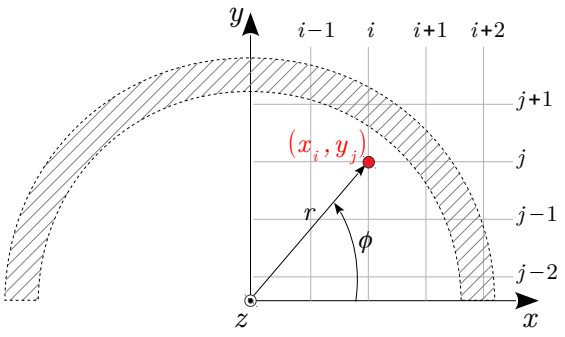

Figure 2.3: Relationships between the transverse-xy Cartesian coordinates and the cylindrical coordinates r and ϕ.

immersed boundary region, which corresponds to the annular volume $R \leq r \leq R_o$, i.e. the wall thickness $(R_o - R)$. Note that the region $r > R_o$ corresponds to a buffer fluid zone with a *dual* role of ensuring the success of the reconstruction of the solution while allowing the imposition of periodic boundary conditions at the boundaries of the computational domain in the transverse-xy directions, more details are given in sections 2.3 and 2.5

Special care must be taken when choosing the longitudinal length L_z. As periodic boundary conditions are enforced in the longitudinal direction, the domain size must be appropriately chosen in order to avoid an artificial influence on the statistics while enabling to capture the largest turbulent velocity and thermal structures. In an experimental study in 1999, [56] introduced the term 'very large-scales of motion' (VLSM) to put in evidence structures observed with lengths of $5R$ up to $20R$ in the outer layer of fully developed turbulent pipe flow. More recently, these observations have been confirmed by [57] and [58] who also underlined the important and active role of these structures, which contain up to half of the turbulent kinetic energy of the streamwise direction. Over the last years, many numerical studies have analyzed the importance of these structures on both velocity and temperature statistics, with the influence of VLSM being widely analyzed on statistics of higher and lower order, one and two-point statistics, going from low to high Reynolds and Prandtl numbers [59, 22, 60, 61, 62, 63]. Following these considerations, $L_z = 12.5D$ have been selected as a sufficient pipe length to properly capture the long structures and ensure reliable first and second-order statistics for the range of Reynolds and Prandtl numbers considered in the present work.

2.3 Governing equations

As mentioned in chapter 1, the incompressible Navier-Stokes equations (continuity, momentum and the passive transport equation for the temperature field) are solved for the turbulent pipe flow. To allow scaling to real flow conditions and comparison with analogous flow configurations (such as boundary layer and channel flows), the quantities of the problem are non-dimensionalized with the bulk velocity U_b and the pipe diameter D:

$$\begin{aligned} t^* &= \frac{t}{D/U_b} \\ x_i^* &= \frac{x_i}{D} \\ u_i^* &= \frac{u_i}{U_b} \\ p^* &= \frac{p}{\rho U_b^2} \\ \Theta &= f(T, T_b, T_w) \ . \end{aligned} \tag{2.8}$$

For the sake of convenience, we introduce for now the dimensionless temperature Θ without providing a formal expression. When imposing one or another type of thermal boundary condition (TBC),

distinct dimensionless expressions can be conveniently defined in terms of the bulk T_b and wall temperature T_w. Hence, appropriate expressions will be presented at due time in chapter 5.

Henceforth, only dimensionless quantities are used unless stated otherwise, we may therefore drop the asterisk notation $(^*)$ for non-dimensional quantities. The substitution of the above expressions into the governing equations (1.2, 1.3, 1.20) leads to the following dimensionless governing equations

$$\frac{\partial u_i}{\partial x_i} = 0 \tag{2.9}$$

$$\frac{\partial u_i}{\partial t} + \frac{1}{2}\left(u_j\frac{\partial u_i}{\partial x_j} + \frac{\partial u_i u_j}{\partial x_j}\right) = -\frac{\partial p}{\partial x_i} + \frac{1}{Re}\frac{\partial^2 u_i}{\partial x_j \partial x_j} + f_i \tag{2.10}$$

$$\frac{\partial \Theta}{\partial t} + u_j\frac{\partial \Theta}{\partial x_j} = \frac{1}{Pe}\frac{\partial^2 \Theta}{\partial x_j \partial x_j} + f_\Theta \tag{2.11}$$

with $Pe = RePr$ according to eq.(1.30). Note that the convective term of the momentum equation (2.10) is expressed in skew-symmetric form. When computed this way, aliasing errors are reduced while remaining energy conservative for the spatial discretization of the code [64, 7]. In contrast to the classical LES approach, for the implicit LES (ILES) technique used here, no explicit SGS modelling is applied to the equations, instead, numerical dissipation is used to regularise the solution as a substitute to explicit SGS modelling [65]. For this reason, the governing equations are the same either solved in DNS or ILES mode. The forcing term f_i corresponds to the mean pressure gradient that drives the flow. Following the discussions in section 1.1.1, only the streamwise component has a non-zero value,

$$f_i = (0, 0, f_z) \quad ,$$

which here is constant in space but adjusted every time step to compensate the viscous friction in order to sustaining a stationary regime. Similarly, f_θ is the source term that arises from the non-dimensionalization and sustains stationary thermal regime for the temperature field Θ. The numerical treatment for f_i is presented further below in section 2.7, whereas f_Θ is described in chapter 5, section 5.2.3.

2.3.1 Boundary conditions

Within the present numerical strategy, the pipe geometry is fully immersed in the computational domain and thus 3 well defined regions can be identified: the fluid subdomain $r < R$, the solid subdomain $R \leq r \leq R_o$ and the surrounding buffer zone $r > R_o$ which consists of fluid at rest (no driving force is applied here). Accordingly, boundary conditions are to be defined at (i) the inner immersed boundary $r = R$; (ii) the (inner and) outer immersed boundaries ($r = R$ and) $r = R_o$; and (iii) at the boundaries of the computational domain.

The prescription of BCs (i, ii) are made with the IBM described further below in section 2.5. Concerning the domain boundaries (iii), in the streamwise-z direction, periodic boundary conditions are

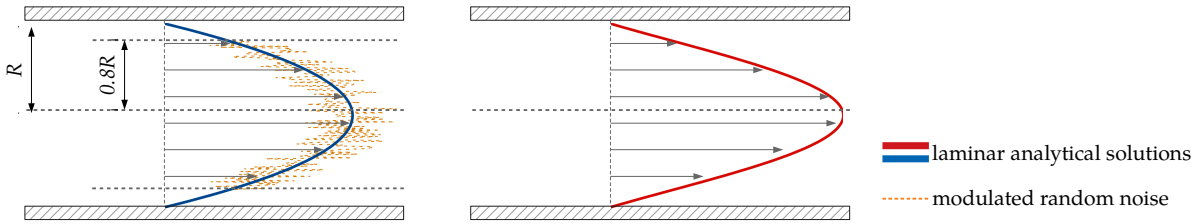

(a) Velocity (b) Temperature

Figure 2.4: Illustration of the initial conditions for (a) velocity and (b) temperature fields.

prescribed, which is only possible thanks to the compensation of friction losses along the duct performed through the source term f_i. Periodic boundary conditions are equally prescribed in the transverse-xy directions, which is only possible thanks to the insertion of the buffer zone $r > R_o$. The insertion of this zone corresponds to an oversizing of the computational domain in these directions. Although this may be seen as disadvantageous in terms of computational performance, this region is extremely important for the present numerical strategy as it allows us not only to prescribe tri-periodic boundary conditions (and thus conserve the accuracy of the high-order finite-difference schemes at the boundaries of the domain), but also to ensure the success of the present IBM.

2.4 Initial conditions

2.4.1 Velocity

The initial condition for the velocity field is the Poiseuille laminar flow:

$$u_z(r) = 2\left(1 - \frac{r^2}{R^2}\right), \quad u_r = u_\phi = 0 \ . \tag{2.12}$$

In order to force transition, a modulated random disturbance of large amplitude is superimposed to the laminar profile at the core of the pipe as illustrated in Figure 2.4-(a). Such a perturbation contains a large initial turbulent kinetic energy and for a matter of numerical stability it is introduced only in $r < 0.8R$, i.e., sufficiently far from the near-wall region. This disturbance is then naturally spread towards the wall during the first time iterations. During the transient phase, the level of turbulent kinetic energy drops before raising again to reach the fully-developed turbulent state, in agreement with observation of [23].

2.4.2 Temperature

Two types of local imposition of thermal boundary conditions are considered in this work, namely mixed-type (MBC) and isoflux (IF), they will described in details in due time in chapter 5. The initial conditions for the temperature filed corresponds to the analytical laminar solution according to the thermal boundary condition used

$$\Theta(r) = 2Nu\left(\frac{3}{16}+r^4-r^2\right) \qquad \text{for MBC} \tag{2.13}$$

$$\Theta(r) = 2\left(\frac{3}{16}+r^4-r^2\right)-\frac{1}{Nu} \qquad \text{for IF} \ . \tag{2.14}$$

No extra perturbation is needed here to force transition as the disturbance introduced in the velocity field is naturally transmitted to the temperature through the convective term in eq.(2.11).

2.5 Immersed boundary method

The immersed boundary method (IBM) plays the role of conciliating the cylindrical pipe geometry with the Cartesian regular mesh. In section 1.2.2 we have briefly introduced the concept of IBM by reviewing traditional approaches, here, the different IBM strategies used in Incompact3d over the years are outlined then the technique used in the present work is described.

Since its development in the mid 90's, Incompact3d makes use of simple Cartesian grids[3] for spatial discretization, implying that immersed boundary methods have been constantly used over the years to simulate flows around solid bodies. In this period of about 30 years, the user's community grew and some strategies have been further developed, updated and/or replaced, but always using discrete forcing approaches of direct nature. The IBM implemented in its first version was the simple direct forcing originally proposed by [66]. This strategy satisfies the no-slip condition by roughly imposing a null velocity on mesh nodes found in the solid region and thus, the modification on the governing equations is brought on the time integration in a straightforward manner [67]. Its advantage is found, as mentioned, in its simplicity, whereas the biggest disadvantages are: *i*) the lack of accuracy since the precise position of the boundary is never defined, this incertitude being of the order of the mesh size and implying a global error convergence of only 1^{st} order; *ii*) the presence of discontinuities on the derivative at the solid-fluid interface leading to strong spurious oscillations around the interface when high-order compact schemes are used.

To overcome this problem, [68] proposed a new method in which the forcing term creates an internal flow by mirroring the flow around the body. In this way, besides ensuring the no-slip condition, first derivatives across the immersed boundary are also conserved. The method has been developed and validated in the framework of the flow around a cylinder and to manage the discontinuity of the forced

[3]For which a mesh refinement is available in one direction of space.

flow at the centre of the body, a modulation function was used [68, 69, 70, 44]. This strategy based on mirrored flows had been already used by [39, 38] among others - but only to impose a mirrored velocity at the first solid node, never to reconstruct a fictitious flow inside the object. Within this approach an outstanding reduction on the spurious oscillations near the boundary was obtained, nonetheless the method lacked of flexibility and automatism since it could not be straightforwardly implemented for different geometric shapes (the modulation function and the mirroring procedure are not so easy to define for other complex geometries than the cylinder one). For aeroacoustics applications, [71, 72, 73] used the IBM of [38] to perform shape optimisation of cylinders for aeolian noise reduction. In this version, the presence of the solid was modelled by a forcing term in the momentum equations, defined as damped oscillator.

In 2013, [67, 50] implemented a new direct forcing technique specially developed to answer to the fundamental needs uncovered by the technique of [68]. Within this new strategy, the no-slip condition is softly satisfied while preserving the first derivatives continuity across the interface. This is accomplished through an *unidimensional* reconstruction of the physical solution into the body domain by means of *Lagrange polynomial interpolation*, allowing the spatial differentiation to be performed without any particular treatment near the fluid/solid interface. The 1D interpolation feature makes the method robust and flexible, applicable to any type of geometry with no need of estimating the distance to the closest wall. In terms of computational implementation, the technique is customised for Incompact3d's massively parallel architecture, the inner fluid interpolation is enchained with the derivatives computation as they are carried out along each *pencil* (each direction) at time. In this sense, the resulting forcing term can be seen as changeable depending on the spatial direction of the finite-difference operator, hence the name *"Alternating Direct Forcing"* was used. The method has been first used to simulate the active control of turbulent micro-jets [50]. Later, it has also been used by [8] to perform DNS of turbulent pipe flow at low Reynolds number $Re = 5300$ and [74] to investigate heat transfer in channel and pipe flow configurations up to $Re = 19000$. In the present work, the technique has been very important to perform DNS/ILES of turbulent pipe flow [75, 76, 77, 78], being also the key-factor to successfully produce filtered-DNS data [76] (see chapter 3, the article is also provided in Appendix A) and further developed to impose Neumann boundary conditions at the pipe wall [79] (see chapter 5, the article is also provided in Appendix A).

Alternating Direct Forcing

As mentioned, the alternating forcing has been developed to work optimally with the $2D$ decomposition of Incompact3d/Xcompact3d. To illustrate the principle, let us take the computation of the right-hand side (RHS) of the momentum equation (2.10). The diagram in Figure 2.5 provides an outline of the procedure. On account of the $2D$ MPI decomposition, the computation of the first and second derivatives of the required terms $(u_x, u_y, u_z, u_x u_x, u_x u_y, ...)$ starts in X-*pencils* progressing to Y and finishing in Z. High-order compact schemes are particularly sensitive to the presence of discontinuities. Due to its spectral-like behaviour, strong spurious oscillations might be not only generated but also spread over the surrounding nodes. For this reason, the polynomial reconstructions are performed before each finite-difference operation in order to suppress the step-like change on the derivatives while (indirectly) imposing the boundary condition.

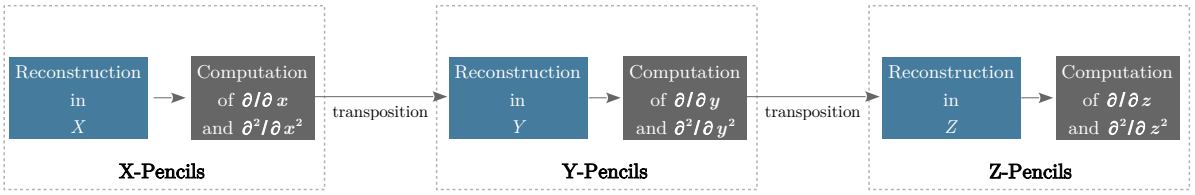

Figure 2.5: Schematic diagram of the 1D interpolations in the framework of the $2D$ decomposition implemented in Incompact3d.

The full characterization of the strategy allowing to manage different geometric shapes is found in chapter 6 of [67], in here, we focus on detailing its operation for the present pipe geometry. There are two possible scenarios when performing the 1D reconstruction, they are schematized in Figure 2.6. In the first case, only one object is identified along the *grid row*, and the reconstruction is simply a reconnection of the buffer zone through the solid which does not affect the inner flow solution. For the second one, two objects are identified. In this case the interpolations connect buffer and inner zones while satisfying the boundary condition and conserving first-derivatives across the inner wall.

The local reconstruction schemes are Lagrange polynomials according to

$$L_{N-1}(x) = \sum_{j=1}^{N} \frac{\prod_{\substack{i=1 \\ i\neq j}}^{N} (x - x_i)}{\prod_{\substack{i=1 \\ i\neq j}}^{N} (x_j - x_i)} \Phi_j \tag{2.15}$$

where L is the polynomial of order $N-1$, passing through N points (input points) and Φ_j is the solution of the scalar field Φ at the point x_j. In the present work, *fifth-order Lagrange polynomials* are used (i.e. $N = 6$ input points), as in [8]. Out of the six input points, two correspond to the boundary condition at inner and outer boundaries

$$\Phi(r = R) = \Phi(r = R_o) = \Phi_b \tag{2.16}$$

where Φ_b is the value to be imposed at the immersed boundary - the same value is imposed at the inner and outer boundaries to optimize the smoothness of the reconstruction. The immersed boundary location, which does not coincide with mesh organization, is defined through a 'search method' that determines the wall intersection coordinates with an extra-refinement of $100\times$ on the each direction [67]. The remaining four input points are information collected from the adjacent fluid nodes, symmetrically, two from the inner zone and two from the buffer zone. The six input points are represented by the white-crossed markers in Figure 2.6. Note however that the closest fluid nodes are skipped, in fact, due to the irregular distribution of the Cartesian mesh points with respect to the cylindrical geometry, some of these nodes can be found very close to the wall and the resulting interpolation coefficients of eq.(2.15) - although algebraically correct - can become very large and lead to critical numerical instability.

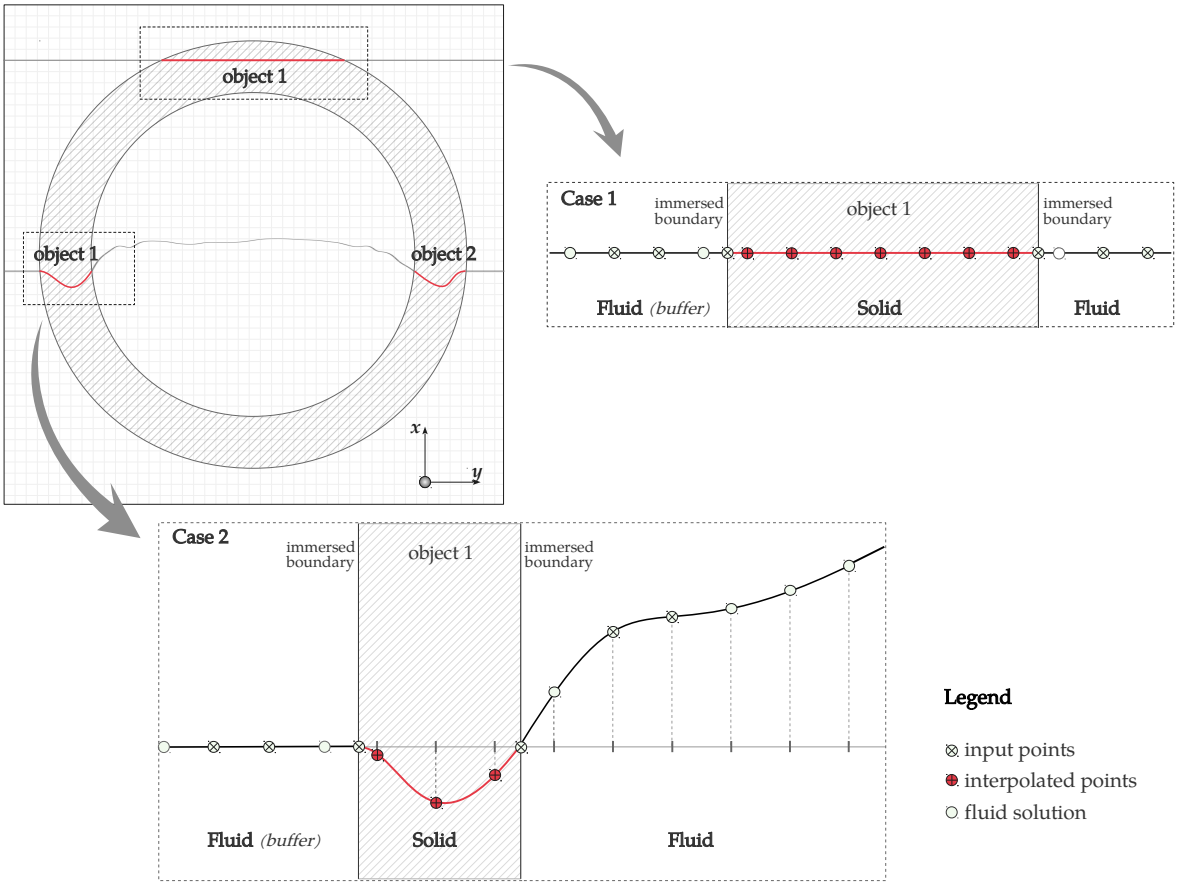

Figure 2.6: Schematic view of the polynomial reconstruction into the pipe wall. Red crossed points are the interpolated nodes, white crossed points are the input nodes for the Lagrange polynomial interpolation (note that the closest fluid nodes are skipped).

Fluid and solid zones are distinguished by the scalar field $\varepsilon(r)$

$$\varepsilon(r) = \begin{cases} 1, & \text{if } R \leq r \leq R_o \\ 0, & \text{otherwise} \end{cases} \tag{2.17}$$

which is used to mask the action of the forcing term when solving the Poisson equation, more details are given in section 2.7.

Formal analysis of the error carried out by [67] for the flow around a cylinder at $Re = 40$ and later by [74] for laminar pipe and channel flows presented a global 2^{nd} order convergence. It has been shown also by [74] that, although small, the domain size (i.e., the buffer zone extension) plays a role on the global error amplitude and thus, for the sake of accuracy, a minimum amount of external points must be provided in $r > R_o$.

2.6 Spatial discretization

In Incompact3d/Xcompact3d, the entire spatial differentiation is based on *sixth-order centred compact schemes*[4]. In this section, the general formulation of the sixth-order schemes used for first and second derivatives are described. Afterwards, the resolution characteristics of the schemes are assessed in the Fourier space in order to present the concept of numerical dissipation control through second derivatives, the foundation of the present implicit LES technique.

2.6.1 Compact schemes

First derivatives

The formulations are generically presented here for the x-direction, which can be naturally extended to y and z. The discrete distribution of mesh nodes x_i is given by eq.(2.2)

$$x_i = (i-1)\Delta x - L_x/2 \ ,$$

and the value of a continuous function $f(x)$ at the nodal positions $x = x_i$ is denoted $f_i = f(x_i)$. The approximation of the first derivative $f_i' = f'(x_i)$ accurate up to eighth-order can be achieved with the

[4]When periodic (or free-slip) boundary conditions are used, as in here, the centred formulation can be also kept for mesh nodes close to the boundaries of the domain, which allows the order of accuracy to be conserved while suppressing dissipative errors.

3-7 stencil formulation [80]

$$\alpha f'_{i-1} + f'_i + \alpha f'_{i+1} = a\frac{f_{i+1} - f_{i-1}}{2\Delta x} + b\frac{f_{i+2} - f_{i-2}}{4\Delta x} + c\frac{f_{i+3} - f_{i-3}}{6\Delta x} + O(\Delta x^n) \tag{2.18}$$

Where $O(\Delta x^n)$ is the truncation error and the choice of coefficients (α, a, b, c) is constrained by Taylor series expansion according to the desired order of accuracy $n \leq 8$. The higher is the order, the higher is the number of conditions to be met and more constrained is the choice of the coefficients

$$\begin{aligned}
&(i) && a + b + c = 1 + 2\alpha && \text{for} \quad n \geq 2 \\
&(ii) && a + 2^2 b + 3^2 c = 2\tfrac{3!}{2!}\alpha && \text{for} \quad n \geq 4 \\
&(iii) && a + 2^4 b + 3^4 c = 2\tfrac{5!}{4!}\alpha && \text{for} \quad n \geq 6 \\
&(iv) && a + 2^8 b + 3^8 c = 2\tfrac{9!}{8!}\alpha && \text{for} \quad n = 8
\end{aligned} \tag{2.19}$$

For sixth-order accuracy, the set of four coefficients must meet the three conditions (i,ii,iii). By imposing $c = 0$ the compactness of the scheme is reinforced and the solution of the system gives

$$\alpha = 1/3, \quad a = 14/9, \quad b = 1/9, \quad c = 0 \tag{2.20}$$

Second derivatives

Likewise, the second derivative approximation $f''_i = f''(x_i)$ can be made accurate up to tenth-order with the 3-9 stencil formulation [65]

$$\alpha f''_{i-1} + f''_i + \alpha f''_{i+1} = a\frac{f_{i+1} - 2f_i + f_{i-1}}{\Delta x^2} + b\frac{f_{i+2} - 2f_i + f_{i-2}}{4\Delta x^2} + c\frac{f_{i+3} - 2f_i + f_{i-3}}{9\Delta x^2} + d\frac{f_{i+4} - 2f_i + f_{i-4}}{16\Delta x^2} + O(\Delta x^n) \tag{2.21}$$

And the conditions to be met are

$$\begin{aligned}
&(i) && a+b+c+d = 1+2\alpha && \text{for} \quad n \geq 2 \\
&(ii) && a+2^2b+3^2c+4^2d = \tfrac{4!}{2!}\alpha && \text{for} \quad n \geq 4 \\
&(iii) && a+2^4b+3^4c+4^4d = \tfrac{6!}{4!}\alpha && \text{for} \quad n \geq 6 \\
&(iv) && a+2^6b+3^6c+4^6d = \tfrac{10!}{8!}\alpha && \text{for} \quad n \geq 8 \\
&(v) && a+2^8b+3^8c+4^8d = \tfrac{18!}{16!}\alpha && \text{for} \quad n = 10
\end{aligned} \tag{2.22}$$

The conventional sixth-order scheme of [80] is obtained by meeting conditions (i,ii,iii) while imposing $c = d = 0$. The solution of the system gives

$$\alpha = 2/11, \quad a = 12/11, \quad b = 3/11, \quad c = 0, \quad d = 0 \ . \tag{2.23}$$

In the next section however, it will be shown that the spectral behaviour of the second derivative scheme can be adjusted through the establishment of extra-constraints, which leads to a new family of FD schemes, the foundation of the present implicit LES technique [81, 65].

2.6.2 Fourier analysis of compact schemes

Very often, FD schemes are evaluated based only on its formal order of accuracy. However, this information only tells us the rate at which the error decreases as the mesh spacing is reduced $\Delta x \to 0$, i.e., as $n_x \to \infty$ [31]. As discussed in section 1.2, generally, a compromise needs to be found between mesh resolution and computational resources, therefore it might be interesting to evaluate the accuracy of a numerical scheme also for a given (fixed) grid. This can be done through a Fourier analysis of the errors associated with the FD approximations (2.18),(2.21) [80]. This type of analysis is well known nowadays and it is fully described by [82]. This is a classic approach for comparing difference schemes and it has been used, for instance, by Robert and Weiss [83], Kreiss and Oliger [84] and Swartz and Wendrof [85].

Let $f(x)$ be the solution to a given partial differential equation, defined in the interval $[0, L_x]$ with $f(x) \in \mathbb{R}$. We assume that $f(x)$ is periodic - $f(x_1) = f(x_{n_x})$ - and $\Delta x = L_x/n_x$. Then, the function $f(x)$ can be broken down into a weighted sum of sinusoidal functions, i.e. its discrete Fourier series, according to

$$f(x_j) = \sum_{k=-N/2}^{N/2} \hat{f}_k e^{ikx_j} \qquad \text{with} \quad j = 1, 2, ..., n_x \tag{2.24}$$

where k is the wavenumber, $i = \sqrt{-1}$ is the unit imaginary number, x_j is the discrete position of the node j (as in eq.(2.2)) and $\hat{f}_k \in \mathbb{C}$ are the Fourier (or spectral) coefficients that weight the sum of

the sinusoidal functions. Since $f(x)$ is real valued, we have $\hat{f}_k = \hat{f}_k^*$ and $\hat{f}_0 = \hat{f}_0^*$ where * denotes the complex conjugate [80].

We take here the complex exponential

$$f(x) = e^{ikx} \tag{2.25}$$

representing the ensemble of sinusoidal functions of the family e^{ikx_j}. Thus, the exact first derivative of $f(x)$ is given by

$$f'(x) = ike^{ikx} \tag{2.26}$$

and its second derivative

$$f''(x) = -k^2 e^{ikx} \ . \tag{2.27}$$

Then, the error associated to a difference scheme can be evaluated in the Fourier space through the comparison of its exact derivatives in eqs.(2.26) and (2.27) with their respective numerical approximations

$$[f'(x)]_{FD} = ik' e^{ikx} \tag{2.28}$$

and

$$[f''(x)]_{FD} = -k'' e^{ikx} \tag{2.29}$$

obtained with the FD scheme. The *modified wavenumber* k' and *modified square wavenumber* k'' are the variables through which comparisons are carried out. For each finite difference scheme, expressions of $k'\Delta x$ or $k''\Delta x^2$ as functions of $k\Delta x$ can be derived. For the exact differentiation, the curve $k'\Delta x(k\Delta x)$ corresponds to the straight line $k'\Delta x = k\Delta x$, and the curve of $k''\Delta x(k\Delta x)$ corresponds to the parabola $k''\Delta x^2 = k^2\Delta x^2$.

First derivatives

By replacing the RHS of eq.(2.18) with eq.(2.25) and its LHS with eq.(2.28), the following expression for the modified wavenumber $k'\Delta x$ for scheme (2.18) is obtained

$$k'\Delta x = \frac{a \sin k\Delta x + \frac{b}{2} \sin 2k\Delta x + \frac{c}{3} \sin 3k\Delta x}{1 + 2\alpha \cos k\Delta x} \ . \tag{2.30}$$

Figure 2.7 compares the curves of $k'\Delta x$ for different variants of scheme (2.18). Low values of the wavenumber k correspond to the large-scale motions that are actually captured by a given grid and the shortest scale which can be captured is associated to the cut-off wavenumber $k_c = \pi/\Delta x$ with corresponding wavelength

$$\lambda_c = \frac{2\pi}{k_c} = 2\Delta x \ .$$

This means that, with a mesh of size Δx, the smallest phenomenon that can be described is $\lambda_c = 2\Delta x$, i.e., two times larger. This is true however, only in the best-case of scenario, when the scheme is actually capable of providing $k'\Delta x = k\Delta x$ as $k \to k_c$. The first relevant information from Figure 2.7 is that, although a physical process of a certain scale might be captured by the grid, it does not

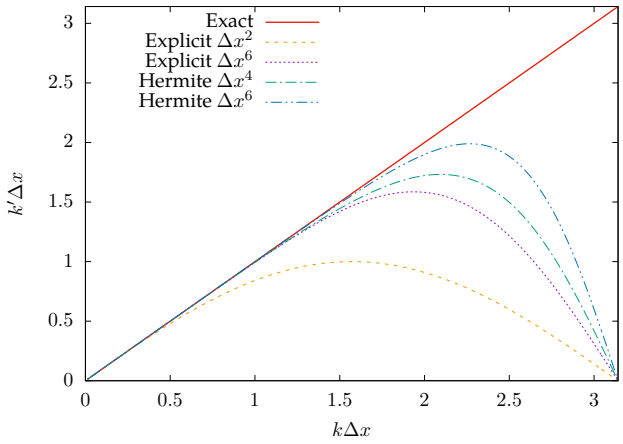

Figure 2.7: Modified wavenumber $k'\Delta x$ for different schemes obtained from (2.18). The Hermite (compact) Δx^6 corresponds to the one used in the present work.

necessarily mean that the predicted information is reliable. The modified wavenumber provides indeed a straightforward way of evaluating - at a given mesh resolution - the range of well-resolved scales with a certain FD scheme. This range corresponds to the interval $k\Delta x$ for which the modified wavenumber $k'\Delta x$ approximates the exact differentiation [80].

Thus, when dealing with turbulent flows characterized by a wide range of scales of motion, it is advantageous to use FD schemes capable of properly describing perturbations as close as possible to the cut-off wavenumber. For all the simulations carried out throughout this work, the sixth-order compact scheme (2.18, 2.20) is used for the computation of first spatial derivatives in eqs.(2.10, 2.11).

Second derivatives

Likewise, by replacing the RHS of eq.(2.21) with eq.(2.26) and its LHS with eq.(2.29) the expression of the modified square wavenumber $k''\Delta x^2$ is obtained for scheme (2.21)

$$k''\Delta x^2 = \frac{2a\left[1-\cos k\Delta x\right] + \frac{b}{2}\left[1-\cos 2k\Delta x\right] + \frac{2c}{9}\left[1-\cos 3k\Delta x\right] + \frac{d}{8}\left[1-\cos 4k\Delta x\right]}{1+2\alpha\cos k\Delta x} \tag{2.31}$$

In Figure 2.8, the curve of $k''\Delta x^2$ for the conventional sixth-order scheme (2.21, 2.23) of [80] is compared to the exact differentiation. Although compact schemes may be characterized by the extended range of well-resolved scales, one sees that at the cut-off wavenumber $k_c\Delta x = \pi$, the estimation of the second derivative with scheme (2.21, 2.23) presents a significant drop $k''\Delta x^2(\pi) = 48/7$ compared to its exact value $k^2\Delta x^2(\pi) = \pi^2$. The numerical error associated to this underestimation reveals, in fact, the sub-dissipative behaviour of scheme (2.21, 2.23) at high wavenumbers [81, 65]. In the next section,

we shall see how this feature can be controlled and profitably used to regularise the numerical solution in both DNS and LES applications.

2.6.3 High-order numerical dissipation schemes

By perceiving that eq.(2.31) admits a singularity at the cut-off wavenumber for $\alpha = 1/2$, [81] proposed a new family of schemes with flexible behaviour at small scales, the fundamentals of this approach are summarized in this section.

Together with conditions (i,ii,iii) in eqs.(2.22), which ensures sixth-order accuracy, an extra-constraint can be introduced to remold the shape of $k''\Delta x^2$ by imposing a target value at the cut-off wavenumber $k''\Delta x^2(\pi) = k''_c\Delta x^2$. This target value can either correspond to the exact differentiation $k''_c\Delta x^2 = \pi^2$ or even to an over-estimation of the form

$$k''_c\Delta x^2 = m\pi^2 \tag{2.32}$$

where m is a value that determines the level of the over-estimation. The extra-condition (2.32) requires $c \neq 0$ in (2.21) and a new family of sixth-order compact schemes with high-order dissipation concentrated at small scales is introduced

$$\begin{aligned}
\alpha &= \frac{272 - 45k''_c\Delta x^2}{416 - 90k''_c\Delta x^2} \\
a &= \frac{48 - 135k''_c\Delta x^2}{1664 - 360k''_c\Delta x^2} \\
b &= \frac{528 - 81k''_c\Delta x^2}{208 - 45k''_c\Delta x^2} \\
c &= \frac{-432 + 63k''_c\Delta x^2}{1664 - 360k''_c\Delta x^2} \quad .
\end{aligned} \tag{2.33}$$

Curves of $k''\Delta x^2$ associated with scheme (2.21, 2.33) for different values of m are presented in Figure 2.8. In this context, it can be said that the second derivative operator is made *hyperviscous* at small scales and, algebraically, we observe $\alpha \to 1/2$ as $m \to \infty$. However, it is important to properly understand what is the advantage of employing this extra-numerical dissipation and how to determine its appropriate level and distribution among the scales. Formally, when dealing with FD schemes (even compact ones), numerical errors are inevitably higher at high wavenumbers [65], this is evidenced by the under-dissipative behaviour of the conventional (and widely used) sixth-order scheme (2.21, 2.23) of [80], which is also plotted in Figure 2.8 for comparison. The interest in switching to a rather over-dissipative behaviour resides in the capability that high-order numerical dissipation offers to control aliasing errors that arise at high wavenumbers. In fact, when used in this way, numerical dissipation can regularise the solution at small scales, playing the role of a subgrid-scale model in the context of LES, being, for instance, an alternative to the conventional Smagorinsky approaches based on explicit SGS modelling [65]. Indeed, this is the foundation of the Spectral Vanishing Viscosity (SVV) method, presented hereafter.

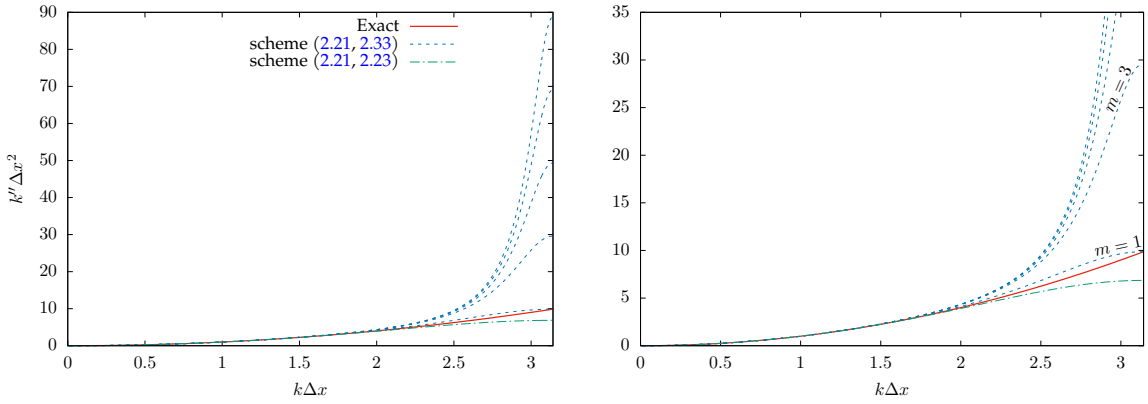

Figure 2.8: Modified square wavenumber $k''\Delta x^2$ for scheme (2.21, 2.33) imposing different levels of over-estimation at the cut-off wavenumber $k_c''\Delta x^2 = m\pi^2$ with $m = 1, 3, 5, 7, 9$. The conventional scheme (2.21, 2.23) is also plotted for comparison.

Spectral Vanishing Viscosity (SVV)

The SVV method was first introduced by [86] in the framework of spectral methods applied to the Burger's equation and it has been later adapted for finite element methods [87, 88]. The principle of the technique is to selectively add a small amount of numerical dissipation at the small scales of the computational grid to control high wavenumber oscillations [87]. In the Fourier space, this added numerical dissipation takes the form of a spectral viscosity $\nu_s(k)$ which is summed to the molecular viscosity ν. Thus, free from discretization errors, the viscous operator takes the form

$$(\nu + \nu_s)\, k^2 \tag{2.34}$$

while the spectral viscosity (numerical dissipation) may assume, for instance, the kernel [87]

$$\nu_s(k) = \nu_0 \exp\left[-\left(\frac{k_c - k}{\gamma k_c - k}\right)^2\right] \qquad \text{with } \gamma = 0.3 \tag{2.35}$$

where $\nu_0 = \nu_s(k_c)$ is the parameter that controls the desired value of numerical dissipation to be applied at the cutoff wavenumber and γ defines its scale selectivity. The kernel of the spectral viscosity (2.35) is plotted in Figure 2.9. For $k/k_c \leq \gamma$, we have $\nu_s = 0$, i.e., the spectral viscosity vanishes at low wavenumbers, leaving the large-scales virtually free from any influence. Conversely, $\gamma < k/k_c < 1$ corresponds to the range of small scales that actually receives the extra-numerical dissipation that regularises the LES solution by controlling the numerical errors.

Implicit Spectral Vanishing Viscosity (ISVV)

The above reasoning can be also extended to FD schemes. In the Fourier space, the viscous operator $\nu k''$ takes into account the discretization errors associated to the FD scheme used for the second derivative. If we desire to express the numerical dissipation introduced in k'' through condition (2.32) (which formally corresponds to an error of discretization) as a numerical viscosity ν_s'', we may follow eq.(2.34) to write the equality

$$(\nu + \nu_s'')\, k^2 = \nu k'' \tag{2.36}$$

And the associated numerical viscosity may be then expressed as

$$\nu_s''(k) = \nu \frac{k'' - k^2}{k^2} \quad . \tag{2.37}$$

Note that the ratio on the RHS plainly corresponds to the numerical error associated to the second derivative approximation. Then, in order to tune the distribution of numerical dissipation among the scales, the spectral viscosity ν_s'' can be, for instance, adjusted to mimic the SVV kernel[5] (2.35) at the cut-off wavenumber by setting $\nu_s(k_c) = \nu_0$. Thus, condition (2.32) can be re-expressed now in terms of the spectral viscosity with

$$k_c'' \Delta x^2 = \left(1 + \frac{\nu_0}{\nu}\right) \pi^2 \quad . \tag{2.38}$$

Note that the parameter ν_0/ν needs to be defined by the user and prescribes the proportion of spectral viscosity ν_0 to be embedded in the solution with respect to the molecular viscosity ν.

Dairay *et. al* [65] showed that the present technique is the finite difference counterpart of the Spectral Vanishing Viscosity. Yet, differently from the SVV - for which the spectral viscosity is explicitly included through an extra term on the momentum equation and involves additional computational operations - within the present approach, both molecular and spectral viscosities are embedded in one single operator. Also, the numerical dissipation is implicitly embedded in the computation of second derivatives, which means that no-extra computational cost is involved. Hence, the method went by the name of *Implicit Spectral Vanishing Viscosity* (*ISVV*) [81, 65]. Furthermore, the role of the scale selectivity provided by the adjustment of the dissipation kernel has been demonstrated by [75] through rigorous comparisons with DNS results based on *a priori*/*a posteriori* analysis with a particular attention to distant triad interactions between subgrid-scales and very large scales.

ISVV for DNS

Now, through eq.(2.37), the spectral behaviour of scheme (2.21, 2.33) can be assessed in terms of spectral viscosity. Figure 2.9-left compares its hyperviscous kernel to the SVV one given by eq.(2.35) for the arbitrary value $\nu_0 = \nu$. The viscous kernel associated to the conventional scheme (2.21, 2.23) is also plotted and its under-dissipative behaviour is confirmed by the negative value displayed at the cut-off wavenumber. Concerning scheme (2.21, 2.33), Figure 2.9-left shows that, when compared to the

[5] The spectral viscosity ν_s'' can also be adjusted to mimic a hyperviscous kernel [89], for more details see [81].

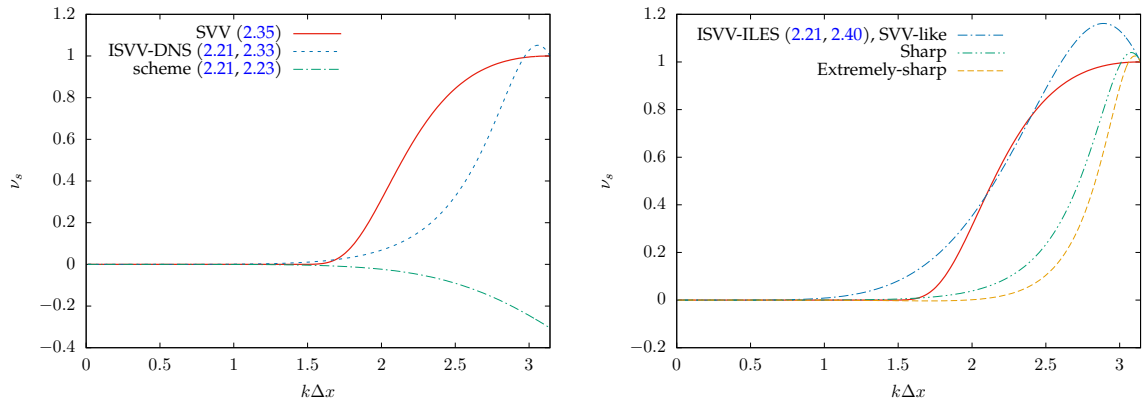

Figure 2.9: Spectral viscosity kernels associated with (right) scheme (2.21, 2.33) for DNS applications and (left) scheme (2.21, 2.40) for ILES applications. The range of the dissipation in (right) is adjusted through the variable c_1: SVV-like ($c_1 \approx 0.44$), Sharp ($c_1 = 0.055$) and Extremely-sharp ($c_1 = 0.007$).

SVV kernel, the global dissipation is considerably reduced since the numerical dissipation introduced is much more concentrated near k_c [81]. In fact, this turns out to be a well-suited choice for DNS. When used in this way, numerical dissipation is efficient for controlling the numerical oscillations at the smallest scales (which are inevitably compromised when FD is used) while preserving the quality of the large-scales prediction [90]. Indeed, this scheme has been successfully used to perform DNS of the Taylor-Green-vortex [75], turbulent jet [90], channel [91], micro-channel [50] flows, as well as direct computation of sound [81] (which is well known for being very demanding in terms of numerical accuracy), among many others. In the present framework, scheme (2.21, 2.33) has been used for the discretization of second derivatives when performing DNS with the small amount of numerical dissipation $\nu_0/\nu = 3$.

ISVV for implicit LES

In LES applications, higher levels of numerical dissipation are required to control the numerical errors. In this sense, [81, 90] proposed to introduce an extra-condition to spectrally mimic the SVV kernel (2.35) at an intermediate scale $k_m = \frac{2}{3}k_c$. By introducing the constant c_1 to express the proportion of $\nu_s(k_m)$ with respect to its maximum value at the cut-off wavenumber $\nu_s(k_c) = \nu_0$, the extra-condition may be expressed as

$$k_m'' \Delta x^2 = \left(1 + c_1 \frac{\nu_0}{\nu}\right) \frac{4}{9}\pi^2 \tag{2.39}$$

with $c_1 \approx 0.44$ for the SVV formulation (2.35). Then, by allowing $d \neq 0$ in (2.21), sixth-order accuracy can be kept through the relationships (i,ii,iii) in eqs.(2.22), and, together with eqs.(2.38, 2.39), 5 con-

ditions are provided for the set of 5 coefficients (α, a, b, c, d). The solution of the system leads to the sixth-order scheme introduced by [90] with extended range of numerical dissipation

$$\begin{aligned}
\alpha &= \frac{405k_c''\Delta x^2 - 1280k_m''\Delta x^2 + 2736}{810k_c''\Delta x^2 - 1280k_m''\Delta x^2 + 288} \\
a &= -\frac{4329k_c''\Delta x^2 - 256k_m''\Delta x^2 - 1120k_c''\Delta x^2 k_m''\Delta x^2 + 2288}{3240k_c''\Delta x^2 - 5120k_m''\Delta x^2 + 1152} \\
b &= \frac{2115k_c''\Delta x^2 - 1792k_m''\Delta x^2 - 280k_c''\Delta x^2 k_m''\Delta x^2 + 1328}{405k_c''\Delta x^2 - 640k_m''\Delta x^2 + 144} \\
c &= -\frac{7695k_c''\Delta x^2 + 2304k_m''\Delta x^2 - 1440k_c''\Delta x^2 k_m''\Delta x^2 - 20592}{3240k_c''\Delta x^2 - 5120k_m''\Delta x^2 + 1152} \\
d &= \frac{198k_c''\Delta x^2 + 128k_m''\Delta x^2 - 40k_c''\Delta x^2 k_m''\Delta x^2 - 736}{405k_c''\Delta x^2 - 640k_m''\Delta x^2 + 144}
\end{aligned} \tag{2.40}$$

Figure 2.9-right illustrates the ability of the present FD scheme to mimic the SVV kernel (2.35). Note that, the separation between dissipative and artificial-viscosity free ranges is less sharp for the present *SVV-like* kernel ($c_1 \approx 0.44$). Nonetheless, the shape of the dissipation kernel can be flexibly adjusted by setting different values for the constant c_1, which leads to a more or less sharp behaviour while regulating the global dissipation [65]. Two other examples are shown in Figure 2.9-right for $c_1 = 0.055$ (*Sharp*) and $c_1 = 0.007$ (*Extremely-sharp*).

Because of the equivalence with spectral viscosity, the artificial dissipation introduced by the second derivative can be seen as a subgrid-scale model in the context of LES [81, 90, 65]. Furthermore, it has been shown by [65] that, oppositely to the popular Smagorinsky approaches, the numerical solution with the present technique is more efficient and can be actually seen as converged at the mesh scale. Moreover, since the modelling is entirely (and implicitly) contained in the regularisation provided by the numerical dissipation, it is referred to as an *Implicit LES* (*ILES*) strategy. In addition, in the present pipe flow framework, it has been shown that its very profitable features have also the ability to function as a (implicit) wall-layer model for LES [76] (see article in Appendix A), this is the subject of chapter 3.

The method is very flexible, since the dissipation kernel can be freely adjusted by setting ν_0/ν (level) and c_1 (shape/range). Still, the choice of these parameters must not be done arbitrarily. For this purpose, [65] presented a simplified spectral closure - based on the solution of the Pao-lin equation - to constrain the choice of this parameters based on an appropriate physical scaling. This approach assumes the validity of Kolmogorov's statistical stationarity assumption, i.e. in an equilibrium framework, non-equilibrium [92] modifications of the model are still to be developed. The formalism, for the sake of brevity, is not presented here, for a full description the reader is referred to [65]. In general lines, from the specification of the ratio between a reference DNS and a given LES mesh resolution, a Pao-like solution of the Lin equation provides a prediction of the influence of the numerical dissipation on the kinetic energy spectrum in the context of homogeneous and isotropic turbulence. Then, the appropriate level of numerical dissipation is defined to provide, at the cut-off wavenumber of the LES

grid, the same (low) level of energy at the cut-off wavenumber of the DNS grid, which actually verifies numerical convergence for the LES solution.

As its DNS counterpart, the sixth-order scheme (2.21, 2.40) has been widely utilised to perform ILES at many different flow configurations, in the present framework, it has been used for the discretization of second derivatives when performing ILES.

2.7 Time integration

In this section, the time-integration of the momentum equation (2.10) is described. For the sake of convenience, time integration of the energy equation (2.11) is only presented in chapter 5. Firstly, the fractional step method and pressure treatment are briefly described and then, the numerical treatment for the forcing term that ensures stationary regime in the pipe is presented.

Fractional step method

In the incompressible context, the velocity components must respect the incompressibility condition by constituting a divergence free vector field, this condition is expressed by the continuity equation (2.9). In this sense, this equation can be rather interpreted as a kinematic constraint to be respected by the velocity components when solving the momentum equations (2.10) [31]. Furthermore, with the 3 velocity components being issued from the solution of the 3 momentum equations, it is the pressure field which should be held accountable for the incompressibility condition, providing a closed system. However, the well known difficulty when dealing with incompressible flows is the lack of direct coupling between pressure and velocity (which, for compressible flows, is done through the equation of state). To overcome this obstacle, since only the pressure gradient is relevant in the incompressible context, the pressure field may be "constructed" such that its gradient provides a divergence free velocity field through its action on the momentum equations (2.10). The classic approach to do so is to take the divergence of the momentum equation and simplify the resulting expression with the continuity equation, the outcome will be a Poisson equation for the pressure field satisfying the continuity constraint [31, 23].

In the history of numerical simulation, many different strategies have been proposed for the pressure treatment in the incompressible framework [31]. For unsteady flows, it is common to use non-iterative techniques such as the fractional step method first introduced by [93], whose principle is to split the time integration of the momentum equation in sub-steps. As pointed out by [31], the fractional step concept is more a generic approach than a particular method and, since its introduction in the mid 80's, many kinds of splitting have been proposed. In Incompact3d/Xcompact3d, the method of [94] - developed in the framework of DNS of turbulence based on central difference approximations - is used. It consists of splitting the time advancement of the momentum equation (2.10) according to:

1. As a first step, the convective and diffusive terms are advanced in time. With a third order

Adams-Bashforth scheme (AB3), an intermediate velocity u_i^* may be computed as:

$$\frac{u_i^* - u_i^n}{\Delta t} = \sum_{j=0}^{p-1} \alpha_j H_i^{n-j} \quad , \tag{2.41}$$

where $p = 3$ for an AB3 and $\alpha_0 = 23/12$, $\alpha_1 = -16/12$, $\alpha_2 = 5/12$ are the time scheme coefficients; H_i is the operator that represents the discretized convective-diffusive terms

$$H_i = -\frac{1}{2}\left(u_j \frac{\partial u_i}{\partial x_j} + \frac{\partial u_i u_j}{\partial x_j} \right) + \frac{1}{Re} \frac{\partial^2 u_i}{\partial x_j \partial x_j} \quad .$$

2. In a second-step the velocity components u_i^* are corrected by the pressure gradient in order to be projected in the divergence-free space

$$\frac{u_i^{n+1} - u_i^*}{\Delta t} = -\frac{\partial p^{n+1}}{\partial x_i} + f_i^{n+1} \quad . \tag{2.42}$$

The forcing with f_i - which ensures the stationary state - have been expressed here together with the pressure gradient correction in one single step, its numerical treatment is detailed hereafter. The above pressure gradient is computed from the pressure field p^{n+1} issued from the solution of the Poisson equation

$$\frac{\partial^2 p^{n+1}}{\partial x_i \partial x_i} = \frac{1}{\Delta t} \frac{\partial \left((1 - \varepsilon^-) u_i^* \right)}{\partial x_i} \quad , \tag{2.43}$$

where the scalar ε^- acts as a mask that transforms the Poisson equation (2.43) into a Laplace equation where $\varepsilon^- = 1$, more details are given in the next section. Note that a forcing term associated to the IBM does not explicitly appear in the time advancement since, as discussed in section 2.5, the no-slip condition is indirectly imposed within the reconstruction of the velocity components prior to the computation of spatial derivatives of H_i.

Pressure treatment

As in [44, 50], the Poisson equation (2.43) is modified by the introduction of the mask $(1 - \varepsilon^-)$, where ε^- corresponds to the scalar ε (see eq.(2.17)) with one-mesh retraction from the solid region in the transverse-xy directions [50], the principle is illustrated in Figure 2.10-left. Note that in this way, eq.(2.43) implies that a Poisson equation is solved in the expanded fluid region defined by $\varepsilon^- = 0$ whereas a Laplace equation is recovered for the retracted solid region[6] defined by $\varepsilon^- = 1$. Tests performed by [50] showed that the use of ε^- instead of ε allows a better mass conservation near solid regions.

The numerical treatment of the Poisson equation is a sensitive matter here. As stressed by [7, 54], when higher-order FD schemes are used for the spatial discretization of the pressure, sophisticated

[6] As well as for the buffer zone $r > R_o$, which consists of fluid at rest.

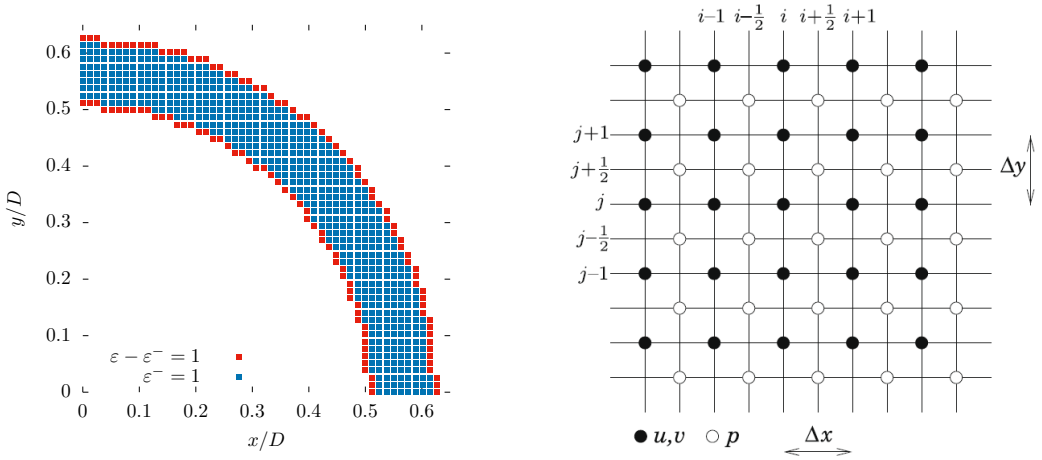

Figure 2.10: (Left) Illustration of the solid zone $\varepsilon^- = 1$ obtained from the one-mesh retraction of ε in both transverse-xy directions, the retracted elements $\varepsilon - \varepsilon^- = 1$ are enhanced in red. (Right) Schematic arrangement in two dimensions of the half-staggered mesh for the pressure, taken from [7]. The velocity components are always located in the same positions while the pressure is shifted by a half-mesh in each spatial direction.

procedures might be required to invert the Poisson equation in physical space every time step and the substantial effort added may be computationally disastrous. In Incompact3d/Xcompact3d, with the help of Fast Fourier Transforms (*FFT*), the pressure treatment is made in the Fourier space where the equivalent operations in (2.43) are simpler and cheaper. Also, the strategy combines well with high-order compact schemes, as shown by [7]. The pressure nodes are staggered by a half-mesh with respect to the velocity grid to avoid spurious oscillations observed by [7] in the full-collocated configuration (see illustration in Figure 2.10-right). When solving the Poisson equation (2.43) at the staggered nodes, mid-point operators are used to compute first derivatives and to interpolate the velocity at the pressure nodes, the former is done with the scheme of [7] while for the latter, the optimized scheme of [65] is used. For a comprehensive description of the numerical treatment for the pressure in Incompact3d, see [7, 11].

Forcing term

In a real pipeline, the external force applied to the flow to overcome the friction losses is usually provided by a pump or gravity. Likewise, in numerical simulation of confined flows this external forcing must be modelled. The three most popular approaches - namely *Constant Flow Rate* (*CFR*), *Constant Pressure Gradient* (*CPG*) and *Constant Power Input* (*CPI*) - have been assessed by [95] and it has been shown that the use of one or the other does not have an important influence on the turbulence statistics of the flow field.

In here, *CFR* is ensured through the action of the forcing term f_i^{n+1} in eq.(2.42) every time step in order to keep a constant bulk velocity U_b. More especifically, the forcing can be explicitly expressed by splitting eq.(2.42) in two steps as follows

$$u_i^{**} = u_i^* + \Delta t f_i^* \tag{2.44}$$

$$\frac{u_i^{n+1} - u_i^{**}}{\Delta t} = -\frac{\partial p^{n+1}}{\partial x_i} \ , \tag{2.45}$$

where u_i^{**} is another intermediate velocity and the notation f_i^* points to the fact that the forcing is applied on the intermediate velocity u_i^* so that the gradient pressure correction discussed above may have the last word on the final velocity u_i^{n+1}. Furthermore, as discussed in section 1.1.1, this forcing is constant and unidirectional in z - i.e. $f_i = (0, 0, f_z)$ with

$$f_z = -\frac{\partial \langle p \rangle}{\partial z} = cst \ . \tag{2.46}$$

In order to express f_z in terms of the bulk velocity U_b, we take the volumetric average $\frac{1}{\Omega_f}\int_{\Omega_f} d\Omega_f$ of the streamwise-z component of eq.(2.44). By rearranging, we may express it as

$$\frac{\Delta t}{\Omega_f}\int_{\Omega_f} f_z^* d\Omega_f = \frac{1}{\Omega_f}\int_{\Omega_f} u_z^{**} d\Omega_f - \frac{1}{\Omega_f}\int_{\Omega_f} u_z^* d\Omega_f \ . \tag{2.47}$$

Following eq.(2.46), the left-hand-side of the above equation can be reduced to

$$\frac{\Delta t}{\Omega_f}\int_{\Omega_f} f_z^* d\Omega_f = \Delta t f_z^* \ . \tag{2.48}$$

Furthermore, by using the definition of the bulk velocity given by eq.(1.7), we obtain the expression for the forcing term in eq.(2.44) as it is actually computed in the code

$$\Delta t f_z^* = U_b^{**} - U_b^* \ , \tag{2.49}$$

where $U_b^{**} = 1$ is imposed every time in order to keep the constant flow rate (stationary regime) and

$$U_b^* = \frac{1}{\Omega_f}\int_{\Omega_f} u_z^* d\Omega_f \ , \tag{2.50}$$

is the intermediate bulk velocity. The integral on the right-hand-side of eq.(2.50) is computed with a simple rectangular method.

In summary, in the correction step (2.44), the intermediate streamwise velocity u_z^* is adjusted, every time step[7], with the forcing term (2.49) in order to ensure stationary regime by providing $U_b^{**} = 1$. In addition, the friction velocity u_τ, defined from eqs.(1.15, 1.13)

$$u_\tau = \sqrt{-\frac{R}{2}\frac{\partial \langle p \rangle}{\partial z}} \ , \tag{2.51}$$

[7] In a physical sense, how much U_b^* distances from $U_b^{**} = 1$ at each time step represents the loss due to viscous friction at the wall within the time frame Δt.

can be directly predicted, every time step, from the the application of the forcing term (2.49)

$$u_\tau = \sqrt{\frac{R}{2} f_z^*} \ , \tag{2.52}$$

following eq.(2.46).

2.8 Statistical averaging

Statistical analyses of both velocity and temperature field are always carried out in fully developed turbulent state. The quantities assessed to monitor the turbulent transition are the instantaneous friction Reynolds number $Re_\tau(t)$ (calculated from the friction velocity u_τ according to eq.(1.18)) for the velocity and the instantaneous Nusselt number $Nu(t)$ for the temperature. Once reached the fully developed state, the quantities of the flow are then gathered on the fly.

Azimuthal-ϕ projection

To perform the azimuthal averaging, we use the technique introduced by [8] which is summarized in this section. As discussed in section 1.1.1, the present pipe flow is homogeneous in time, streamwise-z and azimuthal-ϕ directions, implying that a certain quantity $u(r, \phi, z, t)$ of the flow, once averaged, depends only on the radial direction, that is $\langle u \rangle(r)$. With the present Cartesian mesh, the quantity $u(x, y, z, t)$ may be straightforwardly averaged in time and streamwise-z direction, leading to $\langle u \rangle_{z,t}(x, y)$. As stressed by [8], statistical convergence is established when $\langle u \rangle_{z,t}(x, 0)$ and $\langle u \rangle_{z,t}(0, y)$ collapse together while corresponding to $\langle u \rangle(r)$. Nonetheless, such a statistical convergence is very demanding, thus an extra-average needs to be used in the azimuthal-ϕ direction.

Here, we perform a direct projection of the data from the Cartesian mesh nodes (x_i, y_j) to the discretized coordinate r_k, with $i = 1, ..., n_x$, $j = 1, ..., n_y$ and $k = 1, ..., n_r$. The number of radial points n_r can be freely chosen so that the radial mesh size Δr may be smaller than its Cartesian counterparts $\Delta x = \Delta y$, providing the set of radial positions $r_k = (k-1)\Delta r$, as represented in Figure 2.11. The simplest method to perform this projection is to distribute all the contributions of the raw data $\langle u \rangle_{z,t}(x_i, y_j)$ on r_k through an average in the interval $[r_k, r_{k+1}]$ for contributions such as $r_{ij} = \sqrt{x_i^2 + y_j^2} \in [r_k, r_{k+1}]$ at the azimuthal location $\phi_{ij} = \arctan(y_j / x_i)$ [8]. Yet, such an average would be only first order accurate. In order to improve the accuracy, a second-order Taylor expansion can be used to extrapolate every $\langle u \rangle_{z,t}(x_i, y_j)$ from the Cartesian mesh nodes (x_i, y_j) to the closest radial locations r_k with [8]

$$\langle u \rangle_{z,t}(r_k) = \langle u \rangle_{z,t}(x_i, y_j) + \left(x_i \left. \frac{\partial \langle u \rangle_{z,t}}{\partial x} \right|_{x_i, y_j} + y_j \left. \frac{\partial \langle u \rangle_{z,t}}{\partial y} \right|_{x_i, y_j} \right) + O(\Delta r^2) \ . \tag{2.53}$$

As highlighted by [8], the non-regular distribution of (x_i, y_j) tends to generate small irregularities on the radial profile $\langle u \rangle_{z,t}(r_k)$, especially when $\Delta r \ll \Delta x$. As the simulation advances, these irregularities will naturally disappear as the statistical convergence is improved through the establishment of

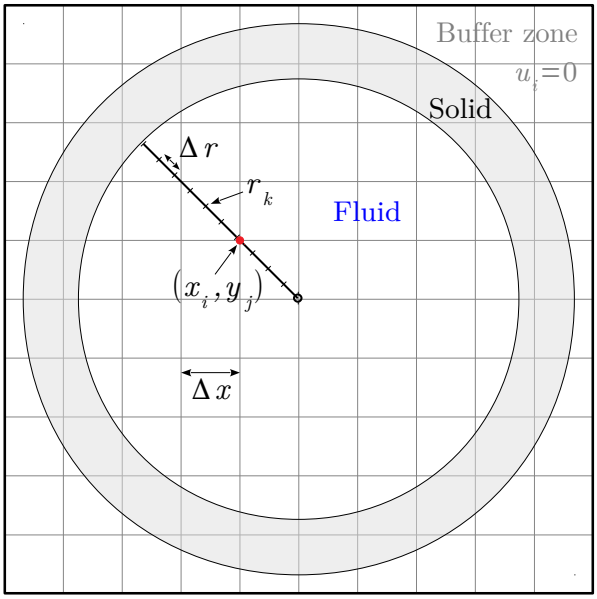

Figure 2.11: Sketch of the parameters for the projection from the Cartesian mesh (x_i, y_j) to the discretized radial coordinate r_k. Figure adapted from [8].

rotational symmetry on $\langle u \rangle_{z,t}(x_i, y_j)$. To reduce them, the contribution of every mesh node can also be distributed more widely using the Taylor expansion (2.53) for the n_s closest radial location r_k. Here, $n_s = 3$ for $\Delta r = \Delta x/8$ were used as a compromise, limiting the correction of raw data while improving the smoothness of radial profiles after this particular projection with $\Delta r < \Delta x$ [8].

In Figure 2.12, the establishment of statistical convergence and the resulting projected profiles are exemplified for the mean velocity $\langle u_z \rangle^+$ normalized in viscous units from one of our DNS at low Reynolds number $Re = 5300$. Prior to be projected, the raw data $\langle u_z \rangle^+_{z,t}(x_i, y_j)$ can be visualized as the 2D surface map shown in Figure 2.12-top. Then, in Figure 2.12-bottom, this same raw data can be presented as a cloud of points, since each coordinate (x_i, y_j) corresponds to a radial location $r_{ij} = \sqrt{x_i^2 + y_j^2}$ and therefore to a normalized wall distance $(R - r)^+$. Note that a slimming of the cloud of raw data is perceived as statistical convergence is reached. As a result, the irregularities on the projected profile $\langle u_z \rangle$ progressively vanish. Furthermore, it can be seen that, by setting $\Delta r = \Delta x/8$, information from mesh nodes very close to the wall - at radial distances smaller than the reference Cartesian mesh size $\Delta x = \Delta y$ due to the irregular distribution with respect to the wall geometry - can be profitably taken into account when projecting statistics on r_k.

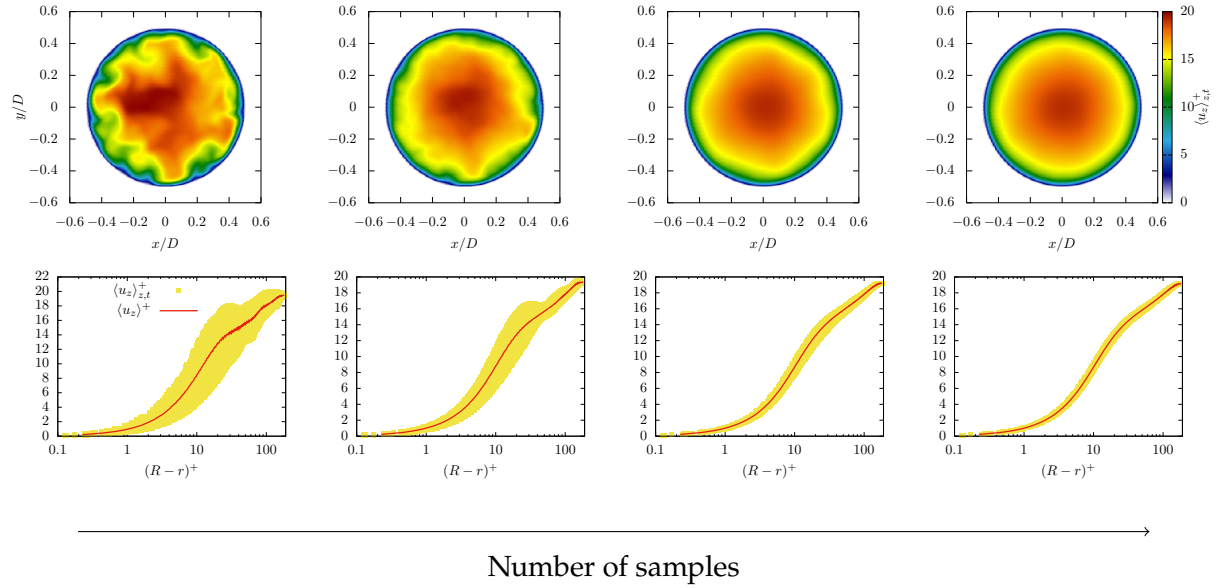

Figure 2.12: Statistical convergence of $\langle u_z \rangle^+$ with increasing number of samples. The raw data $\langle u_z \rangle^+_{z,t}$ may be visualized as a map (top) or a cloud of points in function of their radial position (bottom). Irregularities on the projected profile $\langle u_z \rangle^+$ (bottom) slowly vanish as statistical convergence is reached.

2.9 General conclusion

The fundamental numerical features of the code Incompact3d/Xcompact3d are described in this chapter. Many of them have been subject of further development in the framework of this thesis, the numerical developments brought to the code are progressively described, at due time, in the following chapters. The computational configuration consists of a pipe geometry fully immersed in the computational domain, discretized with a regular Cartesian grid. The governing equations (presented in this chapter only for the fluid side) are the incompressible Navier-Stokes equations: continuity, momentum and the passive transport for the temperature field. The conciliation between the mesh nodes distribution and the wall geometry is done with the customized immersed boundary method (IBM) developed by [50]. The technique is based on Lagrange reconstructions of the solution into the immersed region, which indirectly imposes boundary conditions at the wall, so that no explicit forcing term is introduced in the governing equations and the spatial differentiation can be performed without any particular treatment near the fluid/solid interface.

The spatial discretization is entirely based on sixth-order centred compact schemes. Not only the order of accuracy of first and second-derivative schemes is considered but also their resolution characteristics in the Fourier space. Moreover, following the work of [81], it is detailed how the spectral behaviour of the second-derivative schemes can be controlled, leading to a family of finite-difference schemes based on high-order numerical dissipation. The over-dissipation introduced by these schemes is concentrated at small scales and can effectively control aliasing errors arising at high-wavenumbers to regularise the numerical solution. Furthermore, this extra numerical dissipation can be shaped to behave as a Spectral Vanishing Viscosity (SVV) and therefore, in the context of LES, it can be interpreted as a subgrid scale modelling. As shown by [65], this strategy can ensure convergence of the numerical solution at the mesh scale, oppositely to the popular Smagorinsky approaches. As this modelling is entirely (and implicitly) contained in the numerical dissipation introduced by the second-derivative scheme, the method is referred to as an *Implicit LES* (*ILES*) strategy. The appropriate level of numerical dissipation to be used is based on the simplified spectral closure proposed by [65]. Since the role of the numerical dissipation is to regularise the solution at small scales, this strategy founds also wide applicability for DNS, this is point will be further addressed in chapters 3 and 5.

Finally, the fractional step method used for the time integration of the momentum equation is presented. The treatment of the Poisson equation is briefly described as well as the numerical treatment of the forcing term that ensures stationary regime (constant flow rate) in the pipe.

Version française

Les caractéristiques numériques de base du code Incompact3d/Xcompact3d sont décrites dans ce chapitre. Celles qui ont fait l'objet de développements dans le cadre de cette thèse seront progressivement décrites dans les chapitres suivants. La configuration de calcul consiste en une géométrie de conduite entièrement immergée dans le domaine de calcul, lequel est discrétisé à partir d'une grille Cartésienne régulière. Les équations du problème (présentées dans ce chapitre uniquement pour le fluide) sont les équations de Navier-Stokes incompressibles : continuité, quantité de mouvement et transport passif pour le champ de température. Pour concilier la géométrie de la paroi avec la dis-

tribution des nœuds du maillage, la méthode des frontières immergées (IBM) développée par [50] est utilisée. Cette technique est basée sur une reconstruction de la solution dans la zone immergée par polynômes de Lagrange. Elle permet d'imposer indirectement les conditions aux limites à la paroi sans introduire de terme de forçage dans les équations d'évolution avec une différenciation spatiale qui ne nécessite pas de traitement particulier à proximité de l'interface fluide/solide.

La discrétisation spatiale est entièrement basée sur des schémas compacts centrés de sixième ordre. En plus de l'ordre de précision de ces schémas de dérivées première et seconde, il est pris en compte leurs caractéristiques de résolution dans l'espace de Fourier. De plus, suite aux travaux de [81], il est détaillé comment le comportement spectral des schémas à dérivée seconde peut être contrôlé, conduisant à une famille de schémas aux différences finies basés sur la dissipation numérique d'ordre élevé. La surdissipation introduite par ces schémas est concentrée à petite échelle et peut contrôler efficacement les erreurs de repliement survenant à des nombres d'onde élevés pour régulariser la solution numérique. De plus, cette dissipation numérique supplémentaire peut être conçue pour se comporter comme une Viscosité Spectrale Evanescente (SVV en sigle anglo-saxon) interprétable comme une modélisation sous-maille dans le contexte de la simulation des grandes échelles (LES en sigle anglo-saxon). Comme le montre [65], cette stratégie peut assurer la convergence de la solution numérique à l'échelle du maillage, contrairement aux approches plus standard basées de type Smagorinsky. Comme cette modélisation est entièrement (et implicitement) contenue dans la dissipation numérique introduite par le schéma à dérivée seconde, cette technique peut être vue comme une stratégie *LES implicite* (*ILES en sigle anglo-saxon*). Le niveau approprié de dissipation numérique à utiliser est définie à partir d'une fermeture spectrale simplifiée proposée par [65]. Puisque le rôle de la dissipation numérique est de régulariser la solution à petite échelle, cette stratégie est applicable dans le contexte de la simulation numérique directe (DNS en sigle anglo-saxon). Ce point sera traité plus en détail dans les chapitres 3 et 5.

Enfin, la méthode à pas fractionnaires utilisée pour l'intégration temporelle de l'équation de quantité de mouvement est présentée. Le traitement de l'équation de Poisson est brièvement décrit ainsi que le traitement numérique du terme de forçage qui assure le régime stationnaire (débit constant) dans la conduite.

Chapter 3

Implicit Wall-Layer Modelling

Traditional Large-Eddy Simulation (LES) of wall-bounded turbulence is based on the explicit computation of all the energy containing near-wall eddies while modelling the effect of the smallest scales. In order to do so, it is recommended to use a mesh resolution between 10 and 100 wall units for the streamwise direction discretization, from 10 to 20 wall units in the spanwise direction, and typically one wall unit in the wall normal direction through the application of a near-wall mesh refinement for instance. When these resolution criteria are too demanding in terms of computational resources, an alternative is to use a discretization which do not capture the inner layer while compensating this bypass with a wall-layer model [19, 34].

Nonetheless, in a previous work from our team, Dairay *et al.* [65] showed that excellent first and second order turbulence statistics of pipe flow can be obtained with a mesh resolution coarser than the viscous sublayer without using any explicit wall-layer modelling. In this context, the near-wall regularization is simply performed by the implicit LES (ILES) technique introduced in section 2.6.3 which - without any extra cost or adaptation in the near-wall region - displays a wall modelling feature. In these previous investigations, two Reynolds numbers $Re_\tau = 180, 550$ were considered when comparing ILES results to unfiltered DNS data of [9]. As discussed in section 2.6.3, the originality of the present ILES method is found in the built-in numerical dissipation that does not come from the discretization of the convective term, but from the diffusive term in the Navier-Stokes equations. This strategy has also been successfully used by [81, 90] to perform LES of turbulent plane channel and impinging jet configurations with regular Cartesian meshes, nonetheless, the near-wall behaviour of the implicit SGS modelling was not yet thoroughly investigated.

Previous comparisons of the ILES technique with reference data were based on basic statistics of unfiltered DNS data, which means that, although a good agreement was observed, no rigorous assessment could be made. Here, this matter is examined at higher Reynolds number ($Re_\tau = 1000$) while determining to what extent it can be generalized in terms of near-wall region bypass. To do so, a DNS database is presented with an original method to easily produce filtered statistics which can be gen-

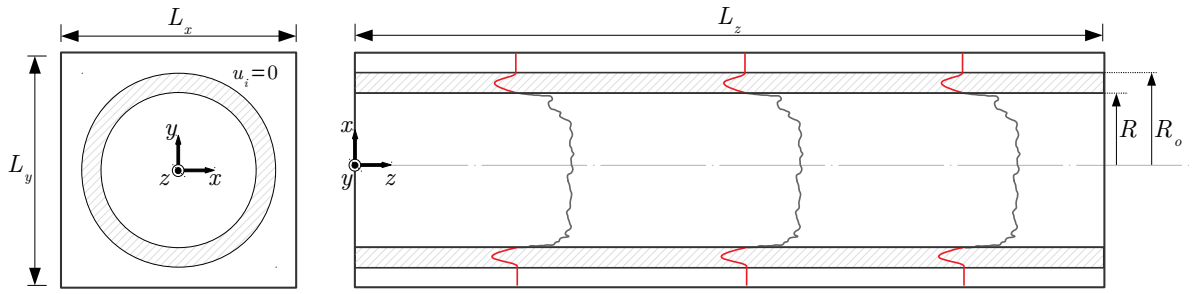

Figure 3.1: Schematic view of the computational configuration. A regular Cartesian mesh is used and the fifth-order Lagrange polynomial reconstruction is illustrated in $R \leq r \leq R_o$.

uinely and consistently compared to ILES at any mesh resolution. The goal is to assess the present implicit LES in terms of ability to predict near-wall statistics despite the use of very coarse grid for which even the near-wall turbulent production region is fully bypassed.

3.1 Numerical methodology and computational configuration

As detailed in section 2.2, the present computational configuration consists of a pipe geometry of inner radius R and outer radius R_o fully immersed in a computational domain of dimensions $L_x \times L_y \times L_z$, discretized with a Cartesian mesh of $n_x \times n_y \times n_z$ nodes regularly distributed. For the sake of completeness, a schematic view of the computation configuration is once again provided in Figure 3.1. The cylindrical coordinates system relates to the Cartesian one according to

$$r = \sqrt{x^2 + y^2} \tag{3.1}$$
$$\phi = \arctan(y/x) \tag{3.2}$$
$$z = z \ . \tag{3.3}$$

To model the presence of the solid body, the IBM described in section 2.5 is used. This technique consists of locally satisfying the no-slip condition with Lagrange polynomial reconstructions of the fluid solution into the immersed region (i.e., the annular volume $R \leq r \leq R_o$), clearly improving the accuracy of compact finite difference schemes such as those used in the code Incompact3d/Xcompact3d (see representation in Figure 3.1). Periodic boundary conditions are prescribed at the boundaries of the computational domain for all three Cartesian directions. The longitudinal length of the domain is kept constant for all simulations $L_z = 12.5D$, whereas the transverse dimensions L_x and L_y are adjusted according to the mesh resolution in order to provide a minimum number of grid points in the buffer zone $r > R_o$. This enables us to prescribe periodic conditions for the transverse-xy directions while ensuring the success of the reconstruction technique.

Table 3.1: Numerical parameters of DNS/LES performed.

	Re	Δz^+	Δr^+	c_1	ν_0/ν	Re_τ
DNS						
[9]	37700	< 9.98	$0.15 - 5.12$	-	-	999
Present	37700	13	≈ 2.9	-	3	996.8
LES marginal resolution						
Implicit model	37700	19.5	≈ 4.5	0.055	3	990.6
No-model	37700	19.5	≈ 4.5	-	-	1053.1
LES low resolution						
Implicit model	37700	26	≈ 12	0.055	7	981.2
No-model	37700	26	≈ 12	-	-	1242.7

The governing equations are the incompressible Navier-Stokes[1] (2.9, 2.10). The full-explicit time advancement of the momentum equation (2.10) is carried out with a third order Adams-Bashforth scheme, as described in section 2.7. The implicit SVV method described in section 2.6.3 is used here to perform LES (ILES) at different mesh resolutions as well as a DNS at marginal resolution. Within Incompact3d/Xcompact3d, the desired numerical dissipation can be easily calibrated for the different spectral viscosities (c_1 and ν_0/ν), the numerical parameters for all the simulations performed are reported in Table 3.1.

3.2 Mesh distribution *vs.* Mesh resolution

The term *mesh resolution* refers here to the size of the cells in each Cartesian direction regardless of the location of the nodes with respect to the wall [8]. In the present framework, a regular Cartesian mesh is used for the spatial discretization which provides computational cells of fixed size $\Delta x \times \Delta y \times \Delta z$. The corresponding mesh resolution in wall units for a grid spacing Δx is therefore given by

$$\Delta x^+ = \frac{\Delta x}{R} Re_\tau \ . \tag{3.4}$$

The corresponding mesh resolutions for each one of the simulations are also reported in Table 3.1. In previous investigations in a similar computational configuration, Dairay *et al.* [8] presented very good basic DNS statistics of turbulent pipe flow at $Re_\tau = 550$ with a transverse mesh resolution $\Delta x^+ = \Delta y^+ = 5.5$ wall units. Based on the concept of minimal scale computed with accuracy (see schematic

[1]For the investigations presented in this chapter, the transport of temperature is not concerned.

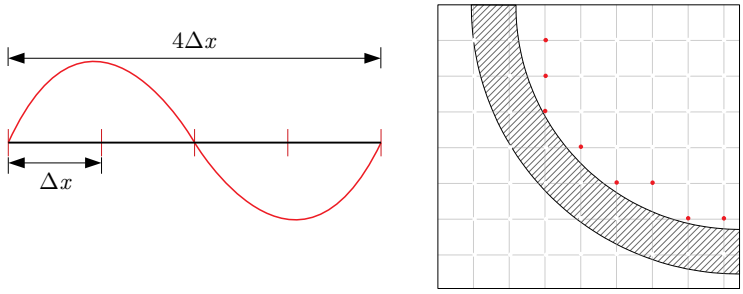

Figure 3.2: (Left) The accurate description of a scale requires a minimum of $4\Delta x$ [8], reason why a extra refinement of the near-wall region providing ≤ 1 wall unit is usually recommended in order to properly describe physical phenomena within the viscous sublayer. (Right) Illustration of the irregular distribution of Cartesian mesh nodes. The nodes marked in red for instance, are found in a distance from the wall smaller than the mesh resolution.

representation in Figure 3.2-left), the minimal scale to be actually captured with such a mesh resolution should be of the order $L^+_{min} \approx 4 \times 5.5 \approx 22$ wall units. Such a value should not only bypass the viscous sublayer $(R-r)^+ < 5$, but also the entire production region $(R-r)^+ < 15$. Nonetheless, the near-wall statistical signature was remarkably well-reproduced, even up to a scale smaller than the mesh resolution itself.

The success of the method has been mainly attributed to the *mesh distribution*, which refers to the location of the grid points with respect to the wall [8]. Moreover, as the geometry boundaries are disconnected from the mesh arrangement in this scenario, mesh nodes are irregularly distributed with respect to the wall. Figure 3.2-right exemplifies how some of the mesh nodes may be found very close to the wall (even inside the viscous sublayer) despite the coarse mesh resolution used, and thus, their near-wall knowledge of the solution can advantageously contribute to the computation of turbulence statistics in distances smaller than the mesh resolution by applying the projection technique described in section 2.8.

3.3 Filtered DNS database

Having described the numerical methodology, we shall now proceed to the establishment of a filtered DNS database to be consistently compared to ILES results at any mesh resolution. Firstly, DNS of pipe flow is carried out at $Re = 37700$ with a mesh of $n_x \times n_y \times n_z = 768 \times 768 \times 1920$ in a computational domain $L_x \times L_y \times L_z = 1.12D \times 1.12D \times 12.5D$, corresponding to a (marginal) mesh resolution of $(\Delta x^+, \Delta y^+, \Delta z^+) = (2.9, 2.9, 13)$. Statistics are gathered on the fly once the fully developed turbulent

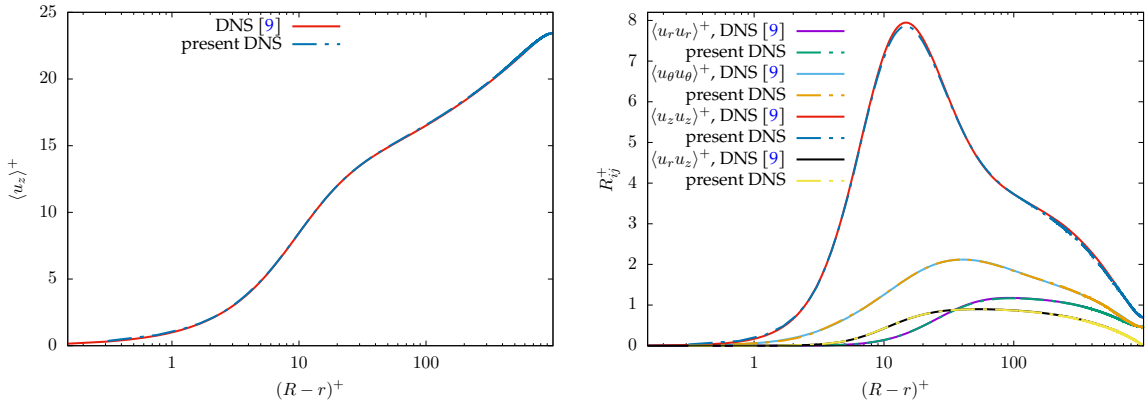

Figure 3.3: (Left) Mean velocity and (right) Reynolds stress profiles for the DNS at $Re_\tau = 37700$ with marginal resolution. The turbulence statistics are compared to DNS data of [9].

state is reached. The evolution of the friction velocity $u_\tau(t)$, predicted every time step with eq.(2.52) is the criterion used to monitor the flow development.

For the sake of validation, in Figure 3.3 first and second-order statistics normalized in viscous units are compared to DNS results of [9], obtained with the high-order spectral element code Nek5000. A very good agreement is recovered, with only -1% underprediction of the friction Reynolds number Re_τ. Despite the marginal mesh resolution employed, such a satisfactory result could be achieved thanks to a small amount of numerical dissipation introduced to regularise the solution ($\nu_0/\nu = 3$ is used in the framework of the ISVV strategy for DNS described in section 2.6.3[2]). The good results are also attributed to the mesh distribution factor discussed in the previous section and the use of high-order spatial schemes (this point is further addressed in chapter 5, section 5.5.2).

In what follows, we introduce an original methodology to generate filtered statistics from this DNS database. It is interesting to note that, thanks to the high resolution mesh in which the database was created, the filtered data is also obtained in high resolution.

3.3.1 Pao-filter

In the present ILES framework, the appropriate level of high-order numerical dissipation required to regularise the LES solution is defined from the simple Pao-like spectral closure proposed by [65]. In the framework of homogeneous and isotropic turbulence at small scales, this simple model provides a pragmatic way to calibrate physically the numerical viscosity required by the LES, i.e., the value at the cutoff wavenumber ν_0/ν and its spectral distribution c_1 (c.f. section 2.6.3). Although it has been

[2]Scheme (2.21, 2.33) is used for the computation of second derivatives.

recognized by [65] that a rigorous formalism is still missing, this regularisation technique can and have been successfully used to investigate near-wall turbulence of channel flow [81], turbulent jet impinging on a heated wall [90] and turbulent pipe flow [8, 76, 78]. Furthermore, [65] highlights that, even for the treatment of inhomogeneous and anisotropic turbulent flows, the only input required by the Pao-like model is the ratio between the DNS and the LES mesh resolutions. It is recommended to firstly design the mesh that the hypothetical DNS would require, and then, by inputting the desired LES mesh resolution, the model provides an estimation of the level of numerical dissipation (ν_0/ν and c_1) to be introduced in the ILES as well as an estimation of the filtering operator associated with the reduction of the number of degrees of freedom.

Here, the transfer function of the filtering operator is used in the spectral space to produce a filtered DNS database. More precisely, as the filter transfer function is defined according to the numerical dissipation introduced in the ILES, filtering the DNS solution allows us to define a rigorous target solution for the ILES, thus enabling consistent *a priori*/*a posteriori* comparisons. This type of filter is referred here as *Pao-filter* and it is defined as a homogeneous filter whose transfer function is given by [65]

$$T_f(k) = \sqrt{\frac{E_{LES}(k)}{E_{DNS}(k)}} \ , \tag{3.5}$$

where E_{DNS} and E_{LES} are the kinetic energy spectra associated to the DNS and LES respectively. An example of the filtering effect[3] is illustrated in Figure 3.4-left for a filter length $\Delta = 4\Delta x$ applied once in each spatial direction, representing a LES mesh resolution $4\times$ coarser than the DNS in each Cartesian direction, i.e., a reduction of degrees of freedom by a factor 64. It is interesting to note that very good levels of global energy should still be nonetheless captured by the LES despite this significant reduction of degrees of freedom. In Figure 3.4-right, some transfer functions are exemplified for different filter lengths. It can be said that the Pao-filter displays a behaviour between a cutoff and a Gaussian filter.

The filter is applied once in each spatial direction in order to take the anisotropy of the LES mesh into account, which means that different filter transfer functions may be used for the streamwise-z and transverse-xy directions, representing different mesh resolutions. This type of *a priori*/*a posteriori* analysis has already been performed by [75], but in the context of homogeneous and isotropic turbulence with the Taylor Green Vortex problem. However, in the presence of a wall, it is generally difficult to define a homogeneous filter because of the loss of homogeneity in the near-wall region. This is possible here thanks to the use of periodic boundary conditions in all three Cartesian directions together with the smoothness of the solution across the fluid-solid interface provided by the present IBM. This point is made very clear in Figure 3.5. When the fluid solution is not reconstructed prior to the application of the Pao-filter, the sharp fluid-solid interface is strongly felt by the filtering operator. This effect appears as a no-slip condition poorly ensured in the mean velocity profile, compromising the reliability of filtered data. Such a problem is nearly suppressed when the solution is reconstructed before filtering. Nonetheless, even in this case, the consistency of the filtered data needs to be assessed. In fact, in the present framework, the no-slip condition is softly prescribed during the reconstruction but it is never literally imposed to the solution. This way, a subsequent application of the filter operator can eventually re-shape the near-wall behaviour of the solution. In other words, particular attention should be

[3] For the purpose only of illustrating the filtering effect, the spectrum represented is computed at the centre-line $r = 0$ along the pipe length L_z

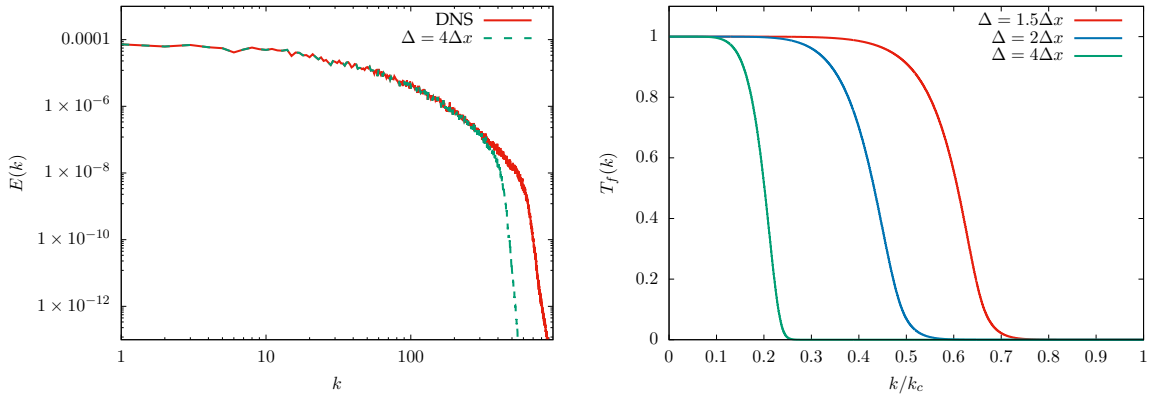

Figure 3.4: (Left) Filtering effect of the Pao-filter on the Kinetic energy spectra $E(k)$. (Right) Pao-filter transfer functions for different filter lengths Δ.

paid to possible antagonisms between the application of the homogeneous filter and the conservation of the no-slip condition.

3.3.2 Streamwise *vs.* Transverse directions filtering

As a first assessment, the effect of the Pao-filter is tested on the transverse-xy and streamwise-z directions separately in order to evaluate how the reduction of degrees of freedom along each Cartesian direction affects the levels of energy to be captured by the ILES. To do so, in Figure 3.6, we analyse the normalized turbulent kinetic energy profiles $k^+ = \frac{1}{2}\langle u_i' u_i' \rangle^+$ for filtered DNS data corresponding to different xy (left) and z (right) mesh resolutions. Such an assessment can help us to define interesting mesh resolutions to carry out our ILES. For instance, the profiles in Figure 3.6-left, give us quantitative estimations of the levels of energy that would still be captured when the viscous sublayer ($\Delta x^+ = 6$) and/or even the entire near-wall production region ($\Delta x^+ = 12$) are structurally bypassed by the mesh resolution.

It can be seen that filtering the transverse-xy directions impacts mostly the inner region whereas the streamwise-z filtering extracts energy mostly from the outer region. It is also interesting to note that, *a priori*, even a LES mesh $2\times$ coarser than the DNS in all directions - which would represent a non-negligible reduction of degrees of freedom by a factor 8 - should hardly affect the level of energy captured.

Surprisingly, the use of a coarse mesh resolution of $\Delta x^+ = \Delta y^+ = 12$ wall units for the transverse-xy directions should still allow us to capture the large majority of the energetic scales that compose the flow, as shown by Figure 3.6-left. Such a result suggests that, in the absence of wall-modelling, the use of very small cells close to the wall is not mandatory in order to capture the energy containing near-wall

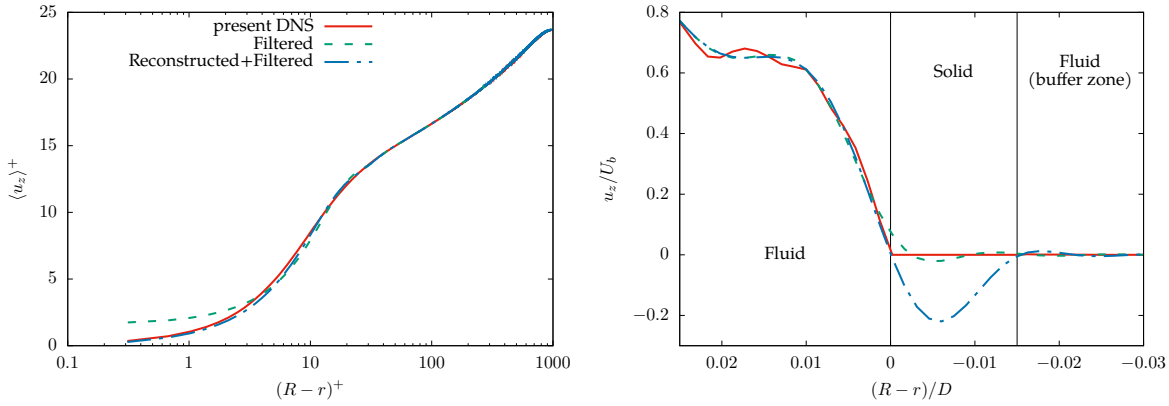

Figure 3.5: (Left) mean and (right) instantaneous velocity profiles highlight the necessity of reconstructing the fluid solution before filtering the transverse-xy directions. In this example, DNS data have been filtered at a corresponding mesh resolution of $\Delta x^+ = \Delta y^+ = 12$.

eddies. This goes against the typical recommendations for LES mentioned in the introduction section of this chapter [19, 34]. Furthermore, Figure 3.6-right shows that the use of a streamwise resolution of $\Delta z^+ = 104$ wall units would result in a significant loss of turbulent kinetic energy. Such a mesh resolution (and even coarser) is often used to perform LES of wall turbulence. However, the present results suggest that the use of very large cells in the flow direction should be considered with more caution as it would imply neglecting many energetic scales that compose the flow.

It is also important to mention that the capability of the reconstruction to ensure the success of the transverse-xy filtering is limited to not so high values of the filter length. In fact, this is related to the previously mentioned dependence of the transverse-xy filtering on the reconstruction technique and a potential poor conservation of the no-slip condition. For instance, when DNS data is filtered at a corresponding cell size of $\Delta x^+ = \Delta y^+ = 24$ wall units (see Figure 3.6-left), an abnormal near-wall rising of kinetic energy is observed as a consequence of a poorly ensured no-slip condition. Additional tests showed that this unrealistic rising of k^+ in the near-wall region could be avoided up to $\Delta x^+ = 15$. Yet, a strange behaviour could still be observed with, for instance, $k^+ \approx 0.156$ at $(R-r)^+ \approx 1.03$, which is erroneously higher than the unfiltered value $k \approx 0.124$, showing that persistent non-physical velocity fluctuations (spurious oscillations) were still emerging for $\Delta x^+ = 15$. Therefore, for a matter of certainty, we have decided to limit our analysis to transverse mesh resolutions $\Delta x^+ \leq 12$ for which the filtering procedure does not produce abnormal levels of kinetic energy in the inner layer while still providing a good prediction in the outer layer.

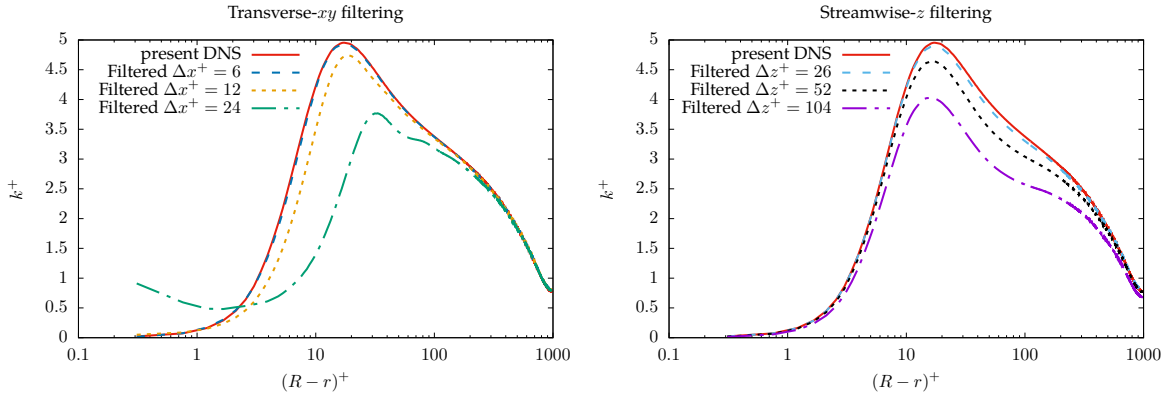

Figure 3.6: (Left) Turbulent kinetic energy from filtered quasi-DNS at different mesh resolutions. The drop of energy is analysed for the filter applied separately in (left) transverse-xy directions and (right) streamwise-z direction.

3.4 Implicit LES assessment

From the *a priori* analysis of the previous section, two interesting configurations have been selected to perform implicit LES of turbulent pipe flow at $Re = 37700$:

1. *Marginal Resolution:* $n_x \times n_y \times n_z = 512 \times 512 \times 1280$ mesh nodes in a computational domain of dimensions $L_x \times L_y \times L_z = 1.12D \times 1.12D \times 12.5D$ (similarly to the DNS), corresponding to a mesh resolution, in wall units $\Delta x^+ = \Delta y^+ \approx 4.5$, $\Delta z^+ \approx 19.5$.
2. *Low Resolution*: $n_x \times n_y \times n_z = 256 \times 256 \times 960$ nodes in a computational domain $L_x \times L_y \times L_z = 1.5D \times 1.5D \times 12.5D$, which corresponds in wall units to $\Delta x^+ = \Delta y^+ = 12$, $\Delta z^+ = 26$.

The mesh resolutions have been chosen based on the levels of turbulent kinetic energy to be captured while enabling the assessment of the present numerical strategy in terms of viscous and near-wall production region bypass respectively. Filtered DNS results presented henceforth are obtained from the sequential application - once in each Cartesian direction - of the Pao-filter, which allows us to produce filtered statistics consistent with the ILES mesh resolution and numerical dissipation used.

Implicit wall-layer modelling Before proceeding to the results, few words should be said about the use of the term *implicit wall-layer modelling*. As previously mentioned in this chapter, typical recommendations for LES suggest that first mesh nodes should be found inside the viscous sub-layer, in a distance of at least $(R-r)^+ = 1$ from the wall, in order to obtain a correct prediction of the wall friction. Alternatively, a coarser mesh may be used while explicitly including a wall-layer model to

provide the friction prediction. Here, the term *implicit wall-layer model* is used to emphasize that the capability of the present methodology in regularising the near-wall solution is accomplished without any explicit wall-model. The improvement brought by the technique is the direct result of the damping of spurious oscillations arising from small scales, which is simply achieved by using scheme (2.21, 2.40) for the computation of second derivatives - i.e., with the implicit SVV technique described in section 2.6.3. In other words, instead of relying on a model, it is the solver itself that takes charge of improving the near-wall solution. To highlight this implicit wall modelling feature, the ILES statistics are also compared, in the next section, to *no-model LES* results, which is performed without any (implicit nor explicit) SGS/wall-layer modelling while using the popular sixth-order compact scheme of [80] to compute second derivatives.

3.4.1 Marginal resolution

Figure 3.7 compares first and second-order statistics of the ILES at *Marginal Resolution* with DNS filtered at the corresponding mesh resolution and *no-model* LES results. This *a posteriori* analysis points to the existence of numerical-modelling errors given the deviation between ILES and filtered k^+ profiles observed at the production peak. Yet, it can be stated that the overall agreement is very satisfactory. Moreover, the precision of the statistics are the confirmation at higher Reynolds number that accurate turbulent statistics can be obtained despite the use of a mesh resolution that clearly bypasses the viscous sublayer.

In particular, one sees that the peak of k^+ is remarkably well predicted at a level of detail clearly higher than the minimal scale computed with accuracy $4\Delta x^+ = 18$. If compared to *no-model* results, numerical dissipation is found definitely necessary so that it can be seen as playing the role, in this context, of an implicit viscous sublayer modelling. To explain this improvement, it must be mentioned that the no-model solution is subjected to small-scale oscillations which make inaccurate the prediction of the friction velocity u_τ with an overestimation of about $+6\%$, as reported in Table 3.1. Here, the use of numerical dissipation can remove these spurious oscillations making the friction velocity prediction clearly more accurate with a deviation of only -1% by comparison to the DNS prediction.

3.4.2 Low resolution

Figure 3.8 compares first and second-order statistics for the *Low Resolution* ILES. As reported in Table 3.1, a good prediction of the mean velocity is recovered by the ILES with an acceptable -2% underprediction of u_τ (see Fig. 3.8-left). The filtered profile of k^+ predicted by the ILES in Figure 3.8-right shows that good levels of energy could still be captured despite the astonishing resolution of 12 wall units used for the transverse-xy discretization. Even though the profile of k^+ is somewhat irregular in the region of the peak, its amplitude is only underestimated by -11% and its shape reproduced with a precision evidently smaller than the minimum scale computed with accuracy $4\Delta x^+ = 48$. Furthermore, in the outer layer, the agreement with filtered DNS is very satisfactory.

Conversely, *no-model* results present for both mean velocity and kinetic energy profiles completely

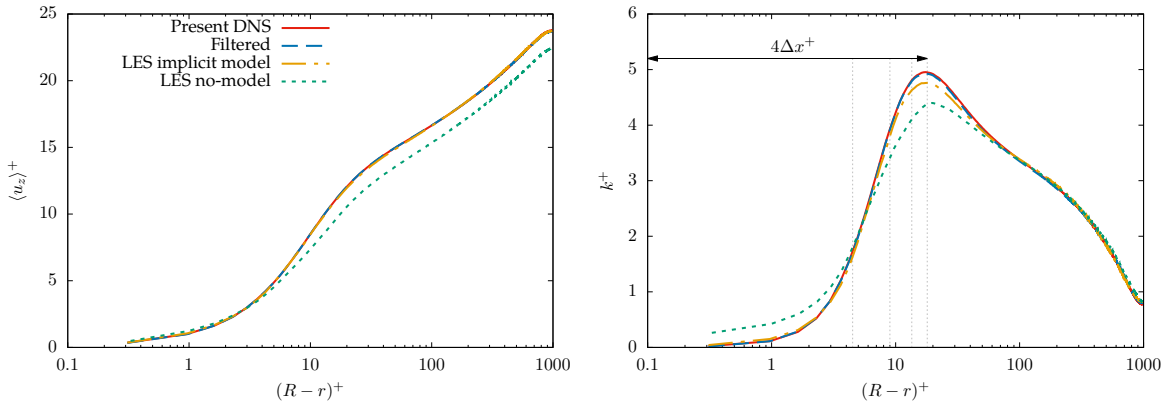

Figure 3.7: (Left) Mean velocity and (right) turbulent kinetic energy profiles for ILES at $Re_\tau = 37700$ with marginal resolution. The turbulence statistics are compared to filtered DNS data and 'No-model LES'.

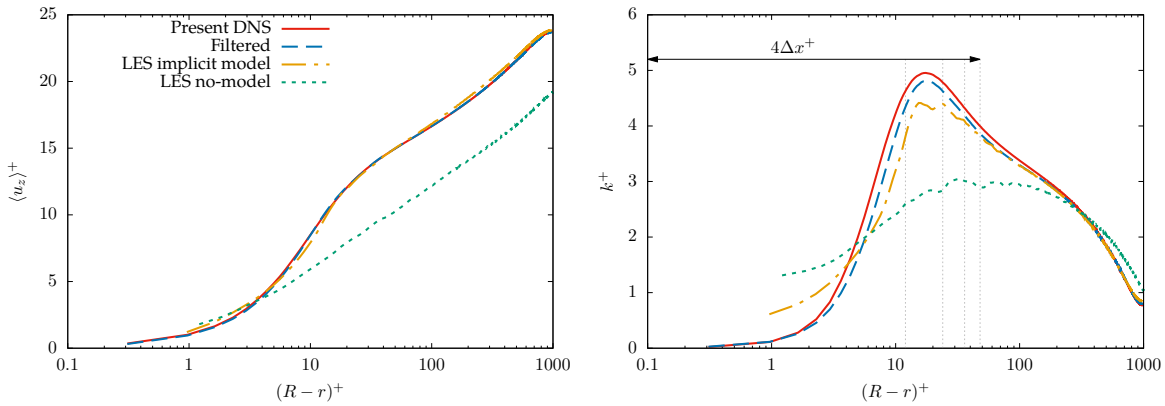

Figure 3.8: (Left) Mean velocity and (right) turbulent kinetic energy profiles for ILES at $Re_\tau = 37700$ with low resolution. The turbulence statistics are compared to filtered DNS data and 'No-model LES'.

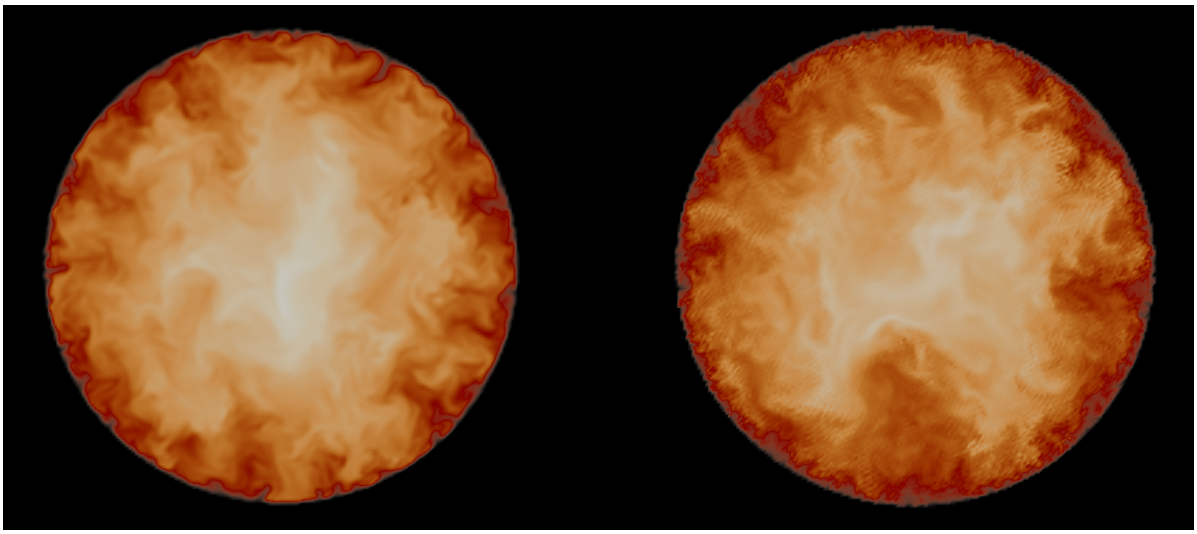

Figure 3.9: Snapshots of the instantaneous streamwise velocity u_z for (left) present implicit LES technique and (right) no-model LES. The suppression of wiggles in the near-wall region reveals the implicit wall modelling feature embedded in the method.

nonphysical behaviours with such a coarse mesh. These results confirm the implicit wall-layer modelling feature intrinsic to the present implicit SVV technique for LES, given its ability to restore the quality of the wall friction from $+24\%$ to -2% while enabling the realistic prediction of the fluctuating velocity profiles (embedded in the calculation of k). This very favourable improvement is the result of the damping of spurious oscillations promoted by the use of numerical dissipation concentrated at the small scales. In Figure 3.9, snapshots of the instantaneous streamwise velocity u_z demonstrate the reduction of wiggles in the near-wall region.

It interesting to note however that the problem related to the weak conservation of the no-slip condition observed *a priori* seems to appear also *a posteriori* in the form of a non-physical raising of kinetic energy levels in the inner region (Figure 3.8-right). Some preliminary tests have showed that this effect seems to be related to the azimuthal location of the nodes, especially those close to the cardinal points. These errors, mostly associated to the immersed boundary technique, tend to compensate each other leading to the acceptable k^+ profile presented in Figure 3.8-right. Further investigations of this anomaly are planned in order to suppress immersed boundary artefacts.

3.5 General conclusion

In this chapter, fundamental aspects of the present numerical strategy are highlighted through Direct and Implicit Large-Eddy Simulation (DNS/ILES) of turbulent pipe flow. Firstly, DNS turbulence statistics at $Re = 37700$ with the present strategy are presented with a remarkable agreement with reference results. The success of the method is attributed to the small amount of numerical dissipation used to regularise the solution at small scales, as well as the irregular distribution of mesh nodes with respect to the wall and the use of high-order spatial schemes.

An original filtering strategy is subsequently introduced to produce a filtered DNS database for rigorous *a priori*/*a posteriori* comparisons with ILES results. The filter transfer function is defined in the Fourier space, consistently with the numerical dissipation introduced in the ILES. The filter is applied once in each direction to take into account the anisotropy of the ILES mesh. It is also shown how the interfacial smoothness provided by Lagrange reconstruction of the fluid solution is fundamental for filtering the transverse-xy directions.

Then, two different mesh resolutions - namely *marginal* and *low resolutions* - are chosen to perform ILES based on the levels of turbulent kinetic energy to be captured with the present numerical strategy when the viscous sub-layer and even the near-wall production region are bypassed. The comparison with filtered DNS results points to the existence of modelling errors, yet, turbulence statistics are described with a level of detail clearly higher than the minimal scale computed with accuracy for both *marginal* and *low resolution* cases. Furthermore, it is shown through comparison with *no-model* LES results that the present Implicit SVV strategy for LES functions also as an implicit wall-layer modelling thanks to the damping of spurious oscillations (aliasing errors) promoted by the use of numerical dissipation concentrated at small scales. It is recognised that for the *low resolution* case, errors associated to the immersed boundary technique tend to compensate each other leading to the acceptable second-order statistics presented. Further investigations of this problem are scheduled.

Version française

Dans ce chapitre, les caractéristiques essentielles de la présente stratégie numérique sont mises en évidence par simulation directe et des grandes échelles implicite (DNS/ILES) de l'écoulement turbulent dans une conduite. Les statistiques turbulentes obtenues par DNS à $Re = 37700$ sont présentées en montrant un accord remarquable avec les résultats de référence. Le succès de la méthode est attribué à la dissipation numérique utilisée de façon ciblée pour régulariser la solution à petite échelle, à la distribution irrégulière des nœuds du maillage par rapport à la paroi ainsi qu'à l'utilisation de schémas de différentiation spatiale d'ordre élevé.

Une stratégie de filtrage originale est ensuite introduite pour produire une base de données DNS filtrée pour des comparaisons *a priori*/*a posteriori* rigoureuses avec les résultats ILES. La fonction de transfert du filtre est définie dans l'espace de Fourier, en cohérence avec la dissipation numérique introduite dans le type d'ILES mené. De cette façon, les résultats DNS filtrés correspondent à la solution ILES cible. De plus, le filtre est appliqué une fois dans chaque direction pour prendre en compte

l'anisotropie du maillage ILES. Il est également montré comment la régularité interfaciale fournie par la reconstruction par polynôme de Lagrange de la solution fluide est fondamentale pour filtrer correctement les directions transverses-xy.

Ensuite, deux maillages différents (résolutions *marginale* et *basse*) sont choisis pour effectuer des ILES en considérant les niveaux d'énergie cinétique turbulente à reproduire lorsque la sous-couche visqueuse et même la région de production en proche paroi ne semblent pas correctement capturées par la grille de calcul. Même si la comparaison avec les résultats DNS filtrés indique la présence d'erreurs de modélisation significatives, les statistiques turbulentes de base sont décrites avec un niveau de détail nettement supérieur à l'échelle minimale calculée avec précision pour les deux résolutions considérées. En outre, il est montré par comparaison avec des résultats LES sans modèle sous-maille (*no-model* LES) que la stratégie SVV implicite suivie ici fonctionne comme un modèle de paroi implicite grâce à l'amortissement des oscillations parasites (produites notamment par les erreurs de repliement) favorisé par l'utilisation d'une dissipation numérique concentrée à petite échelle. Il est reconnu que pour le cas *basse résolution*, les erreurs associées à la technique de frontières immergées ont tendance à se compenser, ceci conduisant à des statistiques du second ordre d'une qualité acceptable. Des investigations plus approfondies sur ce phénomène sont prévues.

Chapter 4

Viscous and hyperviscous filtering for direct and large-eddy simulation

In the course of this thesis, a novel solution filtering technique for DNS and LES has been developed. This approach is in fact equivalent to the use of spectral viscosity as a possible ersatz of subgrid-scale modelling for LES (or regularisation at small scales for DNS), according to the discussions developed in section 2.6.3. The method is detailed in this chapter and it should be stressed that its development/implementation has been mutually important for the advancement of this thesis and the validation of this novel technique. More precisely, as discussed in section 2.7, a full-explicit time integration with third-order Adams-Bashforth scheme have been used for the governing equations. However, as it is shown in this chapter, when an IBM is used, diffusivity can easily become more constraining than the CFL condition, requiring the use of very small time steps in order to ensure numerical stability. This condition can be further aggravated if heat transfer is to be considered with $Pr \ll 1$ together with a hyperviscous second-derivative operator as it is done in here. As a consequence, the heat transfer simulations scheduled for this thesis would be too costly, especially for low Prandtl number fluids and/or the Conjugate Heat Transfer problem (CHT) which requires dealing simultaneously with distinct temporal and spatial scales when simulating the forced convection in the fluid coupled to the heat conduction in the solid.

In this context, it can be even said that the development of the present viscous filtering technique came at the perfect timing as its major highlight is precisely the strong relaxation on the diffusivity constraint, allowing the use of much larger time steps which ultimately led to remarkable savings of computational resources. In the light of the article recently published where the methodology is fully detailed [78], we have decided not to re-describe it from scratch here but to directly provide the reader with the article. Turbulent heat transfer results presented with Mixed-type boundary conditions (MBC) in section 7.2 are re-addressed in the next chapter when describing the IBM strategies implemented for prescribing thermal boundary conditions in the framework of this thesis.

Journal of Computational Physics 431 (2021) 110115

Contents lists available at ScienceDirect

Journal of Computational Physics

www.elsevier.com/locate/jcp

Viscous and hyperviscous filtering for direct and large-eddy simulation

Eric Lamballais [a,*], Rodrigo Vicente Cruz [a], Rodolphe Perrin [b]

[a] Curiosity Group, Pprime Institute, CNRS - University of Poitiers - ENSMA, France
[b] Department of Mechanical Engineering, Faculty of Engineering, Kasetsart University Sriracha, Thailand

ARTICLE INFO

Article history:
Available online 19 January 2021

Keywords:
Direct and large-eddy simulation
Solution filtering
Finite-difference schemes
High-order methods
3D Taylor-Green vortex flow
Turbulent pipe flow

ABSTRACT

This work is dedicated to the solution filtering technique for performing direct and large-eddy simulation. It is shown that this approach is equivalent to the use of spectral viscosity as a possible ersatz of subgrid-scale modelling. In the framework of finite-difference schemes, the filter operator can be designed to ensure time consistency while easily controlling the level and scale selectivity of the dissipation thus introduced. Then, a new family of filter schemes is developed in order to represent both the molecular and artificial dissipations. The resulting viscous filter operator is straightforward to implement through a simple modification of its coefficients that depend on the molecular/artificial viscosity and the time step. A definitive advantage in terms of computational efficiency is obtained for computational configurations where the time step is restricted by the Fourier condition, as a simple alternative to implicit time integration of the viscous term. Numerical tests clearly show that this viscous filtering method is flexible, accurate and numerically stable at large Fourier number.

1. Introduction

In the context of large-eddy simulation (LES), spatial filtering can refer to different concepts and techniques, as a potential source of misunderstanding between users and developers in this field of computational fluid dynamics. The essential meaning of spatial filtering is related to the LES formalism itself as a tool of decomposition between the large-scale component of the solution and its residual small-scale component designated as the subgrid-scale (SGS) part. This first concept has been widely developed with the purpose to derive the governing equations of the large-scale motion while introducing the unknown SGS tensor in the framework of a closure problem. For the general background based on this way to define the LES problem, the reader is referred to the textbooks [1–3] which also include the presentation of the most popular SGS models. In this study, this primitive meaning of spatial filtering is not addressed. The related SGS modelling is also not considered, avoiding the difficult questions about the way to account for this "implicit filtering" in the SGS model itself. For the most popular SGS model, namely the Smagorinsky model, the spatial filtering, to which the solution is actually subjected, is a model feature. This feature can only be known *a posteriori*, as an output of the LES, with a major role of the numerical error for the filtering actually obtained [4].

In this study, we are interested in the technique that consists in the application of spatial filtering every time step on the solution during the time advancement of the governing equations. This technique is sometimes referred as "solution

* Corresponding author.
E-mail address: eric.lamballais@univ-poitiers.fr (E. Lamballais).

https://doi.org/10.1016/j.jcp.2021.110115
0021-9991/

filtering" [5] or as "relaxation filtering" [6,7]. It can also be designated as "explicit filtering", but this term is potentially confusing with the SGS modelling approach where the non-linear convective terms, based on the implicitly filtered (i.e. large-scale) solution, are themselves filtered with a given operator to define an alternative SGS tensor in a modified closure problem [8–10]. Here, for simplicity, the term "solution filtering" is preferred to clearly express that the filter operation is applied directly on the solution without any reference to other formalisms or non-linearity treatments. We also only focus on the systematic application of the filter every time step, even if a periodic application every n time steps can also be an option to control the resulting artificial dissipation while saving computational time [11–14].

The solution filtering approach is shared by a wide community in the field of LES as well as in direct numerical simulation (DNS), see for instance [15,16,11,17–19]. When used in DNS, it can be viewed as a way to control the development of numerical oscillations, due for instance to aliasing errors, when the viscous term is not strong enough to ensure this control [20]. Typically, it enables simulators to perform DNS at marginal resolution while improving the physical realism of their solutions which can be virtually free from small-scale spurious oscillations. When this idea is pushed further using coarse computational mesh at high Reynolds number, the filtering solution strategy is referred as an ersatz of SGS modelling in a fuzzy formalism mainly based on considerations about the expected functional role of the SGS uncaptured by the computational mesh. Viewed in this perspective, this approach may be classified in the field of implicit LES, the solution filtering corresponding to an artificial regularisation process applied throughout the calculation. Since its very beginning through the MILES approach [21], implicit LES has become very popular with the development of a wide range of technics to ensure regularisation (see for instance the collective book [22]). In this work, the goal is not to propose a new approach for implicit LES but to develop a new technique that can be put in this perspective while being firstly useful for DNS.

To introduce artificial dissipation for regularisation purposes, the most popular method is to differentiate the convective term using upwind schemes. An alternative is to boost artificially the viscous term through an overestimation of the second derivatives at small scales, as proposed by [23] where a comparison with the traditional upwind-based strategy is presented for a one-dimensional (1D) linear convection/diffusion equation. In [23], and in a more detailed way in [4], it has been shown that this type of numerical dissipation is the finite-difference counterpart of spectral vanishing viscosity (SVV) [24–27]. In this paper, also based on a finite-difference framework, the links between SVV, boosted second derivative and filtering are clarified to open the way for a new technique of solution filtering.

The manuscript is organized as follows. In section 2, a generic finite-difference operator is defined with a classic definition of its coefficient relations up to a given order of accuracy. Then, the role of solution filtering is described in section 3 by considering a 1D model equation where the filtering operation can be clearly expressed inside the time advancement. In this simplified framework, an equivalent SVV is introduced in section 4 as a function of the filter transfer function. Based on this equivalence, the strength and the scale-selectivity of the filter can be controlled through the scaling of the scheme coefficients while ensuring the time consistency of the resulting regularisation operator. This principle is extended in section 5 in order to incorporate the molecular dissipation into the filter scheme. In section 6, the numerical accuracy and stability of this new type of filtering, called "viscous filtering", is analysed through spatial and temporal convergence tests. Then, DNS/LES results are presented in section 7 to assess the viscous filtering strategy in demanding computational configurations involving fully developed turbulence. The major advantage of viscous filtering, in terms of numerical stability, is clearly exhibited, as an efficient alternative strategy to time implicit integration of the viscous term. The main conclusions are summarized in section 8 while drawing perspectives for further developments. Finally, an appendix is provided to clearly establish the close link between viscous filter and second derivative finite-difference schemes.

2. Filtering scheme and transfer function

Here, the filtering approach is considered in the framework of finite-difference schemes. For simplicity, the discretization is based on a regular mesh and the formalism is presented in 1D through the basic filtering operator expressed as

$$\alpha_f \hat{f}_{i-1} + \hat{f}_i + \alpha_f \hat{f}_{i+1} = a_f f_i + b_f \frac{f_{i-1}+f_{i+1}}{2} + c_f \frac{f_{i-2}+f_{i+2}}{2} + d_f \frac{f_{i-3}+f_{i+3}}{2} + e_f \frac{f_{i-4}+f_{i+4}}{2} \tag{1}$$

with its associated transfer function

$$T(k\Delta x) = \frac{a_f + b_f \cos(k\Delta x) + c_f \cos(2k\Delta x) + d_f \cos(3k\Delta x) + e_f \cos(4k\Delta x)}{1 + 2\alpha_f \cos(k\Delta x)} \tag{2}$$

where $f_i = f(x_i)$ are the values of a generic function $f(x)$ on the nodes $x_i = (i-1)\Delta x$, $\hat{f}_i$ are the filtered values and k is the wavenumber. To provide a low-pass filter, it is common to impose the value of $T(k\Delta x)$ at the cutoff wavenumber $k_c = \pi/\Delta x$ with for instance

$$T(k_c\Delta x) = 1 - \sigma \tag{3}$$

where $0 \leq \sigma \leq 1$. In the context of numerical simulation, the most popular choice is to fully remove the grid-to-grid wavelength using $\sigma = 1$.

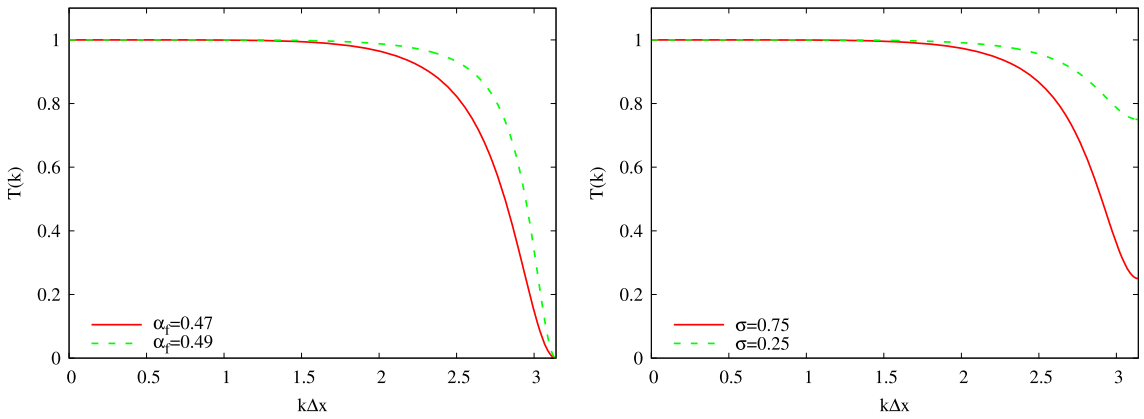

Fig. 1. Left: highly ($\alpha_f = 0.49$) and moderately ($\alpha_f = 0.47$) scale-selective filtering for $\sigma = 1$. Right: soft ($\sigma = 0.25$) and medium ($\sigma = 0.75$) filtering for $\alpha_f = 0.47$.

In addition to condition (3), Taylor's expansion can provide extra constraints on the set of coefficients ($\alpha_f, a_f, b_f, c_f, d_f, e_f$) in order to reach a given order of accuracy, with

$$1 + 2\alpha_f = a_f + b_f + c_f + d_f + e_f \qquad (\Delta x^2) \tag{4}$$

$$2\alpha_f = b_f + 4c_f + 9d_f + 16e_f \qquad (\Delta x^4) \tag{5}$$

$$2\alpha_f = b_f + 16c_f + 81d_f + 256e_f \qquad (\Delta x^6) \tag{6}$$

$$2\alpha_f = b_f + 64c_f + 729d_f + 4096e_f \qquad (\Delta x^8) \tag{7}$$

$$2\alpha_f = b_f + 256c_f + 6561d_f + 65536e_f \qquad (\Delta x^{10}) \tag{8}$$

For the present 6 coefficient scheme, condition (3) expressed as

$$a_f - b_f + c_f - d_f + e_f = (1 - \sigma)(1 - 2\alpha_f) \tag{9}$$

enables 10th-order accuracy.

If only 6th-order accuracy is desired, an option is to reduce the stencil of (1) by imposing $e_f = 0$ while leaving free α_f, this choice leading to the set of coefficients

$$\begin{aligned} a_f &= \frac{\sigma(10\alpha_f - 5) + 16}{16} \\ b_f &= \frac{\sigma(15 - 30\alpha_f) + 64\alpha_f}{32} \\ c_f &= \frac{\sigma(-3 + 6\alpha_f)}{16} \\ d_f &= \frac{\sigma(1 - 2\alpha_f)}{32} \end{aligned} \tag{10}$$

in which the very popular scheme of [28] corresponds to the assumption $\sigma = 1$ with $a_f = \frac{11 + 10\alpha_f}{16}$, $b_f = \frac{15 + 34\alpha_f}{32}$, $c_f = \frac{-3 + 6\alpha_f}{16}$ and $d_f = \frac{1 - 2\alpha_f}{32}$. For the more general scheme given by (10), the two control parameters of the filter behaviour are α_f and σ. The former defines the scale-selectivity of the filtering whereas the latter specifies its attenuation level through its prescription on the grid-to-grid oscillations. These two features are illustrated in Fig. 1.

3. Functional role of solution filtering

Despite its name, as already mentioned in the introduction section 1, this type of filtering operator has no direct connection with the filtering framework of the LES formalism. To make clear this essential point, let us consider

$$\frac{du}{dt} = \lambda u \tag{11}$$

as a simple model equation of the DNS/LES governing equations. The complex variable λ can be defined to consider a generic convection/diffusion equation with $\lambda = -ick - \nu k^2$ where ν is the molecular viscosity, c is the convective velocity

and $u(k,t)$ is the solution expressed in the Fourier space. In LES based on solution filtering, the way to impose the filter is related to the time integration of this type of equation. In practice, the time advancement from t_n to $t_n+\Delta t$ is split into two steps, with

$$u^* = u^n + \int_{t_n}^{t_n+\Delta t} \lambda u \, dt \quad \text{(first step)} \quad , \quad u^{n+1} = T u^* \quad \text{(second step)} \tag{12}$$

with $u^n = u(k,t_n)$ and $u^{n+1} = u(k,t_n+\Delta t)$. Assuming an exact time integration for the first step, these two steps can be summarized as

$$u^{n+1} = T \exp(\lambda \Delta t) u^n \tag{13}$$

to be compared to

$$u^{n+1} = \exp(\lambda \Delta t) u^n \tag{14}$$

obtained from the exact solution of (11). The application of the filter T every time step produces a damping corresponding to an artificial dissipation as long as $0 \leq T \leq 1$. This is precisely the desired effect in LES through the expectation that it can represent the SGS influence in the spirit of implicit LES. The damping of small scales can also be a motivation for performing DNS while controlling spurious oscillations due for instance to aliasing errors [20] or to subdomain boundaries [29].

4. Equivalence with spectral vanishing viscosity

The comparison between the time advancement (13) with its exact counterpart (14) leads to the conclusion that the deviation of T from 1 corresponds to the numerical error introduced, on purpose, by the filtering. It is easy to show that (13) also corresponds to the exact time integration of (11) with $\lambda = -ick - (\nu+\nu_s)k^2$ where ν_s can be interpreted as the SVV associated with the filtering. By the exact identification $T = \exp(-\nu_s k^2 \Delta t)$, the expression of ν_s can be obtained with

$$\nu_s(k\Delta x) = -\frac{\ln T(k\Delta x)}{k^2 \Delta t} \tag{15}$$

This very simple relation clearly shows that solution filtering can be related to an equivalent SVV, at least in a framework where time errors are neglected.

A first remark connected to this equivalence is that the value $T=0$ is a singularity for ν_s which becomes infinite. This singularity is obtained in particular at the cutoff wavenumber k_c when $\sigma = 1$. Even if infinite values for ν_s are numerically feasible, it is difficult to relate them to any SGS contribution when interpreted in the framework of implicit LES. Another remark is related to the asymptotic behaviour of ν_s for vanishing time steps with formally

$$\lim_{\Delta t \to 0} \nu_s(k\Delta x) = \infty \quad \forall k \neq 0 \tag{16}$$

Numerically, this second singular behaviour corresponds to a loss of time consistency. It can be easily understood by remarking that a solution filtering performed in the same way every time step produces a cumulative effect that is more and more pronounced as Δt goes to zero [5].

Fortunately, both singularities can be easily avoided through a scaling of σ on the time step, enabling the application of one filtering to vanish as Δt goes to zero. For this scaling, it is convenient to introduce the numerical viscosity ν_0 which can be defined as the value of ν_s at the cutoff wavenumber with $\nu_0 = \nu_s(k_c \Delta x)$. This value can be chosen by reference to molecular viscosity ν as explained for instance in [4] where the ratio ν_0/ν is estimated using a simplified closure of Lin's equation in the context of implicit LES. Then, σ can be adjusted on a finite value of ν_0 using expression (15) leading to

$$\sigma = 1 - \exp\left(-\nu_0 k_c^2 \Delta t\right) \tag{17}$$

This scaling of σ on Δt can restore the time consistency of the solution filtering as an alternative to the rescaling technique proposed by [5]. It also enables the control of the numerical viscosity introduced by the solution filtering for any Δt while avoiding to impose an infinite value at the cutoff wavenumber k_c. Using the Fourier number

$$F = \frac{\nu \Delta t}{\Delta x^2} \tag{18}$$

it can be convenient to make nondimensional expression (17) with

$$\sigma = 1 - \exp\left(-\pi^2 \frac{\nu_0}{\nu} F\right) \tag{19}$$

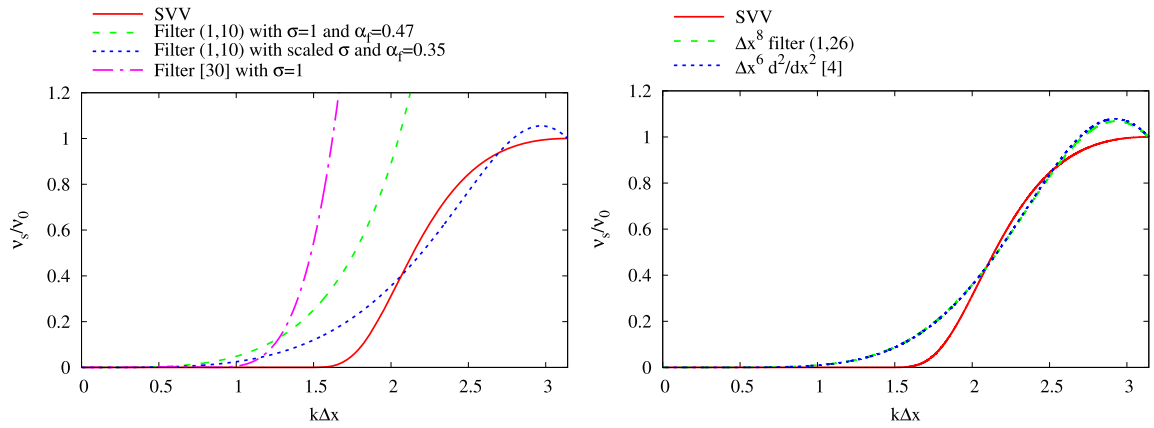

Fig. 2. Left: Comparison between the reference SVV kernel and its equivalent counterparts associated to filter (1), (10) with $\sigma = 1$ or with the scaling (17) and to filter [30] with $\sigma = 1$. Right: Comparison between the reference SVV kernel and its equivalent counterparts associated to filtering using (1), (26) or associated to the computation of second derivative [4]. Examples at $\nu_0/\nu = 10$ and $F = 0.001$.

which shows that the scaled σ is only a function of ν_0/ν and F. In the same way, the nondimensional counterpart of (15) can be written as

$$\frac{\nu_s(k\Delta x)}{\nu_0} = -\frac{\ln T(k\Delta x)}{\frac{\nu_0}{\nu} F k^2 \Delta x^2} \tag{20}$$

To illustrate to what extent solution filtering is equivalent to SVV, the resulting $\nu_s(k\Delta x)$ are compared in Fig. 2-left. Here, the reference SVV corresponds to the kernel

$$\nu_s(k\Delta x) = \begin{cases} 0 & \text{if } k\Delta x < m\pi \\ \nu_0 \exp\left[-\left(\frac{\pi - k\Delta x}{m\pi - k\Delta x}\right)^2\right] & \text{if } m\pi \le k\Delta x \le \pi \end{cases} \tag{21}$$

with the standard value $m = 0.3$. As expected, because of its singular behaviour at the cutoff wavenumber k_c, the filter (1) based on coefficients (10) with $\sigma = 1$ is unable to mimic the standard SVV kernel. For this example, the filter is made highly selective with the value $\alpha_f = 0.47$ close to 0.5. Similar conclusions can be obtained from any filter based on the choice $\sigma = 1$. For instance, the optimized 6th-order filter of [30], despite its good behaviour at low wavenumbers, leads to very high values of equivalent spectral viscosity for $k\Delta x \gtrsim 1$. This behaviour can make highly intrusive the filtering when only moderate values of the numerical viscosity are required. On the contrary, the use of the scaling (19) with $\alpha_f = 0.35$ leads to a kernel close to the standard SVV with a finite value at the cutoff wavenumber k_c as imposed by $\nu_0/\nu = 10$ in the example presented in Fig. 2-left.

So far, only 6th-order filters have been considered using the set of coefficients (10). For reasons that will be explained in the following, we propose here to increase the formal order of the filter by adding the 8th-order condition while using the full stencil of scheme (1). The coefficients are determined using (4)-(7) and to control the shape of the kernel, two extra constraints can be imposed. Here, we choose to impose the transfer function at the cutoff wavenumber k_c and at $k_m = 2k_c/3$ with $T(k_c\Delta x) = T_c$ and $T(k_m\Delta x) = T_m$. These two extra constraints can be written as

$$a_f - b_f + c_f - d_f + e_f = (1 - 2\alpha_f)T_c \tag{22}$$

$$a_f - \frac{b_f}{2} - \frac{c_f}{2} + d_f - \frac{e_f}{2} = (1 - \alpha_f)T_m \tag{23}$$

where T_c and T_m are

$$T_c = \exp\left(-\pi^2 \frac{\nu_0}{\nu} F\right) \tag{24}$$

$$T_m = \exp\left(-\frac{4\pi^2}{9} c_1 \frac{\nu_0}{\nu} F\right) \tag{25}$$

with $c_1 \approx 0.44$ as given by the SVV kernel (21) at $k = k_m$. The system of 6 equations (4)-(7), (22), (23) with the 6 unknowns $(\alpha_f, a_f, b_f, c_f, d_f, e_f)$ leads to the solution

$$\alpha_f = \frac{-256T_m + 81T_c + 175}{-256T_m + 162T_c + 94}$$

$$
\begin{aligned}
a_f &= \frac{T_c(35T_m+46)-163T_m+82}{-128T_m+81T_c+47}\\
b_f &= -\frac{T_c(56T_m-137)+200T_m-119}{-128T_m+81T_c+47}\\
c_f &= \frac{T_c(28T_m-28)-28T_m+28}{-128T_m+81T_c+47}\\
d_f &= -\frac{T_c(8T_m-8)-8T_m+8}{-128T_m+81T_c+47}\\
e_f &= \frac{-T_m+T_c(T_m-1)+1}{-128T_m+81T_c+47}
\end{aligned}
\tag{26}
$$

where T_c and T_m are given by (24), (25) in which the input parameters are ν_0/ν and F.

The spectral viscosity associated to filter (1) based on the set of coefficients (26) is presented in Fig. 2-right. It is found to be slightly less intrusive than the 6th-order filter at low wavenumbers while mimicking correctly the SVV kernel of reference. Interestingly, this spectral viscosity obtained from filtering is almost identical to the one introduced by the finite-difference scheme proposed by [4] to compute second derivatives. This remarkable similarity between filtering and second derivative opens a way for designing a filter to fully mimic a second derivative, i.e. both its numerical and molecular dissipation. This is the subject of the next section.

5. Viscous filtering

In this work, we propose a new approach where the filter is designed to provide both the molecular and artificial dissipations. Thanks to this feature, the viscous term can be removed from (11) by using $\lambda = -ick$. In this way, both the artificial and molecular dissipation have to be included in T. To enable this feature, Taylor's expansions must be performed by reference to the viscous kernel to obtain order conditions between the coefficients $(\alpha_f, a_f, b_f, c_f, d_f, e_f)$. More precisely, the purpose is to approach the exact amplification factor associated with the purely diffusive case,

$$
T_{\text{ref}} = \exp(-\nu k^2 \Delta t) = \exp\left[-F(k\Delta x)^2\right] \tag{27}
$$

with a given order of accuracy. Taylor's expansions of (27), of the denominator and numerator of (2) lead respectively to

$$
\exp\left[-F(k\Delta x)^2\right] = 1 - F(k\Delta x)^2 + \frac{F^2(k\Delta x)^4}{2!} - \frac{F^3(k\Delta x)^6}{3!} + O(k\Delta x)^8, \tag{28}
$$

$$
1 + 2\alpha_f \cos(k\Delta x) = 1 + 2\alpha_f\left[1 - \frac{(k\Delta x)^2}{2!} + \frac{(k\Delta x)^4}{4!} - \frac{(k\Delta x)^6}{6!}\right] + O(k\Delta x)^8 \tag{29}
$$

and

$$
\begin{aligned}
&a_f + b_f\cos(k\Delta x) + c_f\cos(2k\Delta x) + d_f\cos(3k\Delta x) + e_f\cos(4k\Delta x) =\\
&a_f + b_f\left[1 - \frac{(k\Delta x)^2}{2!} + \frac{(k\Delta x)^4}{4!} - \frac{(k\Delta x)^6}{6!}\right]\\
&\quad + c_f\left[1 - \frac{2^2(k\Delta x)^2}{2!} + \frac{2^4(k\Delta x)^4}{4!} - \frac{2^6(k\Delta x)^6}{6!}\right]\\
&\quad + d_f\left[1 - \frac{3^2(k\Delta x)^2}{2!} + \frac{3^4(k\Delta x)^4}{4!} - \frac{3^6(k\Delta x)^6}{6!}\right]\\
&\quad + e_f\left[1 - \frac{4^2(k\Delta x)^2}{2!} + \frac{4^4(k\Delta x)^4}{4!} - \frac{4^6(k\Delta x)^6}{6!}\right] + O(k\Delta x)^8
\end{aligned}
\tag{30}
$$

Then, by identification order by order of (2) with (27), the following set of conditions is obtained with

$$
\begin{aligned}
1 + 2\alpha_f &= a_f + b_f + c_f + d_f + e_f && (\Delta x^2)\\
2F(1+2\alpha_f) + 2\alpha_f &= b_f + 4c_f + 9d_f + 16e_f && (\Delta x^4)\\
12F^2(1+2\alpha_f) + 24F\alpha_f + 2\alpha_f &= b_f + 16c_f + 81d_f + 256e_f && (\Delta x^6)\\
120F^3(1+2\alpha_f) + 360F^2\alpha_f + 60F\alpha_f + 2\alpha_f &= b_f + 64c_f + 729d_f + 4096e_f && (\Delta x^8)
\end{aligned}
\tag{31}
$$

Naturally, for the inviscid case given by $F = 0$ (i.e. $T_{ref} = 1$), conditions (4)-(7) are recovered. For the more general viscous case ($F \neq 0$), as in the previous section, we have 6 coefficients $(\alpha_f, a_f, b_f, c_f, d_f, e_f)$ subjected to the 4 conditions (31).

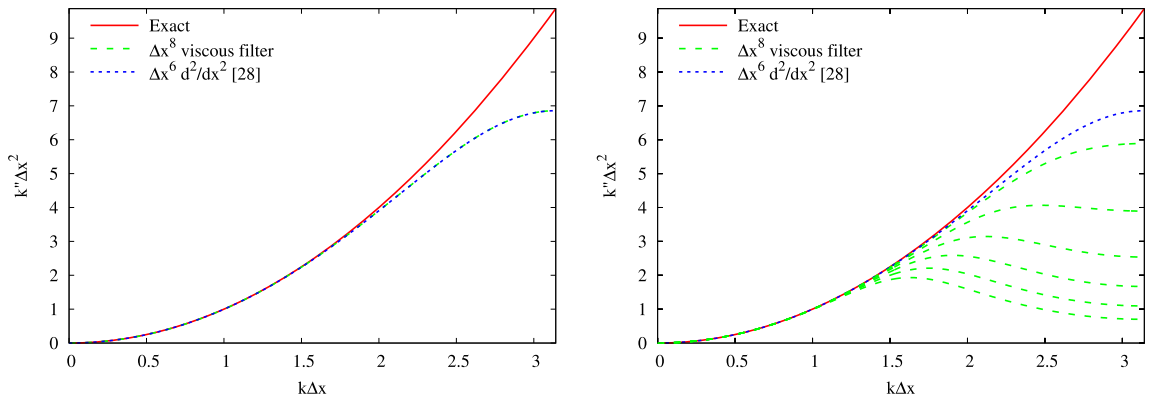

Fig. 3. Comparison between the exact wavenumber and its modified counterparts associated to viscous filtering or to the computation of second derivative. Left: $F = 0.001$ (green-dashed curve). Right: F from 0.5 to 1 by step of 0.1 (from top to bottom green-dashed curves). (For interpretation of the colours in the figure(s), the reader is referred to the web version of this article.)

A first option is to remove 2 coefficients, with $d_f = e_f = 0$ in order to make more compact the resulting scheme. Contrary to a standard filter based on conditions (4)-(7), the present new type of filter, which can be designated as a *viscous filter*, is self-sufficient without requiring any extra condition to avoid the singular solution $a_f = 1$, $\alpha_f = b_f = c_f = 0$. The solving of the corresponding system (31) leads to the set of coefficients

$$\begin{aligned}
\alpha_f &= -\frac{30F^2 - 15F + 2}{60F^2 + 60F - 11} \\
a_f &= \frac{180F^3 - 240F^2 + 171F - 22}{120F^2 + 120F - 22} \\
b_f &= -\frac{120F^3 - 120F^2 - 6F + 4}{60F^2 + 60F - 11} \\
c_f &= \frac{60F^3 - 3F}{120F^2 + 120F - 22}, \quad d_f = 0, \quad e_f = 0
\end{aligned} \tag{32}$$

The associated modified square wavenumber k'' given by

$$k''\Delta x^2 = -\frac{\ln T}{F} \tag{33}$$

is compared in Fig. 3-left to the exact differentiation $k'' = k^2$ and to the modified square wavenumber of the very popular 6th-order scheme of [28] for the computation of the second derivative. The almost perfect collapse between viscous filtering and second derivative suggest that these two finite-difference techniques can produce very similar results to represent physical diffusion. The former can be seen as the counterpart of the latter while including the time integration. This point will be discussed more in the next section and also in Appendix A.

The comparison presented in Fig. 3-left is based on a low value of the Fourier number $F = 0.001$. Lower values of F would produce virtually identical k''. The use of higher values has to be discussed more carefully. First, it can be noticed that all the coefficients (32) become singular for the positive root of their denominator given by $F = \dfrac{\sqrt{390} - 15}{30} \approx 0.158$. In practice, in the neighbourhood of this singularity, the transfer function $T(k\Delta x)$ becomes erratic with strong deviations from its exact reference $\exp(-\nu k^2 \Delta t)$ and sudden changes of sign (with vertical asymptotes) at particular wavenumbers k. In this range of F, this filtering technique becomes inoperable. In a more general way, because $T(k\Delta x)$ corresponds to the amplification factor in the context of von Neumann stability analysis, the present scheme is numerically stable if $|T(k)| \leq 1$. To exhibit its numerical stability, the isocontour $T = 1^+$ in the plane $(k\Delta x, F)$ is presented in Fig. 4. A very thin unstable zone can be identified near the singularity $F \approx 0.158$ suggesting to avoid the range $0.14 < F < 0.17$. For higher values of F, another unstable zone can be noticed, starting from $F > 1.35$ at $k = k_c$.

Even if the present scheme is numerically stable at $F \approx 1$, it is worth to address its accuracy. For that purpose, a map of the error parameter $k''_{\text{err}} = \dfrac{k'' - k^2}{k_c^2}$ in the plane $(k\Delta x, F)$ is presented in Fig. 5. Paradoxically, the unstable/inaccurate zone (plotted in red) near $F \approx 0.158$ is surrounded by regions where the accuracy is slightly improved by reference to the error at low F. Outside the unstable/inaccurate range $F \in]0.14, 0.17[$, low values $F \leq 0.14$ provide similar accuracy. On the contrary, high values $F \geq 0.14$ deteriorate the accuracy as F is increased, with a strong under-estimation of k'' at high wavenumber $k\Delta x \in [\pi/2, \pi]$. This behaviour is also illustrated in Fig. 3-right in the range $0.5 \leq F \leq 1$. Based on these

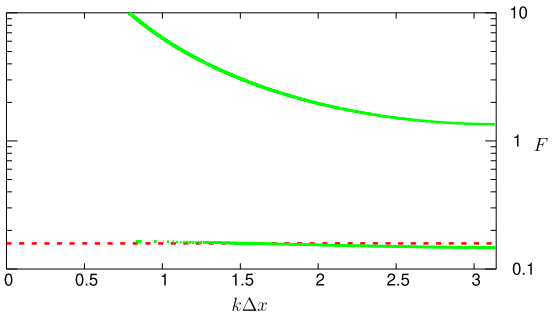

Fig. 4. Isocontour $T = 1^+$ in the plane $(k\Delta x, F)$. The red dashed line indicates the singular value $F \approx 0.158$.

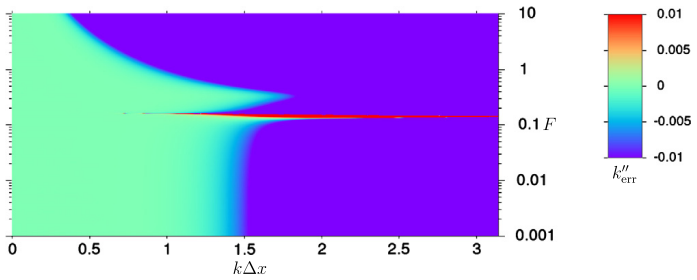

Fig. 5. Map of the error parameter $k''_{\mathrm{err}} = \dfrac{k'' - k^2}{k_c^2}$ in the plane $(k\Delta x, F)$. Saturated colormap for $|k''_{\mathrm{err}}| > 1\%$.

observations, it is suggested that the useful ranges of Fourier number to ensure both stability and accuracy are $F \leq 0.14$ and $0.17 \leq F \leq 0.5$.

To avoid the singular behaviour of the scheme because of the root of its coefficient denominator, it can be decided to make it explicit ($\alpha_f = 0$) while extending its stencil ($d_f \neq 0$) in order to preserve the 8th-order accuracy. With these new constraints, solving system (31) leads to

$$\begin{aligned}
a_f &= -\frac{60F^3 - 84F^2 + 49F - 18}{18} \\
b_f &= \frac{10F^3 - 13F^2 + 6F}{2} \\
c_f &= -\frac{20F^3 - 20F^2 + 3F}{10} \\
d_f &= \frac{30F^3 - 15F^2 + 2F}{90}, \quad \alpha_f = 0, \quad e_f = 0
\end{aligned} \tag{34}$$

A second alternative is to keep its implicit feature ($\alpha_f \neq 0$) while using the stencil extension ($d_f \neq 0$) to ensure an extra constraint designed to impose the transfer function at k_c as in (22). In that case, to take into account both the molecular and numerical viscosities, T_c is given by

$$T_c = \exp\left[-\pi^2 \left(\frac{\nu_0}{\nu} + 1\right) F\right] \tag{35}$$

instead of (24) which was designed to only mimic the numerical dissipation. These extra constraint combined with system (31) leads to the solution

$$\begin{aligned}
\alpha_f &= -\frac{45T_c + 480F^3 - 600F^2 + 272F - 45}{-90T_c + 960F^3 + 240F^2 - 416F + 90} \\
a_f &= \frac{F^3(600T_c - 720) + F(145T_c - 561) - 90T_c + F^2(1158 - 390T_c) + 240F^4 + 90}{-90T_c + 960F^3 + 240F^2 - 416F + 90} \\
b_f &= -\frac{F^3(1800T_c - 240) + F(135T_c + 953) + 180T_c + F^2(-990T_c - 1362) + 240F^4 - 180}{-180T_c + 1920F^3 + 480F^2 - 832F + 180} \\
c_f &= -\frac{F^2(90T_c + 438) + F(81T_c - 81) + F^3(-360T_c - 720) + 240F^4}{-90T_c + 960F^3 + 240F^2 - 416F + 90}
\end{aligned}$$

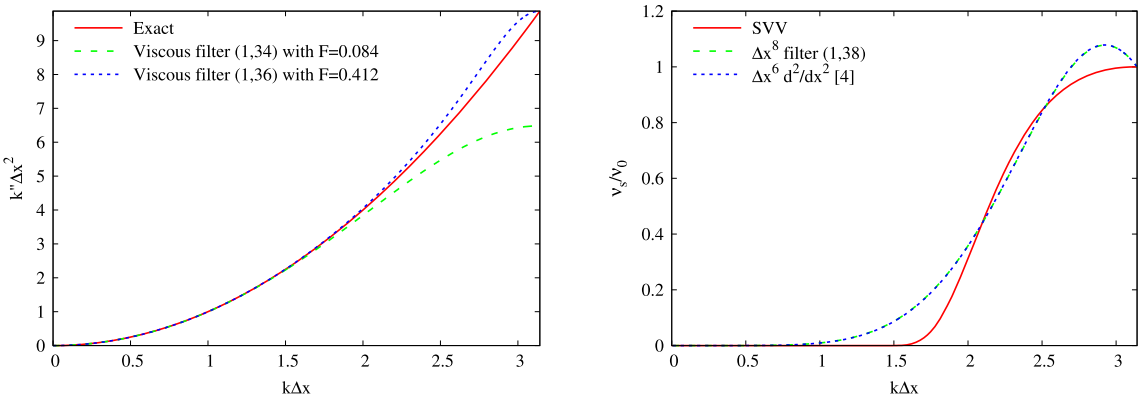

Fig. 6. Left: Comparison between schemes (1), (34) and (1), (36) at 10% of the maximum stable Fourier number F ($\nu_0/\nu = 0$). Right: Comparison between the reference SVV kernel and its equivalent counterparts associated to filtering using (1), (38) or to the computation of second derivative [4] ($\nu_0/\nu = 10$ and $F = 0.001$).

$$d_f = \frac{F(7T_c - 7) + F^2(78 - 30T_c) + F^3(-120T_c - 240) + 240F^4}{-180T_c + 1920F^3 + 480F^2 - 832F + 180}, \quad e_f = 0 \tag{36}$$

Both sets of coefficients (34) and (36) avoid any erratic behaviour around a singular value of F. The stability condition is more favourable for the scheme (1), (36) than for the scheme (1), (34) with $F < 4.12$ for the former and $F < 0.84$ for the latter. More importantly, at 10% of the maximum stable Fourier number, the scheme (1), (36) is significantly more accurate than the scheme (1), (34) as illustrated in Fig. 6-left.

Following the method presented in the previous section to control the shape of the SVV kernel introduced by the filtering, the last option presented here is to use the full stencil ($d_f \neq 0$ and $e_f \neq 0$) of scheme (1) while imposing the transfer function at k_c and k_m through the two constraints (22), (23) where T_c is given by (35) and T_m by

$$T_m = \exp\left[-\frac{4\pi^2}{9}\left(c_1\frac{\nu_0}{\nu} + 1\right)F\right] \tag{37}$$

Then, solving system (31), (22), (23) provides the set of coefficients

$$\begin{aligned}
\alpha_f &= -\frac{1280T_m - 405T_c + 1440F^3 - 3240F^2 + 2736F - 875}{-1280T_m + 810T_c + 2880F^3 - 2160F^2 - 288F + 470}\\
a_f &= \frac{\left(\begin{array}{l}F(3520T_m + 855T_c - 4951) + F^3(3200T_m + 1800T_c - 1520) +\\ T_c(700T_m + 920) - 3260T_m + F^2(-4640T_m - 2430T_c + 5038) + 240F^4 + 1640\end{array}\right)}{-2560T_m + 1620T_c + 5760F^3 - 4320F^2 - 576F + 940}\\
b_f &= \frac{\left(\begin{array}{l}F^2(2560T_m + 6210T_c + 6478) + F(256T_m - 4329T_c - 6871) - 4000T_m +\\ T_c(2740 - 1120T_m) + F^3(-2560T_m - 3960T_c - 1520) + 240F^4 + 2380\end{array}\right)}{-2560T_m + 1620T_c + 5760F^3 - 4320F^2 - 576F + 940}\\
c_f &= -\frac{\left(\begin{array}{l}F(1792T_m - 2115T_c + 323) + F^3(1280T_m - 1800T_c - 1040) + 280T_m +\\ T_c(280 - 280T_m) + F^2(-2240T_m + 2970T_c + 598) + 240F^4 - 280\end{array}\right)}{-1280T_m + 810T_c + 2880F^3 - 2160F^2 - 288F + 470}\\
d_f &= -\frac{\left(\begin{array}{l}F^2(2560T_m - 2430T_c + 2158) + F(256T_m + 855T_c - 1111) +\\ T_c(160T_m - 160) - 160T_m + F^3(-2560T_m + 1800T_c - 1520) + 240F^4 + 160\end{array}\right)}{-2560T_m + 1620T_c + 5760F^3 - 4320F^2 - 576F + 940}\\
e_f &= \frac{\left(\begin{array}{l}F^2(160T_m - 270T_c + 478) + F(64T_m + 99T_c - 163) +\\ T_c(20T_m - 20) - 20T_m + F^3(-640T_m + 360T_c - 560) + 240F^4 + 20\end{array}\right)}{-2560T_m + 1620T_c + 5760F^3 - 4320F^2 - 576F + 940}
\end{aligned} \tag{38}$$

The corresponding SVV can be expressed using this time the exact identification $T = \exp[-(\nu + \nu_s)k^2\Delta t]$ in order to incorporate both the molecular and artificial dissipations while solving (11) with $\lambda = -ick$. Then, the counterpart of (15) becomes

$$\nu + \nu_s(k\Delta x) = -\frac{\ln T(k\Delta x)}{k^2\Delta t} \tag{39}$$

or equivalently in nondimensional form

$$\frac{\nu_s(k\Delta x)}{\nu_0} = -\frac{\ln T(k\Delta x)}{\frac{\nu_0}{\nu} F k^2 \Delta x^2} - \frac{\nu}{\nu_0} \tag{40}$$

As in the previous section, when compared with the approach of [4] based on the explicit computation of the viscous term while boosting it artificially at small scales, the present viscous filtering method can lead to virtually identical spectral viscosity as shown in Fig. 6-right. Both approaches can behave like SVV with an equivalent flexibility through the choice of the input parameters ν_0/ν and c_1 to shape the associated kernel. In terms of stability, the extra constraint at k_m introduces an unstable range $0.023 < F < 0.64$. For higher values of F, numerical stability is ensured as long as $F < 7.94$ but with a strong loss of accuracy (not shown for conciseness). Even if the stability condition $F < 0.023$ is more restrictive than for schemes (34) and (36), it is not at all penalizing in many DNS/LES applications where the typical values of Fourier numbers are clearly smaller.

By comparison to conventional filtering, the present viscous filtering technique enables the bypass of the viscous term and then the saving of computational time. But in terms of computational efficiency, the main advantage of viscous filtering lies in its robustness for large values of the Fourier number F. This fundamental point is discussed in the following section through an analysis of the formal accuracy and numerical stability of this new approach.

6. Accuracy analysis

To validate the present viscous filtering procedure while exhibiting its main accuracy features, the standard convection/diffusion equation

$$\frac{\partial u}{\partial t} + c\frac{\partial u}{\partial x} = \nu \frac{\partial^2 u}{\partial x^2} \tag{41}$$

is solved where $u(x,t)$ is the solution expressed in the physical space. With the initial condition

$$u(x,0) = \exp\left[-\left(\frac{x - L_x/2}{\sigma_x}\right)^2\right] \tag{42}$$

this equation has an exact solution with

$$u(x,t) = \sqrt{\frac{\sigma_x^2}{\sigma_x^2 + 4\nu t}} \exp\left[-\frac{(x - ct - L_x/2)^2}{\sigma_x^2 + 4\nu t}\right] \tag{43}$$

where L_x is the computational domain considered. The problem is solved using periodicity in x while considering a narrow Gaussian with $\sigma_x = L_x/40$ to make negligible the role of the boundary condition for the deviation from the exact solution (43) subjected to same periodicity. Using the nondimensionalisation $L_x = 1$ and $c = 1$, the viscosity considered is $\nu = 1/1000$ and the equation is solved up to $t = 1$.

In this section, we want to address the general features of the viscous filtering by comparison to the conventional approach where the viscosity effects are described through the computation of the right hand side of equation (41) using a finite-difference scheme for the computation of the second derivative. For this classical way to take viscous effects into account, we will refer to explicit diffusion. As generic viscous filter operator, only the scheme given by the set of coefficients (36) is considered for conciseness. In the same way, as generic second derivative scheme, only the 6th-order scheme reported in [23] is used for comparisons. These two schemes are expected to behave very closely as it was observed in the previous section and as it will be checked practically in this section. To reduce the spatial differentiation errors, both schemes are scaled to provide a very small amount of numerical dissipation using $\nu_0/\nu = 0$. This choice to consider only these two schemes is for conciseness reasons. Fundamentally, all the comparisons discussed in what follows can be transposed for other numerical parameters (accuracy order, stencil, imposition of T_c and T_m, etc.) provided that the viscous filter is compared to its counterpart for the computation of the second derivative.

6.1. Spatial accuracy

First, the spatial accuracy is addressed by using a very small time step Δt making negligible the error due to the time integration. For the conventional approach, the advancement is entirely based on a 3rd-order Adams-Bashforth (AB3) scheme. For the technique based on viscous filtering, the AB3 scheme is only used for the convective term while representing the diffusion by the application of the viscous filter operator on the computed solution every time step as explained in section 3. In both cases, the spatial differentiation of the convective term is performed using the same 6th-order compact finite-difference scheme (see [28,31] for information on this standard centred scheme for the computation of first derivative).

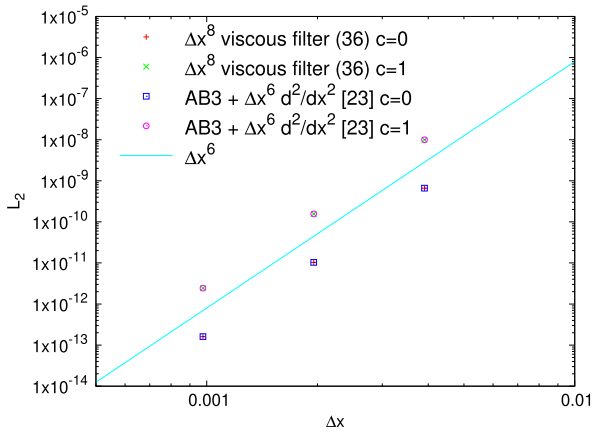

Fig. 7. Spatial convergence for diffusion ($c = 0$) and convection/diffusion ($c = 1$) equations. Comparison between the present viscous filtering technique and the conventional explicit computation of the diffusion term. Three spatial resolutions are considered with $\Delta x = L_x/n_x$ and $n_x = 256, 512, 1024$.

The spatial convergence obtained in each case is shown in Fig. 7 by considering both the convective/diffusive ($c = 1$) and purely diffusive ($c = 0$) situations. Three spatial resolutions have been considered with $\Delta x = L_x/n_x$ where n_x is the number of mesh nodes with $n_x = 256, 512, 1024$. The remarkable matching of the L_2-norm at any spatial resolution clearly confirms that the present viscous filtering technique can mimic almost perfectly an explicit diffusion. A 6th-order accuracy is well recovered. This accuracy order of the viscous filter (1), (36) is expected in view of the almost perfect collapse between modified wavenumbers as illustrated in Fig. 3.[1] However, the 6th-order accuracy may seem like a contradiction in view of the order conditions checked up the 8th order as expressed in (31). In practice, it is worth noting that the 8th-order accuracy is ensured only if F is kept constant with the same number of time steps. For the present investigation of spatial convergence based on a constant time step Δt while computing the L_2-norm at the same time $t = 1$, the variation of F, as Δx is reduced, introduces a division by Δx^2 of the numerical error, explaining the 6th-order accuracy observed in the present tests of spatial convergence. This is the reason why a Δx^8 formulation corresponds in practice to a 6th-order accuracy in terms of spatial convergence. Note that it can be checked that the computation of the L_2-norm based on a spatial convergence at $F = \text{cst}$ with the same number of time steps leads to $L_2\text{-norm} \propto \Delta x^8$ as expected (not shown for conciseness). In Appendix A, the reason of this reduction by Δx^2 of the formal order is exhibited analytically.

6.2. Temporal accuracy

The accuracy in time of the two strategies, namely the viscous filtering and the explicit diffusion, is more difficult to assess. This difficulty is related to the impossibility to make negligible the contribution of the spatial error. For the conventional method based on the explicit computation of the diffusion term, in the framework of von Neumann analysis, it is well known that numerical stability is ensured only if

$$F < \frac{\sigma_r}{k''_{\max}\Delta x^2} \tag{44}$$

where $k''_{\max}\Delta x^2$ is the maximum of the modified square wavenumber while σ_r is a feature of the time advancement scheme with $\sigma_r = 6/11$ for the AB3 scheme used in this study [32]. In the present formalism, $k''_{\max}\Delta x^2 = (1 + \nu_0/\nu)\pi^2$ leads to the Fourier stability condition

$$F < \frac{6}{11(1 + \nu_0/\nu)\pi^2} \tag{45}$$

which reads $F \lesssim 0.055$ for $\nu_0/\nu = 0$. Close to this critical value, thanks to the accuracy of the AB3 scheme, the main contribution to the numerical error comes from the spatial discretisation. A mesh refinement while keeping constant Δt is a way to remove progressively the spatial differentiation error by comparison to the temporal error, but the resulting higher value of F leads to numerical instability, making impossible the evaluation of the time accuracy. To ensure numerical stability, a mesh refinement by a factor 2 requires a reduction of the time step by a factor 4 because of the scaling of F on $1/\Delta x^2$. Then, for the present combination $(\Delta x^6, \Delta t^3)$, the balance between time and spatial errors is kept constant, making impossible a time convergence analysis based on a negligible contribution of the spatial differentiation error.

To overcome this difficulty, the present assessment is based on local accuracy. The principle of local accuracy analysis is to estimate the numerical error introduced only by one time step ($n_t = 1$), in contrast to global accuracy for which the

[1] Fig. 3 actually compares the modified wavenumber of the viscous filter (32) with its second derivative counterpart, but the same agreement (not shown for conciseness) can be obtained for the viscous filter (36) used in the present validation.

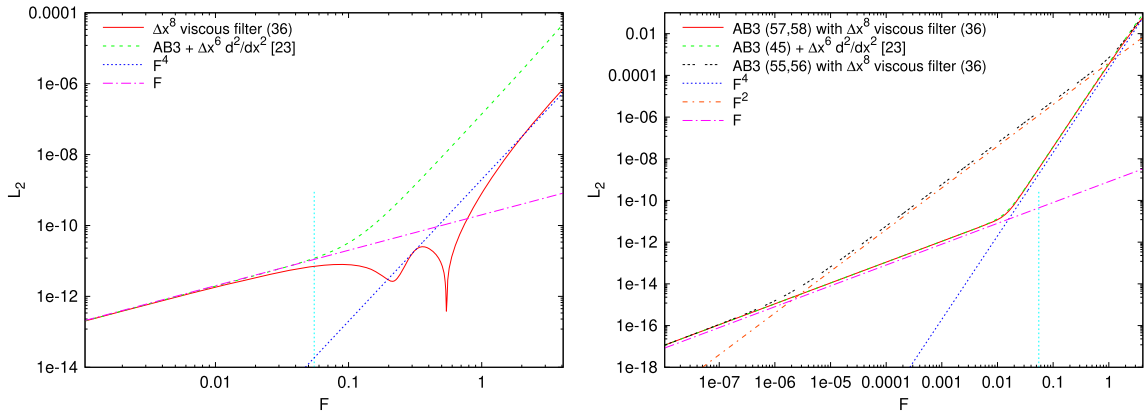

Fig. 8. Local time convergence exhibited as a scaling in F. Left: diffusion ($c = 0$) equation. Right: convection/diffusion ($c = 1$) equation. Comparison between the present viscous filtering technique and the conventional explicit computation of the diffusion term. The blue dashed line indicates the stability limit of the AB3 scheme $F \lesssim 0.055$.

numerical convergence is examined by considering the solution at a given time t while decreasing the time step Δt (i.e. by increasing the number of time steps n_t with $t = n_t \Delta t$). The advantage of local accuracy analysis is that it is not restricted to the stability zone of the scheme, enabling the investigation of high values of F. In present analysis, this convenient property can be used to make negligible the contribution of spatial errors. Local accuracy is connected to global accuracy such that a Δt^n-accurate time scheme exhibits a local convergence proportional to Δt^{n+1}. As a consequence, for the present AB3 scheme, a Δt^4 local convergence is expected. To check this scaling, equation (41) has been advanced in time for one time step Δt using a spatial resolution with $n_x = 512$. To relate more easily the range of considered Δt with the AB3 stability condition $F \lesssim 0.055$, the convergence is exhibited as a scaling in F, a global 3rd-order accuracy corresponding to a F^4 scaling.

Fig. 8 compares the local time convergence of the present viscous filtering technique with the conventional approach where the viscous term is computed explicitly by spatial differentiation (second derivative). To start this analysis, the simpler case of the pure diffusion ($c = 0$) is first addressed. For the explicit diffusion, two zones can be distinguished in Fig. 8-left. From very small F to $F \approx 0.05$, a scaling in F can be clearly noticed. It corresponds to a lack of numerical convergence in terms of global accuracy. This behaviour corresponds to the situation already discussed for which the spatial errors completely dominate the time errors, preventing any convergence in time. At higher F, a scaling in F^4 is established, confirming the 3rd-order accuracy of the AB3 scheme. In this second zone, beyond the stability region, it can be considered that the contribution of spatial error is negligible.

The behaviour of the time error for the viscous filtering also exhibits the non-convergence zone at small F but reveals a more complex behaviour for $F \gtrsim 0.05$. Fortunately, the more or less erratic behaviour of the time error with F in the range $0.1 \lesssim F \lesssim 1$ corresponds to an increase of the accuracy. A more regular dependency on F is recovered for $F \gtrsim 1$ with a scaling close to F^4 corresponding to a global 3rd-order accuracy. The lack of a clear scaling in F is an expected result because of the entanglement between time and spatial errors which is an essential feature of the present viscous filter scheme. The present analysis shows that this feature is not a drawback thanks to the resulting time accuracy which is clearly improved by comparison to the AB3 scheme. In the zone where time error dominates, namely for $F \gtrsim 0.05$, the improvement corresponds to a reduction of about one order of magnitude in the error. At lower F, this reduction is gradually removed, as the contribution of the time error by comparison to the spatial error, but the viscous filtering remains the most accurate approach. As a first conclusion, for the purely diffusive case, it can be stated that the viscous filtering technique is more accurate in time than the AB3 scheme. This feature is of secondary importance at low F for which spatial error dominates. At higher F, the accuracy improvement is a favourable property that supplements the numerical stability which is already a major advantage.

The convective/diffusive case ($c = 1$) must be considered more carefully. In this situation, both approaches (viscous filtering and explicit diffusion) require the time integration of the convective term. For the present technique based on viscous filtering, the way to accurately combine the time integration of the convective term and the application of the filter (in which the time integration is embedded) needs to be clarified. In the general case, the convective term may be non-linear requiring an approximation for the time advancement. The corresponding generic equation, written in the Fourier space, reads as

$$\frac{du}{dt} = F(u) - \nu k^2 u \tag{46}$$

To integrate this equation in time, a simple option is to treat the two terms on the right hand side using the same scheme, with, in the case of an explicit multi-step scheme

$$u^{n+1} = u^n + \Delta t \sum_{i=0}^{p} a_i \left[F(u^{n-i}) - \nu k^2 u^{n-i} \right] \tag{47}$$

for which the AB3 scheme coefficients are given by $p = 2$, $a_0 = 23/12$, $a_1 = -16/12$ and $a_2 = 5/12$. This technique, referred here as the conventional strategy, does not require any filtering given the explicit computation of the diffusion term.

If one desires to integrate exactly the viscous term while approximating the non-linear term with a multi-step scheme, it may be tempting to split the time advancement into two steps with

$$u^* = u^n + \Delta t \sum_{i=0}^{p} a_i F(u^{n-i}) \tag{48}$$

$$u^{n+1} = \exp(-\nu k^2 \Delta t) u^* \tag{49}$$

The drawback of this approach is that a time splitting error is introduced preventing from considering as exact the time advancement of the viscous term in the second step (49). To integrate exactly the viscous term, equation (46) can be multiplied by the so-called integrating factor [33,34] $\exp(\nu k^2 t)$ leading to

$$\frac{d[u \exp(\nu k^2 t)]}{dt} = F(u) \exp(\nu k^2 t) \tag{50}$$

Then, the time advancement scheme no longer requires a splitting with

$$u^{n+1} \exp(\nu k^2 t_{n+1}) = u^n \exp(\nu k^2 t_n) + \Delta t \sum_{i=0}^{p} a_i \exp(\nu k^2 t_{n-i}) F(u^{n-i}) \tag{51}$$

or, after division by $\exp(\nu k^2 t_{n+1})$,

$$u^{n+1} = \exp(-\nu k^2 \Delta t) \left[u^n + \Delta t \sum_{i=0}^{p} a_i \exp(-i \nu k^2 \Delta t) F(u^{n-i}) \right] \tag{52}$$

Expressed into two steps, as a more convenient way to implement it, this time advancement can be written as

$$u^* = u^n + \Delta t \sum_{i=0}^{p} a_i \exp(-i \nu k^2 \Delta t) F(u^{n-i}) \tag{53}$$

$$u^{n+1} = \exp(-\nu k^2 \Delta t) u^* \tag{54}$$

without introducing any time splitting error.

The exact amplification factor (27) is recovered in these two steps. Because the present approach consists in the approximation of this amplification factor by a discrete filtering operator of transfer function T, the analogues of the two-step time advancements (48), (49) and (53), (54) are respectively

$$u^* = u^n + \Delta t \sum_{i=0}^{p} a_i F(u^{n-i}) \tag{55}$$

$$u^{n+1} = T u^* \tag{56}$$

and

$$u^* = u^n + \Delta t \sum_{i=0}^{p} a_i T^i F(u^{n-i}) \tag{57}$$

$$u^{n+1} = T u^* \tag{58}$$

The advantage of (55), (56) is that it only requires one filtering per time step. In the present framework of finite-difference schemes, the computational cost of this type of filter is equivalent to that of a second derivative, avoiding any extra-cost due to the viscous filtering strategy. The drawback is the time splitting error resulting in a loss of time accuracy. The time advancement (57), (58), free from any time splitting error, is more accurate but also more expensive through the need to filter three times per time step for an AB3 scheme: twice in (57) and once in (58). By comparison to the computation of one second derivative, the extra-cost is 200%. This may be seen as very penalizing, but as it will be discussed in the next session, when implemented in a full Navier-Stokes solver, the relative extra-cost brought about by the viscous filtering is much lower while offering very advantageous features in terms of numerical stability.

Fig. 8-right presents the local convergence obtained for the convection/diffusion equation. For the present balance between convection and diffusion given by $c = 1$ and $\nu = 1/1000$, the time accuracy is mainly driven by the time integration of the convective term. As a consequence, schemes (47) and (57), (58) are close to each other with a global 3rd-order accuracy (i.e. a scaling of the local error in F^4) provided by the AB3 scheme for $F \gtrsim 0.01$. For lower values of F, the time convergence saturates because of the spatial errors as indicated by the scaling in F. The loss of accuracy using the scheme (55), (56) is clearly exhibited in Fig. 8-right with a scaling in F^2 (i.e. global 1st-order accuracy) in the extended range $10^{-5} \lesssim F \lesssim 1$. For the present accuracy analysis performed with very low spatial errors, the superiority of scheme (57), (58) by comparison to scheme (55), (56) is clearly shown. However, the time splitting error of scheme (55), (56) can become insignificant in the context of multidimensional non-linear governing equations. The generalisation of present viscous filtering in this more demanding context is the main subject of the next section.

7. DNS/LES results

In this section, the present viscous filtering technique is used to perform DNS/LES of two academic turbulent flows. The corresponding scheme has been implemented in the finite-difference code Incompact3d that numerically solves the incompressible Navier-Stokes equations. This code is massively parallel and 6th-order accurate in space when free-slip or periodic boundary conditions are used, as in the present study. The computational mesh is Cartesian with $n_x \times n_y \times n_z$ nodes regularly distributed in the domain $L_x \times L_y \times L_z$.[2] For more information about this code, the reader is referred to [31,35,36] and also to [37] for an extension of its capabilities in the new framework called Xcompact3D.

The implementation of the viscous filter in Incompact3d was straightforward thanks to the generic form of the finite-difference scheme (1). The only sensitive point is to carefully code the sets of coefficients, e.g. (36) or (38), as functions of F and ν_0/ν given the dependency of T_c and T_m on these two parameters. Note that these two sets of coefficients preserve the 6th-order accuracy of Incompact3d.

When the Navier-Stokes equations are solved in the conventional way through the explicit computation of the second derivatives in the viscous term while integrating in time the governing equations as in (47), we will refer to "Navier-Stokes" results. When the viscous filtering is used, because the viscous term is removed from the governing equations, the corresponding results will be designated by the term "Euler+VF" with VF designating Viscous Filtering. More precisely, we will make the distinction between "Euler+VF^1" and "Euler+VF^3" to refer to a time advancement based respectively on one VF (55), (56) or three VF (57), (58) operations per time step.

In what follows, the goal is to assess the concept of viscous filtering in the general framework of high-fidelity simulation of turbulent flows. Subsection 7.1 is mainly a validation based on a widely documented fundamental flow in order to show the remarkable equivalence between a computation based on "Navier-Stokes" or "Euler+VF" formulations. Then, a problem with wall turbulence and heat transfer is addressed in subsection 7.2. The equivalence between "Navier-Stokes" and "Euler+VF" formulations is also well recovered, but more importantly, the interest of "Euler+VF" approach is evidenced through its high computational efficiency for numerical stability reasons.

7.1. Taylor-Green Vortex problem

In this subsection, the Taylor-Green Vortex (TGV) problem is used as a benchmark to assess the present viscous filtering technique. The corresponding solution is triperiodic in a cubic domain $(2\pi)^3$. Two Reynolds numbers $Re = 1/\nu$ are addressed from $t = 0$ to $t = 20$. In this time interval, the flow is subjected to a strong turbulent breakdown up to a fully developed state of turbulence. Formally, the low Reynolds number case $Re = 1250$ may not be seen as turbulent because of the deterministic nature of the flow evolution. However, a multiscale state is well established at $t = 20$, as an important feature in common with turbulence. The advantage of the deterministic dynamics is that it enables an easy assessment of the numerical accuracy based on instantaneous states obtained by DNS. For the higher Reynolds number $Re = 10000$ considered, this attractive feature is lost because of non-deterministic evolution of the flow after the turbulent breakdown. In this second framework, the LES capabilities of the present viscous filter will be examined more qualitatively.

At $Re = 1250$, using a spatial resolution of 480^3 nodes,[3] the DNS accuracy is fully reached. Fig. 9-left compares the time evolution of the kinetic energy E_k for the conventional "Navier-Stokes" strategy and for the present "Euler+VF^1" and "Euler+VF^3" alternatives. The former is based on the second derivative scheme documented in [23] whereas in the two latter cases, the viscous filter is given by (1), (36). As already mentioned and checked in section 6, these two finite-difference schemes are expected to behave almost identically for the discrete representation of viscous effects as well as the slight artificial dissipation using $\nu_0/\nu = 3$ to control aliasing errors. The collapse between the three curves in Fig. 9-left confirms this point. The viscous dissipation, that drives the free decay of this turbulence problem, is found to be numerically equivalent for the three approaches. Thanks to the deterministic nature of the flow, defining the reference solution as the one obtained from the "Navier-Stokes" formulation, the relative deviation $\frac{E_k - E_{k\mathrm{ref}}}{E_{k\mathrm{ref}}}$ can be monitored throughout the simulation.

[2] The mesh refinement in one direction, enabled by Incompact3d, is not used here.

[3] The symmetries of the problem have been used to reduce by a factor 8 the number of degrees of freedom actually computed in the impermeable sub-box π^3.

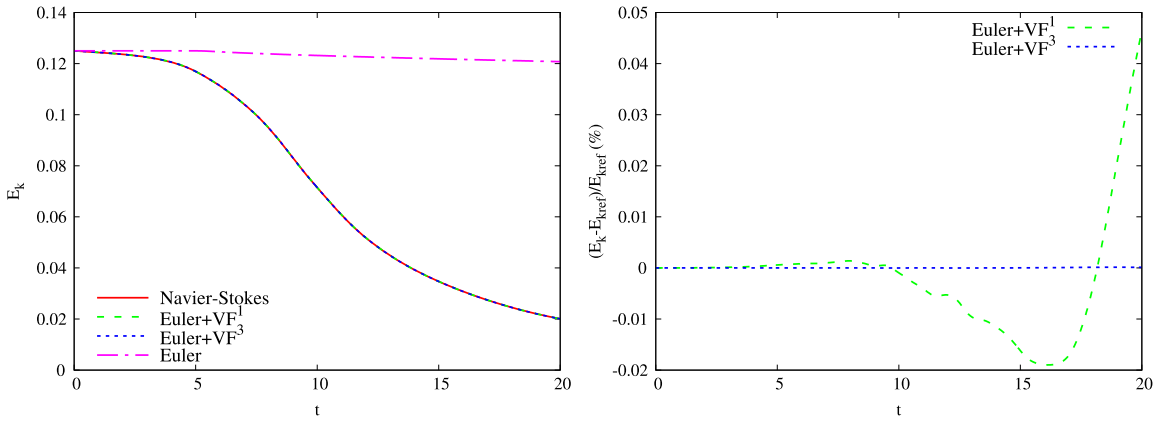

Fig. 9. Time evolution of the kinetic energy E_k (left) and its relative error $\frac{E_k - E_{k\mathrm{ref}}}{E_{k\mathrm{ref}}}$ in % (right).

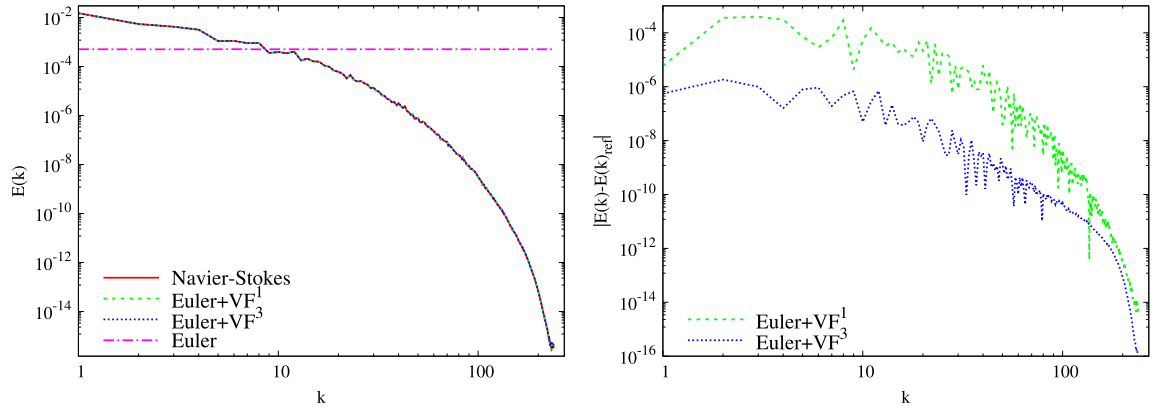

Fig. 10. Kinetic energy spectra $E(k)$ (left) and its absolute error $|E(k) - E(k)_{\mathrm{ref}}|$ (right) at $t = 14$.

Fig. 9-right compares the time evolution of this deviation. For the "Euler+VF^1" case, the maximum deviation of about 0.045% remains acceptable without compromising the DNS accuracy. However, it can be observed that the "Euler+VF^3" strategy enables a drastic improvement of the agreement with the reference solution through a reduction of the maximum deviation by more than 300. This behaviour is consistent with the results reported in subsection 6.2 where the clear improvement of accuracy was observed using the time advancement scheme (57), (58) by comparison to (55), (56).

The "Euler" case is also presented in Fig. 9 to exhibit the behaviour of the code Incompact3d when computing a discrete solution free from any viscous effect. Thanks to the use of the skew-symmetric form for the convective terms, this code can ensure the kinetic energy conservation up to the time integration error. Using the same time step as for the three other cases, a slight decrease of E_k can be observed beyond the start of the turbulent breakdown due to the time error associated to the AB3 scheme. The use of a smaller time step can easily make insignificant this deviation from a pure kinetic energy conservation (not shown).

The multiscale dynamics produced at $t = 14$, after the turbulence breakdown, is illustrated in Fig. 10-left where the kinetic energy spectra $E(k)$ are presented. For the "Euler" case, a flat spectrum corresponding to a white noise can be clearly observed, as expected. The excellent agreement between the three other strategies is well recovered on the whole range of wavenumbers k, confirming practically the equivalence between the present viscous filtering and the conventional technique where the viscous term is computed explicitly. The quality of this agreement is particularly remarkable at the smallest scales captured by the computational mesh, i.e. at $k \approx 240$. A scale-by-scale estimation of the difference between these two basic approaches can be provided by plotting the absolute deviation $|E(k) - E(k)_{\mathrm{ref}}|$ at any computed wavenumber k for the present mesh resolution (see Fig. 10-right). The maximum deviation of about 10^{-4} can be considered as satisfactory for the "Euler+VF^1" case. If a higher accuracy is expected, the use of "Euler+VF^3" enables a spectacular improvement as shown by Fig. 10-right with a reduction by about two orders of magnitude of the deviation $|E(k) - E(k)_{\mathrm{ref}}|$ in this case.

The capability of the viscous filtering technique is now addressed in the context of LES. For that purpose, a higher Reynolds number is considered with $Re = 10000$. The reference results are from a DNS performed at the resolution 2048^3 whereas the corresponding LES are based on meshes reduced by a factor 8 or 16 in every direction with 256^3 and 128^3 nodes respectively. These two levels of mesh refinement are referred as high-resolution (HR) and low-resolution (LR). By comparison to DNS, their associated reduction of the number of degrees of freedom corresponds to a drastic decrease of the computational cost with a division by a factor of about 4000 for HR LES and more than 65000 for LR LES. Both LES

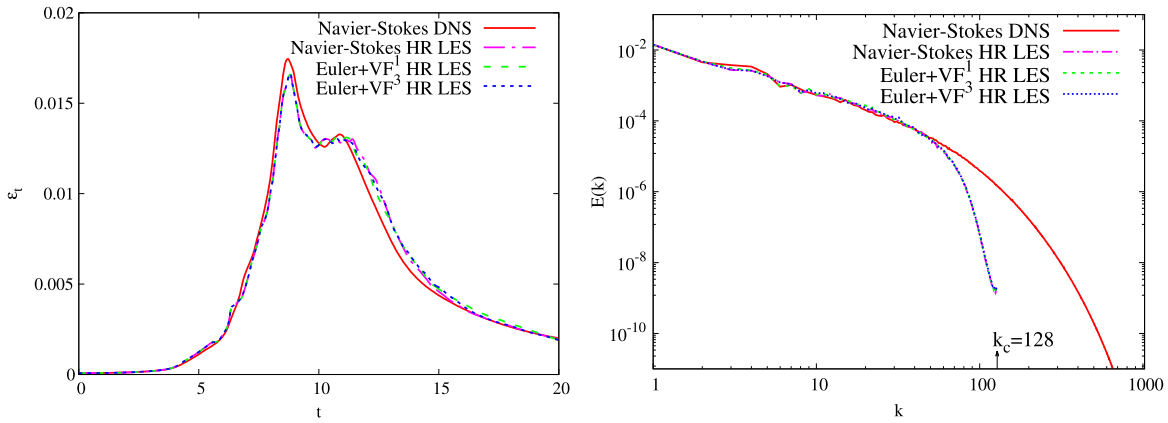

Fig. 11. Left: time evolution of the kinetic energy dissipation ε_t. Right: kinetic energy spectra $E(k)$ at $t = 14$.

configurations can be considered as challenging in terms of SGS modelling quality, with naturally a stronger demand for LR LES.

A comparison between HR LES and DNS results is presented in Fig. 11 for the dissipation ε_t (left) of the kinetic energy E_k and for its spectrum $E(k)$ at $t = 14$ (right). The observation of dissipation, estimated as

$$\varepsilon_t = -dE_k/dt \tag{59}$$

by finite difference, enables a closer analysis of the differences between one result to another. The HR LES results of [4] are also included in the comparison. This calculation of reference has been performed using an implicit SVV as SGS model. For this approach, belonging to the family of implicit LES, the artificial dissipation is provided by a boost of the second derivative at small scales [23,4] while shaping the modified wavenumber to mimic SVV. For the present HR LES, the counterpart of this technique is used through a viscous filtering based on the set of coefficients (38) while using the same level of numerical dissipation with $\nu_0/\nu = 63$. Despite the non-deterministic behaviour of the flow at this Reynolds number, an excellent matching can be observed in Fig. 11 between present results and those from [4]. The time evolution of ε_t is in good agreement with the DNS results of reference as well as the kinetic energy spectrum $E(k)$ in the wavenumber range $0 \leq k \lesssim k_c/2$ as already reported in [4]. In the second part of the spectrum $k_c/2 \lesssim k \leq k_c$, the damping of $E(k)$ is almost identical for the reference LES [4] (referred as "Navier-Stokes LES") and for both cases "Euler+VF^1" and "Euler+VF^3" LES. This is the practical confirmation that the present viscous filtering technique can be used in the context of implicit LES as the counterpart of implicit SVV initially introduced by [23,4] through the computation of second derivatives in the viscous term.

An attractive feature of this remarkable correspondence is that it provides a way to explicitly estimate the kinetic energy dissipation provided by the viscous filtering. As explained in [4], the estimation of ε_t can be based on the computation of second derivatives with

$$\varepsilon_t = -\nu \left\langle u_i \frac{\partial^2 u_i}{\partial x_j \partial x_j} \right\rangle \tag{60}$$

using the counterpart scheme of present viscous filtering technique. Estimations of ε_t given by (59) or (60) are virtually identical as shown in Fig. 12-top-left where the symbols are superimposed on the curve. The availability of an accurate procedure to estimate the total dissipation ε_t (i.e. including its artificial component) is a clear advantage of the present viscous filtering technique. For instance, in the production of turbulent budgets, it is common to estimate the contribution of the artificial dissipation as the residual term assuming that budgets are perfectly balanced. With the present approach, the total dissipation can be explicitly estimated and thus this assumption is no longer required, enabling the analysis of unbalanced budget in transient turbulent states (as for the present TGV flow) or to estimate the lack of statistical convergence when a stationary state is reached.

A slight loss of quality can be observed in Fig. 12 (bottom) for the LR LES results. However, it is worth noting that despite the coarse mesh, the present implicit SGS modelling enable to capture the peak of dissipation with an acceptable accuracy. This means that the brutal kinetic energy cascade during the turbulent breakdown is correctly taken into account by the hyperviscous filtering, as far as the time evolution of the kinetic energy is concerned. The shape of the spectrum $E(k)$ is qualitatively similar for LR LES by comparison to HR LES (see Fig. 12-right-bottom) with a comparable fall from $k_c/2$ to k_c. It must be noted that the reduction of the spatial resolution requires to increase the numerical viscosity with $\nu_0/\nu = 182$ for LR LES against $\nu_0/\nu = 63$ for HR LES. These two values are predicted by the very simple Pao-like closure proposed by [4] to choose the level of artificial dissipation knowing the ratio between the LES and DNS cell sizes. Here, this ratio is 8 and 16 for HR and LR LES respectively, leading to the aforementioned values of ν_0/ν. The similar damping of the second part of the spectrum for HR and LR LES suggests that these predicted values are physically consistent while being transposable to the present hyperviscous filter operator.

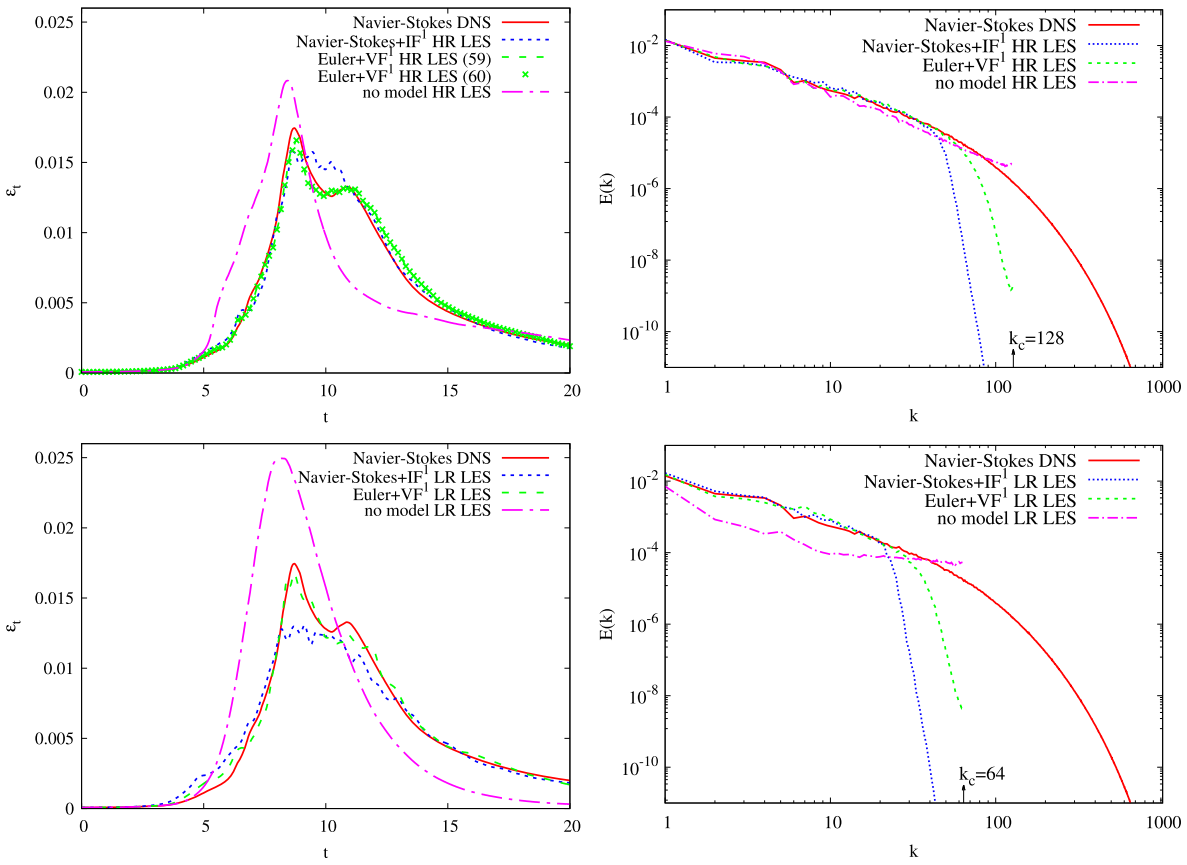

Fig. 12. Left: time evolution of the kinetic energy dissipation ε_t. Right: kinetic energy spectra $E(k)$ at $t = 14$. Top: high-resolution LES. Bottom: low-resolution LES. The case "Navier-Stokes+IF^1 has been performed using the optimized 6th-order filter of [30].

Let us consider now the use of filtering in combination with the explicit computation of the viscous term in Navier-Stokes equations. In that case, the filtering has to vanish at large scales, so that this approach can be referred as "Navier-Stokes+IF^1" with IF for "Inviscid Filtering". For conciseness, only the case with one filtering per time step is considered as it is commonly used in the literature. As inviscid filter, an option could be to use the set of coefficients (26) in combination with a conventional scheme for the computation of second derivatives. In practice, because this strategy would be less computationally efficient by comparison to the present viscous filtering technique while being equivalent in terms of accuracy, this specific combination is not addressed. As an example of "Navier-Stokes+IF^1" case, a filter fully removing the grid-to-grid wavelength is used with $\sigma = 1$. This is, by far, the most popular choice when the filtering solution strategy is used in DNS/LES. The filter developed by [30] is chosen for its good features of spectral vanishing at low wavenumber as illustrated in Fig. 2-left. The results of the corresponding calculation are presented in Fig. 12 for the time evolution of ε_t (left) and for the kinetic energy spectrum $E(k)$ at $t = 14$ (right). Despite the favourable scale-selective features of the filter from [30], the prediction of the total dissipation ε_t is found to be of lower quality by comparison to "Euler+VF^1" LES, the latter being less expensive thanks the dispense of second derivative computation. For HR LES, the phase of turbulent breakdown around the secondary peak of dissipation at $t \approx 12$ is not correctly captured. Even the first peak of dissipation, corresponding to early transition, is less accurately predicted by "Navier-Stokes+IF^1" HR LES. This loss of accuracy, significantly magnified for LR LES, may be attributed to the too invasive influence of the filtering at small scales. This behaviour is well illustrated in Fig. 12-right by the abrupt fall of $E(k)$ due to the use of $\sigma = 1$ that corresponds to an infinite value of the numerical viscosity ν_0 because of the full removing of turbulent scales at k_c. This intrusive effect at small scales is consistent with the equivalent SVV kernel presented in Fig. 2-left. A more gradual scale-selection of numerical dissipation seems to be a preferable option, with in particular a finite value for ν_0.

A fundamental issue is the evaluation of the actual role of the artificial dissipation while relating it to what can be expected from a SGS model. The simplest way to assess the activity of any SGS modelling, whether implicit or explicit, is to switch off the model and then observe the consequences on the results. This type of calculation can be referred as "no model" LES. For the present approach, no model means that no filtering is applied while using a conventional scheme, free from any artificial dissipation, for the computation of second derivatives. For both HR and LR LES, the lack of regularisation is found to lead to very inaccurate results. The loss of accuracy can be directly observed on the time evolution of the kinetic energy, with in particular a clear overestimation of the dissipation (see Fig. 12-left). As expected, no model LR LES results are worse than their HR LES counterparts. An examination of instantaneous solutions (not shown) reveals that no model LES solutions are subject to small-scale oscillations. These spurious oscillations tend to magnify the viscous friction,

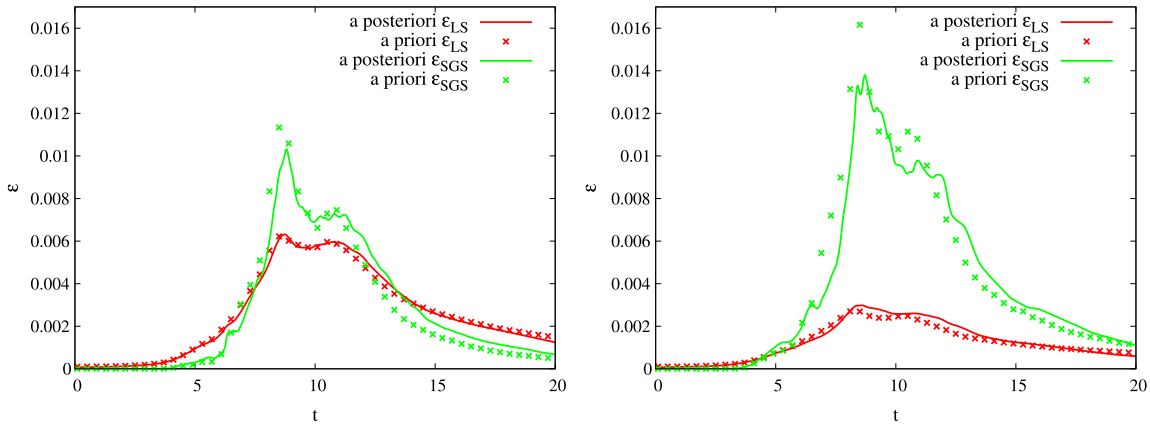

Fig. 13. Time evolution of the viscous large-scale kinetic energy dissipation ε_{LS} and of its SGS counterpart ε_{SGS} with $\varepsilon_t = \varepsilon_{LS} + \varepsilon_{SGS}$. Left: high-resolution LES. Right: low-resolution LES.

explaining the paradox that the lack of artificial dissipation leads to an overdissipative behaviour. The signature of these unphysical oscillations on the spectrum $E(k)$ can be observed in Fig. 12-right as a pile-up of kinetic energy in the spectral range $k_c/2 \lesssim k \leq k_c$, especially for LR LES for which $E(k)$ becomes almost flat in an extended range of k, indicating the establishment of an unphysical white noise which can be seen as a partial thermalization of the flow.

Another way to assess the role of the artificial dissipation is to estimate its relative contribution to the total dissipation. Here, we propose to make indirectly this estimation by computing first the viscous large-scale dissipation ε_{LS}. Then, in agreement with the standard definitions of SGS modelling, the SGS dissipation ε_{SGS} can be defined as $\varepsilon_{SGS} = \varepsilon_t - \varepsilon_{LS}$ where ε_t is the total dissipation provided by the hyperviscous filtering as a sum of its artificial (equated with SGS contribution) and viscous (equated with large-scale contribution) parts. A reasonable choice to estimate ε_{LS} is to use a standard second derivative scheme free from extra dissipation to compute the right-hand side of (60). Because these estimations are based on LES results, they can be referred as *a posteriori* analysis. To check their reliability, an *a priori* analysis based on raw and filtered DNS data has also been performed. For that purpose, the same methodology as in [38] has been carried out, enabling to provide an *a priori* estimation of both ε_{LS} and ε_{SGS}. The filtered DNS data are generated consistently with the numerical dissipation through the use of a simplified spectral closure as explained in [4]. For both HR and LR LES, a good agreement is obtained between these *a posteriori* and *a priori* estimations as shown in Fig. 13. Because this agreement is obtained without any constant adjustment, it can be considered as successful. Both *a priori* and *a posteriori* analyses confirm that even HR LES is quite challenging in the sense that ε_{SGS} can correspond, during the turbulent breakdown, to more than 60% of ε_t. For LR LES, this relative contribution of the SGS dissipation to the total dissipation can reach more than 80%. This is a clear confirmation, consistent with the no model results, that the present type of implicit SGS modelling plays a major role.

To conclude this subsection, let us compare the computational efficiency of "Euler+VF" and "Navier-Stokes" DNS/LES. In the code Incompact3d, the Euler (i.e. the convection and pressure terms) and viscous parts require the computation of 24 first and 9 second derivatives respectively. Removing the viscous term while applying a viscous filtering once every time step (referred here as "Euler+VF^1") simply consists in the substitution of these 9 second derivatives by the 9 one-dimensional filter operations (i.e. one by direction) without impacting the computational cost. If the more time accurate strategy "Euler+VF^3" is adopted, the extra application of 18 one-dimensional filters results in an increase of about $+56\%$ of the computational cost. Viewed in this perspective, the viscous filtering technique does not present any advantage by comparison to the traditional solving of Navier-Stokes equations. It can only be said that the "Euler+VF^1" approach reduces the computational cost by about -21% by comparison to the conventional "Navier-Stokes+IF^1" strategy thanks to the dispense of computation of the 9 second derivatives in the viscous term.

Because the strongest time step restriction comes from the CFL condition in the present DNS/LES of TGV, there is no interest in using a viscous filtering as a way to relax the viscous stability condition. In the next subsection, a more challenging situation is addressed where the stability limit is mainly dictated by the time integration of the viscous term.

7.2. Turbulent pipe flow

As a second computational configuration, DNS of a turbulent pipe flow at low and high Reynolds numbers are addressed. Again, the code Incompact3d is used with the solving of an extra governing equation for a passive scalar in order to provide heat transfer predictions. The computational domain $L_x \times L_y \times L_z$ is discretized using a regular Cartesian mesh of $n_x \times n_y \times n_z$ nodes despite the cylindrical geometry which is modelled thanks to an immersed boundary method customised for Incompact3d [39]. This computational configuration enables the imposition of periodic boundary conditions in the streamwise z as well as in the transverse x, y directions.

The physical boundary conditions imposed at the pipe wall are no-slip for the velocity and mixed-type for the temperature [40]. Numerically, both can be treated as Dirichlet-type boundary conditions. Defining the Reynolds number on the

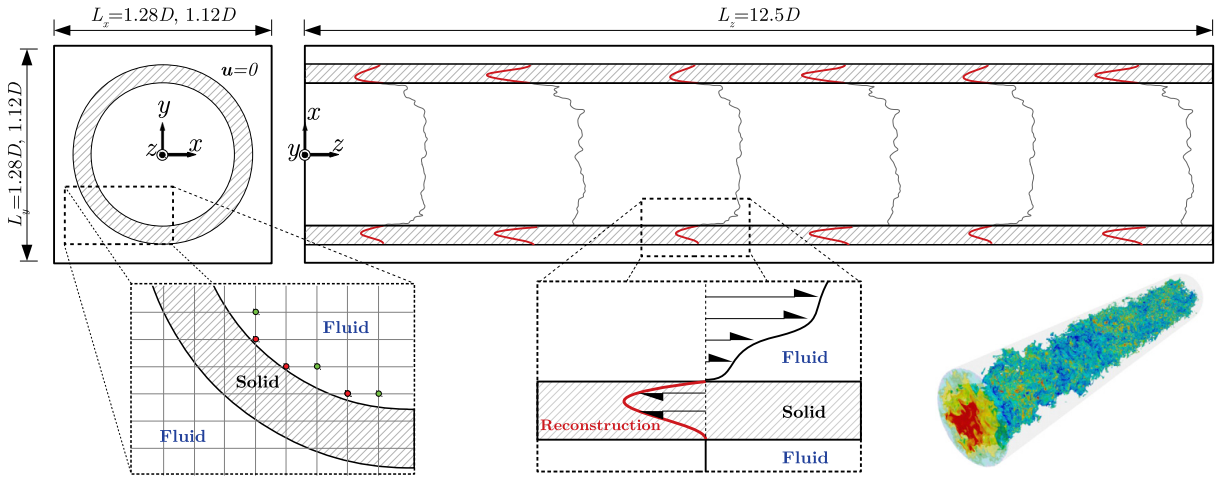

Fig. 14. Schematic view of the computational configuration of the pipe flow. Hatched zone indicates the solid region modelled by a customised immersed boundary based on solution reconstruction inside the solid [39].

bulk velocity U_b and the pipe diameter D, its two addressed values are $Re = (5300, 37700)$ at the same Prandtl number $Pr = 0.71$. For the Reynolds numbers based on the friction velocity u_τ, the two related nominal values are $Re_\tau = 180, 1000$. The streamwise length of the computational domain is the same for both Reynolds numbers with $L_z = 12.5D$; concerning the transverse dimensions, at $Re = 5300$ a slightly larger size is used with $L_x = L_y = 1.28D$ against $L_x = L_y = 1.12D$ at $Re = 37700$. This adjustment of the computational domain enables us to ensure a minimum number of nodes inside the solid region that corresponds to the pipe wall thickness t_w with $t_w \approx 0.075D$ at $Re = 5300$ and $t_w \approx 0.016D$ at $Re = 37700$. The computational mesh is based on $n_x \times n_y \times n_z = 256 \times 256 \times 640$ and $n_x \times n_y \times n_z = 768 \times 768 \times 1920$ nodes for the low and high Reynolds number respectively. For a schematic view of the computational configuration, see Fig. 14 where the principle of the solution reconstruction inside the immersed boundary is illustrated [39].

Expressed in wall units, the related cell sizes are $\Delta z^+ = (7, 13)$ and $\Delta x^+ = \Delta y^+ = (1.8, 2.9)$ at $Re = (5300, 37700)$. These spatial resolutions can be considered as fine except in the near-wall region for $\Delta x^+ - \Delta y^+$, especially for the high Reynolds case. However, it has been shown by [41,42] that this type of Cartesian mesh can provide basic turbulent statistics reaching the DNS accuracy. This is why we refer to DNS in this subsection, as a reliable computational configuration to assess the present viscous filtering technique while showing its major advantage in terms of computational efficiency.

The principle of comparison is the same as in the previous section. The reference data are from DNS based on the conventional way to compute the viscous term in the governing equations, referred here as "Navier-Stokes" DNS. The original data are obtained by the strategy "Euler+VF" DNS, namely through the solving of Euler equations while applying the viscous filter once ("Euler+VF^1" DNS) or three times ("Euler+VF^3" DNS) per time step. The viscous filter is given by (1), (36) as the counterpart of the second derivative scheme from [23] on which are based the reference "Navier-Stokes" DNS. As in the DNS of TGV presented in the previous subsection, aliasing errors are controlled using a moderate value of the numerical viscosity with $\nu_0/\nu = 3$. For the present pipe flow DNS, this artificial dissipation significantly improves the results contrary to the TGV flow for which it is of secondary importance.

It is important to stress that, unlike the previous subsection, the present comparisons between "Navier-Stokes" DNS and "Euler+VF" DNS are not based on the same time step. For the "Navier-Stokes" DNS, the most severe restriction on Δt comes from the AB3 Fourier condition (45) which reads $F < 0.0138$ for $\nu_0/\nu = 3$.

In the present computational flow configuration, based on immersed boundary condition, the correct definition of F is not obvious. Firstly, because of the Prandtl number less than unity, the most restrictive condition comes from the diffusion term in the temperature equation so that it is more convenient to define the Fourier number using the thermal diffusivity α instead of the viscosity ν. Secondly, concerning the reference length in F, an option could be to simply consider the smallest cell size given by Δx or Δy. From this definition of F, the maximum time step ensuring numerical stability should be $U_b \Delta t/D \approx (1.30\,10^{-3}, 8.87\,10^{-4})$ for $Re = (5300, 37700)$. In practice, for the present "Navier-Stokes" DNS, these maximum values cannot be approached without losing numerical stability when an immersed boundary method is used. These maximum time steps have been therefore determined empirically. For the two configurations addressed here, the obtained values are $U_b \Delta t/D \approx (4\,10^{-4}, 2\,10^{-4})$ for $Re = (5300, 37700)$, about 25%-30% of their reference values predicted by numerical stability analysis, corresponding to a strong reduction of the computational efficiency.

One reason of this difficulty lies in the mesh node distribution disconnected from the wall geometry. This feature, which is a strength of immersed boundary methods, imposes the computation of the solution on mesh nodes very close to the wall, namely at a clearly smaller distance than the mesh size. Fig. 14 illustrates this situation with a red mark for these very near-wall nodes by contrast to the others marked in green. This irregular mesh topology in terms of wall distance suggests that Δx may not be the correct length scale to estimate the maximum Fourier number. To the best of the authors' knowledge, a numerical stability analysis of this problem, inherent to the immersed boundary method, is not documented

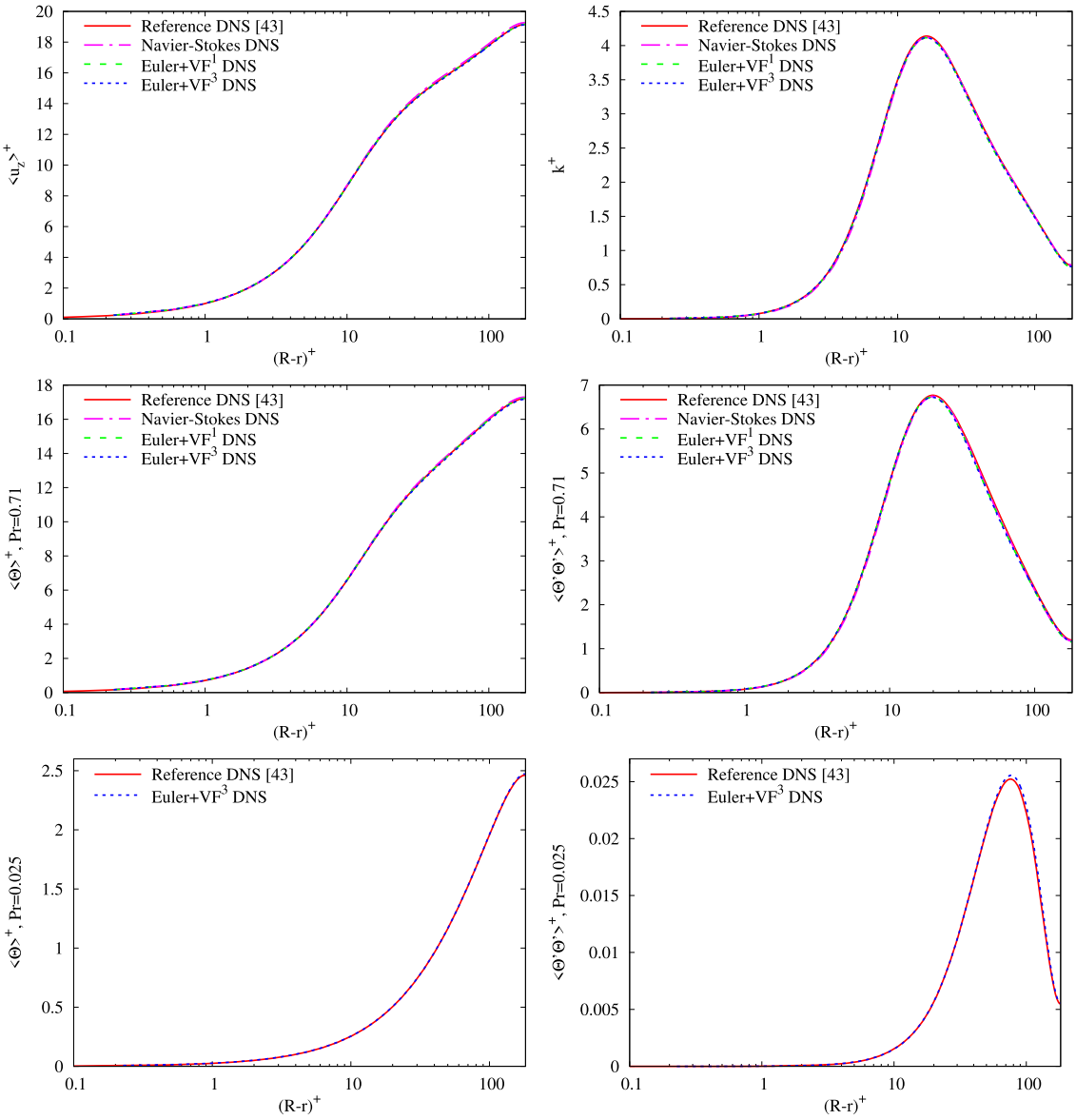

Fig. 15. Profiles of mean velocity $\langle u_z \rangle$, turbulent kinetic energy k, mean temperature $\langle \Theta \rangle$ and temperature variance $\langle \Theta' \Theta' \rangle$ at $Re = 5300$. Temperature statistics at $Pr = 0.71$ (middle) and $Pr = 0.025$ (bottom).

in the literature. Here, we presume that, when expressing the Fourier condition, its reference length should be corrected in order to take into account the occurrence of mesh nodes very close to the wall. This corrected cell size Δc can be estimated from the empirical determination of the maximum numerically stable Δt. Based on the 25%-30% reduction of the time step previously mentioned, we get the crude estimation $\Delta c \approx 0.5 \Delta x$ which can be seen, in first approximation, as a median value of the distance of the closest mesh nodes from the wall.

The crucial advantage of the present viscous filtering technique is the strong relaxation on the Fourier condition with $F < 4.12$ for the present scheme (1), (36) as already mentioned in section 6. For the present DNS, this condition is clearly less restrictive on the time step than the CFL condition which enables the use of a time step $(6, 3.5)$ times larger in "Euler+VF" DNS by comparison to "Navier-Stokes" DNS for the case $Re = (5300, 37700)$ respectively. Naturally, the point is to ensure that the resulting computational saving is not against accuracy. The following comparisons address this key issue.

Profiles of mean velocity, turbulent kinetic energy, mean temperature and temperature variance are presented in Fig. 15 at $Re = 5300$ for "Navier-Stokes" DNS, "Euler+VF^1" DNS and "Euler+VF^3" DNS. Present turbulent statistics are estimated through a smoothed projection from the Cartesian mesh to the cylindrical coordinates (r, θ) with an average in time and in the azimuthal direction θ (see [41] for more details on the data projection technique). The DNS data of [43] are also included for reference. For all of these quantities, an excellent agreement can be observed. The very small discrepancies are within the statistical convergence uncertainty. As in the previous subsection, the difference between "Euler+VF^1" DNS and "Euler+VF^3" DNS is found to be insignificant, making questionable the practical interest of the extra cost of +56% due to

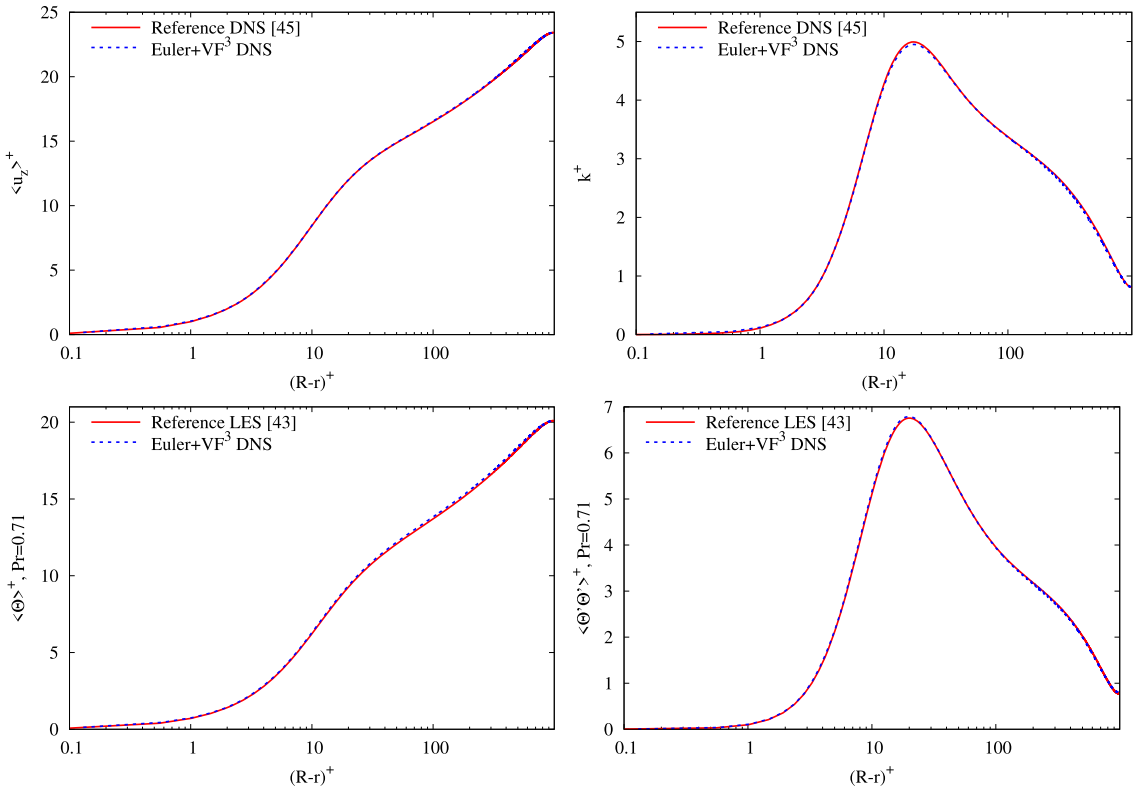

Fig. 16. Profiles of mean velocity $\langle u_z \rangle$, turbulent kinetic energy k, mean temperature $\langle \Theta \rangle$ and temperature variance $\langle \Theta' \Theta' \rangle$ at $Re = 37700$. Temperature statistics at $Pr = 0.71$.

the two additional filtering applications per time step. This conclusion is not unexpected: it is well-known that because of time-scale ratio between convection and diffusion processes, the viscous term can be integrated in time using a scheme of lower accuracy by comparison to the convection term. By accepting the negligible loss of time accuracy of "Euler+VF^1" DNS, it can be concluded that the present viscous filtering strategy reduces by -83% the computational cost by comparison to an explicit time integration of the viscous term. For "Euler+VF^3" DNS, the computational saving is only -74% which is nonetheless very satisfactory.

The advantage of viscous filtering can be even more spectacular at low Prandtl number Pr. This can be particularly useful in applications involving liquid metals, such as advanced cooling devices, in which the prediction by DNS/LES of heat-transfer in turbulent flows of low-Pr fluids is necessary for design purposes. Because of the corresponding high value of the thermal diffusivity α, an explicit time integration of the viscous term becomes extremely penalizing requiring the use of a very small time step in order to ensure the Fourier condition. With the present viscous filtering technique, low-Pr fluids can be addressed without any extra-cost. To illustrate this capability, a case at $Pr = 0.025$ has been considered by DNS at $Re = 5300$. At this high level of diffusion, there is no need to apply any artificial dissipation for the temperature equation ($\nu_0 = 0$). Despite the corresponding less restrictive Fourier condition $F < 0.00425$, the high value of the diffusivity would make too expensive a "Navier-Stokes" DNS. On the contrary, an "Euler+VF" DNS without changing the time step can be easily performed. A comparison of the resulting temperature statistics with the reference data of [43] is presented in Fig. 15-bottom. Again, an excellent agreement is obtained. The same computation by "Navier-Stokes" DNS would have required a time step 30 times smaller, leading to a computational saving of -95% for the "Euler+VF^3" DNS.

To confirm the good behaviour of the present viscous filtering approach, a more demanding computational configuration at $Re = 37700$ is now considered. As already mentioned, expressed in wall units, the spatial resolution is marginal, especially in the near-wall region. In such a situation, the use of artificial dissipation is crucial to compensate the small fraction of viscous dissipation missed due to the too coarse mesh to fully capture the Kolmogorov scale. At this Reynolds number, successful turbulent velocity statistics have been obtained by [44] with the same computational configuration using the conventional strategy "Navier-Stokes" DNS. In Fig. 16, turbulent statistics with the present "Euler+VF^3" DNS approach are compared to the DNS of [45] for velocity and to the well-resolved LES of [43] for temperature.[4] Despite the marginal resolution for this high Reynolds number case, a good overall agreement can be observed. The ability of "Euler+VF^3" DNS to faithfully reproduce the reference results despite the use of a 3.5 times larger time step by comparison to "Navier-Stokes" DNS shows that the present viscous filtering approach is not only attractive for low Reynolds turbulence. It leads to a

[4] As [43], we refer to LES, but it must be noted that, thanks to the very fine mesh used, the accuracy of this calculation is very close to DNS.

reduction of about −55% that can be extended to −71% if the simpler and slightly less accurate "Euler+VF[1]" DNS strategy is used. In conclusion, as a generic, stable, efficient and accurate method, the "Euler+VF" DNS seems to be a convenient technique for solving the Navier-Stokes equations.

8. Conclusion and discussion

In this study, a new approach of spatial filtering is proposed for solving the governing equations of fluid mechanics. The general framework of this approach is the concept of solution filtering which consist in the application of a spatial filter operator every step of the time advancement. The method is developed in the context of finite-difference schemes as a simple spatially discrete integrating factor commonly used in spectral Fourier methods for computational fluid dynamics [33,34].

First, the guiding principles of the solution filtering technique have been discussed while clearly exhibiting the flexibility of the method through the adjustment of the scheme coefficients. In this preliminary part, the equivalence between solution filtering and spectral vanishing viscosity is shown. To the authors' knowledge, this is the first time that this link is clearly established. Thanks to the simple formalism related to this connection, the consequences of using a fixed filter are discussed as well as the physical anomaly that consists in fully removing the grid-to-grid wavelength that must be associated to the application of an infinite artificial viscosity at this scale. Another issue raised by the use of a fixed filter scheme is the lack of time consistency. As a very simple remedy to these drawbacks, it is suggested to make dependent the scheme coefficients on the time step Δt. It leads to a first family of flexible filters that can be shaped to mimic a generic spectral vanishing viscosity while controlling the level of artificial dissipation at small scales through the parameter ν_0 referred as numerical viscosity. As nondimensional parameters to represent Δt and ν_0 in the scheme coefficients, the Fourier number F and the ratio ν_0/ν are introduced. Because of the spectral vanishing behaviour of these finite-difference operators, they can be referred as inviscid filters (i.e. virtually free from any significant dissipation at large scales).

Then, the principle of modifying the filter scheme coefficients is extended in order to incorporate both the molecular and artificial dissipations in one single operator. The development of this new family of filter schemes is performed in the Fourier space to make easier the establishment of relation orders between the scheme coefficients. This leads to the new concept of viscous filtering while keeping the initial philosophy to apply the filter on the solution every time step. Various sets of scheme coefficients are provided on the basis of 8th-order accuracy in space. These coefficients are a function of F and ν_0/ν. Each viscous filter operator is connected to its counterpart as a differentiation operator to compute a second derivative. Based on this link, it can be shown that the actual order of accuracy of the viscous filter is reduced by two levels by comparison to its formal order, leading to 6th-order for the family developed in this study. The same link shows that the solution provided by the viscous filter is a 1st-order approximation in time of its counterpart obtained using a second derivative scheme with an exact time integration (see Appendix A). Spatial convergence test confirms the 6th-order accuracy of the developed viscous filter scheme. Temporal convergence shows that despite the 1st-order previously mentioned, because of the entanglement between spatial and time errors, the viscous filtering is always more accurate in time than an Adams-Bashforth scheme of 3rd-order accuracy. By comparison to this explicit time advancement scheme, it can be observed that the present viscous filtering strategy is much more robust in terms of numerical stability, with a spectacular relaxation of the Fourier condition.

The accuracy as well as the numerical stability features of the viscous filtering technique are recovered for challenging DNS/LES of two academic flows. For the Taylor-Green Vortex problem, the study of a deterministic regime at low Reynolds number has enabled very accurate comparisons between a conventional solving of Navier-Stokes equations (based on the explicit computation of the viscous term) and the present new viscous filtering approach. A higher Reynolds number is also considered by LES to show the capability of the method as an implicit subgrid-scale model. As a generic wall-turbulence problem, the turbulent pipe flow has been calculated by DNS while considering heat transfer. The treatment of this cylindrical geometry with an immersed boundary method and a Cartesian mesh has enabled us to assess the method as a more general approach compatible with complex geometry. Successful results are obtained in the sense that the viscous filtering strategy can reach an excellent accuracy while reducing drastically the computational cost thanks to the use of large time steps. This facility is allowed by the very favourable numerical stability of the time advancement provided by viscous filtering. In particular, this is a definitive advantage in the context of immersed boundary method, low Reynolds and/or low Prandtl turbulent flows.

The present viscous filtering method can be seen as an alternative to implicit time integration of the viscous term which is very popular in the context of DNS/LES of wall turbulence when unconditional stability is expected, enabling to deal with any value of the Fourier number F. For the present method, the conditional stability is not removed but its restriction is so relaxed that it is close to unconditional stability. By comparison to implicit methods, the treatment of the viscous influence as a filtering process offers advantages in terms of flexibility (control of the molecular/artificial dissipations) and efficiency (no operator inversion required). It is also extremely easy to code in the sense that any finite-difference routine can be straightforwardly adapted through the simple change of the scheme coefficients. This is an almost "zero development" method contrary to the implementation of an implicit time integration, especially in a three-dimensional context. Here, because the filtering is explicit in time, the filter operators can be applied sequentially in every direction without any difficulty in terms of coding.

Further work is required to extend the validity of the viscous filtering approach. First, one-sided viscous filter schemes need to be developed for the imposition of Dirichlet and Neumann boundary conditions. A slightly more delicate step is to generalize the viscous filtering for a non-regular computational mesh. The use of a mapping technique may be the most straightforward way to take this step but other methods, possibly more efficient, are probably feasible.

A few words can be added on the anisotropic and inhomogeneous application of the viscous filtering through the choice of ν_0/ν related to the artificial dissipation. Technically, the use of a different value of ν_0/ν depending on the spatial direction is straightforward in the sense that the present filtering strategy is based on one-dimensional finite-difference operators. Then, if there are physical reasons for an anisotropic application of the artificial dissipation, it can be done easily. In the same way, its inhomogeneous application is technically feasible by enabling spatial variation of ν_0/ν for the computation of the coefficients of the finite-difference filter scheme at every mesh node. Another option is to use two sets of constant coefficients, one with $\nu_0/\nu = 0$ and another with a high value of ν_0/ν. Then, a local switch between the two operators (one free from artificial viscosity and another one highly dissipative at small scale) can be performed. This second option has been investigated by [46] for the boosted second derivative which is the counterpart of the present viscous filtering. The simplicity and efficiency of this approach, called Adaptive Numerical Viscosity (ANV), is clearly shown in this study. To summarize, there is no technical barrier for an anisotropic and inhomogeneous application of the artificial dissipation embedded in the present viscous filtering technique.

A more fundamental question is related to the purpose of an anisotropic and inhomogeneous application of numerical dissipation. In terms of physical scales, the use of the same value of ν_0/ν in the three spatial directions does not mean that the artificial dissipation is isotropic. It is only true if the computational mesh itself is isotropic. For instance, in the turbulent pipe flow DNS presented in section 7.2, the use of non-cubic cells, with an aspect ratio of about 4, leads to an anisotropic numerical dissipation despite the same value $\nu_0/\nu = 3$ used in the three spatial directions. For a regular and Cartesian computational mesh, directional values of ν_0/ν would only be useful to compensate a potential mismatch between physics and numerics. In other words, instead of imposing anisotropy on the numerical viscosity, a preferable option would be to adapt the computational mesh. A similar idea can be advocated for the use of inhomogeneous numerical dissipation that should be first reflected by the mesh design. This corresponds to the general recommendation of [4] (see concluding section) who suggest to adapt the LES mesh on its corresponding DNS counterpart using a constant and isotropic derefinement factor everywhere, this choice making meaningful the use of a constant numerical viscosity. This recommendation can be extended to the present viscous filtering, at least in first intention.

A common motivation for spatially varying subgrid-scale viscosity is also the treatment of wall turbulence, with typically a damping of the model activity in the near-wall region. This approach has been investigated by [46] using their technique of Adaptive Numerical Viscosity for LES of turbulent plane channel flow up to very high Reynolds numbers. Their conclusion was that a local adaptation of ν_0/ν was not really needed, even for the most demanding computational configuration addressed. This conclusion is consistent with our pipe flow LES reported in [44] and based on the use of boosted second derivatives. In this previous study, it has been shown that good turbulent statistics can be obtained while using a constant value for ν_0/ν. This easiness probably comes from the high scale-selectivity of the numerical dissipation which is weakly intrusive on the largest scale dynamics.

Naturally, in a perspective of advanced subgrid-scale modelling, the spatial variation of ν_0/ν may be a physically meaningful option. For instance, to deal with the unsteady and inhomogeneous component of non-equilibrium turbulent cascade [47], the opportunity of controlling locally and instantaneously the strength of the kinetic energy transfer may be an attractive feature. Hence, scaling of the artificial dissipation, related to the choice of ν_0/ν, can be guided by physical considerations on the kinetic energy transfer from large to subgrid scales. Naturally, because the present approach is purely dissipative, no backscatter phenomenon can be handled in this way. However, in complement to the simple spectral closure of [4] only valid for isotropic turbulence at equilibrium, as a tool for *a priori* estimation of ν_0/ν, a more dynamic evaluation of this parameter, as in the adaptive filtering of [12,14], may be an interesting option.

The extension of the concept of viscous filtering may also be adapted to more sophisticated spectral/*hp* element approaches [48,49], as a contribution to the development of implicit LES in highly accurate DNS/LES solvers [50,51]. In this demanding context, the present combination of high-order finite-difference schemes with an immersed boundary method can be seen as a simple and efficient strategy which is reinforced by this particular way to model viscous effects.

CRediT authorship contribution statement

Eric Lamballais: Conceptualization, Formal analysis, Methodology, Software, Supervision, Validation, Visualization, Writing – original draft, Writing – review & editing. **Rodrigo Vicente Cruz:** Formal analysis, Methodology, Software, Validation, Visualization, Writing – review & editing. **Rodolphe Perrin:** Formal analysis, Validation, Writing – review & editing.

Declaration of competing interest

The authors declare that they have no known competing financial interests or personal relationships that could have appeared to influence the work reported in this paper.

Acknowledgement

This work was granted access to the HPC resources of TGCC/CINES under the allocation A0052A07624 made by GENCI. The authors are indebted to Damien Biau for his insightful remarks on the topics considered here.

Appendix A. Connection between viscous filter and second derivative schemes at small Fourier number

In this appendix, the asymptotic behaviour of the viscous filter when $F \to 0$ is examined. It will be shown that the modified wavenumber given by (33) can be seen as a 1st-order $O(\Delta F)$ approximation of the modified wavenumber of a counterpart second derivative scheme written in the form

$$\alpha f''_{i-1} + f''_i + \alpha f''_{i+1} = a\frac{f_i}{\Delta x^2} + b\frac{f_{i-1}+f_{i+1}}{2\Delta x^2} + c\frac{f_{i-2}+f_{i+2}}{2\Delta x^2} + d\frac{f_{i-3}+f_{i+3}}{2\Delta x^2} + e\frac{f_{i-4}+f_{i+4}}{2\Delta x^2} \tag{A.1}$$

with its associated modified wavenumber

$$k''\Delta x^2 = -\frac{a + b\cos(k\Delta x) + c\cos(2k\Delta x) + d\cos(3k\Delta x) + e\cos(4k\Delta x)}{1 + 2\alpha\cos(k\Delta x)} \tag{A.2}$$

where f''_i is an approximation of the second derivative $f''(x_i)$ at the node x_i. Here, to make easier the connection between this scheme and the viscous filter, the adopted form mimics the generic form of a filter scheme without any loss of generality in the framework of centred schemes based on a given stencil. For this scheme, the order conditions can be easily obtained with

$$\begin{aligned} 0 &= a + b + c + d + e && (\Delta x^0)\\ 2 + 4\alpha &= b + 4c + 9d + 16e && (\Delta x^2)\\ 24\alpha &= b + 16c + 81d + 256e && (\Delta x^4)\\ 60\alpha &= b + 64c + 729d + 4096e && (\Delta x^6) \end{aligned} \tag{A.3}$$

This set of conditions has similarities with the order conditions (31) of the viscous filter which can also be written as

$$\begin{aligned} 0 &= \frac{a_f - 1}{F} + \frac{b_f - 2\alpha_f}{F} + \frac{c_f}{F} + \frac{d_f}{F} + \frac{e_f}{F} && (\Delta x^2)\\ 2 + 4\alpha_f &= \frac{b_f - 2\alpha_f}{F} + 4\frac{c_f}{F} + 9\frac{d_f}{F} + 16\frac{e_f}{F} && (\Delta x^4)\\ 12F(1 + 2\alpha_f) + 24\alpha_f &= \frac{b_f - 2\alpha_f}{F} + 16\frac{c_f}{F} + 81\frac{d_f}{F} + 256\frac{e_f}{F} && (\Delta x^6)\\ 120F^2(1 + 2\alpha_f) + 360F\alpha_f + 60\alpha_f &= \frac{b_f - 2\alpha_f}{F} + 64\frac{c_f}{F} + 729\frac{d_f}{F} + 4096\frac{e_f}{F} && (\Delta x^8) \end{aligned} \tag{A.4}$$

In particular, it can be concluded that the set of coefficients

$$\left(\alpha_f, \frac{a_f - 1}{F}, \frac{b_f - 2\alpha_f}{F}, \frac{c_f}{F}, \frac{d_f}{F}, \frac{e_f}{F}\right) \tag{A.5}$$

is a $O(\Delta F)$ approximation of the set of coefficients (α, a, b, c, d, e).

The logarithmic term $\ln T$ in (33) can be written and approximated as

$$\ln\left[1 + F\frac{\frac{a_f-1}{F} + \frac{b_f-2\alpha_f}{F}\cos(k\Delta x) + \frac{c_f}{F}\cos(2k\Delta x) + \frac{d_f}{F}\cos(3k\Delta x) + \frac{e_f}{F}\cos(4k\Delta x)}{1 + 2\alpha_f\cos(k\Delta x)}\right] = F\frac{\frac{a_f-1}{F} + \frac{b_f-2\alpha_f}{F}\cos(k\Delta x) + \frac{c_f}{F}\cos(2k\Delta x) + \frac{d_f}{F}\cos(3k\Delta x) + \frac{e_f}{F}\cos(4k\Delta x)}{1 + 2\alpha_f\cos(k\Delta x)} + O(\Delta F^2) \tag{A.6}$$

Then, using (33), the corresponding approximated modified wavenumber is

$$k''\Delta x^2 = -\frac{\frac{a_f-1}{F} + \frac{b_f-2\alpha_f}{F}\cos(k\Delta x) + \frac{c_f}{F}\cos(2k\Delta x) + \frac{d_f}{F}\cos(3k\Delta x) + \frac{e_f}{F}\cos(4k\Delta x)}{1 + 2\alpha_f\cos(k\Delta x)} + O(\Delta F) \tag{A.7}$$

as the counterpart of (A.2) for a second derivative scheme where the set of coefficients (A.5) is recovered to replace (α, a, b, c, d, e).

These developments show that the present viscous filter corresponds to a second derivative which behaves asymptotically as a conventional second derivative finite-difference scheme when $F \to 0$. The scaling in F means that this approximation is 1st-order accurate in time while leading to a reduction of 2 for the spatial order of accuracy. It explains why the present 8th-order filter formulation can only provide 6th-order accuracy.

References

[1] B. Geurts, Elements of Direct and Large-Eddy Simulation, Edwards, 2004.
[2] P. Sagaut, Large Eddy Simulation of Incompressible Flow: An Introduction, 2nd edition, Springer-Verlag, 2005.
[3] M. Lesieur, O. Métais, P. Comte, Large-Eddy Simulation of Turbulence, Cambridge University Press, 2005.
[4] T. Dairay, E. Lamballais, S. Laizet, C. Vassilicos, Numerical dissipation vs. subgrid-scale modelling for large eddy simulation, J. Comput. Phys. 337 (2017) 252–274.
[5] A.K. Edoh, N.L. Mundis, C.L. Merkle, A.R. Karagozian, V. Sankaran, Comparison of artificial-dissipation and solution-filtering stabilization schemes for time-accurate simulations, J. Comput. Phys. 375 (2018) 1424–1450.
[6] J. Berland, P. Lafon, F. Daude, F. Crouzet, C. Bogey, C. Bailly, Filter shape dependence and effective scale separation in large-eddy simulations based on relaxation filtering, Comput. Fluids 47 (2014) 65–74.
[7] F. Kremer, C. Bogey, Large-eddy simulation of turbulent channel flow using relaxation filtering: resolution requirement and Reynolds number effects, Comput. Fluids 116 (2015) 17–28.
[8] T. Lund, The use of explicit filters in large eddy simulation, Comput. Math. Appl. 46 (4) (2003) 603–616.
[9] Klein, An attempt to assess the quality of large eddy simulations in the context of implicit filtering, Flow Turbul. Combust. 75 (2005) 131–147.
[10] S. Bose, P. Moin, D. You, Grid-independent large-eddy simulation using explicit filtering, Phys. Fluids 22 (105103) (2010) 1.
[11] C. Bogey, C. Bailly, Large eddy simulations of transitional round jets: influence of the Reynolds number on flow development and energy dissipation, Phys. Fluids 18 (6) (2006) 1–14.
[12] T. Tantikul, J.A. Domaradzki, Large eddy simulations using truncated Navier-Stokes equations with the automatic filtering criterion, J. Turbul. 11 (21) (2010) 1–24.
[13] D. Fauconnier, C. Bogey, E. Dick, On the performance of relaxation filtering for large-eddy simulation, J. Turbul. 14 (1) (2013) 22–49.
[14] G. Sun, J.A. Domaradzki, Implicit LES using adaptive filtering, J. Comput. Phys. 359 (2018) 380–408.
[15] M.R. Visbal, D.P. Rizzetta, Large-eddy simulation on curvilinear grids using compact differencing and filtering schemes, J. Fluids Eng. 124 (4) (2002) 836–847.
[16] D.P. Rizzetta, M.R. Visbal, G.A. Blaisdell, A time-implicit high-order compact differencing and filtering scheme for large-eddy simulation, Int. J. Numer. Methods Fluids 42 (6) (2003) 665–693.
[17] C. Bogey, C. Bailly, Computation of a high Reynolds number jet and its radiated noise using large eddy simulation based on explicit filtering, Comput. Fluids 35 (2006) 1344–1358.
[18] C. Bogey, C. Bailly, Turbulence and energy budget in a self-preserving round jet: direct evaluation using large eddy simulation, J. Fluid Mech. 627 (2009) 129–160.
[19] G. Aubard, P.S. Volpiani, X. Gloerfelt, J.-C. Robinet, Comparison of subgrid-scale viscosity models and selective filtering strategy for large-eddy simulations, Flow Turbul. Combust. 91 (3) (2013) 497–518.
[20] A.K. Edoh, N.L. Mundis, A.R. Karagozian, V. Sankaran, Balancing aspects of numerical dissipation, dispersion, and aliasing in time-accurate simulations, Int. J. Numer. Methods Fluids 92 (11) (2020) 1506–1527.
[21] J. Boris, F. Grinstein, E. Oran, R. Kolbe, New insights into large-eddy simulation, Fluid Dyn. Res. 10 (1992) 199–228.
[22] F.F. Grinstein, L.G. Margolin, W.J. Rider (Eds.), Implicit Large Eddy Simulation: Computing Turbulent Fluid Dynamics, Cambridge Univ. Press, 2007.
[23] E. Lamballais, V. Fortuné, S. Laizet, Straightforward high-order numerical dissipation via the viscous term for direct and large eddy simulation, J. Comput. Phys. 230 (2011) 3270–3275.
[24] E. Tadmor, Convergence of spectral methods for nonlinear conservation laws, SIAM J. Numer. Anal. 26 (1) (1989) 1–30.
[25] Y. Maday, E. Tadmor, Analysis of the spectral vanishing viscosity method for periodic conservation laws, SIAM J. Numer. Anal. 26 (4) (1989) 854–870.
[26] G.-S. Karamanos, G.E. Karniadakis, A spectral vanishing viscosity method for large-eddy simulations, J. Comput. Phys. 163 (11) (2000) 22–50.
[27] R. Pasquetti, Spectral vanishing viscosity method for large-eddy simulation of turbulent flows, J. Sci. Comput. 27 (1–3) (2006) 365–375.
[28] S.K. Lele, Compact finite difference schemes with spectral-like resolution, J. Comput. Phys. 103 (1992) 16–42.
[29] J.W. Kim, R.D. Sandberg, Efficient parallel computing with a compact finite difference scheme, Comput. Fluids 58 (2012) 70–87.
[30] C. Bogey, N. de Cacqueray, C. Bailly, A shock-capturing methodology based on adaptative spatial filtering for high-order non-linear computations, J. Comput. Phys. 228 (2009) 1447–1465.
[31] S. Laizet, E. Lamballais, High-order compact schemes for incompressible flows: a simple and efficient method with quasi-spectral accuracy, J. Comput. Phys. 228 (2009) 5989–6015.
[32] R. Peyret, Introduction to high-order approximation methods for computational fluid dynamics, in: E.K.R. Peyret (Ed.), Advanced Turbulent Flow Computations, Springer, Vienna, 2000, pp. 1–79.
[33] R.S. Rogallo, An illiac program for the numerical simulation of homogeneous, incompressible turbulence, Tech. Rep., NASA TM-73203, 1977.
[34] C. Canuto, M.Y. Hussaini, A. Quarteroni, T.A. Zang, Spectral Methods in Fluid Dynamics, Springer-Verlag, New York, 1988.
[35] S. Laizet, E. Lamballais, J.C. Vassilicos, A numerical strategy to combine high-order schemes, complex geometry and parallel computing for high resolution DNS of fractal generated turbulence, Comput. Fluids 39 (3) (2010) 471–484.
[36] S. Laizet, N. Li, Incompact3d: a powerful tool to tackle turbulence problems with up to $O(10^5)$ computational cores, Int. J. Numer. Methods Fluids 67 (11) (2011) 1735–1757.
[37] P. Bartholomew, G. Deskos, R. Frantz, F. Schuch, E. Lamballais, S. Laizet, Xcompact3d: an open-source framework for solving turbulence problems on a Cartesian mesh, SoftwareX 12 (2020) 100550.
[38] E. Lamballais, T. Dairay, S. Laizet, C. Vassilicos, Implicit/explicit spectral viscosity and large-scale SGS effects, in: M. Salvetti, V. Armenio, J. Fröhlich, B. Geurts, H. Kuerten (Eds.), Direct and Large-Eddy Simulation XI, in: ERCOFTAC Series, vol. 25, Springer, Cham, 2019, pp. 107–113.
[39] R. Gautier, S. Laizet, E. Lamballais, A DNS study of jet control with microjets using an immersed boundary method, Int. J. Comput. Fluid Dyn. 28 (6–10) (2014) 1–18.
[40] M. Piller, Direct numerical simulation of turbulent forced convection in a pipe, Int. J. Numer. Methods Fluids 49 (2005) 583–602.
[41] T. Dairay, E. Lamballais, S. Benhamadouche, Mesh node distribution in terms of wall distance for large-eddy simulation of wall-bounded flows, Flow Turbul. Combust. 100 (3) (2018) 617–626.

[42] E. Lamballais, R. Vicente Cruz, From explicit to implicit subgrid-scale and wall modelling in large-eddy simulation, in: B. Skallerud, H.I. Andersson (Eds.), MekIT'19, Tenth National Conference on Computational Mechanics, Trondheim, Norway, 2019, pp. 1–24.
[43] S. Straub, P. Forooghi, L. Marocco, T. Wetzel, R. Vinuesa, P. Schlatter, B. Frohnapfel, The influence of thermal boundary conditions on turbulent forced convection pipe flow at two Prandtl numbers, Int. J. Heat Mass Transf. 144 (2019) 118601.
[44] R. Vicente Cruz, E. Lamballais, R. Perrin, Implicit wall-layer modelling in turbulent pipe flow, in: S.M. García-Villalba, H. Kuerten (Eds.), Direct and Large Eddy Simulation XII, in: ERCOFTAC Series, vol. 27, Springer, Cham, 2020, pp. 425–431.
[45] G.K.E. Khoury, P. Schlatter, A. Noorani, P.F. Fischer, G. Brethouwer, A.V. Johansson, Direct numerical simulation of turbulent pipe flow at moderately high Reynolds numbers, Flow Turbul. Combust. 91 (3) (2013) 475–495.
[46] O.A. Mahfoze, S. Laizet, Non-explicit large eddy simulations of turbulent channel flows from $Re_\tau = 180$ up to $Re_\tau = 5,200$, Comput. Fluids (2020) 1–46.
[47] J.-C. Vassilicos, Dissipation in turbulent flows, Annu. Rev. Fluid Mech. 47 (2014) 95–114.
[48] M.O. Deville, P.F. Fischer, E.H. Mund, High-Order Methods for Incompressible Fluid Flow, Cambridge University Press, 2002.
[49] G. Karniadakis, S. Sherwin, Spectral/hp Element Methods for Computational Fluid Dynamics, 2nd edition, Oxford Science Publications, 2005.
[50] M. de la Llave Plata, E. Lamballais, F. Naddei, On the performance of a high-order multiscale DG approach to LES at increasing Reynolds number, Comput. Fluids 194 (2019) 104306.
[51] F. Navah, M. de la Llave Plata, V. Couaillier, A high-order multiscale approach to turbulence for compact nodal schemes, Comput. Methods Appl. Mech. Eng. 363 (2020) 112885.

Version française

Au cours de cette thèse, une nouvelle technique de filtrage de solutions DNS et LES a été développée. Cette approche est en fait équivalente à l'utilisation de la viscosité spectrale comme un ersatz de modélisation sous-maille (ou simplement de régularisation à petite échelle dans le cas de la DNS), conformément aux discussions développées dans la section 2.6.3. La méthode est détaillée dans ce chapitre et il faut souligner que son développement/implémentation a été extrêmement important pour l'avancement de cette thèse qui a permis sa validation en retour. Plus précisément, comme discuté dans la section 2.7, une intégration temporelle pleinement explicite avec un schéma d'Adams-Bashforth du troisième ordre est utilisée ici pour les équations d'évolution. Cependant, comme il est montré dans ce chapitre, lorsqu'une méthode de frontière immergée est utilisée, la condition de Fourier peut facilement devenir plus contraignante que la condition CFL, ceci nécessitant l'utilisation de très petits pas de temps afin d'assurer la stabilité numérique. Cette contrainte peut être encore aggravée en cas de transferts de chaleur s'opérant à faible nombre de Prandtl ($Pr \ll 1$) ainsi que par l'usage d'un opérateur hyper-visqueux via la dérivée seconde comme c'est le cas ici. En pratique, les simulations de transferts de chaleur prévues pour cette thèse dans ce cadre auraient été trop coûteuses, pour les fluides à faible nombre de Prandtl et même simplement pour traiter un cas avec transfert thermique conjugué (CHT en sigle anglo-saxon) qui nécessite de traiter simultanément des échelles temporelles et spatiales fortement distinctes associées à la convection forcée dans le fluide et la conduction thermique dans le solide.

Dans ce contexte, on peut même dire que le développement de la présente technique de filtrage visqueux est arrivé au bon moment, car son principal atout est précisément la forte relaxation de la contrainte de Fourier, permettant l'utilisation de pas de temps beaucoup plus grands, ce qui a conduit à une économie remarquable des ressources de calcul. En cela, on peut voir cette approche par filtrage comme une alternative au traitement implicite du terme diffusif avec l'efficacité de calcul en plus. A la lumière de l'article récemment publié où la méthodologie est entièrement détaillée [78], nous avons décidé de ne pas la décrire à nouveau ici mais de fournir au lecteur l'article par son insertion directe dans le manuscrit. Les résultats de transferts de chaleur turbulents présentés avec des conditions aux limites de type mixte (MBC) dans la section 7.2 sont repris dans le chapitre suivant lors de la description des stratégies IBM mises en œuvre pour prescrire les conditions aux limites thermiques dans le cadre de cette thèse.

Chapter 5

Heat Transfer in Turbulent Pipe Flow

The choice of appropriate boundary conditions for the governing equations is crucial to obtain accurate representations of real life phenomena. For instance, the velocity boundary conditions for the Navier-Stokes are well-defined from the no-slip condition. Nonetheless, specifying a thermal boundary condition (TBC) that fairly describes a certain real heat transfer phenomenon for the energy equation may not be so straightforward since the most employed TBCs are idealized simplified representations. To illustrate this point, let us consider the conjugate heat transfer problem represented in Figure 1.3, where a certain heat exchange process is occurring between the external surroundings $r > R_o$, the pipe body $R \leq r \leq R_o$ and the confined turbulent flow $r < R$. What is commonly done in heat transfer simulations is to solve only the fluid temperature field $r < R$ while modelling the heat exchange across the solid wall with a boundary condition. More precisely, the heat conduction taking place across the solid subdomain $R \leq r \leq R_0$ is not computed, it is instead represented by an ideal TBC directly prescribed at the fluid solid interface $r = R$, as represented in Figure 5.1. This approach is referred to as *local imposition* and the most generic TBCs are *isothermal* or *isoflux* boundary conditions prescribed at the wall. The former consists of enforcing a wall temperature which is spatially uniform, whereas for the second, it is the wall heat flux that is uniform. Furthermore, in this chapter, we will be dealing with *ideal local imposition*, where the term *ideal* implies, as in [29], that the instantaneous quantity imposed is not only uniform (space) but also constant (time).

Therefore, *ideal isoflux*, denoted by IF in this monograph, means that the instantaneous wall heat flux q_w in Figure 5.1 is uniform and constant. As a consequence, the instantaneous wall temperature T_w admits fluctuations but its (time-)averaged value displays a linear increase along the duct. On the other hand, for *ideal isothermal*, denoted by *IT*, the instantaneous wall temperature is uniform and constant but the associated heat flux admits fluctuations [96, 29]. We reinforce that, these are idealized representations of real heat transfer phenomena and, in practical applications, it is rather the time-averaged quantities that are more likely to display a uniform behaviour [27]. For instance, in the DNS literature of turbulent heat transfer in channel and pipe configurations, a uniform time-averaged heat flux $\bar{q}_w$ is very frequently prescribed. This can be done by imposing the instantaneous wall temperature as free of

fluctuations and linearly increasing along z. In this way, the wall temperature can be regarded as locally isothermal, because of the vanishing fluctuations, yet, still displaying the linear increase characteristic of isoflux conditions [17]. In other words, the time-averaged wall heat flux $\bar{q}_w$ is uniform (space), while the instantaneous wall temperature T_w is constant (time). For this reason, this type of TBC has been commonly referred to as *Mixed-type* (*MBC*) [29].

In recent years, turbulent heat transfer in wall-bounded configurations has been widely investigated by numerical simulations. In the DNS framework for instance, thanks to the progressive development of super computers, the physics of forced convection in wall-bounded turbulent flow has been analysed in increasingly more demanding computational configurations, with most of the investigations being performed nonetheless for channel flow [60]. The first successful DNS involving heat transfer was performed by [24] for a turbulent channel flow at low Reynolds number $Re_\tau = 180$ (based in the half channel height) for different Prandtl numbers $Pr = 0.1, 0.7, 2.0$. The passive scalar was uniformly produced internally with cold isothermal walls, which allowed to treat the heat in the same way as the mean pressure gradient that drives the flow. It is considered as the first successful DNS with heat transfer for its good agreement with formulas by [97] as well as for its relevant observations concerning the turbulent Prandtl number, very important quantity for the development of RANS closure models. Later on, [27] investigated how the fluctuating temperature at the wall can be properly specified for near-wall heat flux models in channel configuration.

Through the budgets of temperature variance and turbulent heat fluxes, [98] investigated the effects of Reynolds ($Re_\tau = 180, 395$) and Prandtl numbers ($Pr = 0.025, 0.2, 0.71$) on the turbulent heat flux transport in channel flow configuration. Satake *et. al* [99] focused mostly on the effect of the friction Reynolds number when performing the first DNS of pipe flow with passive scalar transport for Re_τ ranging from 150 up to 1050 for $Pr = 0.71$ with MBC. Even for the highest Reynolds number $Re_\tau = 1050$, a pipe length of $15R$ was used, which may be too short to properly capture the very large structures in the flow, both thermal and hydrodynamic [100, 10]. [101, 25] performed DNS of turbulent flow with passive temperature transport in a flume for $Re_\tau = 171$ (based on the height of the flume) with $Pr = 1, 5, 4$ [101] and in a channel for $Re_\tau = 150$ with Pr ranging from 0.71 to 7 [25]. In both studies, the role of different TBCs has been addressed. Lower and higher-order statistics, as well as plots of the instantaneous velocity and temperature fields were compared for MBC and IF.

In his comprehensive work in 2005, [29] compared also the effect of different TBCs for pipe flow at low Reynolds number $Re = 5300$ with $Pr = 0.71$. Turbulence statistics up to fourth order, budgets of temperature fluctuations and snapshots of the instantaneous temperature fields have been assessed. It has been shown that the imposition of either MBC or IF affects the temperature statistics only within the conductive sublayer. Moreover, he showed that MBC acts as IT in the inner layer and as IF in the outer layer. The term *Mixed* (*MBC*) was then used for the first time to address this type of TBC.

Later, [100] focused his analysis on the effect of the Prandtl number on the turbulent heat transfer in a pipe flow at $Re_\tau = 186$. More specifically, this is the first DNS of pipe flow at various Prandtl numbers (ranging from 0.026 to 1). Also, by comparison with turbulent channel statistics, it has been found that the wall curvature in the pipe configuration slightly enhances the temperature fluctuations (in agreement with observation of [29]) but without a major impact on turbulent heat transfer. Then, [60] investigated the effect of the computational domain length on the turbulent heat transfer predictions

by means of DNS of pipe flow at $Re = 5000$ and $Pr = 0.025, 0.71, 2$. As a validation step for performing *Conjugate Heat Transfer* (*CHT*) in channel flow, [102] presented temperature statistics for MBC and IF at different (and slightly higher) Reynolds numbers $Re_\tau = 180, 395, 590$ for a very-low Prandtl number $Pr = 0.01$, characteristic of liquid sodium-steel systems.

Ultimately, [10] investigated the effect of different TBCs - namely IF, IT and MBC - for pipe flow at higher Reynolds numbers (ranging from 5300 to 37700) and two different Prandtl numbers $Pr = 0.025, 0.71$. These results represented an expansion of the findings of [29] to high Re and low Pr. Lower-order statistics have been analysed, as well as budgets of temperature fluctuations and power spectral densities. It has been shown that large thermal structures and thermal structures located right at the wall - which are characteristic of low Prandtl numbers - are only reproduced with IF. Furthermore, it has been shown that the suppression of temperature fluctuations at the wall - which is enforced with MBC and IT - leads to different near-wall behaviours of the turbulent heat fluxes. Hence, it is suggested that the appropriate TBC for local imposition should be chosen depending on the Prandtl number and on which statistics are to be evaluated.

The present chapter is dedicated to the development of a numerical strategy for the ideal local imposition of MBC and IF with Incompact3d/Xcompact3d. For this purpose, our IBM based on Lagrange polynomials reconstruction is further developed to impose as well the thermal boundary conditions. Special attention is given to IF as an original methodology based on IBM is developed for the imposition of Neumann boundary conditions. Additionally, for the non-body fitted grid used here, the imposition of a wall-normal heat flux while leaving free the wall-tangential one represents a real challenge. The results of validation provided in this chapter paves the way for the introduction of a novel technique to perform conjugate heat transfer (*CHT*) in pipe configuration, the subject of chapter 6.

This chapter is divided as follows. Firstly, basic concepts of heat transfer between a solid wall uniformly heated and a fluid are recalled. Then, the numerical methodology is presented while highlighting the non-dimensional forms used for the temperature field. Afterwards, the numerical strategy used to prescribe MBC is shortly described and major focus is given to the strategy and different techniques conceived to impose IF in the present numerical framework. Finally, the IF techniques are compared and the strongest one is selected, results of validation are subsequently presented for IF and MBC while highlighting the profitable accuracy/cost ratio of the present numerical strategy.

5.1 Ideal local imposition of a uniform heat flux

In this section we provide a brief discussion on the physics of heat transfer between an incompressible Newtonian fluid and a solid wall delivering a uniform heat flux q_w. The fluid properties are assumed constant and buoyancy effects are neglected, we consider therefore a passive thermal flow, governed by the advection-diffusion energy equation

$$\frac{\partial T}{\partial t} + u_j \frac{\partial T}{\partial x_j} = \alpha \frac{\partial^2 T}{\partial x_j \partial x_j} \quad , \tag{5.1}$$

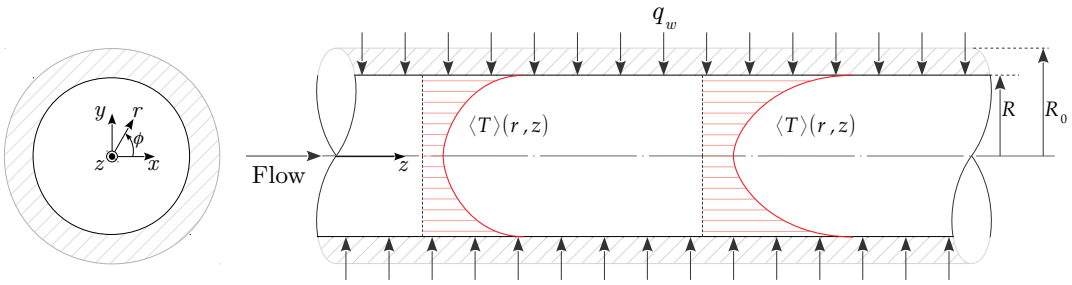

Figure 5.1: Schematic representation of the pipe flow geometry subjected to a uniform heat flux q_w imposed at the fluid-solid interface $r = R$.

where $T(r, \phi, z, t)$ is the temperature field and $\alpha = \lambda/\rho c_p$ is the thermal diffusivity of the fluid, with λ its thermal conductivity and c_p the specific heat at constant pressure. Both the TBCs considered here - namely isoflux (IF) and mixed-type (MBC) - correspond to the prescription of an uniform heat flux at the fluid-solid interface , the fundamental difference between them is the assumption made concerning the behaviour of the temperature at the wall T_w. For IF, T_w is left free and thus admits (spatial and temporal) fluctuations $T_w(\phi, z, t)$, whereas for MBC, the wall fluctuations are assumed to be zero $T_w(z)$.

In this section, we denote thermal quantities averaged in time and homogeneous ϕ direction by $\langle\cdot\rangle$,

$$\langle T\rangle(r,z), \quad \langle T_w\rangle(z), \quad T_b(z) \ . \tag{5.2}$$

We consider the flow in fully developed turbulent conditions, subjected to a uniform heat flux q_w imposed at the fluid-solid interface $r = R$, as illustrated in Figure 5.1.

The basic requirement for heat transfer to take place between the pipe wall and the fluid is the existence of a temperature gradient along the streamwise direction, which implies variations of the bulk temperature T_b and mean temperature profile $\langle T\rangle$ along the tube. This is illustrated in Figure 5.1 by the evolution of the mean profile $\langle T\rangle$ along the streamwise direction.

Let us consider now the cylindrical control volume $\pi R dz$ illustrated in Figure 5.2-left. A balance of energy provides,

$$\begin{aligned} dq_{\text{conv}} &= \dot{m} c_p \left[(T_b + dT_b) - T_b\right] \\ q_w (2\pi R) dz &= \rho c_p U_b (\pi R^2) dT_b \end{aligned}$$

$$\frac{dT_b}{dz} = \frac{2q_w}{\rho c_p U_b R} = cst \ . \tag{5.3}$$

That is, under uniform heat flux conditions, the bulk temperature increases linearly along z.

Newton's law of cooling states that,

$$q_w = h\left(\langle T_w\rangle - T_b\right) \ , \tag{5.4}$$

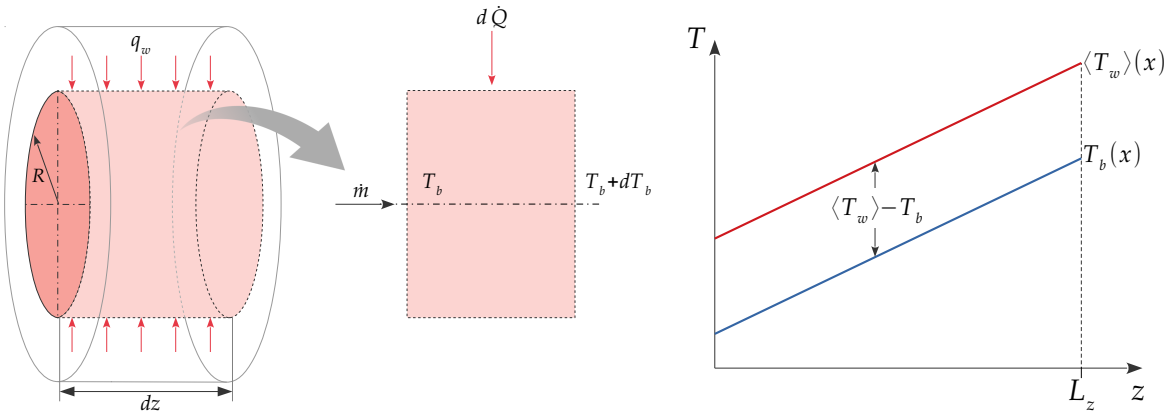

Figure 5.2: (Left) Cylindrical differential control volume under uniform heat flux. dq_{conv} is the infinitesimal amount of heat exchanged through the infinitesimal lateral area dA_L. (Right) Linear increase of the temperature quantities along the tube for uniform heat flux.

where the heat transfer coefficient h is constant and independent of z in fully developed conditions [17]. Hence,

$$\langle T_w\rangle - T_b = \frac{q_w}{h} = cst \ , \tag{5.5}$$

and furthermore, with eq.(5.3)

$$\frac{d\langle T_w\rangle}{dz} = \frac{dT_b}{dz} = \frac{2q_w}{\rho c_p U_b R} = cst \ . \tag{5.6}$$

That is, under uniform heating conditions, $\langle T_w\rangle$ follows the same linear increase as T_b with a uniform difference along the tube, expressed by eq.(5.5)

$$\langle T_w\rangle - T_b = cst \ ,$$

and illustrated in Figure 5.2-right.

Also, the no-slip condition implies that heat transfer is entirely due to conduction at the wall. Thus, from Fourier's law,

$$q_w = -\lambda \left.\frac{\partial T}{\partial n}\right|_w = \lambda \left.\frac{\partial T}{\partial r}\right|_{r=R} \ . \tag{5.7}$$

That is, the prescription of an uniform heat flux corresponds virtually to the imposition of the wall normal derivative

$$\left.\frac{\partial T}{\partial r}\right|_{r=R} = \frac{q_w}{\lambda} \tag{5.8}$$

as a Neumann boundary condition.

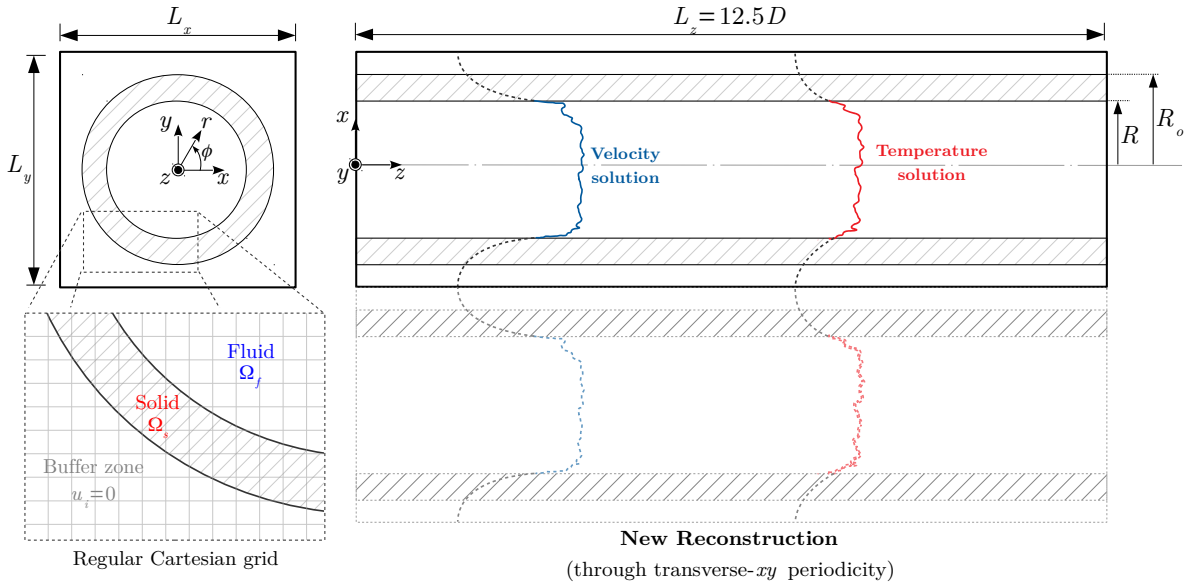

Figure 5.3: Schematic view of the computational configuration. A regular Cartesian mesh is used with the new reconstruction strategy performed through the periodicity of the transverse-xy directions. Physical solutions are represented by solid lines and reconstructed solutions by dashed lines. Reconstructions are performed with the same fifth-order polynomial functions.

5.2 Numerical Methodology

This section is dedicated to describing the numerical treatment of the temperature transport equation in Incompact3d /Xcompact3d. A schematic view of the computational configuration is presented in Figure 5.3. DNS of pipe flow including heat transfer is performed with Mixed-type (MBC) at low and moderately high Reynolds numbers $Re = 5300, 37700$ for two different Prandtl numbers $Pr = 0.71, 0.025$, characteristic of air and liquid metals respectively. As the implementation of the numerical technique for prescribing Neumann conditions required an extensive numerical development, results of validation with isoflux conditions (IF) are presented only at low Reynolds number $Re = 5300$, also for $Pr = 0.71, 0.025$. First and second-order temperature statistics are presented, as well as budgets of temperature fluctuations.

As for the DNS performed in chapters 3 and 4, a regular Cartesian grid is used. For the low Reynolds simulations $Re = 5300$, a mesh of $(n_x \times n_y \times n_z) = (256 \times 256 \times 640)$ nodes is used for the discretization of the computational domain of dimensions $(L_x, L_y, L_z) = (1.28D, 1.28D, 12.5D)$, corresponding to a mesh resolution $(\Delta x^+, \Delta y^+, \Delta z^+) = (1.81, 1.81, 7.07)$ in wall units. For $Re = 37700$, a mesh of $(n_x \times n_y \times n_z) = (768 \times 768 \times 1920)$ points is used for a slightly smaller domain

in the transverse directions $(L_x, L_y, L_z) = (1.12D, 1.12D, 12.5D)$, providing a marginal mesh resolution $(\Delta x^+, \Delta y^+, \Delta z^+) = (2.92, 2.92, 13.02)$. This adjustment of the computational domain enables us to prescribe periodic boundary conditions for the transverse-xy directions while ensuring a minimum number of nodes in the solid and buffer zones $r \geq R$ to ensure the success of the (new) reconstruction technique, described hereafter.

As discussed in section 5.1, because of the heat transfer at the wall, in fully developed conditions, the mean temperature profile is expected, by construction, to evolve along the streamwise-z direction. Nonetheless, periodic conditions are also prescribed in z for the temperature by introducing a corrected dimensionless temperature Θ capable of ensuring, for each TBC, statistical homogeneity by providing $\frac{\partial \langle \Theta \rangle}{\partial z} = 0$, see section 5.2.2.

The viscous filtering technique is used here with scheme $(1, 36)$ of [78][1], which is the counterpart of the ISVV DNS scheme (2.21, 2.33) for second derivatives. The association of the viscous filtering technique with a third-order Adams-Bashforth scheme for the time integration of the energy equation is described in details further below, in section 5.2.3. A small amount of numerical dissipation is used for regularisation $(\nu_0/\nu = 3)$, except for the lowest Prandtl number $Pr = 0.025$, for which the level of diffusivity $(Re\ Pr)^{-1}$ is already high enough and thus no extra artificial dissipation is necessary $(\nu_0/\nu = 0)$.

5.2.1 New reconstruction strategy

During the extensive phase of development of the technique to prescribe Neumann boundary conditions, a variation of the Lagrange reconstruction strategy was also implemented. In this updated version, a direct re-connection of the fluid zone through the periodicity of the transverse-xy directions is performed. The principle is illustrated in Figure 5.3.

In this scenario, all the N input values Φ used to define the $(N-1)^{th}$-order Lagrange polynomial function L, according to eq.(2.15)

$$L_{N-1}(x) = \sum_{j=1}^{N} \frac{\prod_{i \neq j i=1}^{N} (x - x_i)}{\prod_{i \neq j i=1}^{N} (x_j - x_i)} \Phi_j \ ,$$

come from the relevant fluid zone $r < R$ [2]. This way, we no longer reason in terms of solid and fluid zones, but rather of physical and reconstruction domains. Both the solid $(R \leq r \leq R_o)$ and buffer $(r > R_o)$ zones become the reconstruction domain for the physical domain $(r < R)$ in the present scenario. Thereby, the buffer zone no longer plays the role of intermediation for the reconstruction, being only necessary now to provide a sufficiently long section to ensure the continuity of the interpolation. Also, a small improvement in computational performance is obtained since only one (no longer two)

[1] The article is provided in chapter 4

[2] With the new reconstruction strategy, $N = 6$ points are still used and first fluid points are still skipped, consisting of a fifth-order Lagrange polynomial interpolation

reconstruction is necessary along each transverse grid row. Analysis in laminar regime revealed that the method is more accurate and robust to conserve first-derivatives across the interface and it has been therefore implemented for both velocity and temperature fields henceforth.

5.2.2 Governing equation and non-dimensional temperature

The non-dimensional temperature for each TBC is conveniently defined as a temperature difference ΔT, scaled by a reference temperature T_r

$$\Theta = \frac{\Delta T}{T_r} \ , \tag{5.9}$$

so that, the streamwise-z direction can be practically treated as statistically homogeneous[3]

$$\frac{\partial \langle \Theta \rangle}{\partial z^*} = 0 \ , \tag{5.10}$$

and thermally stationary with

$$\Theta_b = cst \ . \tag{5.11}$$

The replacement of the non-dimensional temperature (5.9) into the energy equation (5.1) (together with the other normalised quantities x_i^*, u_i^*, t^* defined in eqs.(2.8)) leads to the non-dimensional energy equation

$$\frac{\partial \Theta}{\partial t^*} + u_j^* \frac{\partial \Theta}{\partial x_j^*} = \frac{1}{Pe} \frac{\partial^2 \Theta}{\partial x_j^* \partial x_j^*} + f_\Theta \ , \tag{5.12}$$

where $Pe = RePr$ is the Péclet number and f_Θ is the source term arising from the nondimensionalization, responsible for sustaining stationary regime by ensuring the constant bulk temperature (5.11). This term is analogous to the mean pressure gradient forcing acting in the momentum equation which has been detailed in section 2.7. For a complete demonstration of the forcing term f_Θ, the reader is referred to [74]. Expressions for the non-dimensional temperature Θ are presented for each TBC hereafter.

Isoflux boundary conditions (IF)

IF here refers to the imposition of a constant (in time) and uniform (in space) heat flux $q_w = cst$ while admitting non-zero fluctuations at the wall $T_w(\phi, z, t)$. We may conveniently define the following non-dimensional temperature (as in [74]),

$$\Theta = -\frac{1}{Nu} \left(\frac{T - T_b}{\langle T_w \rangle - T_b} \right) \ , \tag{5.13}$$

[3]For the sake of clarity, we denote once again, only in this section, non-dimensional quantities with $(*)$.

for which the scaling reference temperature $T_r = Nu(\langle T_w \rangle - T_b)$ is a constant value, according to eq.(5.5). Furthermore, by using this form, the Nusselt number can be easily estimated from the averaged temperature at the wall,

$$\langle \Theta_w \rangle = \langle \Theta(T = T_w) \rangle \implies \langle \Theta_w \rangle = -\frac{1}{Nu} \ . \tag{5.14}$$

The statistical homogeneity condition (5.10), together with eq.(5.6) leads to the equality

$$\frac{\partial \langle T \rangle}{\partial z} = \frac{dT_b}{dz} = \frac{d\langle T_w \rangle}{dz} = \frac{2q_w}{\rho c_p U_b R} = cst \ , \tag{5.15}$$

implying that, with isoflux conditions, the local averaged temperature $\langle T \rangle$ also presents a linear increase along the tube. The thermal stationary condition (5.11) is ensured by keeping the constant bulk temperature

$$\Theta_b = \Theta(T = T_b) \implies \Theta_b = 0 \ . \tag{5.16}$$

This is done through the source term f_Θ in eq.(5.12), which for IF is given by (cf.[74])

$$f_\Theta = \frac{4u_z^*}{Pe} \left. \frac{\partial \Theta}{\partial n} \right|_w = -\frac{4u_z^*}{Pe} \left. \frac{\partial \Theta}{\partial r^*} \right|_{r^*=1/2} \ . \tag{5.17}$$

Concerning the imposition of the Neumann boundary condition (5.8), the (non-dimensional) wall-normal derivative is given by

$$\left. \frac{\partial \Theta}{\partial r^*} \right|_{r^*=1/2} = -\frac{D}{Nu(\langle T_w \rangle - T_b)} \left. \frac{\partial T}{\partial r} \right|_{r=R} \ , \tag{5.18}$$

which, by replacing eq.(5.8), becomes

$$\left. \frac{\partial \Theta}{\partial r^*} \right|_{r^*=1/2} = -\frac{q_w D}{Nu \, \lambda(\langle T_w \rangle - T_b)} \ . \tag{5.19}$$

From the definition of the Nusselt number in eq.(1.29), the Neumann boundary condition to be imposed is finally reduced to

$$\left. \frac{\partial \Theta}{\partial r^*} \right|_{r^*=1/2} = -1 \ , \tag{5.20}$$

which simplifies its numerical implementation. Additionally, the source term can be re-expressed as

$$f_\Theta = \frac{4}{Pe} u_z^* \ . \tag{5.21}$$

This term represents the mean axial advection [29] and, in the present work, we do not impose its exact value given by eq.(5.21), instead it is implemented as a correction step in the time advancement of the energy equation. Its numerical treatment is presented further below in section 5.2.3.

Note that in the present framework, the use of a Cartesian grid disconnected from the wall geometry does not allow the direct imposition of the wall-normal derivative (5.20). Indeed, the development of an IBM technique for the imposition of Neumann boundary conditions in Incompact3d/Xcompact3d has been a major focus of this thesis [79] (the article is provided in Appendix A).

Mixed-type boundary conditions (MBC)

For MBC, an uniform heat flux is also applied while assuming that the temperature fluctuations at the wall are null. The following non-dimensional form is used

$$\Theta = \frac{\langle T_w \rangle - T}{\langle T_w \rangle - T_b} \ , \tag{5.22}$$

for which the scaling temperature $T_r = \langle T_w \rangle - T_b$ is also uniform, according to eq.(5.5). This way, the temperature fluctuations at the wall

$$T'_w = T_w - \langle T_w \rangle \ , \tag{5.23}$$

can be purposely expressed as the numerator on the rhs of eq.(5.22) when considering the non-dimensional temperature at the wall

$$\Theta_w = \Theta(T = T_w) \implies \Theta_w = \frac{-T'_w}{\langle T_w \rangle - T_b} \ . \tag{5.24}$$

Hence, the assumption of zero fluctuations at the wall can be directly incorporated in the prescription of the boundary condition

$$\Theta_w = 0 \ , \tag{5.25}$$

which is imposed as a Dirichlet boundary condition (DBC).

Furthermore, the statistical homogeneity condition (5.10), together with the energy balance (5.3), leads to same linear increase of averaged quantities presented for IF (5.6)

$$\frac{\partial \langle T \rangle}{\partial z} = \frac{dT_b}{dz} = \frac{d\langle T_w \rangle}{dz} = \frac{2q_w}{\rho c_p U_b R} = cst \ .$$

The behaviour is analogous to isoflux conditions, yet, as temperature fluctuations are assumed to vanish at the wall through the imposition of the DBC (5.25), the wall can also be regarded as locally isothermal, hence the terminology *mixed* first introduced by [29] to address this type of local imposition. As pointed out by [60], this is one of the most common TBCs that occurs in many practical applications.

The thermal stationary condition (5.11) is ensured by keeping the constant bulk temperature

$$\Theta_b = \Theta(T = T_b) \implies \Theta_b = 1 \ , \tag{5.26}$$

which is done through the source term f_Θ, given by eq.(5.21) as for IF (cf.[74])

$$f_\Theta = -\frac{4u_z^*}{Pe} \left. \frac{\partial \Theta}{\partial r^*} \right|_{r^*=1/2} \ .$$

As for IF, this term represents the mean axial advection [29] and it is treated in the present work as a correction step in the time advancement of the energy equation. Its numerical treatment is presented further below.

Table 5.1: Summary of the non-dimensional forms used for each TBC and the related quantities of interest.

	$\boldsymbol{\Theta}$	$\boldsymbol{\Theta_b}$	$\left.\boldsymbol{\frac{\partial \Theta}{\partial r}}\right\vert_{\boldsymbol{w}}$	$\boldsymbol{f_\Theta}$	$\boldsymbol{\Theta^+}$
MBC	$\frac{\langle T_w \rangle - T}{\langle T_w \rangle - T_b}$	1	$-Nu$	$\frac{4Nu}{Pe} u_z$	$\frac{Re_\tau Pr}{Nu}\Theta$
IF	$-\frac{1}{Nu}\left(\frac{T - T_b}{\langle T_w \rangle - T_b}\right)$	0	-1	$\frac{4}{Pe} u_z$	$2Re_\tau Pr\left(\Theta + \frac{1}{Nu}\right)$

The wall-normal derivative is given by

$$\left.\frac{\partial \Theta}{\partial r^*}\right|_{r^*=1/2} = -Nu \ , \tag{5.27}$$

which allows us to reduce the expression of the source term to

$$f_\Theta = \frac{4Nu}{Pe} u_z^* \ . \tag{5.28}$$

from which the Nusselt number can be estimated.

Summary

A summary of the non-dimensional forms used for each TBC is provided in Table 5.1. The direct relationships, from [74], for a scaling in viscous units are also provided. Hereafter we drop the asterisk $(*)$ to denote non-dimensional quantities. For the sake of completeness, we provide once again the energy equation, as solved in the code

$$\frac{\partial \Theta}{\partial t} + u_j \frac{\partial \Theta}{\partial x_j} = \frac{1}{Pe} \frac{\partial^2 \Theta}{\partial x_j \partial x_j} + f_\Theta \ . \tag{5.29}$$

5.2.3 Time integration with viscous filtering

The time integration of the energy equation (5.29) is carried out once completed the time advancement of the velocity field. With the viscous filtering technique, the convective term is integrated with a

third-order Adams-Bashforth (AB3) scheme while representing the diffusion term by the application of the viscous filter operator on the computed solution every time step, as explained in chapter 4 [78].

Thus, the time advancement may be expressed in two steps as follows

$$\Theta^* = \Theta^n + \Delta t \sum_{j=0}^{p} a_j T_\Theta^j F^{n-j} \tag{5.30}$$

$$\Theta^{n+1} = T_\Theta \Theta^* + \Delta t f_\theta^{n+1} \tag{5.31}$$

where

$$F^n = u_j^{n+1} \frac{\partial \Theta^n}{\partial x_j}, \tag{5.32}$$

is the convection term computed at time level n, f_Θ is the source term that ensures thermal stationary regime and $p = 2$, $a_0 = 23/12$, $a_1 = -16/12$, $a_2 = 5/12$ for an AB3 scheme.

In step (5.30), the intermediate temperature Θ^* is calculated from the integration of the convective term with the AB3 scheme. The application of the discrete viscous filtering operator is represented by its transfer function T_Θ, according to eqs.(2, 27) in chapter 4 [78]. The viscous filter scheme (1, 36) in chapter 4 is used for the temperature field, the counterpart of the second-derivative scheme (2.21, 2.33) for DNS applications. Note that with an AB3 scheme, two applications of the viscous filter are required in step (5.30) for F^n and F^{n-1} respectively; a third and final application of the filter is performed in step (5.31), which ultimately provides Θ^{n+1}. As shown in chapter 4 [78], the time advancement performed in this way is free from any time splitting error, however, the requirement of three filter applications per time step rises the computational cost.

Alternatively, by accepting the introduction of a time splitting error, the time advancement may also be carried out with

$$\Theta^* = \Theta^n + \Delta t \sum_{j=0}^{p} a_j F^{n-j} \tag{5.33}$$

$$\Theta^{n+1} = T_\Theta \Theta^* + \Delta t f_\theta^{n+1} \tag{5.34}$$

which requires only one filter application in step (5.34), being therefore less costly. More precisely, in results presented with the present computational configuration in chapter 4 [78], we have showed that the use of scheme (5.30,5.31) with three viscous filter applications (VF^3) represented an extra cost of $+56\%$ with respect to one viscous filter application (VF^1) required by scheme (5.33,5.34). The drawback however is the time splitting error introduced with VF^1 resulting in a loss of time accuracy. Yet, it has been also shown in chapter 4 [78] that, in the context of multidimensional non-linear governing equations, the time splitting error of VF^1 can become insignificant, making questionable the practical interest of the extra cost related to the two additional filtering applications.

In any case, both approaches VF^1 and VF^3 are very cost-effective thanks to the spectacular relaxation

of the stability constraint related to diffusivity[4]. Furthermore, it should be stressed that the development of the viscous filtering technique has been crucially relevant for the present computational configuration. In results presented in [78] for instance (which are re-discussed later in this chapter), for the DNS at $Re = 5300$ and $Pr = 0.71$ with MBC, the use of VF^1 allowed us to save -83% of computational resources if compared to the explicit time integration of the viscous term with AB3. Likewise, very satisfactory -74% could still be obtained with VF^3. For the most advantageous case - with $Re = 5300$, $Pr = 0.025$ and VF^1 - remarkable 95% of computational resources could be spared. Both schemes VF^1 and VF^3 have been used to perform the DNS presented in this chapter.

Source term

The numerical treatment of the source term f_Θ is the same here as in [74]. As expressed by step (5.31) (or (5.34)), the forcing is performed every time step. This is done to ensure a thermally stationary regime by keeping constant the bulk temperature Θ_b. The application of the source term can be explicitly expressed as a correction step by splitting (5.31) in two steps as follows

$$\Theta^{**} = T_\Theta \Theta^* \tag{5.35}$$

$$\Theta^{n+1} = \Theta^{**} + \Delta t f_\Theta^{n+1} \ . \tag{5.36}$$

In order to express the correction step (5.36) in terms of the bulk temperature, we may multiply both sides of the equality by the streamwise velocity u_z^{n+1} and subsequently take the volumetric average

$$\frac{1}{U_b \Omega_f} \int_{\Omega_f} u_z^{n+1} \Theta^{n+1} d\Omega_f = \frac{1}{U_b \Omega_f} \int_{\Omega_f} u_z^{n+1} \left(\Theta^{**} + \Delta t f_\Theta^{n+1} \right) d\Omega_f \tag{5.37}$$

where Ω_f is the inner fluid volume of the pipe (defined in eq.(1.8)). By rearranging, we may express it as

$$\frac{\Delta t}{U_b \Omega_f} \int_{\Omega_f} u_z^{n+1} f_\Theta^{n+1} d\Omega_f = \frac{1}{U_b \Omega_f} \int_{\Omega_f} u_z^{n+1} \Theta^{n+1} d\Omega_f - \frac{1}{U_b \Omega_f} \int_{\Omega_f} u_z^{n+1} \Theta^{**} d\Omega_f \ . \tag{5.38}$$

The source term f_Θ for IF is given by eq.(5.21)

$$f_\Theta = \frac{4}{Pe} u_z \quad \text{for IF} \ ,$$

[4] In the present computational configuration, because the Prandtl numbers considered are always less than unity, the most restrictive condition related to the diffusivity comes from the diffusion term in the energy equation (5.29), so that it is more convenient to use the thermal diffusivity α to define the Fourier number instead of the viscosity ν. Also, in the context of a full explicit time integration of the energy equation with IBM, the diffusivity constraint can easily become more restrictive to ensure stability than the CFL condition. The reader is referred to 4 [78] for more details.

and, for MBC, it is given by eq.(5.28)

$$f_\Theta = \frac{4Nu}{Pe} u_z \quad \text{for MBC} \ .$$

Note that in both cases

$$\frac{f_\Theta}{u_z} = cst \ , \tag{5.39}$$

which allows us to re-express the lhs of eq.(5.38) as

$$\frac{\Delta t}{U_b \Omega_f} \int_{\Omega_f} u_z^{n+1} f_\Theta^{n+1} d\Omega_f \ = \ \frac{f_\Theta^{n+1}}{u_z^{n+1}} \frac{\Delta t}{U_b \Omega_f} \int_{\Omega_f} (u_z^{n+1})^2 d\Omega_f \ , \tag{5.40}$$

and eq.(5.38) then becomes

$$\Delta t \, \frac{f_\Theta^{n+1}}{u_z^{n+1}} = \frac{\frac{1}{U_b \Omega_f} \int_{\Omega_f} u_z^{n+1} \Theta^{n+1} d\Omega_f - \frac{1}{U_b \Omega_f} \int_{\Omega_f} u_z^{n+1} \Theta^{**} d\Omega_f}{\frac{1}{U_b \Omega_f} \int_{\Omega_f} (u_z^{n+1})^2 d\Omega_f} \ . \tag{5.41}$$

From the definition of the bulk temperature in eq.(1.25), we may write

$$\Theta_b^{n+1} = \frac{1}{U_b \Omega_f} \int_{\Omega_f} u_z^{n+1} \Theta^{n+1} d\Omega_f \ ,$$

which consists in fact of the target value to be held constant every time step. By replacing then Θ_b^{n+1} in eq.(5.41)

$$\Delta t \frac{f_\Theta^{n+1}}{u_z^{n+1}} = \frac{1}{\frac{1}{U_b \Omega_f} \int_{\Omega_f} (u_z^{n+1})^2 d\Omega_f} \left(\Theta_b^{n+1} - \frac{1}{U_b \Omega_f} \int_{\Omega_f} u_z^{n+1} \Theta^{**} d\Omega_f \right) , \tag{5.42}$$

which ultimately leads to the expression for the forcing term in eq.(5.36) as it is computed in the code

$$\Delta t f_\Theta^{n+1} = \frac{u_z^{n+1}}{\frac{1}{U_b \Omega_f} \int_{\Omega_f} (u_z^{n+1})^2 d\Omega_f} \left(\Theta_b^{n+1} - \frac{1}{U_b \Omega_f} \int_{\Omega_f} u_z^{n+1} \Theta^{**} d\Omega_f \right) , \tag{5.43}$$

where the constant value ensuring thermal stationary regime is, according to eq.(5.16),

$$\Theta_b^{n+1} = 0 \quad \text{for IF} \ ,$$

and, according to eq.(5.26),

$$\Theta_b^{n+1} = 1 \quad \text{for MBC} \ .$$

The intermediate bulk temperature

$$\Theta_b^{**} = \frac{1}{U_b \Omega_f} \int_{\Omega_f} u_z^{n+1} \Theta^{**} d\Omega_f \ , \tag{5.44}$$

as well as the integral in the denominator on the rhs of eq.(5.43) are computed with a simple rectangular method, just as for U_b.

In summary, in the correction step (5.36), the intermediate temperature Θ^{**} is adjusted every time step with the forcing term (5.43) in order to ensure thermal stationary regime by providing $\Theta_b^{n+1} = cst$.

In the present work, when MBC is prescribed, the Nusselt number is directly predicted at the time level n from the application of the source term since, according to eq.(5.28),

$$Nu = \frac{Pe}{4} \frac{f_\Theta}{u_z} \quad \text{for MBC} \ , \tag{5.45}$$

where the term f_Θ / u_z is computed every time step, on the fly, from (5.42).

5.3 Imposition of MBC - Dirichlet

The mixed-type boundary condition (MBC) is based on the assumption of vanishing temperature fluctuations at the wall through the prescription of eq.(5.25)

$$\Theta_w = 0 \ ,$$

which consists of imposing a constant and uniform value for the temperature field, i.e. a Dirichlet boundary condition. In the present computational configuration, its numerical implementation follows the same rationale of the no-slip condition, and thus, its incorporation in Incompact3d /Xcompact3d did not require any extra numerical development of the immersed boundary technique based on Lagrange polynomial reconstruction [74].

5.4 Imposition of IF - Neumann

The isoflux boundary condition (IF) consists of prescribing the constant and uniform wall-normal derivative given by eq.(5.20)

$$\left. \frac{\partial \Theta}{\partial r} \right|_w = -1 \ ,$$

which is imposed as a Neumann boundary condition (NBC). The technique developed here for that purpose is based on the strategy introduced by [103] in the framework of a turbulent jet impinging on a heated wall, and used later by [74, 91] to perform conjugate heat transfer simulation in plane channel configuration. Here, the method is extended to a pipe geometry as a prototype of *complex geometry*. More precisely, as we work with a Cartesian grid for the discretization of a cylindrical geometry, the imposition of the above wall-normal derivative must be decomposed into its Cartesian components. The numerical implementation of this technique is done here in a generic way - i.e., in terms of the local normal and tangential directions to the surface (local reference frame) - which enables a straightforward application of the method for more complex body geometries without requiring any extra-development.

5.4.1 Expression for the wall-normal flux in Cartesian coordinates

As re-illustrated in Figure 5.4, the Cartesian frame of reference used in the present computational configuration is placed on the axis of the pipe and follows the regular distribution given by eqs.(2.2-2.4), which are recovered here for the sake of completeness

$$\begin{aligned} x_i &= (i-1)\Delta x - L_x/2 \\ y_j &= (j-1)\Delta y - L_y/2 \\ z_k &= (k-1)\Delta z \ . \end{aligned}$$

Where $\Delta x = \Delta y$ and the indices i, j, k run in the transverse-xy and streamwise-z directions respectively. The Cartesian frame of reference relates to the one associated to the pipe geometry according to

$$\begin{aligned} r_{ij} &= \sqrt{x_i^2 + y_j^2} \\ \phi_{ij} &= \arctan\left(\frac{y_j}{x_i}\right) \\ z_k &= z_k \ , \end{aligned}$$

so that, as represented in Figure 5.4, the normal (pointing towards the fluid) and tangential (positive counterclockwise) vectors at any point in the fluid zone can be defined as

$$\vec{e_r} = -\cos\phi\ \vec{x} - \sin\phi\ \vec{y} \tag{5.46}$$

$$\vec{e_\phi} = -\sin\phi\ \vec{x} + \cos\phi\ \vec{y} \ . \tag{5.47}$$

with $\vec{x},\ \vec{y}$ the orthogonal vectors in the transverse-xy directions.

This way, the derivatives at the wall-normal and wall-tangential directions can be expressed in the

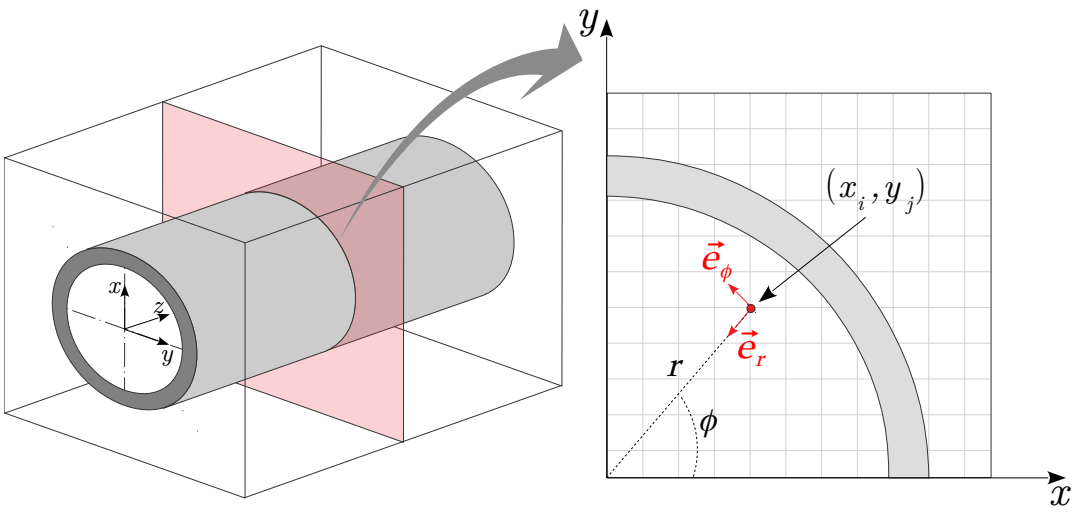

Figure 5.4: Positioning of the Cartesian frame of reference and relationship between the Cartesian and the local frames of reference with the normal and tangential vectors $(\vec{e_r}, \vec{e_\phi})$ represented.

Cartesian frame of reference, at any point in the fluid domain $r < R$, according to

$$\frac{\partial \Theta}{\partial r} = \vec{e_r} \cdot \vec{\nabla}\Theta \tag{5.48}$$

$$\frac{\partial \Theta}{\partial \phi} = \vec{e_\phi} \cdot \vec{\nabla}\Theta \ , \tag{5.49}$$

where $\vec{\nabla}$ is the nabla operator in Cartesian coordinates, leading to

$$\frac{\partial \Theta}{\partial r} = -\cos\phi \frac{\partial \Theta}{\partial x} - \sin\phi \frac{\partial \Theta}{\partial y} \tag{5.50}$$

$$\frac{\partial \Theta}{\partial \phi} = -\sin\phi \frac{\partial \Theta}{\partial x} + \cos\phi \frac{\partial \Theta}{\partial y} \ . \tag{5.51}$$

From the above equations, we can express the Cartesian derivatives as functions of the normal/tangential counterparts

$$\frac{\partial \Theta}{\partial x} = -\cos\phi \, \frac{\partial \Theta}{\partial r} - \sin\phi \, \frac{\partial \Theta}{\partial \phi} \tag{5.52}$$

$$\frac{\partial \Theta}{\partial y} = -\sin\phi \, \frac{\partial \Theta}{\partial r} + \cos\phi \, \frac{\partial \Theta}{\partial \phi} \ , \tag{5.53}$$

which, at the inner wall $r = R$ ("w"), correspond to the Neumann boundary conditions suitable to be implemented in a Cartesian grid

$$\left.\frac{\partial \Theta}{\partial x}\right|_w = -\cos\phi \left.\frac{\partial \Theta}{\partial r}\right|_w - \sin\phi \left.\frac{\partial \Theta}{\partial \phi}\right|_w \tag{5.54}$$

$$\left.\frac{\partial \Theta}{\partial y}\right|_w = -\sin\phi \left.\frac{\partial \Theta}{\partial r}\right|_w + \cos\phi \left.\frac{\partial \Theta}{\partial \phi}\right|_w \quad . \tag{5.55}$$

In the present approach however, the Cartesian wall-derivatives (5.54, 5.55) are indirectly prescribed, in the sense that the derivative values are not imposed but rather ensured through the adjustment of the temperature value at the wall Θ_w. More precisely, a value of Θ_w providing locally the expected derivative at the wall is estimated and then used to perform the Lagrange polynomial reconstruction. In this sense, it can be said that the Neumann boundary condition is virtually ensured with a Dirichlet boundary condition.

5.4.2 Formulation for a NBC ensured through a DBC

The strategy proposed here for the prescription of NBC can be understood as the two steps procedure schematised in Figure 5.5. Firstly, the target value Θ_w satisfying the NBC is defined and then subsequently used as an input to perform the Lagrange reconstruction. Moreover, due to the 2D MPI pencil decomposition of the code (see section 2.1), all operations must be carried out in 1D, which means that, the wall condition (5.54) must be satisfied during the x-direction reconstruction and (5.55) during the y-direction reconstruction.

Let us consider, for instance, the local procedure along a x-row, as illustrated in Figure 5.5. We may define a non-centred finite-difference scheme, such as

$$\left.\frac{\partial \Theta}{\partial x}\right|_w = a\Theta_w + b\Theta_{i+1} + c\Theta_{i+2} + d\Theta_{i+3} \quad , \tag{5.56}$$

so that, Θ_w providing the target derivative $\left.\frac{\partial \Theta}{\partial x}\right|_w$ can be estimated from

$$\Theta_w = \frac{\left.\frac{\partial \Theta}{\partial x}\right|_w - b\Theta_{i+1} - c\Theta_{i+2} - d\Theta_{i+3}}{a} \quad . \tag{5.57}$$

This wall value is subsequently used in *Step 2* of Figure 5.5 as if it was a DBC to perform the reconstruction. Thus, as it is proposed here, the prescription of NBC can be interpreted as an output of the Lagrange interpolation, as the expected wall derivative is going to be approximately recovered only afterwards, when first-derivatives will be computed with the sixth-order compact scheme used in Incompact3d/Xcompact3d.

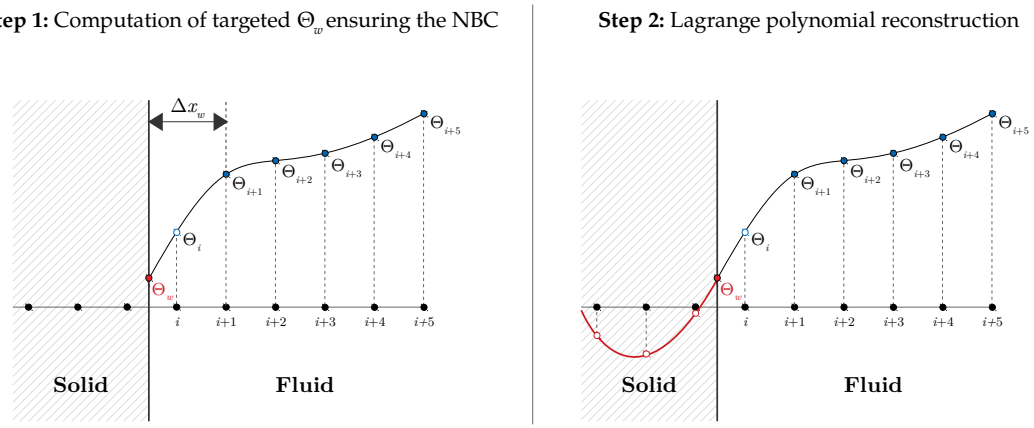

Figure 5.5: The imposition of NBC with the present IBM can be understood as a two steps procedure. Step 1: the target value Θ_w is defined to provide the desired derivative at the wall using a non-centred scheme with skipping of first fluid points. Step 2: The Lagrange reconstruction is performed using the estimated value.

A Taylor expansion from the fluid-solid interface $\square_w$ leads to the following system (the variable r_i is introduced here to simplify the expressions)

$$r_i = \frac{\Delta x_w + i\Delta x}{\Delta x_w} \tag{5.58}$$

$$\begin{aligned} a + b + c + d &= 0 \\ \Delta x_w(b + r_1 c + r_2 d) &= 1 \qquad (\Delta x) \\ \frac{\Delta x_w^2}{2}(b + r_1^2 c + r_2^2 d) &= 0 \qquad (\Delta x^2) \\ \frac{\Delta x_w^3}{6}(b + r_1^3 c + r_2^3 d) &= 0 \qquad (\Delta x^3) \end{aligned} \tag{5.59}$$

Note that the definition of the order of accuracy is not straightforward, since the grid resolution Δx_w in the vicinity of the body is geometry dependent. Therefore, the truncation errors expressed above are based on the supposition that $\Delta x_w \approx \Delta x$, so that $(\Delta x_w + i\Delta x)^n \approx \Delta x^n$.

The solution of system (5.59) for third-order accuracy leads to the following expressions for the finite-difference coefficients

$$a = -\frac{(r_1+1)r_2 + r_1}{r_1 r_2 \Delta x_w} \qquad b = \frac{r_1 r_2}{((r_1-1)r_2 - r_1 + 1)\Delta x_w}$$

$$c = -\frac{r_2}{((r_1^2 - r_1)r_2 - r_1^3 + r_1^2)\Delta x_w} \qquad d = \frac{r_1}{(r_2^3 + r_2^2(-r_1 - 1) + r_1 r_2)\Delta x_w} \tag{5.60}$$

Note that the above coefficients are geometry dependent because of Δx_w. In the code, they are evaluated before the time loop, from the local coordinates of the immersed boundary $r = R$. They are then defined as 3×3 matrices which are used later in the flow solver. One set of coefficients is needed for each of the transverse-xy directions. Because the coefficients are geometry dependent, the values computed for Θ_w with eq.(5.57) will be as well. This point explains how the present strategy is capable of reproducing temperature fluctuations at the wall (a characteristic feature of IF) although it is manly based on the imposition of Dirichlet conditions. Note also that the first fluid point (index i in Figure 5.5) is also skipped, consistently with the Lagrange reconstruction. In fact, if not skipped, Δx_w can assume very small values, leading to very large coefficients given the dependence in the denominators of eqs.(5.60), which, although algebraically correct, can cause several numerical instability of the flow solver.

Besides the indirect imposition of Neumann conditions with the present IBM, another obstacle still needs to be dealt with in the present scenario. The definition of the Cartesian wall derivatives

$$\left.\frac{\partial\Theta}{\partial x}\right|_w \quad \text{and} \quad \left.\frac{\partial\Theta}{\partial y}\right|_w \ ,$$

depends on the knowledge of their normal/tangential counterparts

$$\left.\frac{\partial\Theta}{\partial r}\right|_w \quad \text{and} \quad \left.\frac{\partial\Theta}{\partial \phi}\right|_w \ ,$$

according to eqs.(5.54, 5.55). The wall-normal component naturally corresponds to the isoflux boundary condition we wish to impose, given by eq.(5.20)

$$\left.\frac{\partial\Theta}{\partial r}\right|_w = -1 \ . \tag{5.61}$$

On the other hand, the expected behaviour of the wall-tangential component is unknown, at least in a turbulent context. With a body-conformal grid, which is the typical approach in cases like this, the imposition of the wall-normal derivative is straightforward and the tangential one can be simply left free. Here however, a prediction of the wall-tangential derivative is necessary in order to define the target value Θ_w. Different techniques essentially based on extrapolation with finite-difference schemes have been tested to deal with this hindrance, they are described in the next section.

5.4.3 Estimation of the wall-tangential derivative contribution

In order to estimate the contribution of the wall-tangential derivative, we propose here a method based on extrapolation. As a first step, the wall-tangential derivative is computed everywhere in the fluid domain $r < R$ from eq.(5.51)

$$\frac{\partial\Theta}{\partial\phi} = -\sin\phi\frac{\partial\Theta}{\partial x} + \cos\phi\frac{\partial\Theta}{\partial y} \ .$$

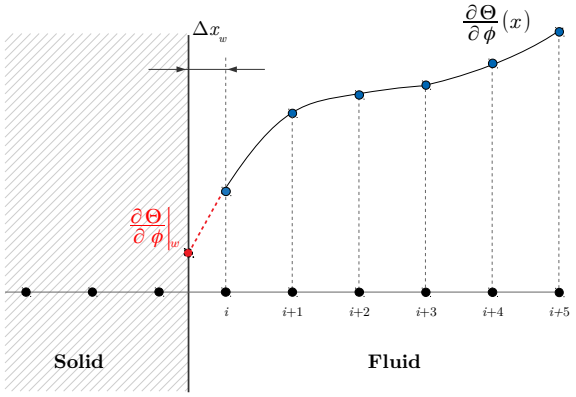

Figure 5.6: Schematic representation of the extrapolation stencil for the tangential heat flux along a x-row. The grid resolution at the vicinity of the body Δx_w is defined as the distance between the interface and the first fluid node.

Note that different numerical schemes may be used to compute the Cartesian derivatives on the rhs. Afterwards, as schematised in Figure 5.6, the wall contribution along a Cartesian grid row can be extrapolated from the fluid values with a finite-difference scheme[5] such as

$$\left.\frac{\partial \Theta}{\partial \phi}\right|_w = a_e \cdot \left.\frac{\partial \Theta}{\partial \phi}\right|_i + b_e \cdot \left.\frac{\partial \Theta}{\partial \phi}\right|_{i+1} + c_e \cdot \left.\frac{\partial \Theta}{\partial \phi}\right|_{i+2} + d_e \cdot \left.\frac{\partial \Theta}{\partial \phi}\right|_{i+3} . \tag{5.62}$$

The grid resolution at the vicinity of the body Δx_w is defined, this time, with respect to the first fluid node. By supposing once again $\Delta x_w \approx \Delta x$ to express the truncation error $(\Delta x_w + i\Delta x)^n \approx \Delta x^n$, a Taylor expansion from the wall leads to the following system (the variable r_i, already defined in eq.(5.58), is given here again to simplify the expressions)

$$r_i = \frac{\Delta x_w + i\Delta x}{\Delta x_w}$$

$$\begin{aligned} 1 &= a_e + b_e + c_e + d_e && (\Delta x) \\ 0 &= a_e + r_1 b_e + r_2 c_e + r_3 d_e && (\Delta x^2) \\ 0 &= a_e + r_1^2 b_e + r_2^2 c_e + r_3^2 d_e && (\Delta x^3) \\ 0 &= a_e + r_1^3 b_e + r_2^3 c_e + r_3^3 d_e && (\Delta x^4) \quad . \end{aligned} \tag{5.63}$$

Extrapolation schemes of different orders of accuracy may be used and first fluid nodes may or may not be skipped depending on the value of the coefficient a_e.

[5]Note that for the present non-body fitted grid, the location of the immersed boundaries do not coincide with mesh nodes

Table 5.2: Techniques evaluated for the estimation of the wall-tangential heat flux.

Method	**Scheme for first-derivatives in eq.(5.51)**	**Scheme for extrapolation with eq.(5.62)**
Method V1	centred Δx^2 + pre-reconstruction	Δx^1 skip
Method V2	conditional Δx^2	Δx^1 skip
Method V3	conditional Δx^2	Δx^1 no-skip
Method V4	conditional Δx^2	Δx^2 skip
Method V5	conditional Δx^2	Δx^2 no-skip
Method V6	conditional Δx^2	Δx^4 no-skip

In summary, the estimation of the wall-tangential derivative proposed here consists of: *i*) predicting $\frac{\partial \Theta}{\partial \phi}$ every time step, everywhere in the fluid domain, using eq.(5.51); *ii*) estimating its wall contribution $\left.\frac{\partial \Theta}{\partial \phi}\right|_w$. Numerically speaking, we seek to define an efficient strategy to: *i*) compute the Cartesian derivatives required in the calculation of $\frac{\partial \Theta}{\partial \phi}$ (i.e., the rhs of eq.(5.51)); *ii*) extrapolate the wall contribution $\left.\frac{\partial \Theta}{\partial \phi}\right|_w$ from the fluid values $\frac{\partial \Theta}{\partial \phi}$.

This procedure must be inserted in the structure of the code before the reconstruction step described in section 5.4.2, since $\left.\frac{\partial \Theta}{\partial \phi}\right|_w$ is needed to define the target Θ_w. Various combinations to meet requirements *i*) and *ii*) have been evaluated and, to avoid any confusion when presenting them further below, a description of the algorithm inserted in the structure of the code is provided in Figure 5.7, where the respective numerical schemes required for each step are listed. We will be constantly referring to this diagram in the next section.

Numerical techniques evaluated

Table 5.2 presents the different strategies tested for the imposition of NBC. They are listed in function of the numerical features employed to estimate the contribution of the wall-tangential derivative (steps I and II in the diagram of Figure 5.7).

Method V1 To compute the Cartesian derivatives, Method V1 employs the following explicit centred scheme of second-order accuracy

$$f'_i = \frac{f_{i+1} - f_{i-1}}{2\Delta x} \quad . \tag{5.64}$$

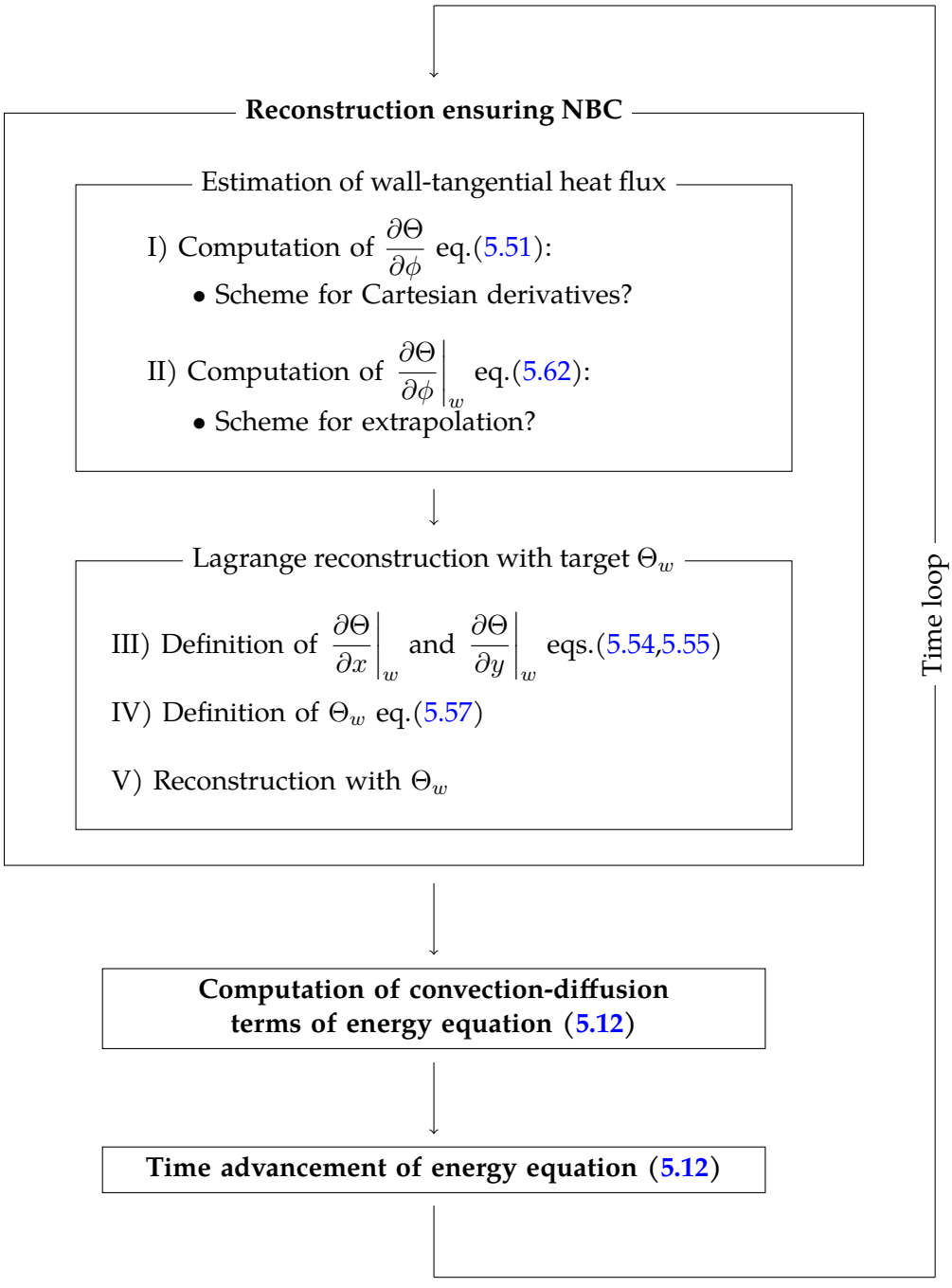

Figure 5.7: Description of the algorithm inserted in the time loop of the energy equation for the prescription of Neumann boundary conditions in the present work.

In the present IBM framework, the use of centred schemes is always combined with a reconstruction of the fluid solution into the solid zone to reduce contamination by spurious oscillations around the interface. Here, reconstructing prior to computing the Cartesian derivatives in step I should allows us to obtain a more consistent prediction of $\frac{\partial \Theta}{\partial \phi}$ at the fluid nodes close to solid-fluid interface. The prefix "pre-" is expressly introduced in Table 5.2 to make the distinction between the reconstruction carried out for this purpose (step I in the diagram of Figure 5.7) and the one which ultimately performs the imposition of the NBC (step V in the diagram). Note however that the pre-reconstruction needs to be carried out for a NBC, which means that a value of Θ_w is required. This makes the problem somehow closed-looped: an information of Θ_w is needed for the pre-reconstruction, whose ultimate goal is to improve the prediction of Θ_w for the reconstruction. To deal with this hindrance, Method V1 uses the estimated wall temperature from the previous time step to carry out the pre-reconstruction, i.e., Θ_w^{n-1}. Once Θ is (pre-)reconstructed, first-derivatives are computed and $\frac{\partial \Theta}{\partial \phi}^n$ is calculated. Next, along each transverse-xy grid row, $\left.\frac{\partial \Theta}{\partial \phi}\right|_w^n$ is extrapolated with scheme (5.62) and the following set of coefficients

$$b_e = 1 \quad a_e = c_e = d_e = 0 \ , \tag{5.65}$$

which consists of a first-order extrapolation with skipping of first fluid nodes (by setting $a_e = 0$).

Methods V2 and V3 To avoid the need for a pre-reconstruction (and the related dependence on information from the previous time step), the following second-order scheme has been implemented for the computation of first-derivatives in step I of the diagram

$$\begin{aligned} f_i' = (1-\varepsilon_i)\Big[& \varepsilon_{i-1}(1-\varepsilon_{i+2})(1-\varepsilon_{i+1})\frac{-3f_i + 4f_{i+1} - f_{i+2}}{2\Delta x} \\ & + \varepsilon_{i+2}\varepsilon_{i-1}(1-\varepsilon_{i+1})\frac{f_{i+1} - f_i}{\Delta x} \\ & + \varepsilon_{i+1}(1-\varepsilon_{i-2})(1-\varepsilon_{i-1})\frac{3f_i - 4f_{i-1} + f_{i-2}}{2\Delta x} \\ & + \varepsilon_{i-2}\varepsilon_{i+1}(1-\varepsilon_{i-1})\frac{f_i - f_{i-1}}{\Delta x} \\ & + (1-\varepsilon_{i+1})(1-\varepsilon_{i-1})\frac{f_{i+1} - f_{i-1}}{2\Delta x}\Big] \ . \end{aligned} \tag{5.66}$$

We recall that ε is the scalar that makes the distinction between solid and fluid zones in the computational domain as defined in eq.(2.17)

$$\varepsilon(r) = \begin{cases} 1, & \text{if } R \leq r \leq R_o \\ 0, & \text{otherwise} \end{cases} \ .$$

As the goal of step I is to provide a prediction of $\frac{\partial \Theta}{\partial \phi}$ only in the fluid domain $r < R$, scheme (5.66) can be understood as a second-order conditional scheme which employs centred difference at fluid

nodes away from the interface and switches to non-centred difference close to the interface, so that the stencil may avoid nodes placed in the solid zone and therefore prevent contamination by interfacial discontinuities. Concerning the extrapolation of $\left.\frac{\partial\Theta}{\partial\phi}\right|_w$, both methods use first-order approximations. First fluid nodes are skipped with Method V2 (scheme (5.62, 5.65) as for Method V1), whereas for Method V3, first fluid nodes are not skipped by employing the following set of coefficients

$$a_e = 1 \quad b_e = c_e = d_e = 0 \ . \tag{5.67}$$

Methods V4 and V5 The conditional scheme (5.66) is kept for the first-derivatives in step I while second-order extrapolation schemes are now tested for step II. With Method V4, first fluid nodes are skipped. The solution of system (5.63) for second-order accuracy with $a_e = d_e = 0$ leads to the following set of coefficients

$$b_e = \frac{r_2}{r_2 - r_1} \qquad c_e = -\frac{r_1}{r_2 - r_1} \qquad a_e = d_e = 0 \ . \tag{5.68}$$

With Method V5, first fluid nodes are not skipped, the solution of system (5.63) for second-order accuracy with $c_e = d_e = 0$ leads to the following set of coefficients

$$a_e = \frac{r_1}{r_1 - 1} \qquad b_e = -\frac{1}{r1 - 1} \qquad c_e = d_e = 0 \ . \tag{5.69}$$

Method V6 By conserving the second-order conditional scheme for first-derivatives, a fourth-order extrapolation is tested for $\left.\frac{\partial\Theta}{\partial\phi}\right|_w$. First fluid nodes are not skipped and thus the solution of system (5.63) for fourth-order accuracy leads to

$$\begin{aligned}
a_e &= \frac{r_1 r_2 r_3}{[(r_1-1)r_2 - r_1 + 1]r_3 + (1-r_1)r_2 + r_1 - 1} \\
b_e &= -\frac{r_2 r_3}{[(r_1-1)r_2 - r_1^2 + r_1]r_3 + (1-r_1)r_1 r_2 + r_1^2(r_1-1)} \\
c_e &= \frac{r_1 r_3}{[r_2^2 - (r_1+1)r_2 + r_1]r_3 - r_2^3 + (r_1+1)r_2^2 - r_1 r_2} \\
d_e &= -\frac{r_1 r_2}{r_3^3 - (r_1+r_2+1)r_3^2 + [(r_1+1)r_2 + r_1]r_3 - r_1 r_2} \ .
\end{aligned} \tag{5.70}$$

Just as for the for the coefficients (a, b, c, d) given by eqs.(5.60), the sets of coefficients (5.68 - 5.70) are geometry dependent because of the dependence on Δx_w, implicit in r_i. In the code, they are initialized together with (a, b, c, d) as 3×3 matrices before the time loop. For the extrapolation coefficients however, Δx_w does not explicitly arise in the denominator, $\Delta x_w \to 0$ does not lead to critical values of (a_e, b_e, c_e, d_e), reason why first fluid nodes may not be skipped.

5.5 Results

In this section, DNS results of validation are presented for Mixed-type (MBC) and Isoflux (IF) boundary conditions. In a first instance, the performance of the different methods conceived for IF is compared and the finest one is selected. Then, basic temperature statistics are presented together with the budget of temperature variance for both IF and MBC. The advantageous features of the present numerical approach are also discussed with the MBC results. Finally, the particularities of each TBC are highlighted through a direct comparison between IF and MBC results.

5.5.1 Validation IF

This section is dedicated to the evaluation of the different techniques conceived and described in section 5.4.3 for the prescription of Neumann boundary conditions with the present Immersed Boundary Method. Then, first and second-order one-point statistics, as well as the budgets of the temperature variance are presented and compared to accurate reference results.

Comparison of IF techniques

As previously mentioned, the expected behaviour of $\dfrac{\partial\Theta}{\partial\phi}$ and its wall extrapolation $\left.\dfrac{\partial\Theta}{\partial\phi}\right|_w$ are unknown in a turbulent framework. Nonetheless, from eq.(5.51)

$$\frac{\partial\Theta}{\partial\phi} = -\sin\phi\frac{\partial\Theta}{\partial x} + \cos\phi\frac{\partial\Theta}{\partial y} \ ,$$

one sees that an accurate prediction of $\dfrac{\partial\Theta}{\partial\phi}$ is intrinsically related to the correct computation of the Cartesian derivatives $\dfrac{\partial\Theta}{\partial x}$ and $\dfrac{\partial\Theta}{\partial y}$. These same derivatives are also found on the rhs of eq.(5.50) which gives the expression for the wall-normal derivative in the Cartesian frame of reference

$$\frac{\partial\Theta}{\partial r} = -\cos\phi\frac{\partial\Theta}{\partial x} - \sin\phi\frac{\partial\Theta}{\partial y} \ ,$$

for which, according to eq.(5.61), $\left|\dfrac{\partial\Theta}{\partial r}\right| \to 1$ is expected as $r/R \to 1$.

Here, therefore, we may define a quantity

$$q_r = \frac{\partial\Theta}{\partial r} \implies q_r = -\cos\phi\frac{\partial\Theta}{\partial x} - \sin\phi\frac{\partial\Theta}{\partial y} \ ,$$

to judge the suitability of the numerical scheme used for the computation of the first-derivatives and also the effectiveness of the pre-reconstruction. However, it is important to stress that, in this analysis, the quantity q_r is assessed as an output, with the one and only purpose of comparing the different techniques. In addition, to judge the quality of the extrapolation techniques, the asymptotic behaviour of the temperature fluctuations $\langle \Theta' \Theta' \rangle$ will be assessed.

All tests have been performed at low Reynolds number $Re = 5300$ ($Re_\tau \approx 181$) with $Pr = 0.71$, representative of air, in a computational domain $(L_x \times L_y \times L_z) = (1.28D \times 1.28D \times 12.5D)$ with $(n_x \times n_y \times n_z) = (256 \times 256 \times 640)$ nodes, corresponding to a mesh resolution of $\Delta x^+ = \Delta y^+ = 1.81$, $\Delta z^+ = 7.07$ in wall units. The viscous filtering technique is combined with a third-order Adams-Bashforth scheme for the time integration of both momentum and energy equations. The one-filtering scheme (5.33, 5.34) described in section 5.2.3 is used here. The resulting relaxation of the stability constraint related to diffusivity allows us to employ a time step $6\times$ bigger if compared to the case of a full-explicit integration in Incompact3d /Xcompact3d (see section 7.2 in chapter 4 [78] for more details). The laminar temperature solution for IF, given by eq.(2.14)

$$\Theta(r) = 2\left(\frac{3}{16} + r^4 - r^2\right) - \frac{1}{Nu} \quad ,$$

is initialized with a fully developed turbulent velocity field from a previous simulation. The transition to turbulence is carried out using Method V6, once reached the fully developed state, new simulations are launched for all the Methods in Table 5.2 and a new, still shorter, transition is required for each one of them. Once completed the transition, the quantity q_r is gathered on the fly. Axial and time averages are carried out during the simulation whereas the azimuthal one is performed during post-processing with the projection technique described in section 2.8. For all the methods, temperature data is averaged over the same physical time window $T_{stat} = 300D/U_b$, being physically transported by the same velocity field. The methods are then compared in terms of the mean quantities $\langle q_r \rangle$ and $\langle q_r \rangle_{z,t}$, where the former consists of data averaged in both homogeneous directions and time (z, ϕ, t), whereas for the latter, data is averaged in (z, t) only - i.e., it is not projected in ϕ - being therefore presented as a cloud of raw data (see discussion in section 2.8). The analysis of the raw data here allows us to assess the performance of the Methods in terms of statistical convergence while taking into account the relative positioning of the Cartesian mesh nodes (x_i, y_j) with respect to the wall.

To confront the two techniques considered for the computation of the Cartesian derivatives - namely the centred scheme (5.64) and the conditional scheme (5.66) - Figure 5.8 compares $\langle q_r \rangle$ and $\langle q_r \rangle_{z,t}$ obtained with Methods V1 and V2. As both methods use extrapolation of first-order with skip, this assessment allows us to plainly compare the first-derivative schemes while putting in evidence the effect of the pre-reconstruction with Θ_w^{n-1} used for Method V1. As a matter of fact, with both methods, the expected behaviour $q_r \to 1$ as $(R - r)^+ \to 0$ is recovered for both the projected profile $\langle q_r \rangle$ and non-projected data cloud $\langle q_r \rangle_{z,t}$. Furthermore, although performed with data from the previous time step, the pre-reconstruction seems to successfully smooth down the discontinuity at the interface, since no abnormal behaviour of the non-projected data cloud V1 is observed in the near-wall region. With Method V2, the quantity q_r presents a similar behaviour with a slight overestimation for the closest nodes to the interface. This is due in fact to the switch from centred to non-centred difference at the edges of the fluid domain, accomplished with formulation (5.66). Despite the slight predominance of Method V1, Method V2 is more favourable and robust as it does not require a pre-reconstruction,

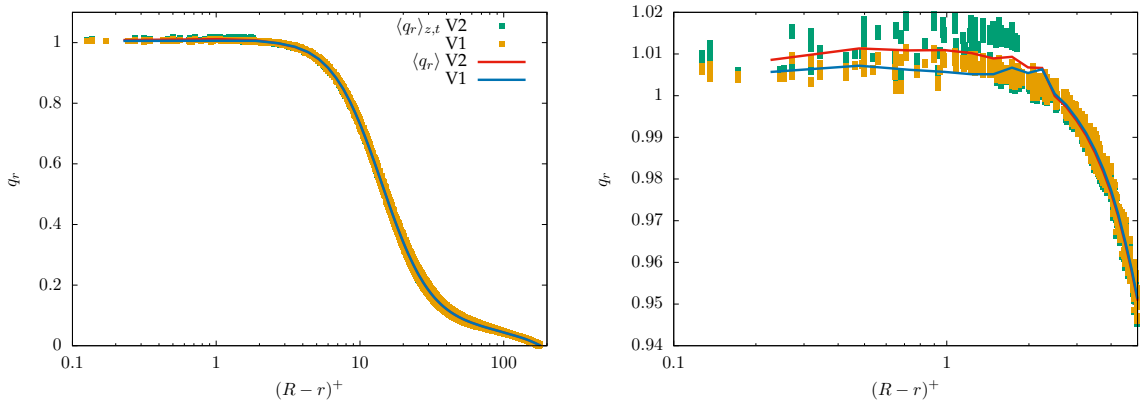

Figure 5.8: Comparison of the quantity $\langle q_r \rangle$ with Methods V1 and V2. A zoomed view of the near wall region is also provided (right). Time average carried out over a time window $T_{stat} = 300D/U_b$.

which suppresses the dependence on data from the previous time step and it is, therefore, retained as a more suitable solution.

To evaluate the different extrapolation techniques, the conditional scheme (5.66) is retained for the derivatives computation and Methods V2 through V6 are now assessed in function of the asymptotic behaviour of the temperature fluctuations. The data is scaled in wall units according to Table 5.1 and, as before, both the projected profile $\langle \Theta'\Theta' \rangle^+$ and non-projected data cloud $\langle \Theta'\Theta' \rangle^+_{z,t}$ are compared in Figures 5.9 and 5.10. More specifically, Figure 5.9-left confronts Methods V2 and V3 as both employs first-order extrapolation and Figure 5.9-right confronts Methods V4 and V5 as both employs second-order extrapolation. Such comparisons allow us to plainly assess the effect of the skipping of first fluid points when extrapolating. Subsequently, in Figure 5.10-left, Methods V3 and V5 are re-plotted in order to confront first and second order extrapolations. Then, in Figure 5.10-right, the best technique from the previous comparisons (namely Method V3) is ultimately compared to Method V6, which employs a higher-order extrapolation without skip. The accurate DNS results of [10] are also plotted for reference.

As a first remark, although here Neumann conditions are indirectly imposed with Dirichlet conditions, results in Figures 5.9 and 5.10 show that the present strategy is consistent as non-zero temperature fluctuations at the wall (characteristic of IF) are well reproduced with all the techniques. Furthermore, the Nusselt number prediction, calculated and averaged on the fly from Θ_w according to eq.(5.14)

$$Nu = -\frac{1}{\langle \Theta_w \rangle} \quad ,$$

is predicted within 1% error for all the techniques, as reported in Table 5.3.

Results presented in Figure 5.9 show that, for both first and second-order extrapolations, better results are obtained without skip of first fluid points, that is, with Method V3 in Figure 5.9-left and

Table 5.3: Nusselt number prediction from the different IF techniques evaluated at $Re = 5300$ and $Pr = 0.71$.

Method	**Nu**
Reference [10]	18.5
Method V2	18.27
Method V3	18.33
Method V4	18.33
Method V5	18.32
Method V6	18.23

Method V5 in Figure 5.9-right. In fact, when first fluid nodes are skipped, an oscillatory behaviour is observed in the data cloud $\langle\Theta'\Theta'\rangle^+_{z,t}$ which may be responsible for the apparent slower statistical convergence as well. These same patterns have been also observed for the mean temperature profile $\langle\Theta\rangle^+$ and streamwise heat flux $\langle u'_z\Theta'\rangle^+$, not shown here for conciseness.

Next, Methods V3 and V5 are compared in Figure 5.10-left. Both projected and non-projected data are nearly superimposed, yet, the data cloud V3 displays slightly higher values with respect to V5 across the near-wall region, resulting in a projected profile $\langle\Theta'\Theta'\rangle^+$ closer to the reference one. This suggests that a slightly quicker statistical convergence is achieved with Method V3. The previous assumption could be verified with the mean temperature profile $\langle\Theta\rangle^+$ (not shown), for which an almost perfect agreement with reference at the core of the geometry $(R-r)^+ \rightarrow Re_\tau$ confirmed a quicker statistical convergence.

Finally, in Figure 5.10-right, the comparison between Methods V3 and V6 - which employ first and fourth-order extrapolations without skip respectively - confirms the predominance of Method V3. Once again, oscillations are observed for the non-projected data cloud V6 as well as a slower statistical convergence. In fact, these high oscillations disturb the azimuthal projection across the conductive sublayer, the visual effect on the projected profile is an apparent misrepresentation of the zero first-derivative of temperature fluctuations at the wall, which is a characteristic feature of isoflux conditions [27, 29]. The use of higher-order extrapolation in the present context seems to go against the efficacy of the strategy. Moreover, the robustness of the technique - which had already displayed solid results with the second-order conditional scheme (5.66) for the computation of first-derivatives - seems to be reinforced now with a simple first-order extrapolation without skip for $\left.\frac{\partial\Theta}{\partial\phi}\right|_w$. Conclusively, Method V3 is retained as the most suitable technique to model isoflux conditions in the present numerical framework.

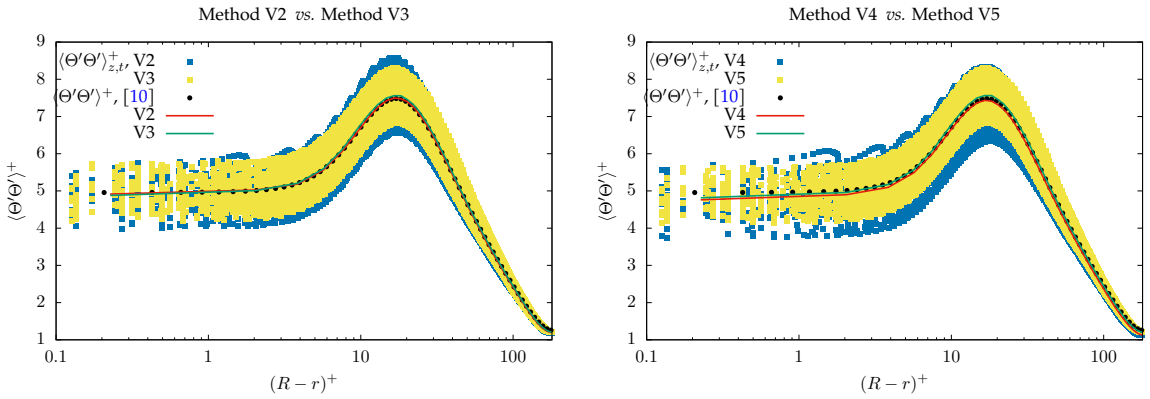

Figure 5.9: Comparison of the temperature variance between (left) Methods V2 and V3 (first-order extrapolation); (right) Methods V4 and V5 (second-order extrapolation). Assessment of the effect of skipping first fluid points when extrapolating $\left.\dfrac{\partial\Theta}{\partial\phi}\right|_w$. Time average carried out over a time window $T_{stat} = 300D/U_b$.

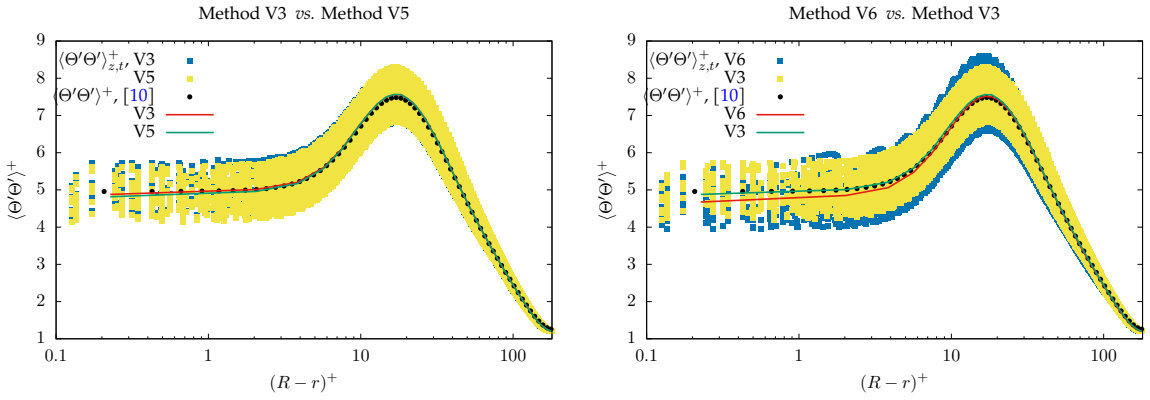

Figure 5.10: Comparison of the temperature variance between (left) Methods V3 and V5; (right) Methods V6 and V3. Evaluation of the effect of different orders of accuracy when extrapolating $q_\phi|_w$. Time average carried out over a time window $T_{stat} = 300D/U_b$.

IF at low Reynolds number

Now, a new simulation with $Re = 5300$ and $Pr = 0.71$ is relaunched from the last realization with Method V3 in order to obtain turbulence statistics over an extended time window $T_{stat} = 1740D/U_b$. The same initial condition are also used to launch a new simulation with $Pr = 0.025$, for which turbulence statistics are only gathered once completed the transition of the thermal field. Such a low Prandtl number is characteristic of liquid metals which are generally used in advanced cooling devices such as solar power plants [10]. The same computational configuration is kept for this low Prandtl case. For the configurations considered here, accurate DNS results of [10] are used as reference.

For $Pr = 0.71$, the Nusselt number is correctly predicted with $Nu = 18.22$, consisting of a -1.5% error with respect to its reference value $Nu = 18.50$. Likewise, for $Pr = 0.025$, $Nu = 6.45$ is obtained similarly to its reference counterpart $Nu = 6.46$. In Figure 5.11, one-point temperature statistics are presented, scaled in viscous units, for both Prandtl numbers. A great agreement with reference results is observed for the mean temperature profiles $\langle\Theta\rangle^+$ as well as for the temperature variance $\langle\Theta'\Theta'\rangle^+$ and streamwise heat flux $\langle u_z'\Theta'\rangle^+$. The slight over-estimation of the peak of temperature fluctuation is within the statistical convergence uncertainty. Moreover, for both Pr, not only the non-zero value of the temperature fluctuations at the wall is correctly estimated but also the plateau effect across the conductive sublayer is well reproduced (zero gradient at the wall), which are essential features of isoflux conditions [29, 27].

The comparison of the mean temperature profiles in Figure 5.11-top shows that with decreasing Prandtl number, the conductive sublayer spreads from the wall towards the core region [100]. Moreover, for the low Prandtl case, neither buffer nor logarithmic layers can be distinguished (at least not for the low Reynolds number considered here), and hence the temperature profile displays a laminar-like aspect, which explains also the proximity of the Nusselt number prediction $Nu = 6.46$ from the analytical laminar solution $Nu = 4.36$. These observations are in agreement with results of [10].

As shown in Figure 5.11-centre, with decreasing Pr, temperature fluctuations are significantly damped by molecular diffusion and the peak moves towards the core of the pipe, exposing the wider conductive sublayer throughout which temperature fluctuations are approximately constant [101, 29, 10]. Furthermore, for both Prandtl cases, the value of $\langle\Theta'\Theta'\rangle^+$ at the wall accounts for $\approx 70\%$ of the peak value, reason why this type of TBC is primarily recommended to model applications where temperature fluctuations at the wall are not negligible, such as unsteady heat conduction and solar plants for instance [27, 10].

As shown in Figure 5.11-bottom, the peak value of the streamwise turbulent heat flux $\langle u_z'\Theta'\rangle^+$ increases with increasing Pr and shifts towards the wall, with for instance $(R-r)^+ \approx 19$ for $Pr = 0.025$ and $(R-r)^+ \approx 16$ for $Pr = 0.71$. In fact, the peak is pushed towards the wall by the conductive sublayer, which becomes thinner with increasing Pr [100]. Besides, the peak location is always found between the peak of streamwise velocity fluctuations $\langle u_z'u_z'\rangle^+$ located at $(R-r)^+ \approx 14$, and the peak of temperature fluctuations $\langle\Theta'\Theta'\rangle^+$, located at $(R-r)^+ \approx 60$ for $Pr = 0.025$ and at $(R-r)^+ \approx 17$ for $Pr = 0.71$, this is in agreement with results of [100].

To further explore the different mechanisms involved in the Prandtl numbers considered, the bud-

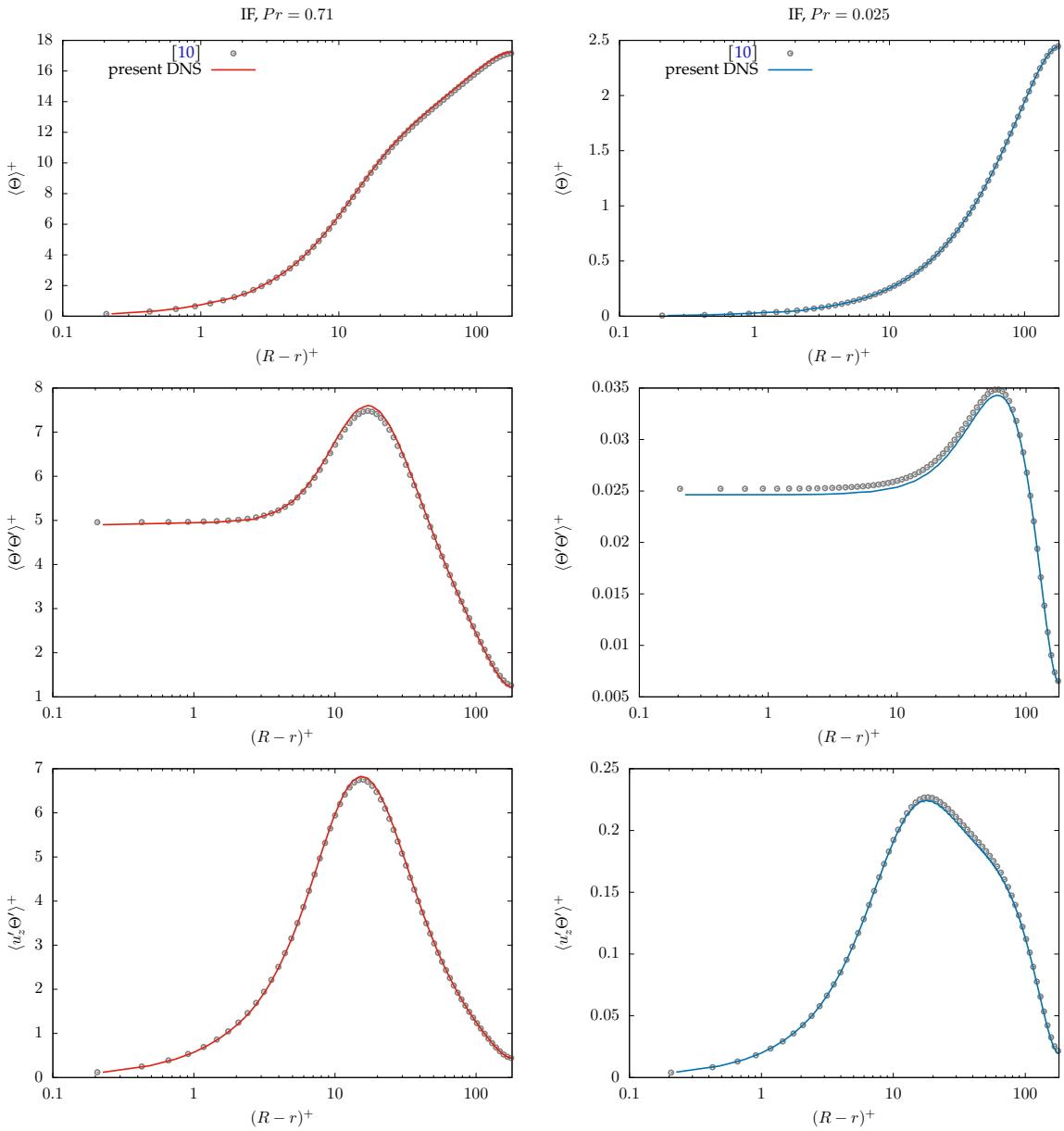

Figure 5.11: First and second-order temperature statistics with IF at $Re = 5300$ with (left) $Pr = 0.71$ and (right) $Pr = 0.025$. (Top) Mean-temperature profile, (centre) temperature variance and (bottom) streamwise heat flux. Symbols are reference results of [10]

gets of the temperature fluctuations are also assessed. The transport equation of the temperature variance, with $k_\theta = \frac{1}{2}\langle\Theta'\Theta'\rangle$, is given by [10]

$$\frac{\bar{D}k_\theta}{\bar{D}t} = P_{k_\theta} - \epsilon_{k_\theta} + MD_{k_\theta} + TD_{k_\theta} + S_{k_\theta} \quad , \tag{5.71}$$

where the individual terms are: production P_{k_θ}, dissipation ϵ_{k_θ}, molecular diffusion MD_{k_θ} and turbulent diffusion TD_{k_θ}. They are defined as (cf.[10])

$$P_{k_\theta} = -\langle u_i\Theta'\rangle\frac{\partial\langle\Theta\rangle}{\partial x_i} \tag{5.72}$$

$$\epsilon_{k_\theta} = -\alpha\left\langle\frac{\partial\Theta'}{\partial x_i}\frac{\partial\Theta'}{\partial x_i}\right\rangle \tag{5.73}$$

$$MD_{k_\theta} = \frac{\alpha}{2}\frac{\partial^2\langle\Theta'\Theta'\rangle}{\partial x_i\partial x_i} \tag{5.74}$$

$$TD_{k_\theta} = -\frac{1}{2}\frac{\partial\langle u_i\Theta'\Theta'\rangle}{\partial x_i} \tag{5.75}$$

and the source term depends on the TBC, which for IF and MBC

$$S_{k_\theta} = 4\frac{\langle u_z\Theta'\rangle}{D} \quad . \tag{5.76}$$

The terms are scaled in viscous units using $u_\tau^2\Theta_\tau^2/\nu$, where the friction temperature is

$$\Theta_\tau = \frac{1}{2Re_\tau Pr} \quad \text{for IF,} \tag{5.77}$$

$$\Theta_\tau = \frac{Nu}{2Re_\tau Pr} \quad \text{for MBC.} \tag{5.78}$$

The normalized budget terms are presented in Figure 5.12 for both Prandtl numbers considered (the source term is masked for clearness). Results from [10] are also plotted for reference. The overall agreement is satisfactory with the balance of terms being well reproduced. For $Pr = 0.71$, the peak of production $P_{k_\theta}^+$ occurs at $(R-r)^+ \approx 15$, whereas for $Pr = 0.025$, the peak spreads over a larger zone, expanding itself towards the core of the pipe with a maximum vale occurring at $(R-r)^+ \approx 50$, reason why a displacement of the peak of $\langle\Theta'\Theta'\rangle^+$ is observed in Figure 5.12 for the low Pr case.

At the wall, MD_{k_θ} balances ϵ_{k_θ}, revealing that the temperature fluctuations are transported to the wall only by diffusion - since the turbulent transport term TD_{k_θ} vanishes because of the no-slip condition - and then are dissipated by molecular dissipation. The turbulent transport term TD_{k_θ} displays two peaks, a positive one closer to the wall, and a negative one at the production peak location. As pointed out by [29], this term drains temperature fluctuations from the region where production is

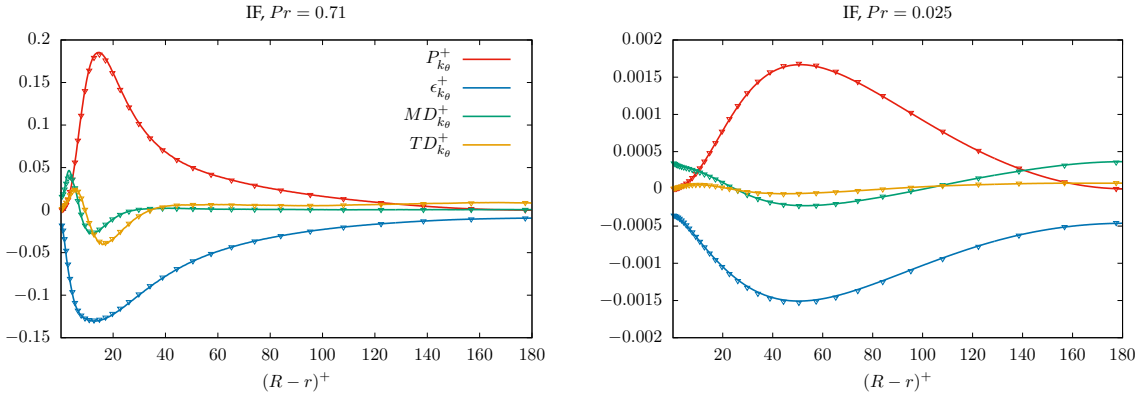

Figure 5.12: Budget of temperature variance with IF at $Re = 5300$ with (left) $Pr = 0.71$ and (right) $Pr = 0.025$. Symbols are reference results of [10].

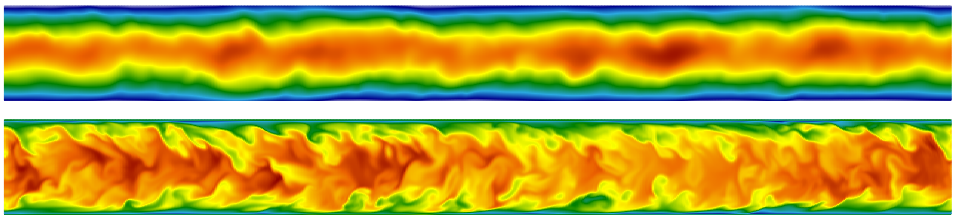

Figure 5.13: Snapshots of the instantaneous temperature Θ at $Re = 5300$ with (top) $Pr = 0.025$ and (bottom) $Pr = 0.71$. Red indicates high values, blue indicates low values.

most intense and conveys them both towards the wall and the core region. At the production peak location, for $Pr = 0.71$, transports by turbulence TD_{k_θ} and molecular diffusion MD_{k_θ} are comparable, with a slight dominance of the former. They account each for $\approx 18\%$ of the production peak amplitude. Contrarily, for $Pr = 0.025$, MD_{k_θ} accounts for $\approx 13\%$ of the production peak amplitude, against only 4% associated to TD_{k_θ}. The same behaviour is also observed in the outer region, where for $Pr = 0.71$ the turbulence transport term shows a positive plateau, ultimately balancing dissipation at the centre of the pipe; whereas for $Pr = 0.025$, it is molecular diffusion that predominantly balances dissipation in the core region (with only a marginal contribution of turbulence transport). The above considerations demonstrate the major role played by molecular diffusion over turbulence transport in low Prandtl fluids. Also, the significant difference on the amplitude of the terms between the two cases shows that thermal turbulent structures are considerably damped in applications with low Prandtl fluids [101], this can be also verified qualitatively through the instantaneous visualizations of the temperature field provided in Figure 5.13.

Table 5.4: Main parameters and results with MBC.

	Re_D	Δz^+	Δr^+	$\Delta(R\theta)^+$	Re_τ	Nu	
						$Pr0.71$	$Pr0.025$
DNS [10]	5300	< 9.4	$0.37 - 4.5$	< 4.9	181.1	18.3	6.43
Present DNS	5300	7	≈ 1.8	≈ 1.8	180	18.13	6.43
Present DNS Δx^2	5300	7	≈ 1.8	≈ 1.8	262.4	36.6	-
DNS [9]	37700	< 9.98	$0.15 - 5.12$	< 4.87	999	-	-
LES [10]	37700	< 18	$0.64 - 11$	< 10	998.9	85.3	-
Present DNS	37700	13	≈ 2.9	≈ 2.9	996.8	84.16	-
Present LES	37700	13	≈ 5.8	≈ 5.8	1000.6	85.27	-

5.5.2 Validation MBC

In this section DNS results with MBC are assessed at low and moderately high Reynolds numbers $Re = 5300, 37700$. Here, major attention is given to the advantageous features of the present computational configuration. In particular, through comparison with reference results from [10], the combination of profitable numerical features, leading to a significant reduction of the computational cost, is demonstrated. Main parameters for each simulation and the predictions of relevant wall quantities are provided all together in Table 5.4.

For the low Reynolds case, the viscous filtering technique VF^1 (scheme (5.33, 5.34)) is used whereas, for the high Reynolds case, VF^3 (scheme (5.30, 5.31)) is employed instead (c.f. section 5.2.3). The accuracy of both strategies have been compared and demonstrated to be very similar in [78]. In fact, the MBC results discussed here have been already presented in chapter 4 [78] to highlight the benefits of viscous filtering for the present computational configuration. Indeed, without the significant relaxation of the stability constraint related to diffusivity allowed by the viscous filtering technique, these simulations, at both low and high Reynolds numbers, would be very expensive to carry out with the full explicit time integration previously used. In particular, as already mentioned in section 5.2.3, up to 95% of computational resources could be spared.

MBC at low Reynolds number

Firstly, the low Reynolds number case is considered for both Prandtl numbers $Pr = 0.71, 0.025$. For this particular flow configuration, accurate DNS results are documented in [10] where the high-order

spectral element code Nek5000 was used with a highly-refined computational mesh in the near wall region. The same calculation has been performed here with the same computational mesh used for the IF investigations, i.e., a computational domain $(L_x \times L_y \times L_z) = (1.28D \times 1.28D \times 12.5D)$ with $(n_x \times n_y \times n_z) = (256 \times 256 \times 640)$ nodes, corresponding to a mesh resolution of $\Delta x^+ = \Delta y^+ = 1.81$, $\Delta z^+ = 7.07$ in wall units. With respect to the reference calculation of [10], twice as much degrees of freedom are used here. Nonetheless, thanks to the numerical efficiency of Incompact3d /Xcompact3d, it is estimated that the actual computational cost of the present DNS is of 60% of its reference counterpart.

The cell size in the near wall region is another important aspect to be addressed. In [10], the closest mesh node is set at a distance of 0.37 wall unit from the wall, whereas here, the Cartesian resolution in the transverse-xy directions is about five times coarser in the near wall region. Recalling the discussions of chapter 3, this is beyond the typical recommendation for DNS/LES which suggests a cell size for which the minimal scale computed with accuracy $L_{min} = 4\Delta x$ may capture the thickness of the viscous sublayer, i. e., $L^+_{min} < 5$. For the present resolution, we have instead $L^+_{min} = 7.2$. Despite the resulting structural bypass of the viscous sublayer, very accurate predictions of the friction Reynolds number and Nusselt numbers are obtained, in all cases within 1% error, as reported in Table 5.4. Likewise, in Figure 5.14 a remarkable agreement with the reference DNS results of [10] is recovered for all the temperature statistics scaled in viscous units.

Besides the mesh distribution factor already addressed in chapter 3 , the preservation of accuracy observed here must be also connected to the use of high-order schemes in Incompact3d /Xcompact3d. Formally, the usage of the present IBM results in a solution that is only second-order accurate in space, as shown by [50]. Despite this limitation, the utilisation of high-order schemes remains highly beneficial to obtain an accurate description of the range of scales of motion that composes the flow (see discussions in section 2.6.2). To illustrate this crucial point, an additional simulation has been conducted for $Pr = 0.71$ using conventional second-order schemes instead of the sixth-order compact schemes normally employed in the code. More precisely, all the finite-difference operators (differentiation and half-staggered mesh interpolation) have been switched from sixth to second-order through a drastic reduction of the stencil while keeping a centred formulation. The corresponding second-order schemes are conventional, with for instance the explicit formulation

$$f'_i = \frac{f_{i+1} - f_{i-1}}{2\Delta x}$$

to compute the first-derivative. The resulting predictions are reported in Table 5.4 and Figure 5.15 for respectively the global quantities Re_τ, Nu and the profiles of basic temperature statistics[6]. The incompatibility of conventional second-order schemes can be clearly seen when a mesh which bypasses the viscous sublayer is used. The friction velocity and temperature are found to be strongly affected by the use of low order schemes. Such a result shows that the present strategy, based on a Cartesian mesh combined with an IBM, is reliable only if high-order schemes are used irrespective of the formal order of the approach. However, we stress that the generalisation of these results to any second-order Navier-Stokes solver should be done carefully. More precisely, the code Incompact3d /Xcompact3d is based on a half-staggered mesh (same location for the velocity components and staggered locations for the pressure nodes). In our experience, this particular mesh arrangement is more demanding in terms of

[6]The reader is referred to [77] for a complete presentation of velocity statistics as well.

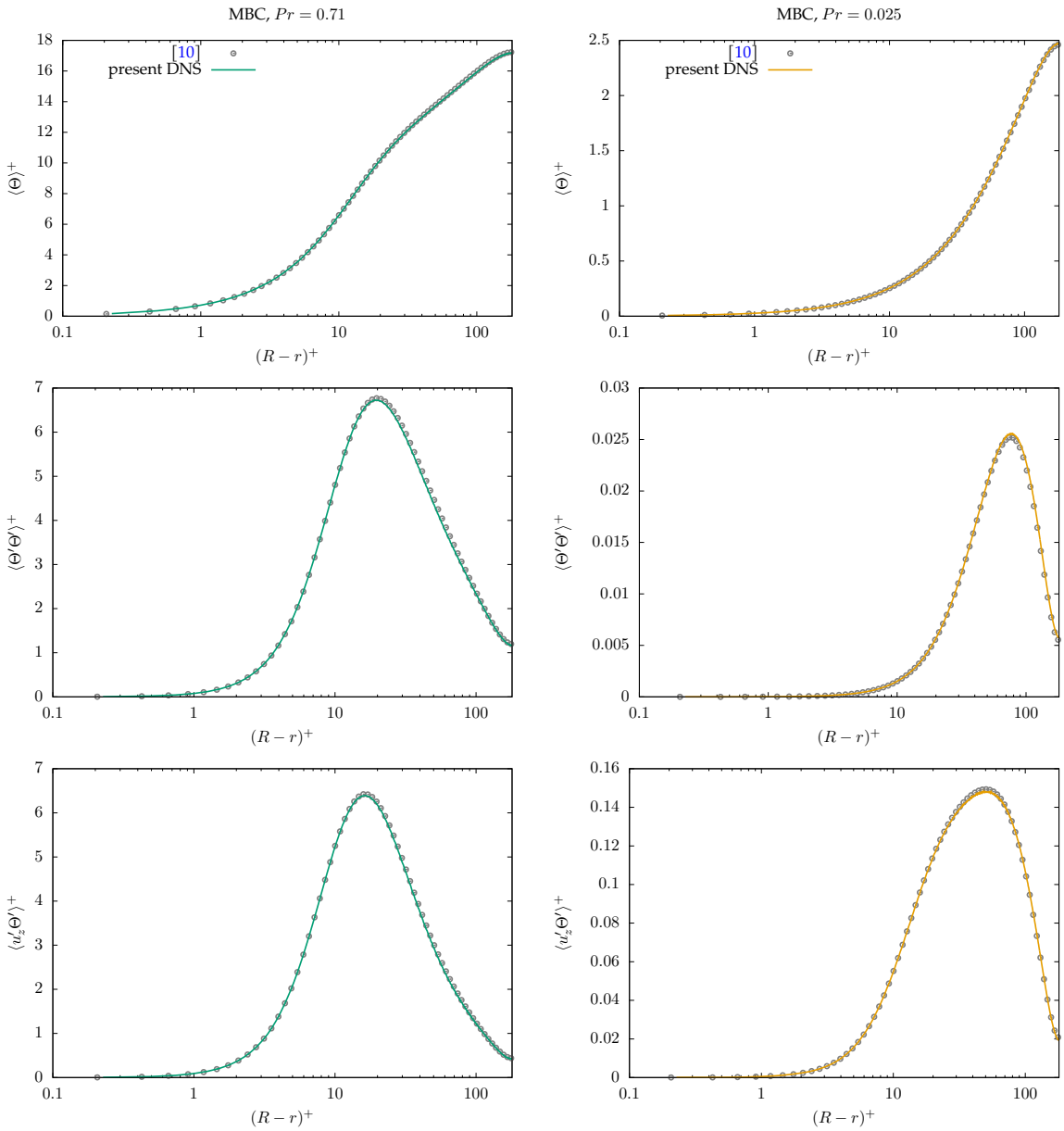

Figure 5.14: First and second-order temperature statistics with MBC at $Re = 5300$ with (left) $Pr = 0.71$ and (right) $Pr = 0.025$. (Top) Mean-temperature profile, (centre) temperature variance and (bottom) streamwise heat flux. Symbols are reference results of [10].

scheme accuracy by comparison to collocated or fully-staggered mesh organisation. Before any general conclusion about the potential of second-order accurate Navier-Stokes solvers in the present computational configuration (that is, coarse mesh in the near wall region and immersed boundary method), it is necessary to investigate other mesh arrangements than the present half-staggered discretisation. This point is planned to be addressed in future work. The present assessment aims to rather highlight the importance of high-order schemes for the present numerical strategy. These observations complement those drawn throughout chapter 3.

In view of the overall agreement, it can be stated that DNS accuracy can be reached despite the use of a structurally coarse resolution in the near wall region even when heat transfer predictions are required. However it has to be recognised that the 40% of computational saving enabled by the present approach is not enough to recommend the use of a simple Cartesian code over Nek5000. The use of the latter is certainly a more rational choice to perform a DNS of turbulent pipe flow, especially if its ability for mesh refinement is taken into account. Another advantage of Nek5000 is its high-order accuracy which is preserved everywhere in the computational domain. On the contrary, the use of an immersed boundary method limits the formal accuracy to second order, as a fundamental drawback of the present approach, even if the use of high-order schemes remains highly beneficial. Nevertheless, it will be shown in the next section that, in more demanding configurations, the loss of accuracy due to the use of an immersed boundary method can be counterbalanced by the computational efficiency of the present approach. Reason why its capability to reach DNS accuracy despite the lack of any mesh refinement in the near wall region can be considered as an attractive feature.

MBC at high Reynolds number

In this second part, MBC is considered at a moderately high Reynolds number $Re = 37700$ and $Pr = 0.71$. For these same physical parameters, the highly-refined DNS simulation of [9] has required the computation of more than 2 billion degrees of freedom. Here, by using a mesh of $(n_x \times n_y \times n_z) = (768 \times 768 \times 1920)$ nodes in a computational domain of dimensions $(L_x \times L_y \times L_z) = (1.12D \times 1.12D \times 12.5D)$, the number of degrees of freedom is nearly cut by half, with a corresponding mesh resolution $\Delta x^+ = \Delta y^+ \approx 2.9$ in the transverse-xy directions. In terms of computational efficiency, the cost of the present simulations is estimated as 5% by comparison to the accurate DNS of [9], whose results have been served also as reference for our velocity statistics in chapters 3 and 4.

Emphatically, as reported in Table 5.4 and Figure 5.16, this great saving of computational resources is not achieved by compromising the accuracy. The global quantities Re_τ and Nu are predicted correctly and a very good agreement with reference results are once again recovered for all the basic temperature statistics. Note that reference data for the temperature statistics are from the well-resolved LES of [10], whose accuracy has been demonstrated to be very close to DNS through their excellent agreement with results of [9]. By comparison to the LES of [10], the computational saving associated to the present calculation is about 40%, despite the use of $3.5\times$ more degrees of freedom.

It must be recognized that the capability of the present computational configuration to reach the highest standards of DNS is somewhat unexpected in view of the reasonable cost of the simulation.

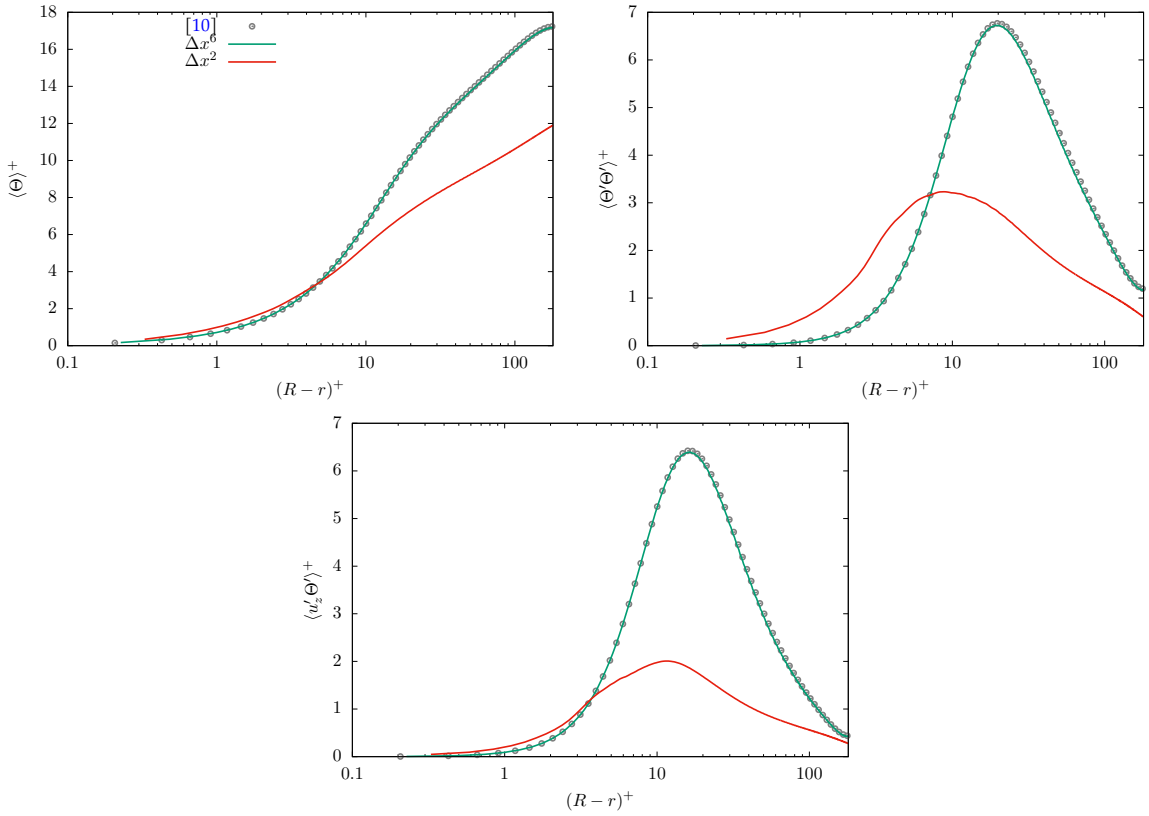

Figure 5.15: Comparison of first and second-order temperature statistics using the standard sixth-order spatial discrezation of Incompact3d /Xcompact3d (Δx^6) or conventional second-order schemes (Δx^2). DNS was performed with MBC at $Re = 5300$ and $Pr = 0.71$. (Top, left) Mean-temperature profile, (top, right) temperature variance and (bottom) streamwise heat flux. Symbols are reference results of [10].

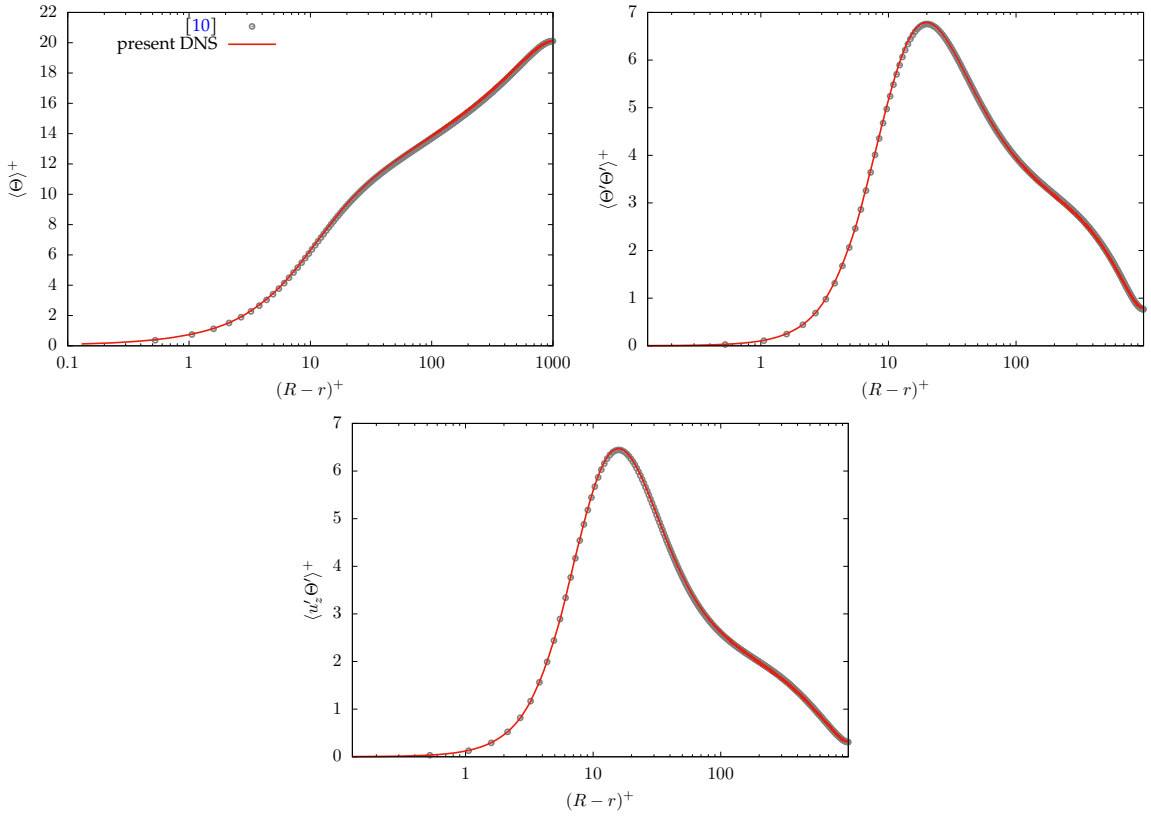

Figure 5.16: First and second-order temperature statistics with MBC at $Re = 37700$ and $Pr = 0.71$. (Top, left) Mean-temperature profile, (top, right) temperature variance, (bottom) streamwise heat flux. Symbols are reference results of [10].

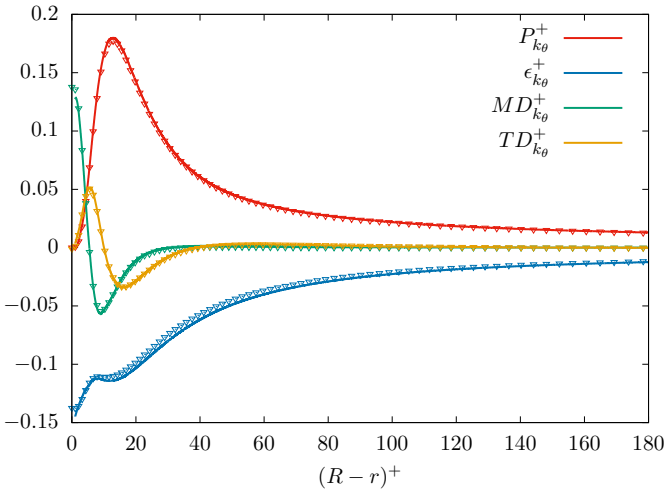

Figure 5.17: Budget terms of temperature variance with MBC at $Re = 37700$ and $Pr = 0.71$. For a better detailing of the near-wall region, the x-axis is limited to $0 < (R-r)^+ < 180$. Symbols are reference results of [10].

In order to highlight this point, the budget terms of the temperature fluctuations, calculated as in eqs.(5.71-5.76), are provided in Figure 5.17. Apart from the small under-prediction of $\epsilon^+_{k\theta}$ at the production peak location, a good overall agreement is once again recovered with, in particular, the balance between the terms being well reproduced. Moreover, very-close to the wall, the shape of the profiles are correctly captured in a precision clearly smaller than the mesh resolution. This ability to accurately predict velocity[7] and temperature budgets with such an advantageous accuracy/cost ratio, makes the present approach very attractive for RANS modelling development.

LES In order to explore the limits of the present strategy, a LES has been also carried out for $Pr = 0.71$ to examine to what extent the DNS accuracy can be challenged with the present LES approach only based on the use of artificial dissipation. By keeping the domain dimensions, we use $(n_x \times n_y \times n_z) = (384 \times 384 \times 1920)$, obtaining a mesh resolution two times coarser in the transverse-xy directions. The choice to keep the same longitudinal cell size $\Delta z^+ = 13$ is motivated by the analysis of the level of turbulent kinetic energy to be captured depending on the mesh resolution, presented in chapter 3, Figure 3.6. In fact, the use of a coarser mesh resolution in z can result in a significant loss of turbulent kinetic energy. On the contrary, for the transverse-xy directions, the present mesh resolution $\Delta x^+ = \Delta y^+ \approx 5.8$ is found to be clearly less intrusive[8].

[7] The reader is referred to [77] for the budget of turbulent kinetic energy as well.

[8] By using the new reconstruction strategy - namely reconstruction in the transverse-xy direction through the periodicity of the domain boundaries (see section 5.2.1) - the filtering technique discussed in section 3.3.1 should

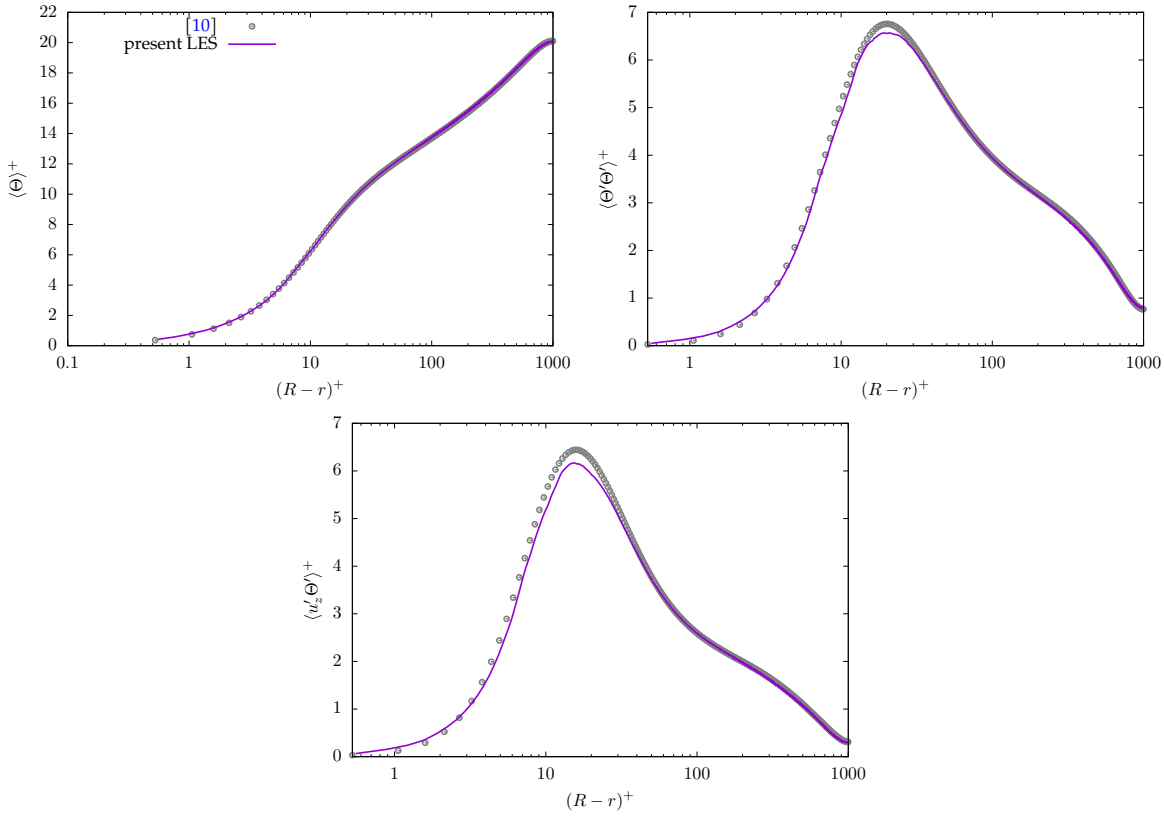

Figure 5.18: First and second-order temperature statistics calculated in LES resolution at $Re = 37700$ and $Pr = 0.71$ with MBC. (Top, left) Mean-temperature profile, (top, right) temperature variance and (bottom) streamwise heat flux. Symbols are reference results of [10].

As reported in Table 5.4, the predictions of Re_τ and Nu remain satisfactory. Velocity and temperature statistics are also presented in Figure 5.18. Even if a slight loss of accuracy is observed, the overall agreement is still suitable. In particular, the deviation of the profiles from their reference counterparts can be considered as small enough if the purpose is to assess RANS data which are typically subjected to higher discrepancies. From this point of view, the present low-cost approach, whose computational cost is about only 0.5% by comparison to the highly accurate DNS of [9], can be presented as a good compromise in terms of accuracy/cost.

Note that in two of our recent studies [76, 75] (see article in Appendix A), it has been shown that, to obtain this level of accuracy despite a poor near-wall resolution, it is mandatory to introduce a significant amount of numerical viscosity in the spirit of implicit LES. Because of the robustness of the

be also improved.

Table 5.5: Nusselt predictions for present DNS with IF and MBC at $Re = 5300$.

	Nu	
	$Pr = 0.71$	$Pr = 0.025$
MBC	18.13	6.43
IF	18.22	6.46

strategy, artificial dissipation was considered to exhibit the features of implicit wall-layer modelling (see discussions in chapter 3). The present results confirm the reliability of the technique also for heat transfer prediction.

5.5.3 MBC *vs.* IF

In this section the previous results at low Reynolds number with IF and MBC are now confronted to highlight the influence of the TBC used to model a constant heat flux.

The Nusselt predictions reported in Table 5.5 reveal a small influence of the TBC as both IF and MBC values are always found within 1% error with respect to reference [10]. This agrees well with results of [29, 10]. In Figure 5.19, first and second-order one-point statistics obtained with IF and MBC are confronted, DNS results of [10] with isothermal boundary conditions (IT) are also plotted for comparison. Results are scaled in viscous units, following Table 5.1. The assumption of zero fluctuations for the wall temperature, intrinsic in MBC, is find to be quite valid for the mean field for both Prandtl cases, given the fact that profiles of $\langle\Theta\rangle^+$ for MBC and IF superimpose each other [27, 10]. Comparisons here are limited to low Reynolds numbers, however, Straub *et. al* [10] have shown that this equivalence of temperature distributions between MBC and IF is also kept with increasing Reynolds number.

Concerning the temperature fluctuations $\langle\Theta'\Theta'\rangle^+$ in Figure 5.19-centre, the effect of the non-zero fluctuating wall temperature of IF affects mostly the conductive sublayer, as MBC and IF profiles draw near to each other in the outer layer for both Prandtl numbers. This same behaviour is also observed for the streamwise heat flux $\langle u_z'\Theta'\rangle^+$, for which IF and MBC profiles differ mostly in the near-wall region and the gap between them is reduced with increasing Pr. For instance, for $Pr = 0.025$, at $(R - r)^+ = 0.5$ the streamwise heat flux with IF gets to be $\approx 70\times$ bigger than MBC, whereas, for $Pr = 0.71$ this difference drops to $\approx 12\times$. The location of the peak also moves closer to the wall with increasing Pr as the conductive sublayer gets thinner. The above observations are in agreement with results presented by [27, 101, 29, 10]. As a matter of fact, the suppression of thermal fluctuations with MBC causes the profiles of both temperature variance and streamwise heat flux to draw near to IT in the near-wall region and to IF in the outer region, evidencing the *mixed* character of MBC [29, 10]

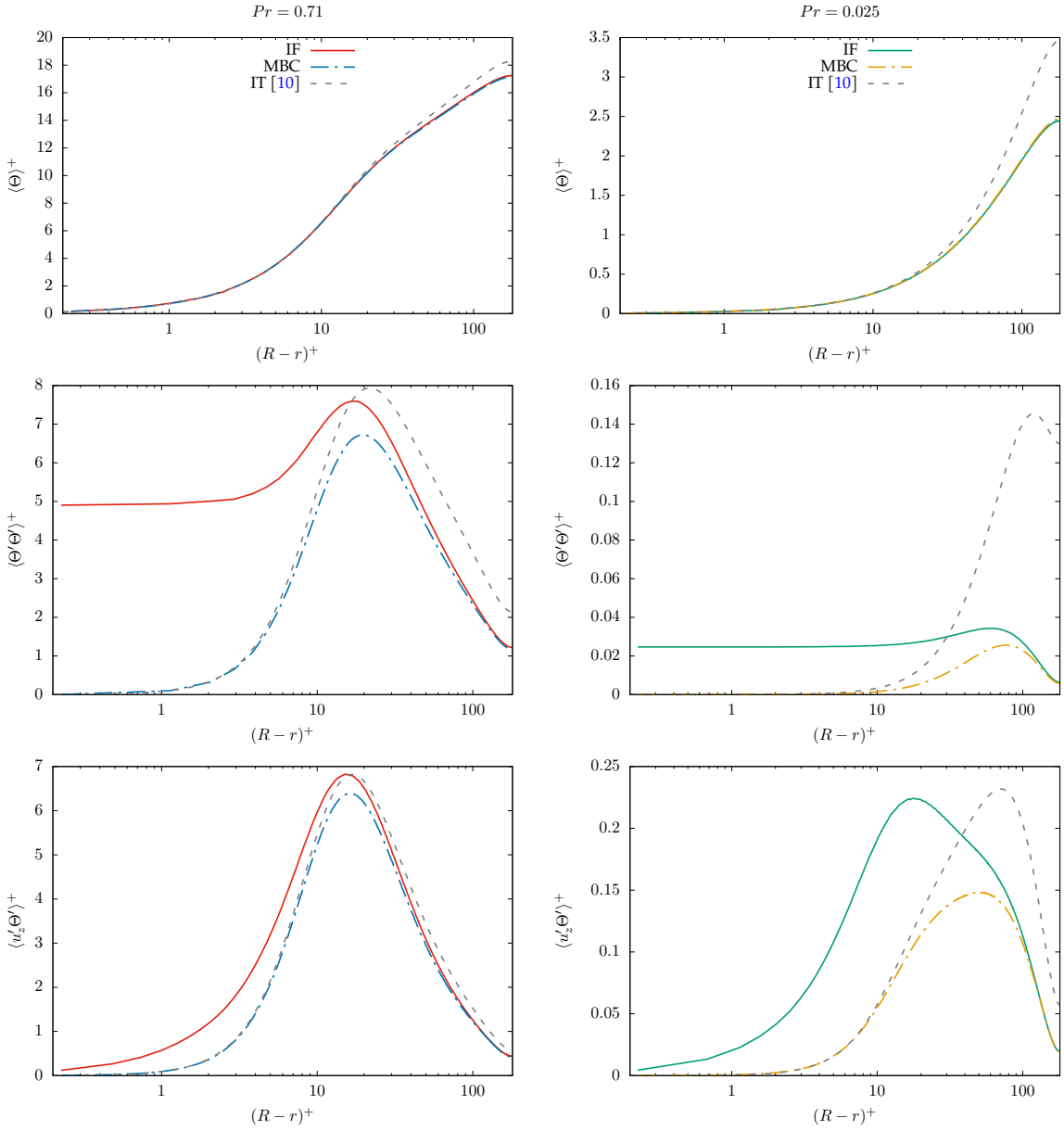

Figure 5.19: Comparison of first and second-order temperature statistics with IF or MBC at $Re = 5300$. (Left) $Pr = 0.71$ and (right) $Pr = 0.025$. (Top) Mean-temperature profile, (centre) temperature variance and (bottom) streamwise heat flux. DNS results of [10] with IT are also plotted for reference.

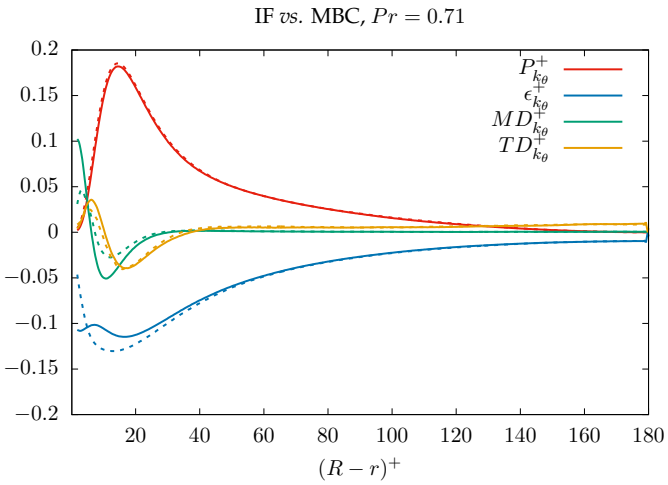

Figure 5.20: Comparison of budget terms of temperature variance with IF or MBC at $Re = 5300$ and $Pr = 0.71$. Solid lines are MBC results and dashed lines are IF results.

In Figure 5.20, the budget terms of temperature variance, calculated with eqs.(5.71 - 5.76), are compared only for the case with $Pr = 0.71$. The production $P^+_{k_\theta}$ profiles are close to each other with slightly higher values being seen with IF across the conductive sublayer. Both transport terms, namely molecular diffusion $MD^+_{k_\theta}$ and turbulent transport $TD^+_{k_\theta}$, play the same functional role of conveying temperature fluctuations from the region of maximum production (where they display a negative value) to the wall and the core region (positive values) [29]. Furthermore, transport by molecular diffusion is always smaller with IF than MBC at the wall. Also with IF, the molecular dissipation $\epsilon^+_{k_\theta}$ decreases across the conductive sublayer. As pointed out by [29], this is associated to the fact that its major contribution, the term containing the radial derivative in eq.(5.73), is damped with isoflux conditions due to the absence of temperature front, that is, absence of sharp temperature gradients along the edge of the viscous sublayer. Because of the similarity with the velocity field, these gradients exist with MBC, but not with IF [101]. All the above considerations are in qualitative agreement with DNS results of [101, 29].

In summary, it can be stated that both IBM strategies developed for the prescription of IF and MBC - which require the imposition of Dirichlet and Neumann conditions respectively - provide solid results, given the good agreement with reference data. Furthermore, the present high-order numerical strategy based on compact finite difference schemes can provide results with accuracy similar to the reference data obtained with a spectral element code [9, 10]. In addition, the present strategy enables the use of structurally coarse meshes thanks to the association of profitable numerical features, resulting in significant savings of computational resources. The viscous filtering technique was also crucial to achieve the advantageous accuracy/cost ratios presented here, especially for the combination high Reynolds/low Prandtl numbers.

5.6 General conclusion

This chapter is dedicated to the development and validation of numerical strategies for the ideal local imposition of a wall heat flux with isoflux (IF) and mixed-type (MBC) boundary conditions. The originality of the method is found in the fact that the imposition of these thermal boundary conditions (TBC) is done through our immersed boundary method (IBM) based on Lagrange polynomial reconstructions, which, additionally, receives an improved and more efficient version.

As MBC consists of imposing a constant and uniform temperature at the wall, i.e., a Dirichlet boundary condition (DBC), its implementation within the IBM is straightforward by applying the same strategy used for the no-slip condition. On the other hand, special attention is given to IF as an original methodology is developed to prescribe the related wall-normal heat flux, which corresponds to the imposition of a Neumann boundary condition (NBC). In order to be compatible with the 2D MPI pencil decomposition and regular Cartesian grid of Incompact3d /Xcompact3d, the imposition of the wall-normal derivative is decomposed into its Cartesian components as functions of the local normal and tangential directions to the surface. Implemented this way, the technique can be straightforwardly employed to investigate more complex geometries. Then, the IBM strategy developed is based on an indirect imposition of the NBC, in the sense that the wall derivative is virtually ensured with a DBC. In other words, a target value for the temperature at the wall is defined locally in order to provide the expected Cartesian wall derivative and, subsequently, the Lagrange reconstruction is performed by imposing this value at the interface as if it was a DBC. Furthermore, a finite-difference strategy - based on the computation of first-derivatives and extrapolation of wall values - is implemented to handle the projection from the local reference frame (associated to the geometry) to the Cartesian components (associated to the grid). Different variants of the technique have been tested and a robust method has been ultimately selected.

Then, DNS results of validation are presented with both IF and MBC for two Prandtl numbers $Pr = 0.71, 0.025$, representative of air and liquid metals respectively. The accuracy of the IF technique has been clearly demonstrated at low Reynolds number $Re = 5300$ through a great agreement for the budget of temperature variance and basic turbulence statistics. For MBC, the great agreement of turbulence statistics with reference results is demonstrated at low and moderately high Reynolds numbers $Re = 5300, 37700$. The very advantageous accuracy/cost ratio of the present numerical strategy is also highlighted. In particular, it is shown that the present numerical strategy can reach the highest standards of DNS while enabling the use of coarse meshes. Such a profitable feature is in fact attributed to the association of an efficient immersed boundary method with use of high-order schemes and viscous filtering technique. The ability to predict accurately the budget of temperature variance is also demonstrated, making of this numerical strategy an attractive tool for RANS modelling development. Finally, IF and MBC results are confronted in order to highlight the main effects of the TBC chosen to model an uniform heat flux. The considerations have been found to be in agreement with results of [101, 29, 100, 10]. The validation of the numerical techniques provided in this chapter paves the way for performing high-fidelity simulation of thermal hydraulics while including conjugate heat transfer (CHT), the subject of next chapter.

Version française

Ce chapitre est consacré au développement et à la validation de techniques numériques pour l'imposition locale idéale d'une condition aux limites thermique (TBC) pariétale de types isoflux (IF) et mixte (MBC). L'originalité réside dans le fait que cette imposition doit être réalisée dans le cadre d'une méthode de frontières immergées qui est basée ici sur des reconstructions polynomiales Lagrangiennes de la solution dans une nouvelle version plus précise et efficace.

Comme le cas MBC consiste à imposer une température constante et uniforme à la paroi, soit une condition aux limites de type Dirichlet (DBC), sa mise en œuvre par IBM est directe par application de la même technique que celle utilisée pour la condition d'adhérence. A l'inverse, une attention particulière doit être accordée au cas IF qui réclame l'imposition de la dérivée normale à la paroi, soit une condition aux limites du type Neumann (NBC). Afin d'être compatible avec la décomposition 2D en crayon de la grille cartésienne régulière d'Incompact3d /Xcompact3d (parallélisme par communications globales via MPI), l'imposition de la dérivée normale à la paroi est décomposée en ses composantes cartésiennes en tant que fonctions des directions normales et tangentielles locales à la surface. Mise en œuvre de cette façon, la technique peut être utilisée directement pour étudier des géométries plus complexes. Par ailleurs, La technique présentée ici ne prescrit pas la condition de Neumann directement, dans le sens où cette dernière est convertie en une condition de Dirichlet. Cette conversion consiste en l'estimation d'une valeur cible pour la température à la paroi qui est définie localement afin de fournir la dérivée normale attendue à la même position. Ensuite, la reconstruction de Lagrange est effectuée en imposant cette valeur à l'interface comme dans le cas DBC. En outre, une stratégie de différences finies - basée sur le calcul des dérivées premières et l'extrapolation des valeurs de paroi - est mise en œuvre pour gérer librement la projection du référentiel local (associé à la géométrie) vers les composantes cartésiennes (associées à la grille). Différentes variantes de la technique ont été testées en conduisant à la sélection d'une méthode robuste.

Ensuite, les résultats DNS de validation par prédiction du transfert de chaleur dans les cas IF et MBC sont présentés pour deux nombres de Prandtl $Pr = 0.71, 0.025$ représentatifs de l'air et de métaux liquides respectivement. La précision de la technique IF a été clairement démontrée à bas nombre de Reynolds $Re = 5300$ au regard du bon accord observé pour le budget des fluctuations de température, ainsi que pour les statistiques turbulentes, par comparaison avec des données de référence. Pour le cas MBC, un bon accord est également obtenu à bas et haut nombres de Reynolds $Re = 5300, 37700$. Le rapport précision/coût très avantageux de cette approche est bien mis en évidence. En particulier, il est montré que cette stratégie numérique peut atteindre les plus hauts standards de la DNS tout en permettant l'utilisation de maillages assez grossiers. Parmi les raisons de ce succès, on peut mentionner la méthode de frontières immergées dédiée à des schémas de haute précision mais aussi la technique de filtrage visqueux. La capacité de prédire avec précision les bilans de fluctuations de température est également bien montrée, faisant de cette stratégie numérique un outil attractif pour la production de données de référence utiles aux développements de modélisations de type RANS. Enfin, les résultats IF et MBC sont confrontés afin de mettre en évidence les différences entre ces deux cas pour la modélisation d'un flux de chaleur uniforme. Les observations sont en accord avec les résultats de [101, 29, 100, 10]. La validation des techniques numériques réalisée dans ce chapitre ouvre la voie à la simulation haute-fidélité de la thermohydraulique avec comme perspective la description réaliste de

transferts thermiques conjugués qui fait l'objet du prochain chapitre.

Chapter 6

Conjugate Heat Transfer in Turbulent Pipe Flow

Let us consider once again our flow configuration illustrated in Figure 6.1. For the investigations performed in the previous chapter, we have performed DNS of this flow configuration with local imposition, which consists of solving the energy equation for the fluid side only while prescribing ideal thermal boundary conditions (TBCs) at the fluid subdomain boundary $r = R$, in the hope that it may represent the heat transfer phenomena occurring in the solid body. Nonetheless, it is widely recognised that idealized TBCs cannot provide realistic representations in every scenario possible [28], since simplifications concerning the behaviour of temperature fluctuations at the wall cannot be avoided as long as the calculations are performed for the fluid side only [27, 25]. This is especially true when the thermal diffusivity of the solid and the fluid are of the same order of magnitude [28].

In the present chapter, the term *Conjugate Heat Transfer* (*CHT*) refers to the multiphysics interaction between a solid body and a fluid in movement subjected to temperature gradients. In this regard, numerical simulations of the CHT problem are by far a more realistic way to investigate heat transfer in wall-bounded configurations as the heat conduction occurring in the solid is not only approximated but explicitly computed and coupled to the fluid solution. This strategy can provide a fine description of the turbulent thermal interaction between fluid and solid media. In particular, for our flow configuration schematised in Figure 6.1, a high-fidelity description of the thermal interaction between the pipe body $R \leq r \leq R_o$ and the wall-bounded turbulent flow in $r < R$ can be obtained, which may be valuable, for instance, to improve RANS/LES modelling in industrial applications where fluctuating thermal stresses are a concern, e.g. in case of a severe emergency cooling or long-term ageing of materials [28, 104].

In practical terms, the numerical simulation of the CHT problem means computing solutions subjected to different physical phenomena in each medium, and, most of the times, handling different governing equations, different time and spatial scales, etc [105]. Very often, these complex phenomena are investigated with high-Reynolds LES and RANS [106, 27, 107, 104, 108], which nonetheless rely

on wall-modelling as the near-wall region is not fully resolved. For instance, in their pioneer work in 1989, Kasagi *et al.* [106] performed simulations of the CHT problem in plane channel configuration by employing a structural two-dimensional model of near-wall turbulence for the velocity field while solving the time-dependent heat conduction in the solid and fluid regions very near the wall. For a very thick wall, a good agreement with results of [109] was recovered, who had previously obtained an analytical solution of the CHT problem for a semi-infinite wall by linearizing the energy equation in the laminar sublayer.

The first DNS with CHT was performed by [25], who coupled the fluid and unsteady solid solution in channel flow for a friction Reynolds number $Re_\tau = 150$ and Prandtl number ranging from 0.71 to 7. In this scenario, different wall thicknesses were considered. A general good agreement with results of [109, 106] - who used less accurate/ cheaper methods - was recovered, and thus, given the uncertainty of available experimental data back then, it could not be stated whether the DNS results obtained were superior. Afterwards, [102] used the same numerical method to investigate CHT in channel configuration at very-low Prandtl $Pr = 0.01$ (representative of liquid sodium) and friction Reynolds number Re_τ ranging from 180 to 590. Fifteen temperature fields for various combinations of fluid and solid material properties were computed in parallel with a single velocity solution. Results pointed to a relatively intensive penetration of turbulent temperature fluctuations into the heated wall in liquid sodium-steel systems (represented by the values of Pr and material properties considered), which are then progressively damped as they infiltrate into the wall.

Then, Flageul *et. al* [28] compared the impact of different TBCs - namely MBC, IF, Robin and CHT - in channel flow using Incompact3d. Simulations were performed for $Re_\tau = 150$ and $Pr = 0.71$ representative of air and the budgets of turbulent heat flux and temperature variance were extensively assessed with a post-processing designed to produce validation data for RANS models. For the CHT case, it was considered equivalency of fluid/ solid thermal conductivities and diffusivities, i.e. $\lambda = \lambda_s$ and $\alpha = \alpha_s$ respectively. Results with Robin boundary conditions were found to be close to the CHT ones for most of the turbulence statistics and their budgets, however some analytical evidences suggested that very large scale thermal structures related to non-local effects cannot be reproduced with a Robin boundary conditions with constant coefficients, being therefore reproducible only with conjugate heat transfer. Subsequently, the authors [110] further investigated the discontinuity generated on the dissipation rate associated to the temperature variance at the fluid-solid interface with CHT. Simulations were performed for the same friction Reynolds and Prandtl numbers, $Re_\tau = 150$ and $Pr = 0.71$ respectively, with 9 different scalar fields being computed in parallel, representing various combinations of fluid/ solid material properties.

Then recently, still with Incompact3d, Narváez *et. al* [91] implemented a *dual* immersed boundary method (IBM) to perform simulations of the CHT problem in channel flow. In this validation framework, a low Reynolds number $Re_\tau = 150$ was considered with a Prandtl number $Pr = 0.71$ and equivalent thermal properties for fluid and solid media as in [28]. The numerical approach was referred to as *dual* because fluid and solid temperature fields are defined separately, everywhere in the computational domain, such that, the solid subdomain is the immersed region for the fluid and, conversely, the fluid for the solid. This strategy allows then the numerical differentiation to individually perceive fluid and solid solutions as smooth for any combination of fluid solid thermal properties since the reconstruction is carried out in its own immersed zone for each temperature field separately.

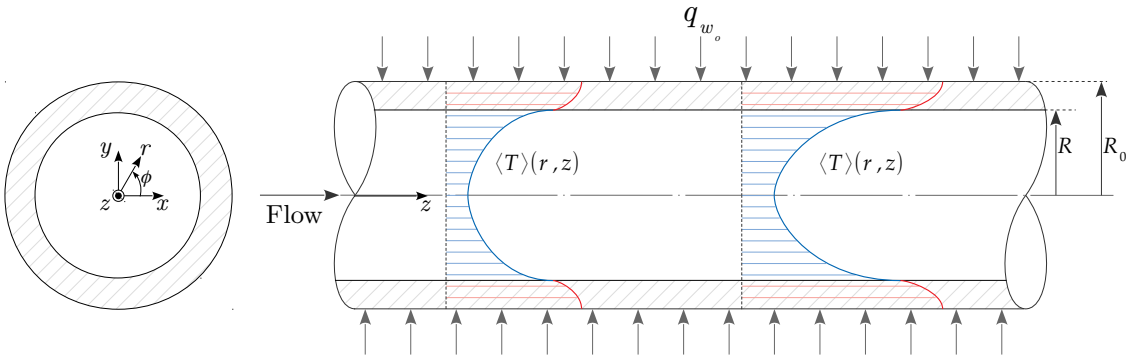

Figure 6.1: Schematic representation of the pipe flow geometry subjected to a uniform heat flux q_{w_o} imposed at the fluid-solid interface $r = R_o$.

The challenge inherent to numerical methods for CHT simulation lies in handling properly the above mentioned physical processes occurring in each medium. For this purpose, in terms of numerical implementation, two approaches are most commonly used. The first one consists of interfacing individual solvers already used to investigate the distinct physics [111, 112, 105]. The second approach, consists of handling the different physics implied in the CHT problem in a single solver. This latter strategy is the one followed here and in this chapter, we describe the numerical developments brought to the code Xcompact3d in order to couple the DNS solution in the fluid to the heat conduction solution in the solid. This coupling between fluid and solid solutions is mainly based on our customised IBM, which is also further developed. This strategy is in fact an expansion of the methodology of [91], which is extended here for a non-body conformal grid. Results of validation are presented and discussed for various combinations of fluid and solid material properties.

6.1 Conjugate heat transfer problem

In the present scenario, the influence of temperature fluctuations on the fluid dynamics is neglected as well as any temperature dependence of fluid and solid material properties, we consider therefore a passive temperature field T. Thus, according to the schematic illustration in Figure 6.1, heat transfer in the fluid medium will occur by forced convection governed by the advection-diffusion equation

$$\frac{\partial T}{\partial t} + u_j \frac{\partial T}{\partial x_j} = \alpha \frac{\partial^2 T}{\partial x_j \partial x_j} \qquad \text{in } r < R \ , \tag{6.1}$$

where $\alpha = \lambda/\rho c_p$ is the thermal diffusivity of the fluid, with λ its thermal conductivity, ρ its density and c_p its specific heat at constant pressure. In the solid stationary medium, heat transfer occurs only by conduction and it is governed by the unsteady heat diffusion equation

$$\frac{\partial T}{\partial t} = \alpha_s \frac{\partial^2 T}{\partial x_j \partial x_j} \qquad \text{in } R \leq r \leq R_o \ , \tag{6.2}$$

where $\alpha_s = \lambda_s/\rho_s c_{p_s}$ is the thermal diffusivity of the solid with λ_s its thermal conductivity, ρ_s its density and c_{p_s} its specific heat at constant pressure. The evolution of the mean profiles $\langle T \rangle$ along the streamwise-z direction in Figure 6.1 exemplifies the existence of a temperature gradient that triggers heat transfer between fluid and solid media.

To make the above expressions non-dimensional, and to be consistent with the imposition of the constant and uniform heat flux at the outer surface, we use the non-dimensional form (5.13)

$$\Theta = -\frac{1}{Nu}\left(\frac{T - T_b}{\langle T_w \rangle - T_b}\right)$$

introduced for isoflux conditions (IF) in the previous chapter, which leads to the following non-dimensional forms of the governing equations

$$\frac{\partial \Theta}{\partial t^*} + u_j^* \frac{\partial \Theta}{\partial x_j^*} = \frac{1}{Pe}\frac{\partial^2 \Theta}{\partial x_j^* \partial x_j^*} + f_\Theta \qquad \text{in } r^* < R/D \tag{6.3}$$

$$\frac{\partial \Theta_s}{\partial t^*} = \frac{1}{G\,Pe}\frac{\partial^2 \Theta_s}{\partial x_j^* \partial x_j^*} \qquad \text{in } R/D \leq r^* \leq R_o/D \ , \tag{6.4}$$

where we denote as Θ and Θ_s the temperature solutions in the fluid and solid subdomains respectively. The quantity $G = \alpha/\alpha_s$ is the fluid-to-solid ratio of thermal diffusivities, $f_\Theta = 4u_z^*/Pe$ is the source term ensuring the thermal stationary condition in the fluid zone (as given by eq.(5.16)) and * denotes non-dimensional quantities but it shall be dropped hereafter for the sake of simplicity.

By defining the temperature field in two individual subdomains, the physical processes related are also considered individually while conjugate boundary conditions are provided at the fluid-solid interface $r = R$ to ensure the continuity of the thermal field. More specifically, these conditions are the equality of temperature

$$\Theta = \Theta_s \qquad \text{at } r = R, \tag{6.5}$$

and heat flux

$$\lambda \left.\frac{\partial \Theta}{\partial r}\right|_w = \lambda_s \left.\frac{\partial \Theta_s}{\partial r}\right|_w \qquad \text{at } r = R, \tag{6.6}$$

which - by introducing the fluid-to-solid ratio of thermal conductivities $G_2 = \lambda_s/\lambda$ - may be re-expressed as

$$\left.\frac{\partial \Theta}{\partial r}\right|_w = G_2 \left.\frac{\partial \Theta_s}{\partial r}\right|_w \qquad \text{at } r = R. \tag{6.7}$$

The boundary condition for the solid body at its outer surface is a constant and uniform heat flux q_{w_o}

$$\left.\frac{\partial \Theta_s}{\partial r}\right|_{w_o} = \frac{q_{w_o}}{\lambda_s} \qquad \text{at } r = R_o. \tag{6.8}$$

In order to illustrate the coupling between conduction and convection in the present configuration, let us briefly analyze a simplified framework. We consider a laminar flow together with steady, one-dimensional radial conduction in the solid. The fluid energy equation (6.3) is therefore reduced to

$$\frac{1}{Pe}\left(4u_z + \frac{1}{r}\frac{d}{dr}\left(r\frac{d\Theta}{dr}\right)\right) = 0 \ , \tag{6.9}$$

and the solid equation (6.4) is reduced to the one-dimensional heat diffusion equation

$$\frac{1}{GPe}\left(\frac{1}{r}\frac{d}{dr}\left(r\frac{d\Theta_s}{dr}\right)\right) = 0 \ . \tag{6.10}$$

To obtain proper boundary conditions to solve eqs.(6.9, 6.10), we apply an energy balance to the annular differential control volume $\pi(R_o^2 - R^2)dz$ represented in Figure 6.2-left. The differential heat rate input $d\dot{Q}_o$ through the outer surface $dA_o = 2\pi R_o dz$ balances the heat rate output $d\dot{Q}_i$ through the inner surface $dA_i = 2\pi R dz$

$$d\dot{Q}_o - d\dot{Q}_i = 0 \implies q_{w_o} dA_o - q_w dA_i = 0 \ , \tag{6.11}$$

where the heat fluxes q_{w_o} and q_w are expressed by Fourier's Law as

$$q_{w_o} = \lambda_s \left.\frac{\partial \Theta_s}{\partial r}\right|_{w_o} \quad \text{and} \quad q_w = \lambda_s \left.\frac{\partial \Theta_s}{\partial r}\right|_{w} \ . \tag{6.12}$$

Thus, from the equality (6.11), the heat flux q_w in transit from the solid into the fluid subdomain (according to the heat flux continuity condition (6.7)) is of the form

$$q_w = \frac{R_o}{R} q_{w_o} = cst \ . \tag{6.13}$$

That is, in these simplified conditions, the fluid temperature field in $r < R$ is subjected to a constant and uniform heat flux $q_w = cst$, i.e., an isoflux condition (IF). These consideration allows us to directly recover, for the fluid temperature field Θ, the laminar solution (2.14) previously presented for IF

$$\Theta(r) = 2\left(\frac{3}{16} + r^4 - r^2\right) - \frac{1}{Nu} \ , \tag{6.14}$$

with $Nu = 4.36$ for a laminar flow. We may recover as well the related boundary conditions at $r = R$, given by eqs.(5.20, 5.14)

$$\left.\frac{\partial \Theta}{\partial r}\right|_w = -1 \tag{6.15}$$

$$\Theta|_w = -\frac{1}{Nu} \ . \tag{6.16}$$

Thereby, for the solid temperature field Θ_s, an expression for the Neumann boundary condition at the outer surface $r = R_o$ (uniform and constant heat flux q_{w_o}) can be conveniently derived from eqs.(6.12, 6.13, 6.15) together with the heat flux continuity condition (6.7)

$$\left.\frac{\partial \Theta_s}{\partial r}\right|_{w_o} = -\frac{1}{G_2}\frac{R}{R_o}. \tag{6.17}$$

A second boundary condition is obtained at the inner interface $r = R$ from the equality of temperatures with eqs.(6.5, 6.16)

$$\Theta_s|_w = -\frac{1}{Nu} \ . \tag{6.18}$$

As the general solution of eq.(6.10) is of the form

$$\Theta_s(r) = c_1 \ln(r) + c_2 \ , \tag{6.19}$$

with the two boundary conditions (6.17, 6.18), the following expression can be finally derived

$$\Theta_s(r) = \frac{R}{G_2} \ln\left(\frac{R}{r}\right) - \frac{1}{Nu} \ . \tag{6.20}$$

Temperature solutions Θ and Θ_s calculated with eqs.(6.14, 6.20) are plotted in Figure 6.2-right for different fluid-to-solid ratios of thermal conductivities $G_2 = \lambda_s/\lambda$. It is interesting to notice the behaviour of the temperature profiles across the interface and how the heat flux continuity condition (6.7) can introduce a paradoxical discontinuity on the slope of the temperature profile for $G_2 \neq 1$. In a finite-difference framework, numerically dealing with the resulting loss of differentiability in such cases can represent an obstacle [91], especially when compact schemes are used, given their well-know sensitivity to local discontinuities. Here, we further develop the *dual* IBM strategy of [91] to deal with this hindrance. Also, $G_2 \gg 1$ represents a scenario where the solid material is much more conductive than the fluid (conducting solid) and, as a result of the very effective heat diffusion in the solid medium, the temperature asymptotes to the interfacial constant value $\Theta_w = -1/Nu$. Conversely, when $G_2 \ll 1$, heat is diffused in the fluid medium much more effectively, in this scenario, the solid acts as an insulating wall [110].

Now, when the flow is turbulent, velocity fluctuations are naturally imparted to the fluid temperature field through the advective term in eq.(6.3). These thermal fluctuations are then transmitted to the solid body through the interface $r = R$ by the thermal coupling conditions (6.5, 6.7). The process of heat conduction in the solid is slow, which may require the simulation of a long transient time as a result of the discrepancy of time and spatial scales involved in the problem [112]. More specifically, the speed of penetration of turbulent fluctuations stemming from the fluid domain certainly depends on the relation between fluid and solid material properties. To better address this point, we introduce the thermal activity ratio defined as [102]

$$K = \sqrt{\frac{\lambda \rho c_p}{\lambda_s \rho_s c_{p_s}}} \ , \tag{6.21}$$

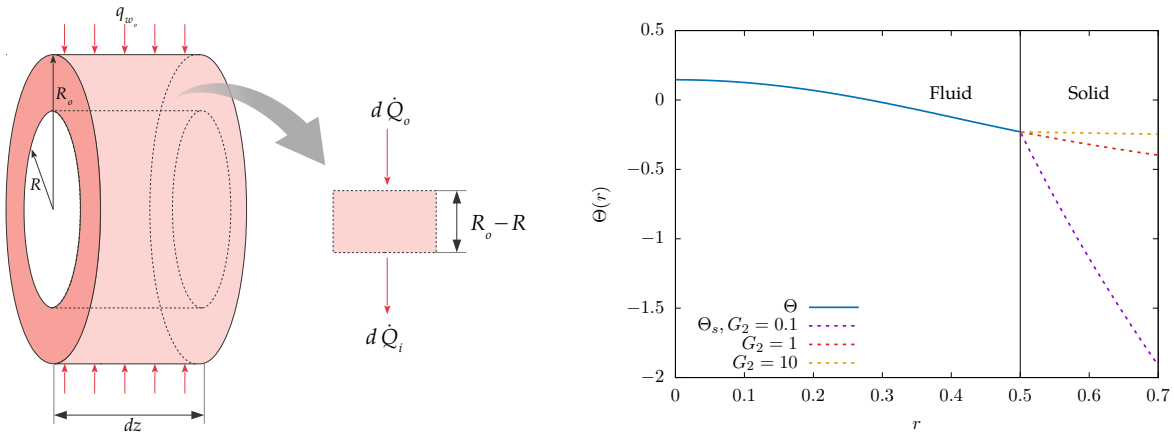

Figure 6.2: (Left) Annular differential control volume $\pi(R_o^2 - R^2)dz$ under uniform heat flux dq_{w_o}. (Right) Fluid and solid temperature solutions for different fluid-to-solid thermal conductivity ratios $G_2 = \lambda_s/\lambda$.

which therefore relates to the thermal diffusivity and conductivity ratios G and G_2 according to

$$K = \frac{1}{G_2\sqrt{G}} \ . \tag{6.22}$$

The thermal activity ratio is a dimensionless quantity that expresses the fluid-to-solid thermal effusivity ratio, with $\sqrt{\lambda\rho c_p}$ the fluid thermal effusivity and $\sqrt{\lambda_s\rho_s c_{p_s}}$ the solid thermal effusivity. Roughly speaking, the effusivity of a material expresses its interfacial ability to exchange heat with its surroundings, thereby, K can express how effective is the thermal interaction between fluid and solid, including how temperature fluctuations may or may not be damped at the vicinity of the fluid-solid interface depending on the materials considered. In fact, this helps to better understand the simplifications intrinsic to the ideal conditions considered in the previous chapter, namely mixed-type (MBC) and isoflux (IF) [25]. MBC corresponds to $K = 0$ and consists of assuming that heat conduction in the wall is ideally more efficient than in the fluid and hence fluctuations are transported away from the wall quickly [27], this is expressed by the assumption of vanishing temperature fluctuations at the wall (see section 5.2.2). On the other hand, IF corresponds to $K = \infty$ and assumes that heat conduction is ideally more efficient in the fluid than in the solid and therefore turbulent fluctuations can plainly penetrate the conductive sublayer, this is represented for instance by the constant value (zero gradient) of the temperature variance across the conductive sublayer in Figure 5.11-middle. In this chapter, CHT simulations are performed for different combinations of material properties, i.e., different values of G and G_2, corresponding to distinct (and finite) values of the thermal activity ratio K. The behaviour of the CHT turbulence statistics is therefore expected to be found between the extreme cases delimited by MBC and IF [109, 106, 110].

In the following section, we provide a full description of the numerical strategy developed here

to simulate the CHT problem. More precisely, the numerical method implemented in Xcompact3d structure is described in details, namely the solver for the heat conduction equation as well as the techniques employed to couple DNS and thermal conduction solutions.

6.2 Numerical methodology

For the present computational configuration illustrated in Figure 6.3, fluid Ω_f and solid Ω_s subdomains are defined as

$$\Omega_f = \{(r,\phi,z) \mid r \in [0,R[,\ \ \phi \in [0,\ \ 2\pi], z \in [0,L_z]\} \quad , \tag{6.23}$$

and

$$\Omega_s = \{(r,\phi,z) \mid r \in [R,R_o],\ \ \phi \in [0,\ \ 2\pi], z \in [0,L_z]\} \tag{6.24}$$

respectively. A solver for the unsteady heat conduction in the solid is implemented in Xcompact3d and (weakly) coupled to the DNS solution in the fluid with the Neumann-Dirichlet coupling method of [113], which is described in details in section 6.2.3. The same finite-difference schemes for spatial differentiation and/or viscous filtering are kept for the solver of the solid energy equation.

This numerical methodology is an expansion of the strategy developed by [91] in the framework of channel flow with Incompact3d. Here, the method is expanded for a non-body fitted grid. Moreover, this approach is mainly based on the customised IBM to couple fluid and solid energy equations through thermal boundary conditions (TBCs) at the interface. In particular, the *dual* IBM technique of [91] is further developed for a non-body fitted grid, more details are given in section 6.2.2.

The numerical simulations presented in this chapter are computed at low Reynolds number $Re = 5300$ ($Re_\tau \approx 180$) for two Prandtl numbers $Pr = 0.71, 0.025$ representative of air and liquid metals respectively. A mesh of $n_x \times n_y \times n_z = 320 \times 320 \times 640$ points regularly distributed in a computational domain of dimensions $L_x \times L_y \times L_z = 1.6D \times 1.6D \times 12.5D$ is used, resulting in the same mesh resolution employed for the low Reynolds cases in the previous chapter: $\Delta x = \Delta y \approx 1.8$, $\Delta z \approx 7$. This same grid is used for the momentum, fluid/ solid energy equations at both Prandtl numbers considered. Tri-periodic boundary conditions are applied for the computational domain in all three Cartesian directions.

With a single velocity solution, several energy equations are solved in parallel to spare computational resources. More precisely, for the CHT simulations, 4 different combinations of fluid/solid material properties G and G_2 (representing different values of thermal activity ratio K according to eq.(6.22)) are considered for each Prandtl number, amounting to 8 CHT scalars. In addition, reference solutions with MBC and IF are also computed for each Pr with the same velocity field, adding 4 additional cases, which leads to 12 scalars in total. The different cases considered are listed in Table 6.1.

Table 6.1: Different TBCs considered for the multi-scalar simulation of the present chapter.

Label	**Pr**	**G**	$\mathbf{G_2}$	$\mathbf{K = (G_2\sqrt{G})^{-1}}$
1) MBC/0.71	0.71	-	-	0
2) IF/0.71	0.71	-	-	∞
3) CHT_{11}/0.71	0.71	1	1	1
4) CHT_{12}/0.71	0.71	1	2	0.5
5) CHT_{21}/0.71	0.71	2	1	0.71
6) CHT_{22}/0.71	0.71	2	2	0.35
7) MBC/0.025	0.025	-	-	0
8) IF/0.025	0.025	-	-	∞
9) CHT_{11}/0.025	0.025	1	1	1
10) CHT_{12}/0.025	0.025	1	2	0.5
11) CHT_{21}/0.025	0.025	2	1	0.71
12) CHT_{22}/0.025	0.025	2	2	0.35

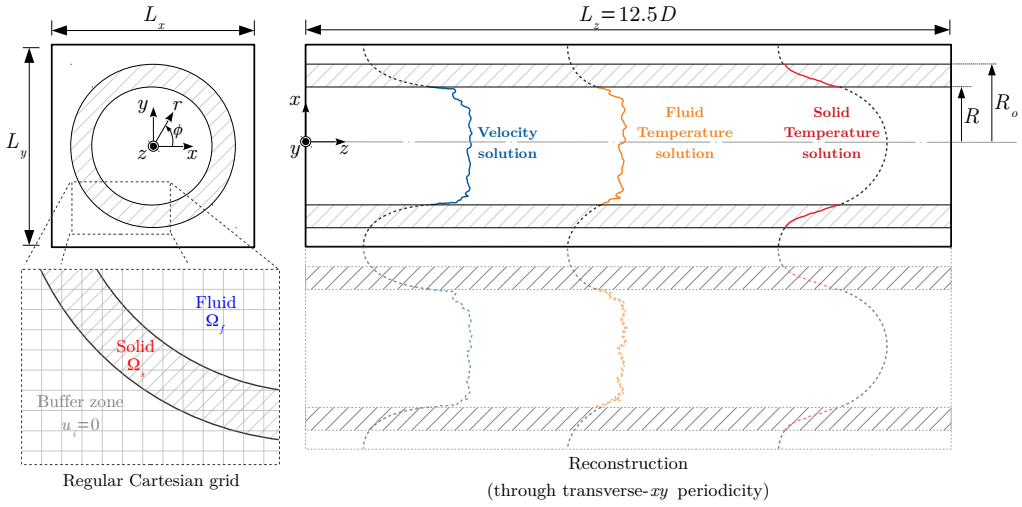

Figure 6.3: Schematic view of the computational configuration. The same regular Cartesian mesh is used to discretize fluid (Ω_f) and solid (Ω_s) subdomains. Physical solutions are represented by solid lines and reconstructed solutions by dashed lines. Lagrange reconstructions are performed separately for fluid and solid solutions in the present *dual*-IBM framework.

6.2.1 Governing equations

As already defined in section 6.1, buoyancy effects are neglected as well as any temperature dependence of fluid and solid material properties. We consider therefore a passive temperature field governed by the following equations [91]

$$\frac{\partial \Theta}{\partial t} + u_i \frac{\partial \Theta}{\partial x_i} = \frac{1}{Pe} \frac{\partial^2 \Theta}{\partial x_i \partial x_i} + f_\Theta \qquad \text{in} \quad \Omega_f \tag{6.25}$$

$$\frac{\partial \Theta_s}{\partial t} = \frac{1}{GPe} \frac{\partial^2 \Theta_s}{\partial x_i \partial x_i} \qquad \text{in} \quad \Omega_s \tag{6.26}$$

$$\Theta = \Theta_s \qquad \text{at} \quad r = R \tag{6.27}$$

$$\frac{\partial \Theta_s}{\partial r} = \frac{1}{G_2} \frac{\partial \Theta}{\partial r} \qquad \text{at} \quad r = R \tag{6.28}$$

$$\frac{\partial \Theta_s}{\partial r} = -\frac{1}{G_2} \frac{R}{R_o} \qquad \text{at} \quad r = R_o \ , \tag{6.29}$$

where $G = \alpha/\alpha_s$ and $G_2 = \lambda_s/\lambda$ are the thermal diffusivity and conductivity ratios respectively, the two independent non-dimensional parameters[1] needed to describe the fluid-solid thermal coupling as stressed by [102]. Θ and Θ_s are the fluid and solid temperature solutions respectively and, within the present *dual* IBM approach, they are computed separately, everywhere in the computational domain. Note also that the calculation of the solid temperature solution with eq.(6.26) is straightforward with the viscous filtering technique, more details are given in section 6.2.4.

Fluid and solid governing equations are coupled to each other through the TBCs (6.27-6.29) with a Neumman-Dirichlet coupling method. More precisely, TBC (6.27) is imposed to the fluid temperature as a Dirichlet boundary condition (DBC), whereas TBCs (6.28) and (6.29) are imposed to the solid temperature as Neumman boundary conditions (NBC). Moreover, TBCs (6.27) and (6.28) are co-dependent and they represent the continuity of temperature and heat flux at the inner interface respectively. The TBC (6.29) on the other hand, corresponds to a constant (time) and uniform (space) heat flux prescribed at the outer wall - i.e., an isoflux condition (IF) - following the simplified framework considered in section 6.1. To be consistent with the imposition of this constant and uniform heat flux, the dimensionless form defined for IF in the previous chapter (eq.(5.13)) is used here for both fluid Θ and solid Θ_s temperature fields. All the above TBCs are ensured with the present IBM by further adapting the DBC/ NBC techniques described in the previous chapter in order to be incorporated to the weak coupling technique, a full description is provided hereafter.

Because of the *dual* approach, the 8 CHT cases considered require the computation of both equations (6.25) and (6.26) in the entire computational domain, $8\times$ every time step. Additionally, the local imposition cases require 4 additional computations of eq.(6.25) with MBC or IF. That is, for the 12 scalars considered here, the fluid energy equation is solved $12\times$ per time step and the solid one $8\times$. In this sense, the viscous filtering technique and the advantageous massively parallel scalability of Xcompact3d were of utmost importance to perform this large simulation. The former on account of the relaxation on the stability constraint linked to the diffusivity, allowing for the use of larger time steps; while the latter enabled to handle the different time scales involved in the problem, making possible to simulate the long transient time required by the solid conduction equation.

6.2.2 Dual immersed boundary strategy

Although numerical investigations of the CHT problem are relatively recent, different techniques have been conceived and/or used to couple fluid and solid energy equations. As stressed by [91], most commonly in the general CHT framework with IBM, both fluid and solid solutions are computed together as a single temperature field and the switch from fluid (6.25) to solid (6.26) transport equation is usually achieved through a change of diffusion coefficients ($\alpha \leftrightarrow \alpha_s$) and the introduction (or suppression) of the volumetric source term f_Θ. Another technique is to compute fluid and solid solutions separately where each temperature field has its own physical domain and common boundary conditions ensure the physical coupling between them [91].

[1] The governing equations may also be expressed in terms of the thermal activity ratio $K = f(G, G_2)$, by following eq.(6.22).

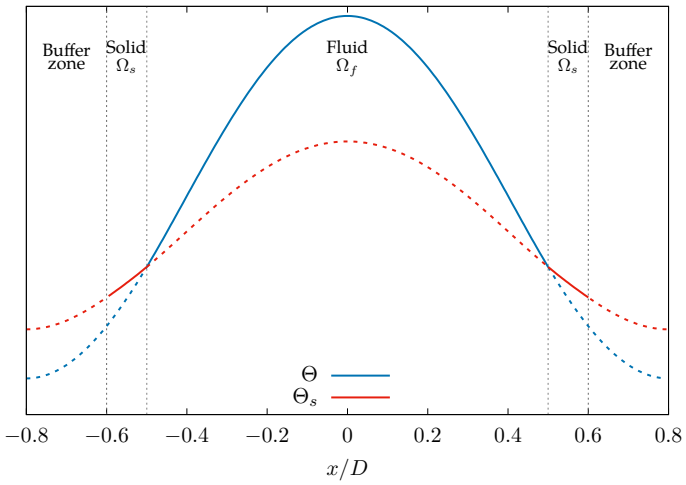

Figure 6.4: Lagrange reconstructions of fluid and solid solutions along a x-row with the *dual* IBM approach. The principle is exemplified for a thermal conductivity ratio $G_2 = 2$. Solid lines are physical solutions, dashed lines are reconstructed solutions.

As pointed out by [91], in most practical applications, thermal conductivities are different in the fluid and in the solid ($G_2 \neq 1$) and hence, because of the heat flux continuity, the wall-normal derivative of the temperature can become discontinuous. This hindrance is expressed by the dependence on G_2 in eq.(6.28) and exemplified in Figure 6.4 for $G_2 = 2$. The resulting lack of smoothness is an obvious obstacle in cases such as this, given the difficulty of numerically dealing with the loss of differentiability, especially in the present context, where the efficiency of our customised IBM has been demonstrated to be intrinsically linked to the use of high-order compact schemes (c.f. section 5.5.2).

In this regard, the dual IBM approach of [91] is expanded here to complex geometries. The approach is *dual* in the sense that fluid and solid temperature fields are defined separately, everywhere in the computational domain. In this way, the solid subdomain Ω_s is the immersed region for the fluid solution and the fluid subdomain Ω_s becomes the immersed region for the solid solution. Consequently, each temperature solution can be freely reconstructed without conflicting (replacing) the physical values of its counterpart and thus the the continuity of fluid and solid solutions are ensured separately, as illustrated in Figure 6.4. Furthermore, compact finite-difference operators of spatial derivatives and viscous filtering perceive a smooth interface for both Θ and Θ_s regardless of the value of G_2. The method is very suitable since not only the efficiency of the IBM is preserved but also a straightforward treatment for the discontinuity of the first-derivative at the wall is provided. The fact that both energy equations are solved everywhere in the computational domain can be seen as a drawback, the associated extra-cost once implemented in Xcompact3d's structure is +17%, which can be considered nonetheless secondary if the goal is to preserve accuracy [91].

As in the previous chapter, the reconstruction of the fluid temperature Θ is performed through the transverse-xy periodicity with fifth-order Lagrange polynomial interpolations (c.f. section 5.2.1). For the solid temperature Θ_s on the other hand, preliminary tests with higher-order polynomial functions presented a better performance to conserve first-derivatives of the logarithmic-like temperature profile[2] in the solid zone and thus, ninth-order Lagrange polynomial interpolations were used. Also, a larger buffer zone $r > R_o$ is required with respect to the computational configuration of the previous chapter in order to ensure the continuity of the reconstruction through xy periodicity for the solid temperature field. Instead of $L_x = L_y = 1.28D$, we use here $L_x = L_y = 1.6D$ with $n_x = n_y = 320$ points in order to keep the same transverse mesh resolutions $\Delta x^+ = \Delta y^+ \approx 1.8$. This switch from $n_x \times n_y = 256 \times 256$ to $n_x \times n_y = 320 \times 320$ nodes in the transverse-xy directions naturally leads to a moderate increase of the computational cost which again, we judge well-justified if the goal is to preserve the efficiency of the IBM.

6.2.3 Weak coupling technique

Fluid and solid energy equations are weakly coupled following the method of [113]. A strong coupling would require the simultaneous solution of eqs.(6.25-6.29) with, for instance, an iterative process, which can considerably increase the computational cost. With the weak coupling technique employed here however, the energy governing equations are sequentially solved while admitting a small discontinuity of the temperature at the interface. The same method has been successfully used by [91, 28, 110] in the framework of channel flow with Incompact3d.

The sequential time advancement is carried out every time step. Firstly, the fluid energy equation (6.25) is solved with TBC (6.27), which is prescribed as the DBC

$$\Theta|_w^{n+1} = \frac{\Theta|_w^n + \Theta_s|_w^n}{2} \quad , \tag{6.30}$$

where the superscript refers to the time-step number and the subscript w refers to the fluid-solid interface $r = R$. Note that for the present mesh arrangement disconnected from the body geometry, the immersed boundary location does not coincide with the Cartesian grid nodes and thus the local wall values $\Theta|_w^n$ and $\Theta_s|_w^n$ must be extrapolated. To do so, following the schematic representation in Figure 6.5, we employ the finite-difference extrapolation scheme (5.62) presented in the previous chapter

$$\Theta|_w^n = a_e \cdot \Theta|_i^n \quad + \quad b_e \cdot \Theta|_{i+1}^n + c_e \cdot \Theta|_{i+2}^n + d_e \cdot \Theta|_{i+3}^n \quad .$$

A Taylor expansion from the wall leads to system (5.63) (the grid resolution at the vicinity of the body Δx_w is defined with respect to the first fluid node, the variable r_i is introduced here to simplify the expressions)

$$r_i = \frac{\Delta x_w + i\Delta x}{\Delta x_w}$$

[2] As turbulent fluctuations are damped by diffusivity in the solid, the instantaneous temperature profiles of Θ_s present a laminar-like behaviour, following eq.(6.20).

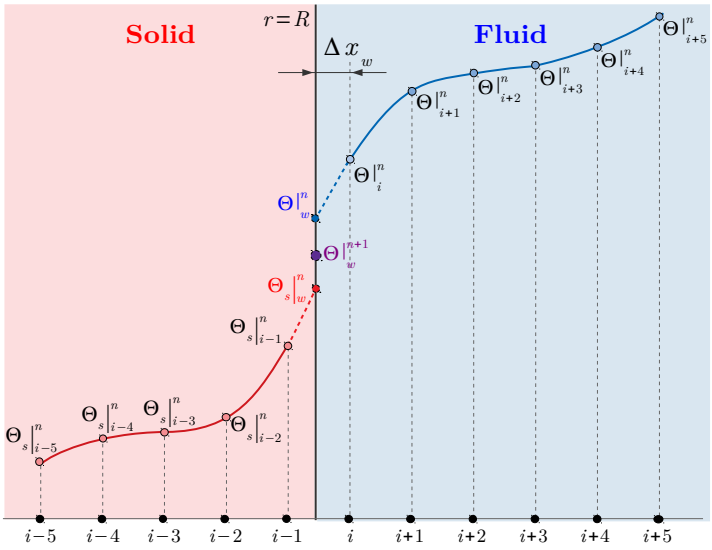

Figure 6.5: Schematic representation of the extrapolation stencils for the wall temperatures (fluid and solid) along a x-row. The grid resolution at the vicinity of the body Δx_w is defined as the distance between the interface and the first fluid node.

$$
\begin{aligned}
1 &= a_e + b_e + c_e + d_e && (\Delta x)\\
0 &= a_e + r_1 b_e + r_2 c_e + r_3 d_e && (\Delta x^2)\\
0 &= a_e + r_1^2 b_e + r_2^2 c_e + r_3^2 d_e && (\Delta x^3)\\
0 &= a_e + r_1^3 b_e + r_2^3 c_e + r_3^3 d_e && (\Delta x^4)
\end{aligned}
$$

Solving the above system for fourth-order accuracy[3] leads to the following set of coefficients

$$
\begin{aligned}
a_e &= \frac{r_1 r_2 r_3}{[(r_1-1)r_2 - r_1 + 1]r_3 + (1-r_1)r_2 + r_1 - 1}\\
b_e &= -\frac{r_2 r_3}{[(r_1-1)r_2 - r_1^2 + r_1]r_3 + (1-r_1)r_1 r_2 + r_1^2(r_1-1)}\\
c_e &= \frac{r_1 r_3}{[r_2^2 - (r_1+1)r_2 + r_1]r_3 - r_2^3 + (r_1+1)r_2^2 - r_1 r_2}\\
d_e &= -\frac{r_1 r_2}{r_3^3 - (r_1+r_2+1)r_3^2 + [(r_1+1)r_2 + r_1]r_3 - r_1 r_2}\ .
\end{aligned}
$$

[3] Lower-order extrapolation have been also considered as in chapter 5. However, tests showed that higher-order extrapolation is a better choice if the goal is to extrapolate Θ_w directly instead of the wall-tangential derivative $\left.\frac{\partial \Theta}{\partial \phi}\right|_w$.

Here, we have exemplified with the extrapolation of the fluid wall value $\Theta|_w^n$. Figure 6.5 illustrates however, how the same procedure is also applied for the solid side to extrapolate $\Theta_s|_w^n$. These extrapolated values are subsequently used to predict $\Theta|_w^{n+1}$, whose imposition is straightforward with the Lagrange reconstruction. Note that the finite-difference coefficients are geometry dependent because of the dependence on Δx_w and therefore fluid and solid coefficients differ from each other. In the code, they are defined before the time loop, from the local coordinates of the immersed boundary $r = R$ and initialized for fluid and solid as distinct 3×3 matrices.

Next, the solid energy equation (6.26) is solved with TBCs (6.28, 6.29) which are imposed as NBCs. At the outer wall "w_o", NBC (6.29) is the isoflux condition

$$\left.\frac{\partial \Theta_s}{\partial r}\right|_{w_o}^{n+1} = -\frac{1}{G_2}\frac{R}{R_o} \quad , \tag{6.31}$$

which is carried out with the IF technique introduced in the previous chapter. Here however, we consider this heat-flux as purely wall-normal while neglecting the effect of turbulence fluctuations that penetrate up to the outer surface[4] and hence the contribution of $\left.\frac{\partial \Theta}{\partial \phi}\right|_w$ (c.f. section 5.4.3) is simply taken as zero.

Now, to impose NBC (6.29) at the inner wall "w"

$$\left.\frac{\partial \Theta_s}{\partial r}\right|_{w}^{n+1} = \frac{1}{G_2}\left.\frac{\partial \Theta}{\partial r}\right|_{w}^{n+1} \quad , \tag{6.32}$$

the wall-normal derivative of the fluid solution (rhs) must be known. Favorably, its Cartesian components[5] can be straightforwardly computed from the fluid solution with the non-centred scheme (5.56) also introduced in the previous chapter

$$\left.\frac{\partial \Theta}{\partial x}\right|_{w}^{n+1} = a\ \Theta|_w^{n+1} + b\ \Theta|_{i+1}^{n+1} + c\ \Theta|_{i+2}^{n+1} + d\ \Theta|_{i+3}^{n+1} \quad ,$$

which is third-order accurate with the set the coefficients (5.60). Then, these Cartesian wall-derivatives are also ensured with the IF technique of the previous chapter. Also in this case, since the values of the Cartesian wall-derivatives can be directly determined, no estimation of $\left.\frac{\partial \Theta}{\partial \phi}\right|_w$ is required, which makes the imposition of NBCs in the CHT framework simpler than for IF. Still, both NBCs (6.31, 6.32) are ensured in two steps with the Lagrange reconstruction (Figure 5.5) as described for IF. More precisely, in the illustration of Figure 6.4, the reconstruction of Θ_s performed through the transverse-xy periodicity satisfies NBC (6.31) and the one performed through the fluid zone $r < R$ satisfies NBC (6.32). Also, it can be clearly seen how the IBM techniques presented in the previous chapter for MBC and IF provide the basis for coupling fluid and solid energy equations in the present CHT framework.

[4] By taking into consideration the damping of temperature fluctuations experienced in the solid zone. The effect of the TBC imposed at the outer wall is not investigated in this work.

[5] See eqs.(5.54, 5.55).

Since no iterative process is used, the sequential computation of fluid and solid solutions introduces a small temperature difference at the wall [91]. When using this same method, [28] mentioned that this discontinuity is negligible and the error introduced $\Theta|_w^{n+1} - \Theta_s|_w^{n+1}$ is first-order accurate in time, being controlled throughout the simulation by the application of scheme (6.30) at the beginning of every time step.

As stressed by [91, 28], the explicit nature of this weak coupling technique can introduce several numerical stability limitations. Yet, the consequent restriction on Δt can be alleviated if DBC and NBC are used for the fluid and solid fields respectively [113], as it is done here. This way, by using the viscous filtering technique, the CFL restriction in the fluid zone becomes stronger than the one related to the weak coupling, at least for $Pr = 0.71$. This would allow us to employ, *a priori*, the same time step used for the local imposition simulation, i.e. $\Delta t = 2.4 \cdot 10^{-3}$. Nevertheless, the more diffusive case with $Pr = 0.025$ required Δt to be cut by half in order to ensure stability. The source of such a restriction remains unclear, this is planned to be investigated in further work while relating this restriction to the investigations of [112].

6.2.4 Time integration

The viscous filtering technique is used here for momentum, fluid and solid energy equations. The time integration of the fluid temperature equation (6.25) uses the VF[1] approach for the diffusive term together with a third-order Adams-Bashforth scheme for the convective term, as given by eqs.(5.33, 5.34)

$$\begin{aligned} \Theta^* &= \Theta^n + \Delta t \sum_{j=0}^{p} a_j F^{n-j} \\ \Theta^{n+1} &= T_\Theta \Theta^* + \Delta t f_\theta^{n+1} \quad , \end{aligned}$$

which has been thoroughly discussed in the previous chapter, section 5.2.3. The source term f_Θ^{n+1} is consistently treated as for IF, as described in section 5.2.3.

With the viscous filtering technique, the time integration of the solid energy equation is straightforward and it can be expressed as

$$\Theta_s^{n+1} = T_{\Theta_s} \Theta_s^n \quad , \tag{6.33}$$

where T_{Θ_s} is the viscous filter transfer function (according to eqs.(2, 27) in chapter 4 [78]) and it represents the application of the discrete viscous filtering operator. Note that only one application of the viscous filter is required and the transfer functions T_Θ and T_{Θ_s}, associated to fluid and solid viscous filtering, are alike only if fluid and solid thermal diffusivities are equal, i.e. if $G = 1$.

6.2.5 Initial conditions

Fluid and solid temperature fields are initialized with the analytical solutions derived in the simplified framework discussed in section 6.1, they are given by eqs.(6.14, 6.20)

$$\Theta(r) = 2\left(\frac{3}{16} + r^4 - r^2\right) - \frac{1}{Nu} \qquad \text{in} \quad \Omega_f$$

$$\Theta_s(r) = \frac{R}{G_2}\,\ln\left(\frac{R}{r}\right) - \frac{1}{Nu} \qquad \text{in} \quad \Omega_s \ .$$

For the velocity, a fully developed turbulent field from a previous simulation is used. Turbulent fluctuations from the velocity field are then imparted to the fluid temperature field through the convective term in eq.(6.25), which, in turn, passes them on to the solid temperature field through NBC (6.28). As discussed in section 6.1, the infiltration of temperature fluctuations in the solid zone is a slow process which may require the computation of long transients. Therefore, for a matter of computational resources, a first complete CHT transient has been calculated for one single scalar with $G = 1$ and $G_2 = 2$ (corresponding to $K = 0.5$). Once fluid and solid solutions reach a statistically stationary state, they are then used as initial conditions for the other cases in Table 6.1. A new, still shorter, transient is required for each case and statistical sampling starts only when all 12 scalars have reached the statistically stationary state.

6.3 Results

In this section, results of validation are discussed for the present numerical strategy. First and second-order statistics as well as the budgets of temperature variance are assessed for the different combinations of fluid/ solid material properties reported in Table 6.1. More precisely, for the 12 temperature solution computed in parallel with a single velocity field, 4 of them are reference cases with MBC/IF and the remaining 8 consist of 4 CHT cases for each Prandtl number considered $Pr = 0.71, 0.025$. The DNS simulation is computed for a Reynolds number $Re = 5300$ with a corresponding friction prediction of $Re_\tau = 180.8$. Data is scaled in wall-units as for IF, according to Table 5.1.

In numerical terms, the treatment of CHT can be seen as combination of MBC for the fluid energy equation (prescription of DBC (6.30)) and IF for the solid (prescription of NBCs (6.31, 6.32)). Therefore, in the light of the validation of the IBM strategies for IF and MBC in the last chapter and given the lack of reference results for CHT with DNS of pipe flow, here, we compare our results (qualitatively) to those of [110], who performed DNS of channel flow with CHT at $Re_\tau = 150$ and $Pr = 0.71$ for different combinations of material properties. Also, as IF, MBC and CHT profiles tend to superimpose each other in the core region, zoomed views of the statistics are also provided for a better assessment of the near-wall behaviour of the quantities scaled in viscous units.

For both Prandtl numbers, Figure 6.6 shows no effect of the thermal boundary conditions (TBC) on the fluid mean temperature profile $(R-r)^+ > 0$, consistently with observations of [29, 28]. On the other

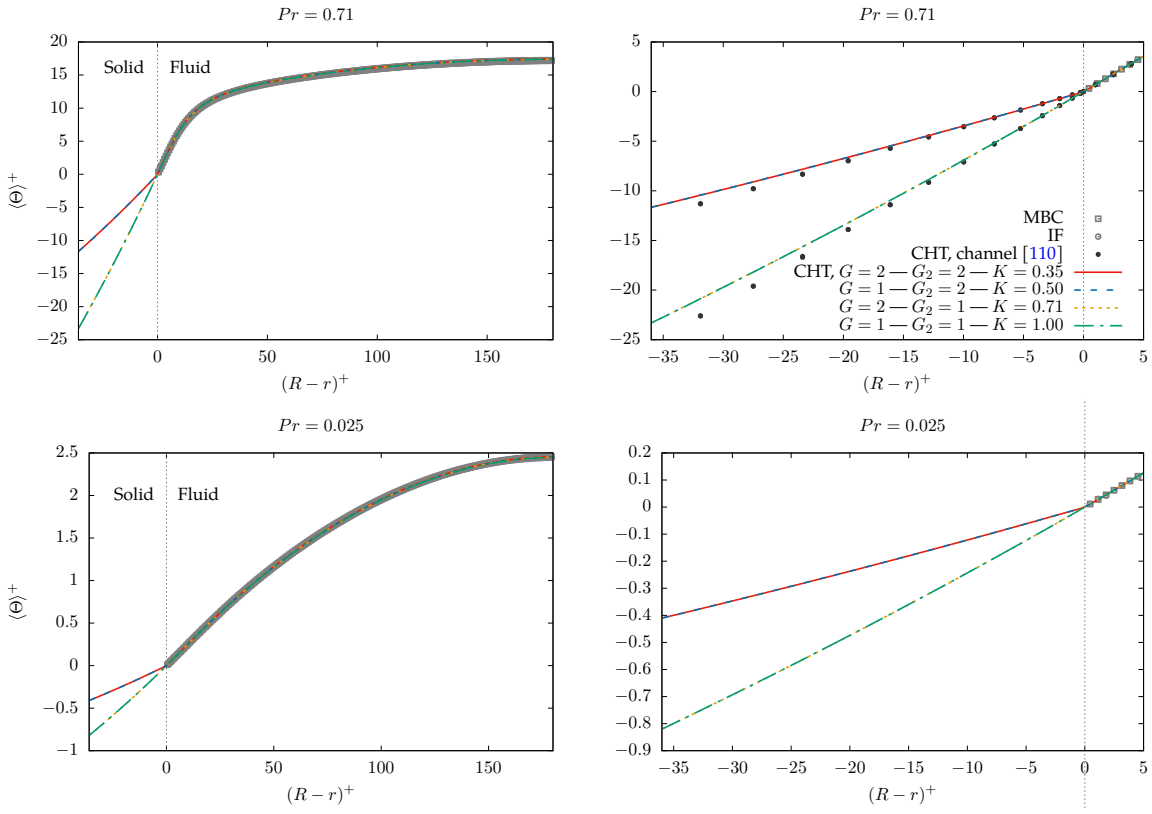

Figure 6.6: Mean temperature profiles with CHT for different combinations of material properties $K = f(G, G_2)$. (Top) $Pr = 0.71$ and (bottom) $Pr = 0.025$. Time average carried out over a time window $T_{stat} = 960D/U_b$.

hand, for the solid side $(R-r)^+ < 0$, the discontinuity on the first-derivative at the interface - provoked by the heat flux continuity condition (6.28) - occurs for the CHT cases with $G_2 = 2$ for both Prandtl numbers considered. These observations are in agreement with results of [25, 110]. Note that thanks to the *dual* immersed boundary technique, the smoothness of the temperature profile is successfully preserved despite this discontinuity and irrespective of the fact that the numerical differentiation for both fluid and solid energy equations are entirely based on high-order compact schemes.

For a channel geometry, the dimensionless mean temperature profile displays a linear decay in the solid zone [28, 91], for a pipe on the other hand, this decay is logarithmic-like, as an effect of the wall curvature, as expressed by eq.(6.10). Anyhow, for the wall thickness $(R_o - R) = 0.1D$ considered here, the wall curvature effect is not so pronounced and therefore does not fully prevent a qualitative comparison between the two cases in Figure 6.6-right. Indeed, pipe and channel profiles seem to follow

the same tendency while the increasing gap between the data observed as $(R-r)^+ \to -\infty$ (i.e., into the solid subdomain) may be associated to the difference in the flow regimes (Reynolds numbers) and the wall curvature effect.

The profiles of the temperature variance $\langle\Theta'\Theta'\rangle^+$ are reported in Figure 6.7 for both Prandtl numbers. Here again, for $Pr = 0.71$, the CHT profiles seem to follow the same trend as plane channel results of [110] into the solid zone $(R-r)^+ < 0$. For both Prandtl numbers, in the fluid zone $(R-r)^+ > 0$, CHT profiles are always delimited by the two ideal cases MBC and IF across the conductive sublayer while essentially superimposing each other away from the wall. Moreover, with increasing thermal activity ratio K, the profiles move from a MBC-like behaviour (which corresponds to $K = 0$) towards IF ($K = \infty$). These conclusions cannot be simply transposed to the solid domain as some of the profiles do cross each other with $Pr = 0.71$, highlighting the complex behaviour of the present conjugate cases where the thermal properties ratio G and G_2 are close to unity [110]. The same behaviour has been also observed by [110] in the channel flow framework. Furthermore, the discontinuity on the first-derivative provoked by the heat flux continuity condition (6.28) can be perceived also on the temperature variance profiles across the interface with increasing thermal conductivity ratio G_2.

Likewise, the streamwise heat flux profiles $\langle u_z'\Theta'\rangle^+$ reported in Figure 6.8 are also bounded by the two ideal cases MBC and IF, moving from a MBC-like pattern towards IF with increasing thermal activity ratio K. Nonetheless, this effect is less evident for this quantity than for the temperature variance since since the no-slip condition causes the streamwise heat flux to vanish at the wall.

Figure 6.9 provides spatial (top) and temporal (bottom) visualizations of the instantaneous temperature fluctuations

$$\Theta' = \Theta - \langle\Theta\rangle \tag{6.34}$$

in the fluid and solid domains with $Pr = 0.71$ and $G = 1$, $G_2 = 2$, case 4) in Table 6.1. For the sake of visibility, distinct scales are used for the color map in each subdomain and only the portion of the computational domain delimited by $\pi/2 \leq \phi \leq 3\pi/2$ and $0 \leq z \leq 3L_z/4$ is shown in the top figure. Indeed, in Figure 6.9-top, very dissimilar spatial structures can be clearly perceived in each subdomain, highlighting the different length scales involved in the CHT problem and the dynamics of the penetration of turbulent structures from the fluid into the solid domain. The same disparity can be also noticed for the time scales in the visualization of Figure 6.9-bottom for two sequential moments of the flow with $t2 > t1$. It can be seen that structures in the fluid zone are found to be substantially more active than their solid counterparts.

Next, the budgets terms of temperature variance - calculated with eqs.(5.72 - 5.75) - are compared for the different TBCs in Figure 6.10 for the case with $Pr = 0.71$. It can be seen that the production term $P^+_{k_\theta}$ is hardly affected by the TBC. Likewise, a small effect is perceived on the turbulent transport term $TD^+_{k_\theta}$. On the other hand, for the molecular dissipation term $\epsilon^+_{k_\theta}$, a progressive damping is observed across the conductive sublayer as $K \to \infty$. The same behaviour is observed for the molecular diffusion $MD^+_{k_\theta}$ as the two quantities balance each other at the wall. This balance explains the intermediary behaviour between IF and MBC observed for the CHT temperature variance profiles in Figure 6.7.

Flageul *et al.* [110] have shown that, in the case of CHT, the dissipation rate ϵ_{k_θ} across the fluid-solid

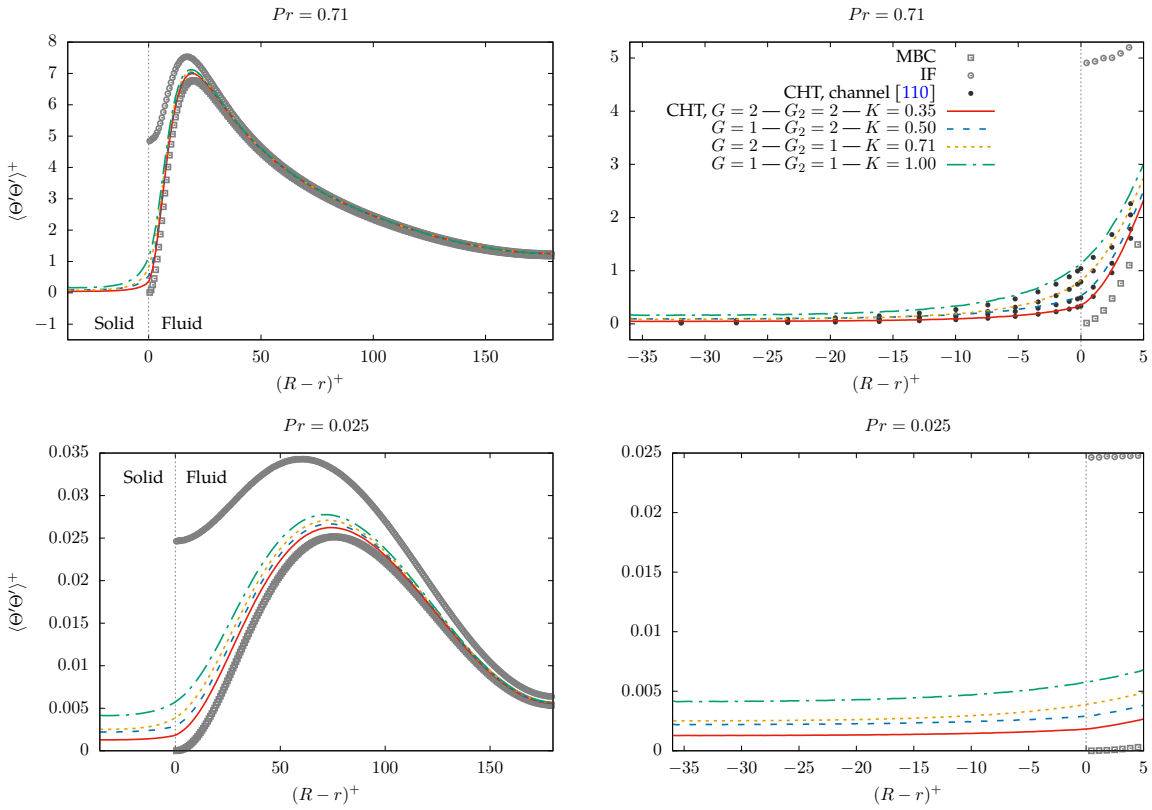

Figure 6.7: Temperature variance with CHT for different combinations of material properties $K = f(G, G_2)$. (Top) $Pr = 0.71$ and (bottom) $Pr = 0.025$. Time average carried out over a time window $T_{stat} = 960D/U_b$.

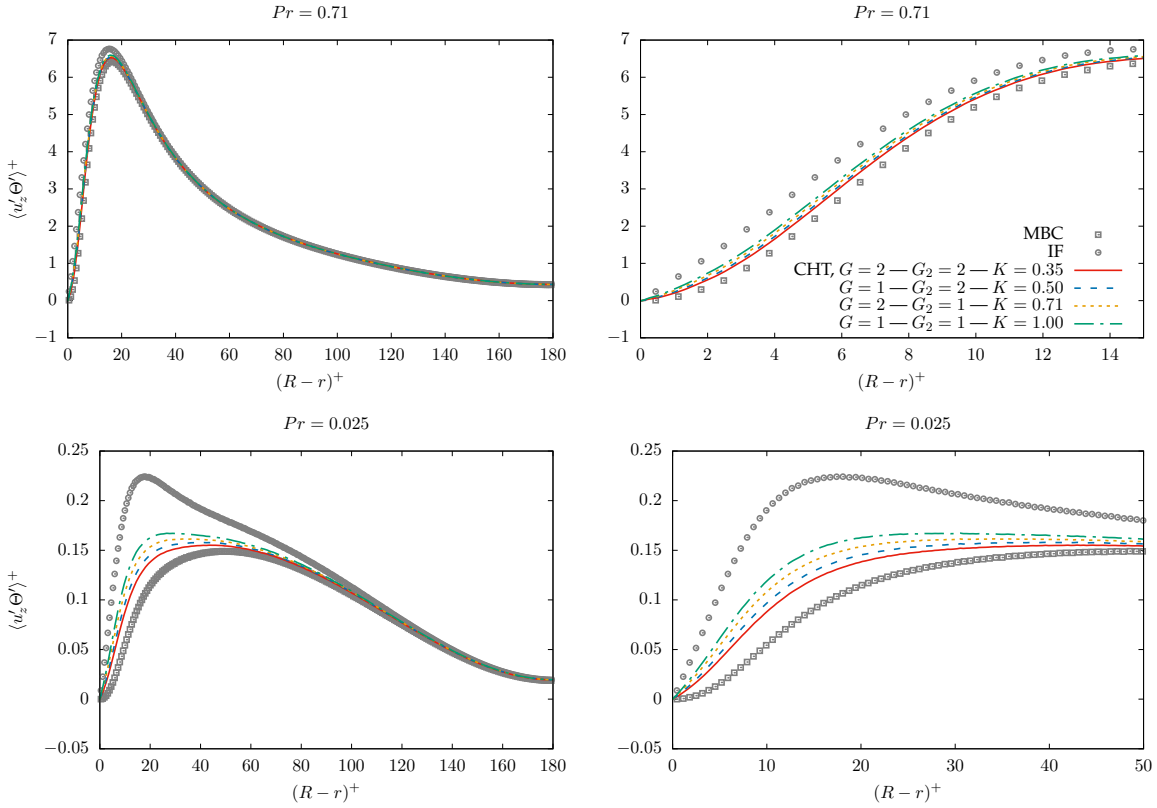

Figure 6.8: Streamwise heat flux (right) with CHT for different combinations of material properties $K = f(G, G_2)$. (Top) $Pr = 0.71$ and (bottom) $Pr = 0.025$. Time average carried out over a time window $T_{stat} = 960D/U_b$.

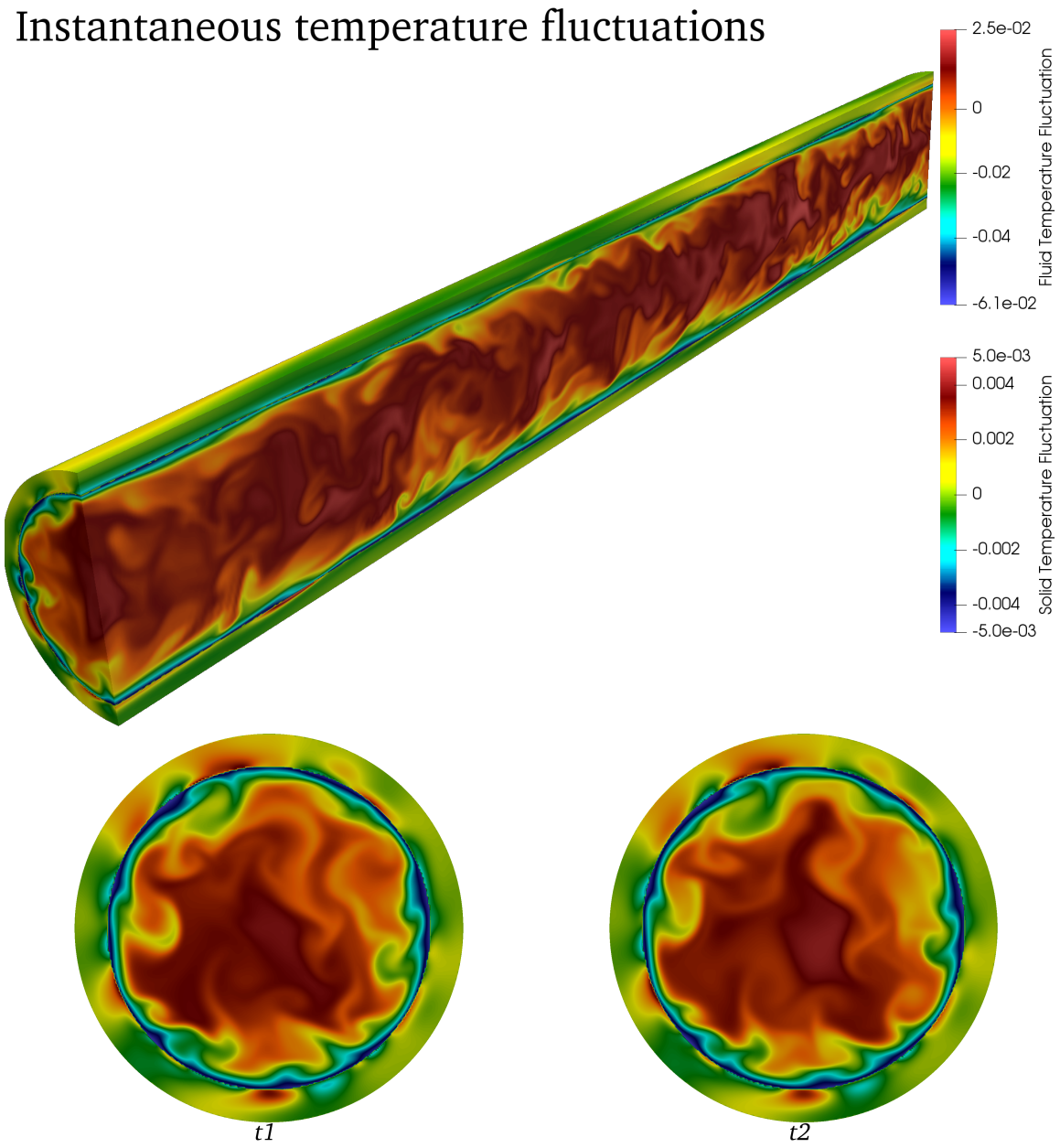

Figure 6.9: Visualization of the instantaneous temperature fluctuations in the fluid and solid subdomains for $Pr = 0.71$ and $G = 1$, $G_2 = 2$ ($K = 0.5$). (Top) Spatial distribution, (bottom) time evolution at two sequential time steps $t2 > t1$. Different scales are used for the color map.

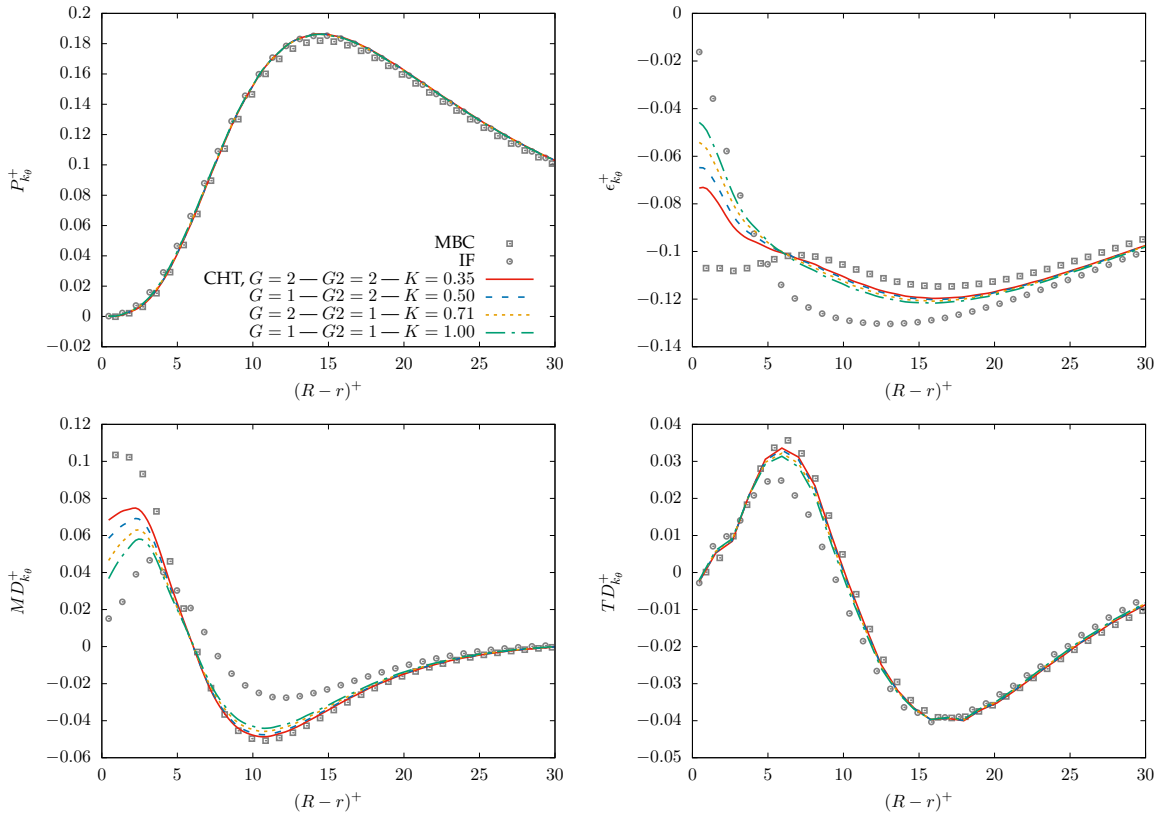

Figure 6.10: Budget terms of temperature variance with CHT with $Pr = 0.71$. (Top, left) Production, (top, right) Dissipation, (bottom, left) Molecular Diffusion and (bottom, right) Turbulent Transport are compared separately to MBC and IF results. For a better detailing of the near-wall region, the x-axis is limited to $0 < (R-r)^+ < 30$.

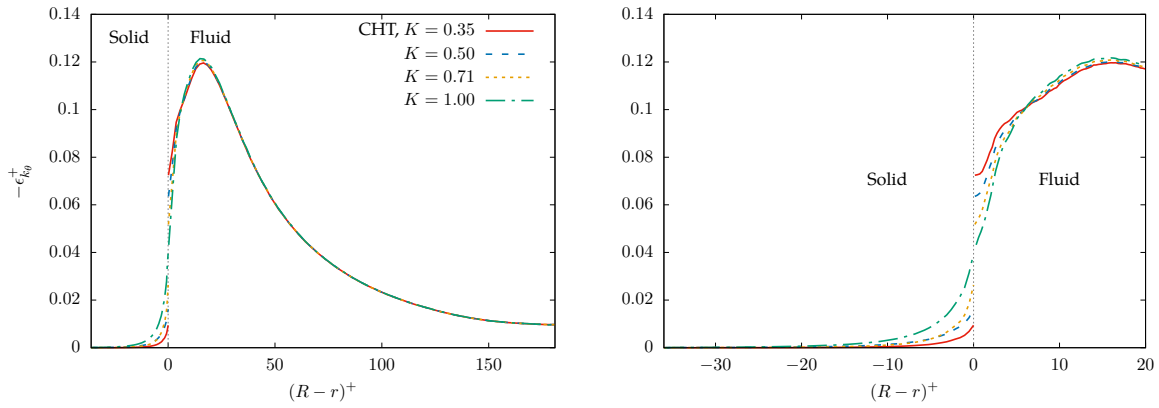

Figure 6.11: Dissipation rate $\epsilon^+_{k_\theta}$ across the fluid-solid interface for different combinations of fluid-solid material properties for the CHT cases with $Pr = 0.71$.

interface satisfies the following compatibility condition

$$\frac{\epsilon_{k_\theta,s}}{\epsilon_{k_\theta,f}} = \frac{\langle \partial_n \Theta' \, \partial_n \Theta' \rangle}{\langle \partial_i \Theta' \, \partial_i \Theta' \rangle} K^2 + \left(1 - \frac{\langle \partial_n \Theta' \, \partial_n \Theta' \rangle}{\langle \partial_i \Theta' \, \partial_i \Theta' \rangle}\right) \frac{1}{G}, \tag{6.35}$$

where $\epsilon_{k_\theta,f}$ and $\epsilon_{k_\theta,s}$ are the dissipation rates associated with fluid and solid temperature variance respectively and ∂_n denotes the wall-normal derivative. Thus, any ratio $\frac{\epsilon_{k_\theta,s}}{\epsilon_{k_\theta,f}} \neq 1$ corresponds to a discontinuity of the dissipation rate ϵ_{k_θ} across the fluid-solid interface. This behaviour was consistently verified by [110] from DNS results in the context of a flat channel flow and here, it can be observed in Figure 6.11 for the present pipe geometry for the CHT cases with $Pr = 0.71$. The discontinuity of the dissipation across the fluid-solid interface is visible for all cases, except for the combination $G = 1$ $G_2 = 1$ $K = 1$, consistently with eq.(6.35). These results are in qualitative agreement with those reported in [110] in the channel flow framework.

Despite the satisfactory results obtained for the analysis of the budget terms, it must be recognised that the closest nodes to the wall are not free of influence from the reconstruction technique. More precisely, an assessment of the Cartesian data cloud of the budget terms[6] showed that mesh nodes at a distance smaller than the mesh resolution itself - that is $(R-r)^+ < 1.8$ - have their behaviour affected by the Lagrange polynomial interpolation used. This seems to be linked as well to the use of compact schemes for the computation of derivatives required to calculate the budget terms with eqs.(5.72 - 5.75). This side-effect jeopardizes mostly the reproduction of the asymptotic behaviour of derivatives of averaged quantities such as for the molecular dissipation term in eq.(5.74)

$$MD_{k_\theta} = \frac{\alpha}{2} \frac{\partial^2 \langle \Theta' \Theta' \rangle}{\partial x_i \partial x_i}$$

[6]That is, prior to perform the azimuthal-ϕ projection, see discussions in section 2.8.

and for the turbulent transport term in eq.(5.75)

$$TD_{k_\theta} = -\frac{1}{2}\frac{\partial\langle u_i\Theta'\Theta'\rangle}{\partial x_i} \quad .$$

This problem may be better handled by using, for instance, a reconstruction that takes into account the asymptotic behaviour of first derivatives such as a cubic spline interpolation. Such an interpolation technique has been already introduced in Xcompact3d by [114] and shall soon be tested for the present computational configuration.

6.4 General conclusion

This chapter is dedicated to the development and validation of a numerical technique for the simulation of Conjugate Heat Transfer (CHT) in turbulent pipe flow. This technique is based on an immersed boundary method (IBM) to prescribe both Dirichlet (DBC) and Neumann (NBC) boundary conditions in a configuration where the mesh arrangement is disconnected from the wall geometry. Moreover, the *dual* IBM approach of [91] is expanded to the present non-body fitted configuration resulting in a versatile strategy for CHT simulations. The solver for the heat conduction in the solid is incorporated in Xcompact3d and, by means of the Neumann-Dirichlet coupling method of [113], the solid solution is (weakly) coupled to DNS results in the fluid, ultimately providing a high-fidelity description of the thermal interaction between fluid and solid subdomains. It has been also described how the IBM techniques introduced in the previous chapter for MBC and IF provide the basis for coupling fluid and solid energy equations in the present CHT framework. Consistent results of validation are presented, including budgets of temperature variance, which makes of this numerical approach an attractive tool for RANS modelling development. However, some stability aspects of the technique remain to be in order to make the coupling method numerically stable for any value of the thermal conductivity ratio G_2. The technique has been implemented in terms of the normal and tangential surface directions which means that the validation presented here for a pipe geometry can be seen as prototype to investigate, in further work, conjugate heat transfer in more complex geometries such as solar power plants and T-junction flow.

Version française

Ce chapitre est dédié au développement et à la validation d'une technique numérique pour la simulation du transfert thermique conjugué (CHT) dans un écoulement turbulent. Cette technique est basée sur une méthode de frontières immergées (IBM) qui nécessite de prescrire à la fois des conditions aux limites de Dirichlet (DBC) et Neumann (NBC) dans une configuration où l'organisation du maillage est déconnectée de la géométrie de la paroi. L'approche IBM *duale* de [91] est étendue à la configuration actuelle considérée comme une géométrie générique utile pour élaborer une stratégie de traitement d'un cas CHT en géométrie complexe. Le solveur pour la conduction thermique dans le solide est incorporé à Xcompact3d et, à travers la méthode de couplage Neumann-Dirichlet de [113], la

solution solide est (faiblement) couplée à son homologue dans le fluide, fournissant ainsi une description haute-fidélité de l'interaction thermique entre les sous-domaines fluide et solide. Il est également décrit comment les développements IBM introduits dans le chapitre précédent pour les cas MBC et IF fournissent les outils techniques permettant de coupler les équations d'énergie fluide et solide dans le cadre CHT de ce chapitre. Des résultats de validation cohérents sont présentés, ceci comprenant des bilans de variance de température, ce qui confirme le potentiel de la présente approche pour la production de bases de données utiles aux développements pour la modélisation RANS. Cependant, certaines contraintes liées à la stabilité numérique restent à lever pour conserver une bonne efficacité de calcul quel que soit le rapport de conductivité thermique G_2. La technique a été mise en œuvre par distinction entre composantes normale et tangentielle localement à la surface, ce qui signifie que la géométrie cylindrique considérée ici peut être vue comme un prototype de géométrie complexe qui peut se définir indépendamment de la topologie du maillage. Ceci conduira à court terme à la réalisation de simulations en géométrie réaliste telle que celle d'un Té de mélange avec plus largement des applications dans le cadre des centrales nucléaires ou solaires.

Chapter 7

Conclusion and Perspectives

The study of wall-bounded turbulence is very pertinent as most turbulent flows present in engineering applications are bounded by solid surfaces. For instance, the turbulent pipe flow - the subject of interest of the present investigations - has a wide spectrum of industrial applications, being found in nearly every engineering design. More specifically, our ultimate goal here is to develop an efficient and accurate numerical tool for the high-fidelity simulation of Conjugate Heat Transfer (CHT) in wall turbulence. Throughout the last three years, by means of Direct and Large-eddy simulations (DNS/LES), the method has been progressively developed in order to finally grow into the desired high-fidelity technique. The various numerical developments implied are implemented in Incompact3d/Xcompact3d [7, 11, 12], a massively parallel open-source code that offers a range of profitable numerical features to investigate incompressible (and low-Mach) turbulent flows, among which we may highlight its spatial differentiation - mainly based on compact finite-difference schemes of sixth-order accuracy, which provides quasi-spectral accuracy - and the treatment of complex geometries, thanks to the efficient IBM of [67, 50] based on Lagrange reconstructions of the physical solution into the immersed region.

Also, in Incompact3d/Xcompact3d, an extra-numerical dissipation can be flexibly introduced at small scales through the computation of second derivatives. In section 2.6.3 it is shown that this technique is equivalent to the use of Spectral Vanishing Viscosity (SVV) and, therefore, it can be seen as a subgrid-scale (SGS) model [81, 65]. Since the modelling is entirely contained in the regularisation provided by the artificial dissipation, this methodology is referred to as implicit SVV (ISVV), an implicit LES (ILES) technique. Furthermore, the use of numerical dissipation is not limited to LES but finds also applications in DNS as it enables us to control numerical oscillations arising at the smallest scales (mesh size), which are inevitably compromised when finite-difference is used [90]. In this regard, in chapter 3, the regularisation provided by the technique have allowed us to ensure DNS accuracy at marginal resolution. Also in chapter 3, it is shown that in the LES context, ISVV displays an *implicit* wall-modelling feature. The term *implicit* is used to emphasize the capability of the methodology to regularise the solution in the near-wall region without any explicit wall-model despite the use of mesh

resolutions that structurally bypass the viscous sub-layer and even the near-wall production region. Ultimately, the improvement observed is achieved thanks to the damping of spurious oscillations provided by the hyperviscous second derivative operator together with the use of high-order schemes and irregular distribution of mesh nodes with respect to the wall geometry.

Then, in chapter 4 [78], a novel solution filtering technique is presented. This approach is equivalent to the use of ISVV and it can be interpreted as the counterpart of the above mentioned hyperviscous second derivative schemes. Within the viscous filtering framework, the extra-numerical dissipation is no longer introduced through the computation of second derivatives, instead, it consists of designing the coefficients of a finite-difference filter to provide both the molecular and artificial dissipations. This way, by filtering the solution every time step, diffusive terms can be actually removed from the governing equations and a substantial relaxation on the diffusivity constraint is obtained, allowing us to use much larger time steps. The implementation of this technique has been of major importance for advancement of this thesis, as it reinforced the strength of the numerical method for the subsequent heat transfer simulations. In chapter 4 [78] for instance, it is shown that for a DNS of heat transfer in turbulent pipe flow with $Re = 5300$ and $Pr = 0.025$, the viscous filtering technique enabled the use of a $30\times$ larger time step with respect to the full-explicit time integration with third-order Adams-Bashforth used before, leading to -95% saving of computational resources.

Having established a solid numerical base, the IBM is now subjected to further developments in chapters 5 and 6 in order to allow the prescription of thermal boundary conditions (TBCs) as well. Moreover, in chapter 5, local imposition is considered with two ideal TBCs, namely mixed-type (MBC) and isoflux (IF). The prescription of MBC is straightforward with the present IBM as it consists of imposing a constant (time) and uniform (space) Dirichlet boundary condition (DBC) at the fluid-solid interface, which follows the same procedure as for the no-slip condition. Thus, the main focus of chapter 5 is the development and validation of a robust IBM strategy for the prescription of IF, which consists of imposing a constant and uniform Neumann boundary condition (NBC) at the fluid-solid interface. Within the present IBM, boundary conditions are to be ensured during the Lagrange reconstruction, which only imposes DBC (a finite value of the solution) at the wall, and thus a NBC (a finite value of wall-normal derivative of the solution) must be indirectly satisfied. This is done by following the strategy proposed by [103] and extended to IBM by [74], where a NBC is virtually ensured through the imposition of a target DBC, so that the desired derivative value (i.e. the NBC) shall be approximately recovered when first derivatives are computed with the sixth-order compact schemes used in the code.

However, the proper prescription of NBC in the present computational configuration must still deal with another hindrance. In fact, when a non-body fitted grid is used, the imposition of a wall-normal first-derivative - while leaving free the tangential one - represents a real challenge. More precisely, as the cylindrical pipe geometry is discretized with a Cartesian grid, the imposition of the NBC must be decomposed into its Cartesian components, which requires the knowledge of the wall-tangential component. To overcome this obstacle, a method based on extrapolation is proposed in chapter 5 and various techniques are tested. Ultimately, a robust and efficient strategy is chosen and consistent results of validation are presented for IF, including budgets of temperature variance. Results of validation for MBC focus rather on the advantageous numerical features of the present numerical tool. Still in chapter 5, the particularities of each TBC are highlighted through direct comparison between IF and MBC results.

The validation of numerical techniques for MBC (imposition of DBC) and IF (imposition of NBC) provided in chapter 5 serves as a pathway to develop a numerical methodology for the simulation of CHT in turbulent pipe flow, the subject of chapter 6. To tackle the CHT problem, the code Xcompact3d is further developed to include a solver for the heat conduction in the solid which is coupled to DNS results in the fluid, providing a high-fidelity description of the thermal interaction between the two physical media. Fluid and solid solutions are (weakly) coupled through TBCs at the fluid-solid interface. More precisely, the Neumann-Dirichlet coupling method of [113] is used while relying on the above mentioned IBM strategies to impose DBCs and NBCs on the fluid and solid solutions respectively. Furthermore, the dual IBM approach of [91] is expanded to the present non-body fitted configuration resulting in a versatile strategy for CHT simulations in pipe configuration. Consistent results of validation are presented including budgets of temperature variance, which makes of this numerical approach an attractive tool for RANS modelling development. Nonetheless, some stability aspects of the technique remain to be understood more in-depth in order to make the coupling method numerically stable for any value of the thermal conductivity ratio G_2.

Perspectives

The pipe flow configuration is considered in this work as a prototype of complex geometry in the sense that the computational mesh does not fit the wall geometry. This way, the IBM strategies for IF and CHT developed in chapters 6 and 5 have been conveniently implemented in Xcompact3d in terms of the normal and tangential surface directions. This enables us to promptly treat more complex geometries such as the T-junction flow, which is scheduled to be studied as a continuation of this work. Besides the fluid/solid thermal treatment, in order to investigate the T-junction flow in fully developed turbulent conditions, inflow conditions will be generated through a direct recycling, following the technique of [115]. The method has been already implemented for the present pipe configuration and consistent results of validation have been obtained.

Although good results could be obtained with the numerical strategy developed for CHT in chapter 6, simulations have been only performed for combinations of material properties G and G_2 around unity, which corresponds to a narrow range of thermal activity ratios $0.35 \leq K \leq 1$. In order to expand these studies, the stability characteristics of the coupling technique - based on the Lagrange reconstruction IBM and extrapolation - must be investigated more in-depth.

The Pao-filtering technique, described in section 3.3.1, remains to be tested with the new reconstruction technique (section 5.2.1). More precisely, the problem observed *a priori* and *a posteriori* related to a poorly ensured no-slip condition may be better managed with the new reconstruction technique. In addition, this new version of the reconstruction showed a dependence on the transverse-xy dimensions of the computational domain, which has not yet been thoroughly investigated. Other interpolation functions shall also be tested for the reconstruction. Since the present IBM has been developed [67, 50], Lagrange polynomials have been continuously used to prescribe Dirichlet conditions at the interface. Yet, for the numerical developments brought about in this work, other strategies may be also interesting to be considered, such as a cubic spline interpolation. This type of reconstruction has been recently

implemented in Xcompact3d [114] and it offers the advantage of taking into account the asymptotic behaviour of first derivatives in its formulation, which may be advantageous for the indirect imposition of Neumann conditions proposed here (section 5.4.2) as well as for the computation of budget terms very close to the wall (see discussion in section 6.3).

Concerning the present ILES technique, the formalism proposed by [65] assumes homogeneous and isotropic turbulence. For a more consistent utilisation in wall-bounded configurations, the development of an in-homogeneous and anisotropic formalism is scheduled.

As the prescription of Neumann boundary conditions with our IBM is now possible, a wall-layer model could also be included in the code to be used in ILES simulations. This would allow us to investigate whether the association of an explicit wall-layer model with the implicit improvement provided by the ISVV technique can improve or not the results presented in chapter 3 and/or perform ILES at even higher Reynolds numbers.

Appendix A

Conference Papers

ERCOFTAC Series

Manuel García-Villalba
Hans Kuerten
Maria Vittoria Salvetti *Editors*

Direct and Large Eddy Simulation XII

DLES 2019

Springer

Chapter 56
Implicit Wall-Layer Modelling in Turbulent Pipe Flow

R. Vicente Cruz, E. Lamballais and R. Perrin

Introduction

In the context of large eddy simulations (LES) of wall-bounded turbulence, the explicit calculation of all the energy-containing near-wall eddies is a key point. To accomplish this goal, it is recommended the employment of a mesh resolution between 10 and 100 wall units for the streamwise direction discretization, from 10 to 20 wall units in the spanwise direction, and typically one wall unit in the wall normal direction through a near-wall mesh refinement. When these resolution criteria are too demanding in terms of computational resources, an alternative is to use a discretization that bypasses the inner layer with the aid of a wall-layer model [1, 2].

However, it was shown by [3] that excellent basic turbulent statistics in a pipe flow can be obtained with a mesh resolution coarser than the viscous sublayer without using any explicit wall-layer modelling. In this context, the near-wall regularization is simply performed by means of an original and robust implicit LES (ILES) technique that—without any extra cost or adaptation in the near-wall region—displays a wall modelling feature. Two Reynolds numbers $\mathrm{Re}_\tau = 180{,}550$[1] were considered when comparing ILES results to unfiltered DNS data of [4].

The term implicit LES refers here to the use of regularization as a substitute of subgrid-scale (SGS) modelling [5, 6]. The originality of the method is found

[1] Based on the friction velocity u_τ and the pipe radius R.

R. Vicente Cruz · E. Lamballais (✉)
Incompressible Turbulence and Control Group, Pprime Institute,
CNRS-Univ-Poitiers-ISAE/ENSMA, Poitiers, France
e-mail: eric.lamballais@univ-poitiers.fr

R. Perrin
Department of Mechanical Engineering, Faculty of Engineering at Sriracha,
Kasetsart University Sriracha Campus, Sriracha, Chonburi 20230, Thailand

M. García-Villalba et al. (eds.), *Direct and Large Eddy Simulation XII*,
ERCOFTAC Series 27,
https://doi.org/10.1007/978-3-030-42822-8_56

in the built-in numerical dissipation that does not come from the discretization of the convective term, but from the viscous term in the Navier–Stokes equation. This strategy has also been used successfully by [7, 8] for turbulent plane channel and impinging jet configurations with regular Cartesian meshes, nonetheless, the near-wall behaviour of the implicit SGS modelling was not specifically investigated.

Until now, the aforementioned conclusions about the ILES technique performance were based on comparisons of basic statistics with unfiltered DNS data, which means that even if a good agreement was observed, no rigorous assessment could be made. In the present investigation, this matter is examined at higher Reynolds number ($\mathrm{Re}_\tau = 1000$) while determining to what extent it can be generalized in terms of near-wall region bypass. To do so, a quasi-DNS database is presented with an original method to easily produce filtered statistics in order to enable rigorous comparisons with ILES at any mesh resolution. The implicit LES results are, thus, analysed in terms of ability to predict near-wall statistics despite the use of very coarse grid for which even the near-wall turbulent production region is fully bypassed.

Numerical Method and Computational Configuration

As a generic numerical tool to investigate this concept of implicit LES, the sixth-order flow solver Incompact3d is used. Thanks to its features of kinetic energy conservation[2] and flexibility for the application of numerical dissipation, this code enables an easy calibration of the implicit SGS modelling. In particular, the role of its scale selectivity has been shown in [6] through rigorous comparisons with DNS results based on a priori and a posteriori analysis with a particular attention to distant triad interactions between SGS and very large scales [5]. In addition, it was shown by [6] that the present implicit LES technique is equivalent to the use of spectral vanishing viscosity (SVV), ensuring high-order accuracy and flexible application. In previous studies using the method [5, 6], the validation framework was based on the Taylor–Green Vortex problem as a prototype of wall-free turbulent flow.

As in [3], a regular Cartesian mesh is combined with the use of an immersed boundary technique to discretize the pipe geometry while considering periodic boundary conditions in the three spatial directions. A one-dimensional reconstruction method [9] is used inside the solid to ensure the smoothness of the solution everywhere in the computational domain. This feature clearly improves the accuracy of compact finite difference schemes as used in the code Incompact3d.

[2] In the discrete and inviscid sense up to the time advancement error.

Filtered Quasi-DNS Database

Quasi-DNS of pipe flow is performed at $\mathrm{Re}_\tau = 1000$ in order to, afterwards, produce the filtered benchmark database for comparison with ILES results. A mesh of $n_x \times n_y \times n_z = 768 \times 768 \times 1920$ cells was used, corresponding, in wall units to $\Delta x^+ = \Delta y^+ = 2.9$ and $\Delta z^+ = 13$. The term "quasi" is naturally used due to the employed mesh resolution, however, as shown in Fig. 56.1, thanks to the success of the technique, a very good agreement with DNS data of [4] is found.

As in [5], the filter is chosen to take the implicit SGS dissipation into account using a spectral Pao-like closure. By specifying the ratio between DNS and LES mesh resolutions, this Pao-like closure provides the spectral transfer functions that are used to define the targeted LES solution. Thus, this targeted solution is determined rigorously and consistently with the artificial dissipation implicitly introduced by the error differentiation in the present ILES framework [6]. The use of periodic boundary conditions enables the application of the present homogeneous filter defined in the Fourier space. The filter is applied once in every direction to take the anisotropy of the LES mesh into account. Following this procedure, a consistent framework is established for rigorous comparisons between LES and filtered DNS data.

The filter effect over streamwise-z and normal xy-directions separately is shown in Fig. 56.2. Acting as a pre-analysis, this information guided the choice of interesting mesh resolutions based on the levels of energy $k = \frac{1}{2}\langle u_i u_i \rangle$ to be potentially captured when the viscous and even near-wall production regions are bypassed. It is important to emphasize that the application of filter in normal xy-directions is only possible thanks to the solution smoothness provided by the reconstruction. As shown in Fig. 56.3, if no extension of the fluid solution is made into the solid zone before filtering, the no-slip condition is poorly ensured and near-wall region results are not reliable, a problem that is strongly reduced with the reconstruction. Nonetheless, reconstruction's ability to ensure the success of normal direction filtering is limited to not so high values of the filter width, as shown in Fig. 56.2 left by the abnormal near-wall behaviour when data is filtered at a corresponding cell

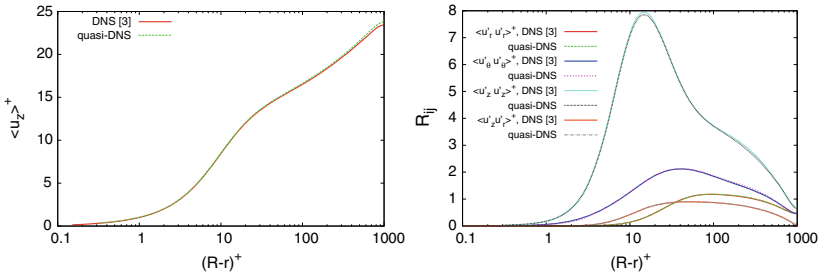

Fig. 56.1 Mean velocity (left) and Reynolds stresses profiles (right) for the quasi-DNS at $\mathrm{Re}_\tau = 1000$ compared to DNS statistics of [4]

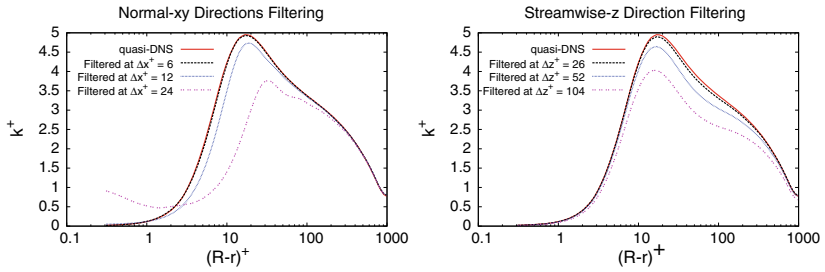

Fig. 56.2 Turbulent kinetic energy from filtered quasi-DNS at different mesh resolutions. The drop of energy is analysed for filtering along (left) streamwise-z direction and (right) normal-xy directions

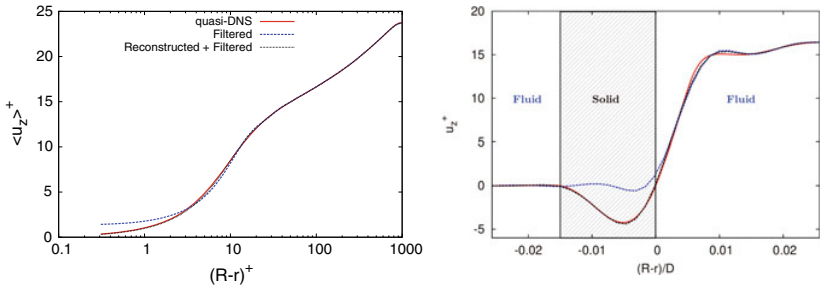

Fig. 56.3 Comparison of mean (left) and instantaneous (right) velocity profiles demonstrates the effect/necessity of reconstruction on the reliability of data filtered in the normal Cartesian directions (x, y). In this illustration, quasi-DNS data have been filtered at a corresponding mesh resolution of $\Delta x^+ = \Delta y^+ = 12$

size $\Delta x^+ = \Delta y^+ = 24$. For $\Delta x^+ = \Delta y^+ = 15$, the unrealistic near-wall rising of the turbulent kinetic energy k can be avoided, but persistent velocity fluctuations are observed close to the wall with for instance $k^+ \approx 0.156$ at $(R - r)^+ \approx 1.03$ to be compared to $k^+ \approx 0.124$ for the reference non-filtered value. Here, we have chosen to limit our analysis to $\Delta x^+ = \Delta y^+ = 12$ for which the filtering procedure produces also $k^+ \approx 0.124$ at this near-wall location.

LES Results

Before proceeding to the results, it is important to highlight that the term "implicit wall-layer modelling" is used to emphasize the ability of the present methodology to regularize the solution in the near-wall region without any explicit wall model. The improvement brought by the technique is the simple result of a targeted choice of

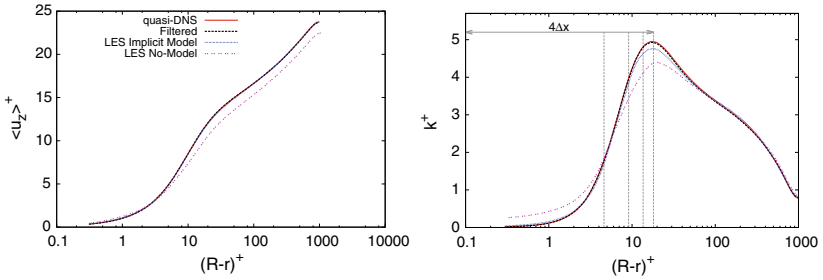

Fig. 56.4 Mean velocity profile (left) and Reynolds stresses profiles (right) for the Marginal Resolution ILES at $\mathrm{Re}_\tau = 1000$. Results are compared to: no-model LES, unfiltered and filtered quasi-DNS statistics

coefficients for the centred compact finite difference scheme used for the discretization of the viscous term in the Navier–Stokes equations [3].

For a Reynolds number of $\mathrm{Re}_\tau = 1000$, two implicit LES have been performed using: (i) Marginal Resolution: $n_x \times n_y \times n_z = 512 \times 512 \times 1280$ cells, corresponding in wall units to $\Delta x^+ = \Delta y^+ \approx 4.5$, $\Delta z^+ \approx 19.5$; and (ii) Low Resolution: $n_x \times n_y \times n_z = 256 \times 256 \times 960$ cells, expressed in wall units: $\Delta x^+ = \Delta y^+ = 12$, $\Delta z^+ = 26$. Mesh resolutions were chosen in order to evaluate the method performance in terms of viscous and near-wall production region bypass, respectively. The implicit wall modelling feature of the present approach is evidenced by comparing ILES to no-model LES results performed without any (implicit or explicit) SGS/wall-layer modelling.

Beginning with the Marginal Resolution comparisons, in Fig. 56.4-right, the deviation between ILES and filtered kinetic energy profiles at the peak points to the existence of numerical/modelling errors. However, the overall precision and agreement of the statistics are the confirmation at high Reynolds number that accurate turbulent statistics can be obtained despite the use of a mesh resolution unable to capture the viscous sublayer. In particular, it can be observed that the peak of k^+ is remarkably well predicted at a level of detail clearly higher than the minimal scale $4\Delta x$ computed with accuracy. When compared to "No-Model" results, numerical dissipation is found definitely necessary so that it can be seen as playing the role, in this context, of an implicit viscous sublayer modelling. To explain this improvement, it must be mentioned that the no-model solution is subjected to small-scale oscillations which make inaccurate the prediction of friction velocity with an overestimation of about $+6\%$. Here, the use of numerical dissipation can remove these spurious oscillations making clearly more accurate the friction velocity prediction with only a deviation of -1% by comparison to DNS.

For the low resolution results, for which the mesh choice was based on the results of Fig. 56.2, a good prediction of the mean velocity is recovered by the ILES with an acceptable -2% underprediction of u_τ (see Fig. 56.5-left). The filtered profile of k^+ in Fig. 56.5-right shows that good level of energy could still be captured despite the

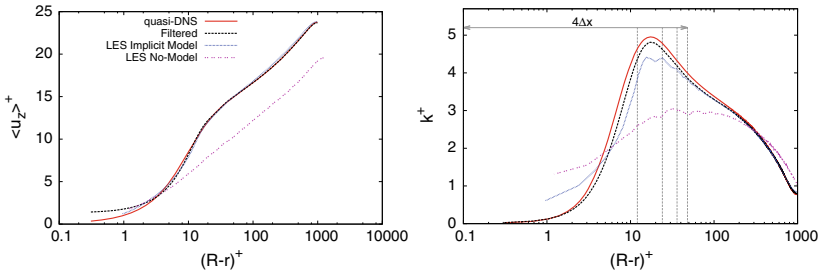

Fig. 56.5 Mean velocity profile (left) and Reynolds stresses profiles (right) for the low resolution ILES at $\mathrm{Re}_\tau = 1000$. Results are compared to: no-model LES, unfiltered and filtered quasi-DNS statistics

astonishing value of 12 wall units used for the normal xy-discretization. Even though the profile of k^+ is somewhat irregular in the region of the peak, its amplitude is only underestimated by -11% with a shape captured at a scale evidently smaller than the minimum scale of accuracy $4\Delta x^+ = 48$. In the outer layer, the agreement with filtered DNS is almost perfect. The same cannot be said about the no-model LES for which both mean velocity and kinetic energy profiles are completely unrealistic when such a coarse mesh resolution is used. Based on these observations, it can be concluded that the present implicit SGS modelling has also a feature of implicit wall-layer model through its ability to restore the quality of the wall friction from $+24\%$ to -2% while enabling realistic prediction of the fluctuating velocity profiles. Note, however, that for the present low resolution, near-wall turbulent statistics are subjected to errors related to the azimuthal location of the nodes, especially those close to the cardinal points. These errors, due to the immersed boundary technique, tend to compensate each other leading to the acceptable k^+ profile presented in Fig. 56.5-right. A development is under progress to remove these immersed boundary artefacts making a room for further improvement of the present implicit wall-layer modelling.

Acknowledgements This work was Granted access to the HPC resources of TGCC/CINES/IDRIS under the allocation A0012A07624/A0032A07624/A0052A07624 made by GENCI.

References

1. Sagaut, P.: Large Eddy Simulation of Incompressible Flow: An Introduction, 2nd edn. Springer (2005)
2. Piomelli, U., Balaras, E.: Wall-layer models for large-eddy simulations. Ann. Rev. Fluid Mech. **34**, 349–374 (2002)
3. Dairay, T., Lamballais, E., Benhamadouche, S.: Mesh node distribution in terms of wall distance for large-eddy simulation of wall-bounded flows. Flow Turbul. Combust. **100**(3), 617–626 (2018)

4. El Khoury, G.K., Schlatter, P., Noorani, A., Fischer, P.F., Brethouwer, G., Johansson, A.V.: Direct numerical simulation of turbulent pipe flow at moderately high Reynolds numbers. Flow Turbul. Combust. **91**(3), 475–495 (2013)
5. Lamballais, E., Dairay, T., Laizet, S., Vassilicos, C.: Implicit/explicit spectral viscosity and large-scale SGS effects. In: Proceedings of the DLES-11, (Pisa, Italy) (2017)
6. Dairay, T., Lamballais, E., Laizet, S., Vassilicos, C.: Numerical dissipation vs. subgrid-scale modelling for large eddy simulation. J. Comput. Phys. **337**, 252–274 (2017)
7. Lamballais, E., Fortuné, V., Laizet, S.: Straightforward high-order numerical dissipation via the viscous term for direct and large eddy simulation. J. Comput. Phys. **230**, 3270–3275 (2011)
8. Dairay, T., Fortuné, V., Lamballais, E., Brizzi, L.: LES of a turbulent jet impinging on a heated wall using high-order numerical schemes. Int. J. Heat Fluid Flow **50**, 177–187 (2014)
9. Gautier, R., Laizet, S., Lamballais, E.: A DNS study of jet control with microjets using an immersed boundary method. Int. J. Comput. Fluid Dyn. **28**(6–10), 393–410 (2014)

13

ETMM

ETMM13 Rhodes, Greece

15-17 September, 2021.

CONFERENCE PROCEEDINGS

TOWARDS HIGH-FIDELITY SIMULATION OF WALL TURBULENCE SUBJECTED TO CONJUGATE HEAT TRANSFER IN COMPLEX GEOMETRY

R. Vicente Cruz[1], *E. Lamballais*[1] *and R. Perrin*[2]

[1] *Curiosity Group, Pprime Institute, CNRS - University of Poitiers - ENSMA, France*
[2] *Department of Mechanical Engineering, Kasetsart University Sriracha, Thailand*

rodrigo.vicente.cruz@univ-poitiers.fr

Abstract

A numerical strategy based on an immersed boundary method is presented for imposing Neumann boundary conditions in configurations where the mesh arrangement is disconnected from the wall geometry. The technique is validated with DNS of heat transfer in pipe flow with isoflux condition and then used to implement a versatile strategy for conjugate heat transfer.

1 Introduction

In recent years, turbulent heat transfer in wall-bounded configurations has been increasingly investigated by DNS. Yet, most part of these studies are carried out for channel flow following the approach of solving the energy equation for the fluid side only while prescribing ideal thermal boundary conditions (TBCs), in the hope that it may represent the heat transfer phenomena occurring in the solid body. It is widely recognised however that idealized TBCs (e.g., isothermal or isoflux) cannot provide realistic representations of real life heat transfer in every possible scenario (Flageul et al, 2015), since simplifications concerning the behaviour of temperature fluctuations at the wall cannot be avoided as long as the calculations are performed for the fluid side only. This is especially true when the thermal diffusivity of the solid and fluid are of the same order of magnitude (Flageul et al, 2015). Alternatively, in the conjugate heat transfer (CHT) framework, the heat conduction occurring in the solid is also solved and coupled to the fluid solution. This strategy can provide a fine description of the turbulent thermal interaction between fluid and solid media which may be valuable, for instance, to improve RANS/LES modelling in industrial applications where fluctuating thermal stresses are a concern (Flageul et al, 2015).

In a previous work (Vicente Cruz et al, 2021), the authors have presented DNS results of pipe flow with ideal mixed-type boundary conditions (MBC). The pipe geometry was discretized with a Cartesian regular grid for a numerical differentiation entirely based on high-order finite-difference schemes. Dirichlet boundary conditions (DBC) were ensured (for both velocity and temperature) at the fluid-solid interface through an efficient immersed boundary method (IBM). Accurate velocity/temperature statistics and budgets of the turbulent kinetic energy have been presented while highlighting the spectacular saving of computational resources allowed by the numerical method. In the present contribution, the same computational strategy is used and the IBM is further developed so that ideal isoflux conditions (IF) can be prescribed, which corresponds to the imposition of a Neumann boundary condition (NBC). The pipe flow configuration is considered as a prototype of complex geometry in the sense that the computational mesh does not fit the wall geometry. Thanks to a dual IBM where the new NBC imposition is implemented, an accurate and versatile numerical strategy for DNS with CHT is proposed.

2 Flow configuration

We consider the fully developed flow of an incompressible Newtonian fluid in a pipe subjected to a constant heat flux at its outer surface, as illustrated in Figure 1-top. In the present CHT framework, heat is conducted through the solid subdomain Ω_s - defined in $R \leq r \leq R_o$ - and then conveyed by the turbulent flow in the fluid subdomain Ω_f - defined in $r < R$. We neglect any temperature dependence of fluid and solid material properties, the temperature field is treated as a passive scalar. Thus, the flow is governed by the incompressible Navier-Stokes equations and - by defining a dimensionless temperature of the form $\Theta = -\frac{1}{Nu}\left(\frac{T-T_b}{\langle T_w\rangle - T_b}\right)$ with T_b and $\langle T_w\rangle$ the bulk and mean wall temperatures respectively - fluid and solid energy equations are expressed as

$$\frac{\partial \Theta}{\partial t} + u_i \frac{\partial \Theta}{\partial x_i} = \frac{1}{Pe}\frac{\partial^2 \Theta}{\partial x_i \partial x_i} + f_\Theta \quad \text{in } \Omega_f \qquad (1)$$

$$\frac{\partial \Theta_s}{\partial t} = \frac{1}{GPe}\frac{\partial^2 \Theta_s}{\partial x_i \partial x_i} \quad \text{in } \Omega_s \qquad (2)$$

where Θ and Θ_s are the temperature solutions in the fluid and solid subdomains respectively, Pe is the Péclet number, $G = \alpha/\alpha_s$ is the fluid-to-solid ther-

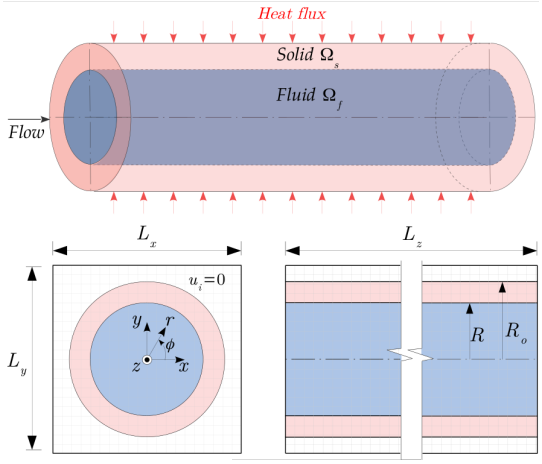

Figure 1: Scheme of flow and computational configuration.

mal diffusivity ratio and $f_\Theta = 4u_z/Pe$ is the source term that ensures thermal stationary state in the fluid domain. At the interface the continuity of temperature and heat flux are expressed, respectively, as

$$\Theta = \Theta_s \qquad \text{at} \quad r = R \tag{3}$$

$$\frac{\partial \Theta_s}{\partial r} = \frac{1}{G_2}\frac{\partial \Theta}{\partial r} \qquad \text{at} \quad r = R \tag{4}$$

where $G_2 = \lambda_s/\lambda$ is the solid-to-fluid thermal conductivity ratio. And the isoflux condition (NBC) applied to outer surface $r = R_o$ is

$$\frac{\partial \Theta_s}{\partial r} = -\frac{1}{G_2}\frac{R}{R_o} \qquad \text{at} \quad r = R_o\,. \tag{5}$$

However, what is commonly done in numerical simulation of heat transfer in wall-bounded configurations is to bypass the heat conduction in the solid (2) and solve only the advection-diffusion in the fluid (1). In this case, the physical process in the solid is simply represented by an ideal TBC imposed to eq.(1). This can be done by assuming, for instance, that the heat flux transmitted from the solid into the fluid domain through the interface $r = R$ is also constant and hence solve eq.(1) with IF, which corresponds to the NBC

$$\frac{\partial \Theta}{\partial r} = -1 \qquad \text{at} \quad r = R\,. \tag{6}$$

A numerical technique for IF is presented here as a pathway into developing the IBM for imposing NBC in complex geometries[1].

3 Numerical methodology

As this work focuses on the validation of two numerical techniques (namely for IF and CHT), results are presented only for a low-Reynolds number $Re = 5300$ based on the pipe diameter ($Re_\tau = 181$ based on the pipe radius) and a Prandtl number $Pr = 0.71$. The massively parallel code Xcompact3d (Bartholomew et al, 2020) is used to carry out the simulations. Its spatial differentiation is entirely based on centred compact finite-difference schemes of sixth-order accuracy when periodic (or free-slip) boundary conditions are applied to the boundaries of the computational domain, as in here. The cylindrical pipe is immersed in the computational domain of dimensions $L_x \times L_y \times L_z = 1.6D \times 1.6D \times 12.5D$ which is discretized with a regular Cartesian grid of $n_x \times n_y \times n_z = 320 \times 320 \times 640$ nodes, see schematic view in Figure 1-bottom. The cylindrical coordinates, associated to the pipe geometry, relate to the Cartesian ones, used by the code, according to $r = \sqrt{x^2 + y^2}$, $\phi = \arctan(y/x)$, $z = z$. The corresponding mesh resolutions in wall units in the transverse-xy and streamwise-z directions are $\Delta x^+ = \Delta y^+ = 1.8$ and $\Delta z^+ = 7$ respectively.

The ability to reach DNS accuracy despite the structurally coarse mesh resolution is a highlight of the present numerical method. This is achieved thanks to a small amount of artificial dissipation selectively applied on the smallest scales to regularise the solution as in the context of implicit LES (Vicente Cruz et al, 2020). However, differently from previous studies (Vicente Cruz et al, 2020, 2021) here, this target numerical dissipation is not introduced through the computation of second derivatives in equations (1, 2). We use instead the viscous filtering technique for DNS/LES recently developed by the authors (Lamballais et al, 2021). It consists of designing the coefficients of a finite-difference filter to provide both the molecular and artificial dissipations. This way, by applying the filter every time step, the diffusive terms can be actually removed from the governing equations. In Lamballais et al (2021) for instance, the authors have shown that for a DNS with this same computational configuration for a Prandtl number $Pr = 0.025$ with MBC, the viscous filtering technique enabled to use a $30\times$ larger time step with respect to the full-explicit time integration with third-order Adams-Bashforth used before, leading to -95% saving of computational resources.

Another headliner of the present approach is the customised IBM which enables the treatment of a complex geometries despite the use of a Cartesian mesh (Gautier et al, 2014). The method is based on the reconstruction of an artificial solution into the immersed region, as illustrated in Figure 2-right, and no-explicit forcing is introduced in the governing equations. To ensure its effectiveness in the present computational configuration, the domain needs to be slightly oversized by introducing the "buffer region" $r > R_o$, discernible in Figure 1-bottom. For a DBC, the imposition is straightforward, the local reconstruction is carried out with Lagrange polynomial functions providing the desired value at the wall (Vicente Cruz et al, 2021). For a NBC on the other hand, the technique

[1]The term complex geometry refers to a mesh arrangement disconnected from the wall geometry.

implemented here is an extension of the strategy introduced by Narváez et al (2021) to perform CHT simulation in channel configuration. The method is expanded here to a pipe as a prototype of complex geometry.

Imposition of IF

For efficiency and simplicity reasons, partially related to the 2D MPI pencil decomposition used in the code, all operations are carried out in 1D. This implies that, when dealing with a complex geometry, the imposition of a NBC - i.e. the wall-normal derivative in eq.(6) - must be decomposed into its Cartesian components according to

$$\left.\frac{\partial\Theta}{\partial x}\right|_w = -\cos\phi \left.\frac{\partial\Theta}{\partial r}\right|_w - \sin\phi \left.\frac{\partial\Theta}{\partial\phi}\right|_w \quad (7)$$

$$\left.\frac{\partial\Theta}{\partial y}\right|_w = -\sin\phi \left.\frac{\partial\Theta}{\partial r}\right|_w + \cos\phi \left.\frac{\partial\Theta}{\partial\phi}\right|_w \quad (8)$$

where "w" denotes an inner wall value. In the present approach however, these Cartesian wall-derivatives are not directly imposed, instead, they are softly ensured with the present IBM. The procedure can be understood in two steps, following the scheme in Figure 2: *i)* Definition of a target value Θ_w that satisfies the NBC; *ii)* Lagrange polynomial reconstruction with Θ_w. In other words, the NBC is ensured through a target DBC. Let us consider, for instance, the local reconstruction along a x-row illustrated in Figure 2. As Narváez et al (2021), we may define a non-centred finite-difference scheme such as

$$\left.\frac{\partial\Theta}{\partial x}\right|_w = a\Theta_w + b\Theta_{i+1} + c\Theta_{i+2} + d\Theta_{i+3} \quad (9)$$

so that the value Θ_w providing the target derivative $\left.\frac{\partial\Theta}{\partial x}\right|_w$ (i.e., the NBC) can be estimated from

$$\Theta_w = \frac{\left.\frac{\partial\Theta}{\partial x}\right|_w - b\Theta_{i+1} - c\Theta_{i+2} - d\Theta_{i+3}}{a} . \quad (10)$$

A Taylor expansion can lead to algebraic expressions for the set of coefficients (a, b, c, d) for different orders of accuracy, they are not shown here for conciseness. Nonetheless, note that these expressions are function of the mesh size Δx, which is constant, and of the local mesh resolution in the vicinity of the body Δx_w, which, in turn, is geometry dependent for a complex geometry. Consequently, the finite-difference coefficients will be geometry dependent as well. In the code, they are defined before the time loop, as 3×3 matrices (using the local coordinates of the immersed boundaries) and used later in the solver. One set of coefficients is needed for each of the transverse-xy directions since NBC (7) is satisfied with x-direction reconstructions and NBC (8) with y-direction reconstructions. Because the coefficients are geometry dependent, values of Θ_w computed with eq.(10) will be as

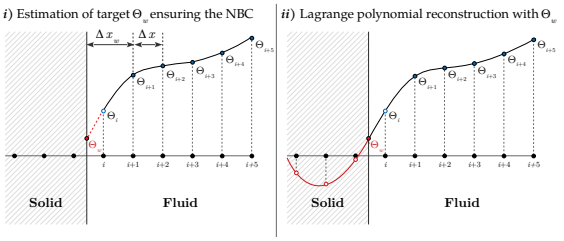

Figure 2: Two-step technique for imposing NBC.

well. This point explains how the present strategy can reproduce temperature fluctuations at the wall (characteristic feature of IF) although it is essentially based on Dirichlet boundary conditions. Note also that first fluid points (index i in Figure 2) are skipped. In fact, if taken into account, Δx_w can assume very small values, leading to very large coefficients. This side effect, although algebraically correct, can cause severe numerical instability in the solver. Here, a third-order accurate scheme has been used which requires a stencil $\{a, b, c, d\} \neq 0$.

Another obstacle still needs to be dealt with in the present scenario. The definition of the Cartesian derivatives with eqs.(7, 8) depends on the knowledge of their cylindrical counterparts on the right-hand side (rhs). The wall-normal component naturally corresponds to the IF condition given by eq.(6). On the other hand, the expected behaviour of the wall-tangential component is unknown, at least in a turbulent context. With a body-conformal grid, which is the typical approach in cases like this, the imposition of the wall-normal derivative is straightforward and the tangential one can be simply left free. Here however, a prediction of the wall-tangential derivative is necessary in order to define the target value Θ_w.

We propose therefore a method based on extrapolation. As a first step, the wall-tangential derivative is computed everywhere in the fluid domain Ω_f from the Cartesian components using

$$\frac{\partial\Theta}{\partial\phi} = -\sin\phi\frac{\partial\Theta}{\partial x} + \cos\phi\frac{\partial\Theta}{\partial y} . \quad (11)$$

If the Cartesian derivatives on the rhs of eq.(11) are to be computed with the same sixth-order compact schemes used in Xcompact3d, the temperature field Θ should be reconstructed beforehand, since in the present IBM framework, the reconstruction role is to reduce contamination by spurious oscillations due to a sharp interface (Vicente Cruz et al, 2020). In this case, this "pre-reconstruction" should also be carried out for a NBC which would require, in turn, a prediction of Θ_w making the problem somehow closed-loop. Alternatively, here, a second-order conditional scheme is used, which consists of employing conventional central difference $f'_i = \frac{f_{i+1} - f_{i-1}}{2\Delta x}$ at nodes sufficiently far from the immersed boundary and progressively switch to non-centred difference at nodes close

to the immersed boundary[2]. The goal is to avoid including nodes from the immersed region in the stencil of the scheme, preventing contamination by interfacial discontinuities.

Next, from its fluid values, the wall-contribution of the tangential derivative can be extrapolated along a Cartesian grid row. It can be done following the same principle described for scheme (9). This time however, instead of first-derivatives, we aim to define a finite-difference extrapolation scheme of the form

$$\left.\frac{\partial\Theta}{\partial\phi}\right|_w = a_e \left.\frac{\partial\Theta}{\partial\phi}\right|_i + b_e \left.\frac{\partial\Theta}{\partial\phi}\right|_{i+1} + c_e \left.\frac{\partial\Theta}{\partial\phi}\right|_{i+2} + d_e \left.\frac{\partial\Theta}{\partial\phi}\right|_{i+3} \tag{12}$$

As for the coefficients of scheme (9), a Taylor expansion leads to expressions for (a_e, b_e, c_e, d_e) for different orders of accuracy (not shown). These coefficients are also geometry dependent because of Δx_w and are initialized in the code together with those of scheme (9). Differently from those however, here Δx_w does not raise stability problems and therefore first fluid nodes may or may not be skipped, depending on the value of the coefficient a_e. Here, we use a simple first-order extrapolation without skip, i.e. with $a_e = 1, \{b_e, c_e, d_e\} = 0$. From a series of preliminary tests for different orders of accuracy, this configuration stood out as a robust and efficient solution to work alongside with the second-order conditional scheme mentioned above. DNS results of validation for this technique are presented in the next section.

Imposition of CHT

The code Xcompact3d is further developed to include a solver for the solid energy equation (2). The method implemented is mainly based on the (post-IF version of the) IBM to couple solid and fluid energy equations trough the TBCs (3-5). Most commonly, in the general CHT framework with IBM, a single computational domain is used for both fluid and solid temperature solutions (Narváez et al, 2021). As pointed out by Narváez et al (2021), in most practical applications, thermal conductivities are different in the fluid and in the solid ($G_2 \neq 1$) and hence, because of the heat flux continuity condition at the interface, the wall-normal derivative of the temperature can become discontinuous. This effect is expressed by the dependence on G_2 in eq.(4). The resulting lack of smoothness is an obvious obstacle when high-order compact schemes are used, as in here, given the difficulty of numerically dealing with a loss of differentiability.

In this regard, the *dual* IBM approach of Narváez et al (2021) is expanded here to complex geometries. The approach is *dual* in the sense that fluid Θ and solid Θ_s temperature fields are defined separately, everywhere in the computational domain. In this way, the solid subdomain Ω_s is regarded as the immersed region for the fluid solution and the fluid subdomain

[2]The complete formulation of the conditional scheme is not given here for the sake of brevity.

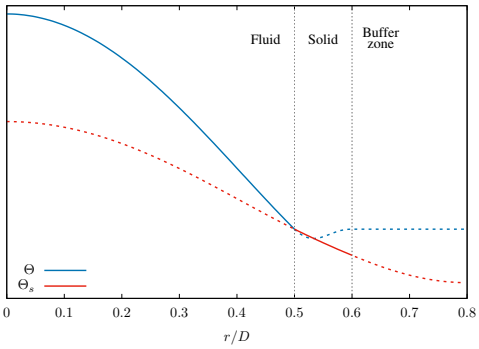

Figure 3: Principle of the reconstructions with the *dual* IBM for $G_2 = 2$. Solid lines are physical solutions, dashed lines are reconstructed solutions.

Ω_f becomes the immersed region for the solid solution. Consequently, each temperature solution can be freely reconstructed without conflicting (replacing) the physical values of its counterpart. Furthermore, compact finite-difference operators of spatial derivatives and viscous filtering perceive a smooth interface for both Θ and Θ_s regardless of the value of G_2, see example in Figure 3 for $G_2 = 2$. Hence, not only the efficiency of the IBM is preserved but also a straightforward treatment for the wall-normal derivative discontinuity is provided.

Fluid and solid energy equations are coupled in time with the Neumann-Dirichlet coupling method of Giles (1997). It consists of a weak coupling where eqs.(1, 2) are solved sequentially while admitting a small discontinuity of the temperature at the interface. Firstly, the fluid energy equation (1) is solved with the TBC (3), which is prescribed as the DBC

$$\Theta|_w^{n+1} = \frac{\Theta|_w^n + \Theta_s|_w^n}{2} \ , \tag{13}$$

where the superscript refers to the time-step number. Note that for the present complex geometry, the immersed boundary location does not coincide with the Cartesian grid nodes and thus the local wall values $\Theta|_w^n$ and $\Theta_s|_w^n$ must be extrapolated. This is done with scheme (12) following the same rationale. Here however, the extrapolation coefficients are defined to provide fourth-order accuracy[3] without skipping the closest nodes to the interface, which requires a stencil $\{a_e, b_e, c_e, d_e\} \neq 0$.

Next, the solid energy equation (2) is solved with TBCs (4, 5) which are imposed as NBCs. At the outer wall "w_o", NBC (5) is the isoflux condition

$$\left.\frac{\partial\Theta_s}{\partial r}\right|_{w_o}^{n+1} = -\frac{1}{G_2}\frac{R}{R_o} \ , \tag{14}$$

which is carried out with the IF technique described hereinbefore. Here however, we consider this heat-flux as purely wall-normal and hence the contribution

[3]Tests showed that higher-order extrapolation is better if the goal is to extrapolate Θ_w instead of the wall-tangential derivative.

of the wall-tangential derivative in eqs.(7, 8) is set to zero[4]. Now, to impose NBC (4) at the inner interface

$$\left.\frac{\partial \Theta_s}{\partial r}\right|_w^{n+1} = \frac{1}{G_2}\left.\frac{\partial \Theta}{\partial r}\right|_w^{n+1}, \qquad (15)$$

the wall-normal derivative of the fluid solution (rhs) must be known. Note that its Cartesian components can be straightforwardly computed from the fluid solution Θ with the non-centred scheme (9). Also in this case, as the Cartesian wall-derivatives are defined directly, the estimation of the wall-tangential derivative is not required, which makes the imposition of NBCs in the CHT case simpler than in IF. Still, both NBCs (14, 15) are ensured in two steps with the Lagrange reconstruction as described for IF. More precisely, in the illustration of Figure 3, the reconstruction of Θ_s performed through the transverse-xy periodicity satisfies NBC (14) and the one performed through the fluid zone $r < R$ satisfies NBC (15).

As stressed by Flageul et al (2015), the explicit nature of this weak coupling technique can introduce several numerical stability limitations. Yet, the consequent restriction on Δt can be alleviated if DBC and NBC are used for the fluid and solid fields respectively (Giles, 1997), as it is done here. This way, for the Prandtl number $Pr = 0.71$ considered here, the CFL restriction in the fluid zone becomes stronger than the one related to the weak coupling. In the next section, CHT results are presented for 4 different combinations of fluid/solid material properties - i.e. different values of G and G_2 - corresponding to distinct thermal activity ratios (Tiselj et al, 2001) $K = (G_2\sqrt{G})^{-1}$. The 8 temperature solutions ($4\ \Theta + 4\ \Theta_s$) are computed in parallel with a single velocity field in order to spare computational resources.

4 Results

Isoflux (IF)

For the sake of conciseness and in order to directly demonstrate the consistency of the present IF technique, only the budget terms of the temperature variance, scaled in viscous units, are assessed in Figure 4. They are calculated as in Straub et al (2019) and compared to their DNS results which were obtained with the high-order spectral element code Nek5000. Besides the small over-prediction of the molecular diffusion term (which may be associated to a lack of statistical convergence), the overall agreement is satisfactory, with in particular, the balance of terms being well reproduced.

At the wall, molecular diffusive transport MD_{k_θ} balances well molecular dissipation ϵ_{k_θ} as the turbulent transport term TD_{k_θ} vanishes due to the no-slip condition. The two peaks of TD_{k_θ} are also well captured, showing that the method reproduces well the role associated to this term which is to drain temperature fluctuations from the region where production is most intense in order to convey them both towards the wall and the core region (Piller, 2005).

[4]The effect of the TBC imposed at the outer wall is not investigated in this work.

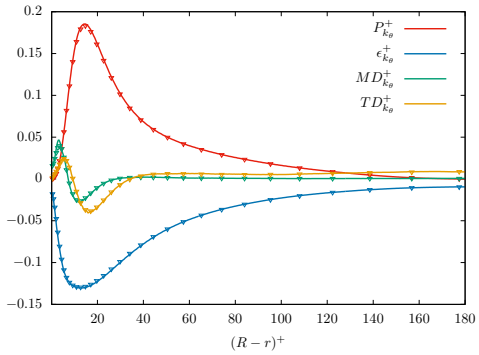

Figure 4: Budget of temperature variance with IF. Symbols are DNS data of Straub et al (2019).

Conjugate heat transfer (CHT)

In numerical terms, the treatment of CHT can be seen as combination of MBC for the fluid energy equation (DBC (13)) and IF for the solid (NBCs (14, 15)). Therefore, in the light of the validation of the IF technique and given the lack of reference results for CHT with DNS of pipe flow, we confront our results here only to IF and MBC (from Vicente Cruz et al, 2021). The analysis are focused on the mean temperature profile $\langle\Theta\rangle$, temperature variance $\langle\Theta'\Theta'\rangle$ and streamwise heat flux $\langle u'_z\Theta'\rangle$ in function of the wall distance $(R - r)$, as reported in Figure 5. As IF, MBC and CHT profiles tend to superpose each other in the core region, axis ranges are readjusted to better assess the near-wall behaviour of the quantities scaled in viscous units.

No effect of the TBC is perceived on the mean fluid temperature $\langle\Theta\rangle^+$ in Figure 5-top, consistently with observations of Piller (2005) and Flageul et al (2015). For the solid temperature $\langle\Theta_s\rangle^+$ on the other hand, the discontinuity on the first-derivative at the interface, provoked by the heat flux continuity condition eq.(4), appears for the CHT cases with $G_2 = 2$. These observations are in agreement with CHT results of Tiselj et al (2001) and Flageul et al (2017) for the channel flow. Note that thanks to the *dual* immersed boundary technique, the smoothness of the temperature profile is successfully preserved across the interface, regardless of this discontinuity and despite the fact that the numerical differentiation for both fluid and solid energy equations (1, 2) is entirely based on high-order compact schemes.

The profiles of the temperature variance $\langle\Theta'\Theta'\rangle^+$ and streamwise heat flux $\langle u'_z\Theta'\rangle^+$ are delimited by the two ideal cases MBC and IF across the conductive sublayer. Moreover, in the fluid region, with increasing thermal activity ratio K, the profiles move from a MBC-like behaviour (which corresponds to $K = 0$)

towards IF ($K = \infty$). This effect is evident for the temperature variance but less visible for the streamwise heat flux since the no-slip condition causes it to vanish at the wall. These conclusions cannot be transposed to the solid domain as some of the profiles do cross each other. The same behaviours has been also observed by Flageul et al (2017) in the channel flow framework.

5 Conclusions

New numerical techniques are introduced for simulating IF and CHT in pipe configuration. The imposition of the NBCs required for both cases are mostly based in an efficient IBM designed to ensure accuracy in the near-wall region. Furthermore, for the CHT treatment, the code Xcompact3d is further developed to include a solver for the heat conduction in the solid which is (weakly) coupled to DNS results in the fluid, providing a high-fidelity description of the thermal interaction between the two media. Consistent results of validation are presented which makes of this numerical approach an attractive tool for RANS modelling development while paving the way for investigating CHT in complex geometries. Some stability aspects of the technique need to be understood in-depth in order to make the coupling method numerically stable for any value of the thermal conductivity ratio G_2.

Acknowledgments

This work was granted access to the HPC resources of TGCC/CINES under the allocation A0092A07624 made by GENCI.

References

Giles, M. (1997), Stability analysis of numerical interface conditions in fluid-structure thermal analysis, *Int. J. Numer. Meth. Fluids*, 25, 421–436.

Tiselj, I., Bergant, R., Mavko, B., Bajsić, I., Hetsroni, G. (2001), Direct numerical simulation of turbulent heat transfer in channel flow with heat conduction in the solid wall, *J. Heat Transf. 123 (5)*, 849–857.

M. Piller (2005), Direct numerical simulation of turbulent forced convection in a pipe, *Int. J. Numer. Meth. Fl.*

Gautier R., Laizet S., Lamballais E. (2014), A DNS study of jet control with microjets using an immersed boundary method, *Int. J. Comp. Fluid Dynamics, 28 (6-10)*, pp. 1–18.

Flageul C., Benhamadouche S., Lamballais E., Laurence D. (2015), DNS of turbulent channel flow with conjugate heat transfer: Effect of thermal boundary conditions on the second moments and budgets, *Int. J. Heat Fluid Flow 55*.

Flageul C., Benhamadouche S., Lamballais E., and Laurence D. (2017), On the discontinuity of the dissipation rate associated with the temperature variance at the fluid-solid interface for cases with conjugate heat transfer, *Int. J. of Heat and Mass Transfer*, 11, pp. 321–328.

S. Straub, P. Forooghi, L. Marocco, T. Wetzel, R. Vinuesa, P. Schlatter, and B. Frohnapfel (2019), The influence of thermal boundary conditions on turbulent forced convection pipe flow at two Prandtl numbers, *Int. J. Heat and Mass Transfer*, 144, pp. 118601.

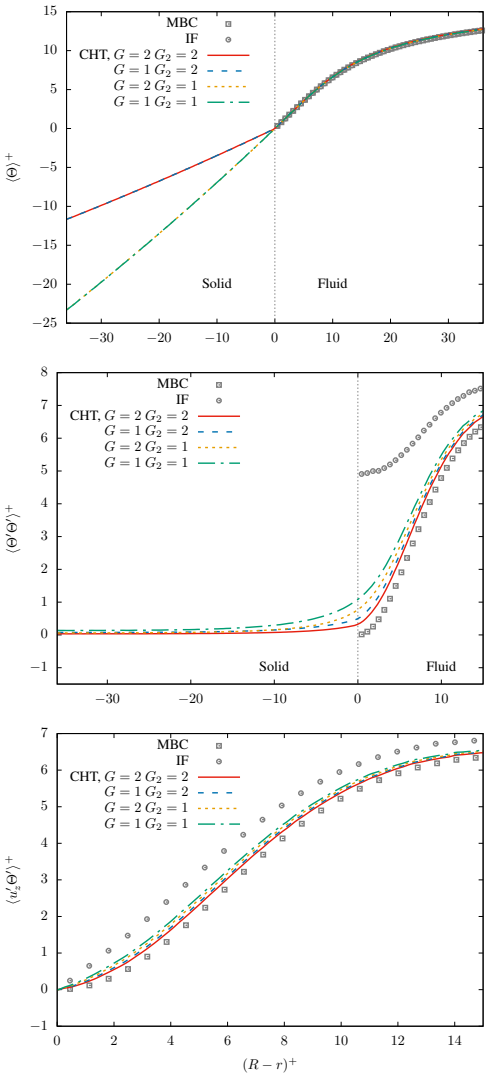

Figure 5: Temperature statistics with CHT at $Re = 5300$, $Pr = 0.71$. Profiles are plotted in increasing order of K. (Top) mean-temperature, (middle) temperature variance, (bottom) streamwise heat flux.

Vicente Cruz R., Lamballais E., Perrin R. (2020), Implicit Wall-Layer Modelling in Turbulent Pipe Flow, in DLES XII, *Eds. Cham: Springer International Publishing*, vol. 27, pp. 425–431.

Vicente Cruz R., Lamballais E., Perrin R. (2021), High-fidelity simulation of heat transfer in turbulent pipe-flow, *Proc. ATH'2020*, Paris, France.

Bartholomew P., Deskos G., Frantz R. A. S., Schuch F. N., Lamballais E., Laizet S., Xcompact3D: An open-source framework for solving turbulence problems on a Cartesian mesh, *SoftwareX*, vol. 12, p. 10055.

Lamballais E., Vicente Cruz R., Perrin R. (2021), Viscous and hyperviscous filtering for direct and large-eddy simulation, *J. Comput. Phys.*, vol. 431, p. 110115.

Narváez G. F., Lamballais E., Schettini E. B. (2021), Simulation of turbulent flow subjected to conjugate heat transfer *via* a dual immersed boundary method, *Comput. Fluids.*, In Press.

Bibliography

[1] "Gas Turbine Blade Simulation and Design Software | Ansys." [Online]. Available: https://www.ansys.com/fr-fr/applications/gas-turbines

[2] S. Xue, "Film Cooling In Turbines." [Online]. Available: https://www.conceptsnrec.com/blog/film-cooling-in-turbines

[3] "Coatings for Corrosion Erosion Protection for Utilities and Condensers." [Online]. Available: https://www.plastocor-international.com/

[4] A. J. Smits, B. J. McKeon, and I. Marusic, "High–Reynolds Number Wall Turbulence," *Annu. Rev. Fluid Mech.*, vol. 43, no. 1, pp. 353–375, Jan. 2011. [Online]. Available: http://www.annualreviews.org/doi/10.1146/annurev-fluid-122109-160753

[5] J. Kim, "Progress in pipe and channel flow turbulence, 1961–2011," *Journal of Turbulence*, vol. 13, p. N45, Jan. 2012. [Online]. Available: https://www.tandfonline.com/doi/full/10.1080/14685248.2012.726358

[6] S. B. Pope, *Turbulent Flows*, 1st ed. Cambridge University Press, Aug. 2000. [Online]. Available: https://www.cambridge.org/core/product/identifier/9780511840531/type/book

[7] S. Laizet and E. Lamballais, "High-order compact schemes for incompressible flows: A simple and efficient method with quasi-spectral accuracy," *Journal of Computational Physics*, vol. 228, no. 16, pp. 5989–6015, Sep. 2009. [Online]. Available: https://linkinghub.elsevier.com/retrieve/pii/S0021999109002587

[8] T. Dairay, E. Lamballais, and S. Benhamadouche, "Mesh Node Distribution in Terms of Wall Distance for Large-eddy Simulation of Wall-bounded Flows," *Flow Turbulence Combust*, vol. 100, no. 3, pp. 617–626, Apr. 2018. [Online]. Available: http://link.springer.com/10.1007/s10494-017-9863-5

[9] G. K. El Khoury, P. Schlatter, A. Noorani, P. F. Fischer, G. Brethouwer, and A. V. Johansson, "Direct Numerical Simulation of Turbulent Pipe Flow at Moderately High Reynolds Numbers," *Flow Turbulence Combust*, vol. 91, no. 3, pp. 475–495, Oct. 2013. [Online]. Available: http://link.springer.com/10.1007/s10494-013-9482-8

[10] S. Straub, P. Forooghi, L. Marocco, T. Wetzel, R. Vinuesa, P. Schlatter, and B. Frohnapfel, "The influence of thermal boundary conditions on turbulent forced convection pipe flow at two Prandtl numbers," *International Journal of Heat and Mass Transfer*, vol. 144, p. 118601, Dec. 2019. [Online]. Available: https://linkinghub.elsevier.com/retrieve/pii/S0017931019323646

[11] S. Laizet and N. Li, "Incompact3d: A powerful tool to tackle turbulence problems with up to O(105) computational cores," *International Journal for Numerical Methods in Fluids*, vol. 67, no. 11, pp. 1735–1757, 2011, _eprint: https://onlinelibrary.wiley.com/doi/pdf/10.1002/fld.2480. [Online]. Available: http://onlinelibrary.wiley.com/doi/abs/10.1002/fld.2480

[12] P. Bartholomew, G. Deskos, R. A. Frantz, F. N. Schuch, E. Lamballais, and S. Laizet, "Xcompact3D: An open-source framework for solving turbulence problems on a Cartesian mesh," *SoftwareX*, vol. 12, p. 100550, Jul. 2020. [Online]. Available: https://linkinghub.elsevier.com/retrieve/pii/S2352711019303620

[13] M. Lesieur, *Turbulence in fluids*, 4th ed., ser. Fluid mechanics and its applications. Dordrecht: Springer, 2008, no. 84, oCLC: 255895179.

[14] B. Eckhardt, T. M. Schneider, B. Hof, and J. Westerweel, "Turbulence Transition in Pipe Flow," *Annu. Rev. Fluid Mech.*, vol. 39, no. 1, pp. 447–468, Jan. 2007. [Online]. Available: http://www.annualreviews.org/doi/10.1146/annurev.fluid.39.050905.110308

[15] O. Reynolds, "XXIX. An experimental investigation of the circumstances which determine whether the motion of water shall be direct or sinuous, and of the law of resistance in parallel channels," *Phil. Trans. R. Soc.*, vol. 174, pp. 935–982, Dec. 1883. [Online]. Available: https://royalsocietypublishing.org/doi/10.1098/rstl.1883.0029

[16] F. M. White, *Fluid mechanics*, 6th ed., ser. Mcgraw-Hill series in mechanical engineering. New York, NY: McGraw-Hill, 2009.

[17] F. P. Incropera and F. P. Incropera, Eds., *Fundamentals of heat and mass transfer*, 6th ed. Hoboken, NJ: John Wiley, 2007, oCLC: ocm62532755.

[18] J. Jimenez, "Coherent structures in wall-bounded turbulence," *J. Fluid Mech.*, vol. 842, p. P1, May 2018, arXiv: 1710.07493. [Online]. Available: http://arxiv.org/abs/1710.07493

[19] P. Sagaut, *Large eddy simulation for incompressible flows: an introduction*, 3rd ed., ser. Scientific computation. Berlin ; New York: Springer, 2006.

[20] J. I. Polanco, "Lagrangian properties of turbulent channel flow: a numerical study," Ph.D. dissertation, Université de Lyon, 2019.

[21] J. Jiménez, "Cascades in Wall-Bounded Turbulence," *Annu. Rev. Fluid Mech.*, vol. 44, no. 1, pp. 27–45, Jan. 2012. [Online]. Available: http://www.annualreviews.org/doi/10.1146/annurev-fluid-120710-101039

[22] C. Chin, J. Monty, and A. Ooi, "Reynolds number effects in DNS of pipe flow and comparison with channels and boundary layers," *International Journal of Heat and Fluid Flow*, vol. 45, pp. 33–40, Feb. 2014. [Online]. Available: https://linkinghub.elsevier.com/retrieve/pii/S0142727X13002403

[23] P. Orlandi, *Fluid Flow Phenomena: A Numerical Toolkit*, ser. Fluid Mechanics and Its Applications. Springer Netherlands, 2000. [Online]. Available: https://www.springer.com/gp/book/9781402003899

[24] J. Kim and P. Moin, "Transport of Passive Scalars in a Turbulent Channel Flow," in *Turbulent Shear Flows 6*, J.-C. André, J. Cousteix, F. Durst, B. E. Launder, F. W. Schmidt, and J. H. Whitelaw, Eds. Berlin, Heidelberg: Springer Berlin Heidelberg, 1989, pp. 85–96. [Online]. Available: http://link.springer.com/10.1007/978-3-642-73948-4_9

[25] I. Tiselj, R. Bergant, B. Mavko, I. Bajsić, and G. Hetsroni, "DNS of Turbulent Heat Transfer in Channel Flow With Heat Conduction in the Solid Wall," *Journal of Heat Transfer*, vol. 123, no. 5, pp. 849–857, Oct. 2001. [Online]. Available: https://asmedigitalcollection.asme.org/heattransfer/article/123/5/849/463772/DNS-of-Turbulent-Heat-Transfer-in-Channel-Flow

[26] B. Weigand, *Analytical methods for heat transfer and fluid flow problems*. Berlin ; New York: Springer, 2004.

[27] T. P. Sommer, R. M. C. So, and H. S. Zhang, "Heat Transfer Modeling and the Assumption of Zero Wall Temperature Fluctuations," *Journal of Heat Transfer*, vol. 116, no. 4, pp. 855–863, Nov. 1994. [Online]. Available: https://asmedigitalcollection.asme.org/heattransfer/article/116/4/855/424859/Heat-Transfer-Modeling-and-the-Assumption-of-Zero

[28] C. Flageul, S. Benhamadouche, É. Lamballais, and D. Laurence, "DNS of turbulent channel flow with conjugate heat transfer: Effect of thermal boundary conditions on the second moments and budgets," *International Journal of Heat and Fluid Flow*, vol. 55, pp. 34–44, Oct. 2015. [Online]. Available: https://linkinghub.elsevier.com/retrieve/pii/S0142727X15000910

[29] M. Piller, "Direct numerical simulation of turbulent forced convection in a pipe," *Int. J. Numer. Meth. Fluids*, vol. 49, no. 6, pp. 583–602, Oct. 2005. [Online]. Available: http://doi.wiley.com/10.1002/fld.994

[30] J. D. Anderson, *Computational fluid dynamics: the basics with applications*, ser. McGraw-Hill series in mechanical engineering. New York: McGraw-Hill, 1995.

[31] J. H. Ferziger and M. Perić, *Computational Methods for Fluid Dynamics*. Springer, 2002, oCLC: 1120912802.

[32] J. Kim, P. Moin, and R. Moser, "Turbulence statistics in fully developed channel flow at low Reynolds number," *J. Fluid Mech.*, vol. 177, pp. 133–166, Apr. 1987. [Online]. Available: https://www.cambridge.org/core/product/identifier/S0022112087000892/type/journal_article

[33] H. Eckelmann, "The structure of the viscous sublayer and the adjacent wall region in a turbulent channel flow," *J. Fluid Mech.*, vol. 65, no. 3, pp. 439–459, Sep. 1974. [Online]. Available: https://www.cambridge.org/core/product/identifier/S0022112074001479/type/journal_article

[34] U. Piomelli and E. Balaras, "Wall-Layer Models for Large-Eddy Simulations," *Annu. Rev. Fluid Mech.*, vol. 34, no. 1, pp. 349–374, Jan. 2002. [Online]. Available: http://www.annualreviews.org/doi/10.1146/annurev.fluid.34.082901.144919

[35] R. Mittal and G. Iaccarino, "IMMERSED BOUNDARY METHODS," *Annu. Rev. Fluid Mech.*, vol. 37, no. 1, pp. 239–261, Jan. 2005. [Online]. Available: http://www.annualreviews.org/doi/10.1146/annurev.fluid.37.061903.175743

[36] C. S. Peskin, "Flow patterns around heart valves: A numerical method," *Journal of Computational Physics*, vol. 10, no. 2, pp. 252–271, Oct. 1972. [Online]. Available: https://linkinghub.elsevier.com/retrieve/pii/0021999172900654

[37] ——, "Numerical analysis of blood flow in the heart," *Journal of Computational Physics*, vol. 25, no. 3, pp. 220–252, Nov. 1977. [Online]. Available: https://linkinghub.elsevier.com/retrieve/pii/0021999177901000

[38] D. Goldstein, R. Handler, and L. Sirovich, "Modeling a No-Slip Flow Boundary with an External Force Field," *Journal of Computational Physics*, vol. 105, no. 2, pp. 354–366, Apr. 1993. [Online]. Available: https://linkinghub.elsevier.com/retrieve/pii/S0021999183710818

[39] E. Fadlun, R. Verzicco, P. Orlandi, and J. Mohd-Yusof, "Combined Immersed-Boundary Finite-Difference Methods for Three-Dimensional Complex Flow Simulations," *Journal of Computational Physics*, vol. 161, no. 1, pp. 35–60, Jun. 2000. [Online]. Available: https://linkinghub.elsevier.com/retrieve/pii/S0021999100964842

[40] S. Majumdar, G. Iaccarino, and P. Durbin, "RANS solvers with adaptive structured boundary non-conforming grids," *Annual Research Briefs, Center for Turbulence Research*, p. 14, 2001.

[41] E. Balaras, "Modeling complex boundaries using an external force field on fixed Cartesian grids in large-eddy simulations," *Computers & Fluids*, vol. 33, no. 3, pp. 375–404, Mar. 2004. [Online]. Available: https://linkinghub.elsevier.com/retrieve/pii/S0045793003000586

[42] N. Peller, A. L. Duc, F. Tremblay, and M. Manhart, "High-order stable interpolations for immersed boundary methods," *Int. J. Numer. Meth. Fluids*, vol. 52, no. 11, pp. 1175–1193, Dec. 2006. [Online]. Available: https://onlinelibrary.wiley.com/doi/10.1002/fld.1227

[43] K. Taira and T. Colonius, "The immersed boundary method: A projection approach," *Journal of Computational Physics*, vol. 225, no. 2, pp. 2118–2137, Aug. 2007. [Online]. Available: https://linkinghub.elsevier.com/retrieve/pii/S0021999107001234

[44] P. Parnaudeau, J. Carlier, D. Heitz, and E. Lamballais, "Experimental and numerical studies of the flow over a circular cylinder at Reynolds number 3900," *Physics of Fluids*, vol. 20, no. 8, p. 085101, Aug. 2008. [Online]. Available: http://aip.scitation.org/doi/10.1063/1.2957018

[45] A. Pinelli, I. Naqavi, U. Piomelli, and J. Favier, "Immersed-boundary methods for general finite-difference and finite-volume Navier–Stokes solvers," *Journal of Computational Physics*, vol. 229, no. 24, pp. 9073–9091, Dec. 2010. [Online]. Available: https://linkinghub.elsevier.com/retrieve/pii/S0021999110004687

[46] P.-É. Weiss and S. Deck, "On the coupling of a zonal body-fitted/immersed boundary method with ZDES: Application to the interactions on a realistic space launcher afterbody flow," *Computers & Fluids*, vol. 176, pp. 338–352, Nov. 2018. [Online]. Available: https://linkinghub.elsevier.com/retrieve/pii/S0045793017302256

[47] M. H. Abdol Azis, F. Evrard, and B. van Wachem, "An immersed boundary method for incompressible flows in complex domains," *Journal of Computational Physics*, vol. 378, pp. 770–795, Feb. 2019. [Online]. Available: https://linkinghub.elsevier.com/retrieve/pii/S0021999118307150

[48] R. Verzicco, M. Fatica, G. Iaccarino, P. Moin, and B. Khalighi, "Large Eddy Simulation of a Road Vehicle with Drag-Reduction Devices," *AIAA Journal*, vol. 40, no. 12, pp. 2447–2455, Dec. 2002. [Online]. Available: https://arc.aiaa.org/doi/10.2514/2.1613

[49] J. H. Silvestrini and E. Lamballais, "Direct Numerical Simulation of Wakes with Virtual Cylinders," *International Journal of Computational Fluid Dynamics*, vol. 16, no. 4, pp. 305–314, Jan. 2002. [Online]. Available: http://www.tandfonline.com/doi/abs/10.1080/1061856021000025184

[50] R. Gautier, S. Laizet, and E. Lamballais, "A DNS study of jet control with microjets using an immersed boundary method," *International Journal of Computational Fluid Dynamics*, vol. 28, no. 6-10, pp. 393–410, Jul. 2014. [Online]. Available: http://www.tandfonline.com/doi/abs/10.1080/10618562.2014.950046

[51] H. Strandenes, B. Pettersen, H. I. Andersson, and M. Manhart, "Influence of spanwise no-slip boundary conditions on the flow around a cylinder," *Computers & Fluids*, vol. 156, pp. 48–57, Oct. 2017. [Online]. Available: https://linkinghub.elsevier.com/retrieve/pii/S0045793017302360

[52] L. Manueco, P.-É. Weiss, and S. Deck, "On the coupling of wall-model immersed boundary conditions and curvilinear body-fitted grids for the simulation of complex geometries," *Computers & Fluids*, vol. 226, p. 104996, Aug. 2021. [Online]. Available: https://linkinghub.elsevier.com/retrieve/pii/S0045793021001626

[53] W. Kim and H. Choi, "Immersed boundary methods for fluid-structure interaction: A review," *International Journal of Heat and Fluid Flow*, vol. 75, pp. 301–309, Feb. 2019. [Online]. Available: https://linkinghub.elsevier.com/retrieve/pii/S0142727X1830691X

[54] B. J. Geurts, *Elements of direct and large-eddy simulation*. Philadelphia, Pa: Edwards, 2004, oCLC: 636328193.

[55] N. Li and S. Laizet, "2DECOMP&FFT - A Highly Scalable 2D Decomposition Library and FFT Interface," *Cray User Group 2010 Conferences, Edinburgh*, p. 13, 2010. [Online]. Available: http://2decomp.org/pdf/17B-CUG2010-paper-Ning_Li.pdf

[56] K. C. Kim and R. J. Adrian, "Very large-scale motion in the outer layer," *Physics of Fluids*, vol. 11, no. 2, pp. 417–422, Feb. 1999. [Online]. Available: http://aip.scitation.org/doi/10.1063/1.869889

[57] J. P. Monty, J. A. Stewart, R. C. Williams, and M. S. Chong, "Large-scale features in turbulent pipe and channel flows," *J. Fluid Mech.*, vol. 589, pp. 147–156, Oct. 2007. [Online]. Available: https://www.cambridge.org/core/product/identifier/S002211200700777X/type/journal_article

[58] M. Guala, S. E. Hommema, and R. J. Adrian, "Large-scale and very-large-scale motions in turbulent pipe flow," *J. Fluid Mech.*, vol. 554, no. -1, p. 521, May 2006. [Online]. Available: http://www.journals.cambridge.org/abstract_S0022112006008871

[59] C. Chin, A. S. H. Ooi, I. Marusic, and H. M. Blackburn, "The influence of pipe length on turbulence statistics computed from direct numerical simulation data," *Physics of Fluids*, vol. 22, no. 11, p. 115107, Nov. 2010. [Online]. Available: http://aip.scitation.org/doi/10.1063/1.3489528

[60] S. Saha, C. Chin, H. Blackburn, and A. Ooi, "The influence of pipe length on thermal statistics computed from DNS of turbulent heat transfer," *International Journal of Heat and Fluid Flow*, vol. 32, no. 6, pp. 1083–1097, Dec. 2011. [Online]. Available: https://linkinghub.elsevier.com/retrieve/pii/S0142727X11001226

[61] S. Saha, A. S. Ooi, and H. M. Blackburn, "Validation Criteria for DNS of Turbulent Heat Transfer in Pipe Flow," *Procedia Engineering*, vol. 90, pp. 599–604, 2014. [Online]. Available: https://linkinghub.elsevier.com/retrieve/pii/S1877705814029002

[62] A. Lozano-Durán and J. Jiménez, "Effect of the computational domain on direct simulations of turbulent channels up to $Re_\tau = 4200$," *Physics of Fluids*, vol. 26, no. 1, p. 011702, Jan. 2014. [Online]. Available: http://aip.scitation.org/doi/10.1063/1.4862918

[63] F. Lluesma-Rodríguez, S. Hoyas, and M. Perez-Quiles, "Influence of the computational domain on DNS of turbulent heat transfer up to Re τ = 2000 for Pr = 0.71," *International Journal of Heat and Mass Transfer*, vol. 122, pp. 983–992, Jul. 2018. [Online]. Available: https://linkinghub.elsevier.com/retrieve/pii/S0017931017343934

[64] A. Kravchenko and P. Moin, "On the Effect of Numerical Errors in Large Eddy Simulations of Turbulent Flows," *Journal of Computational Physics*, vol. 131, no. 2, pp. 310–322, Mar. 1997. [Online]. Available: https://linkinghub.elsevier.com/retrieve/pii/S0021999196955977

[65] T. Dairay, E. Lamballais, S. Laizet, and J. C. Vassilicos, "Numerical dissipation vs. subgrid-scale modelling for large eddy simulation," *Journal of Computational Physics*, vol. 337, pp. 252–274, May 2017. [Online]. Available: https://linkinghub.elsevier.com/retrieve/pii/S0021999117301298

[66] J. Mohd-Yusof, "Combined immersed-boundary/B-spline methods for simulations of flow in complex geometries," Annual Research Briefs, Center for Turbulence Research, NASA Ames/Stanford University, Technical, 1997.

[67] R. Gautier, "Calcul haute fidélité de la turbulence en géométrie complexe : Application au contrôle fluidique d'un jet," Ph.D. dissertation, Universite de Poitiers, Poitiers, 2013.

[68] P. Parnaudeau, "Etude numérique d'un écoulement cisaillé turbulent complexe à basse vitesse : application à la protection rapprochée," Ph.D. dissertation, Universite de Poitiers, Poitiers, 2004.

[69] J. Carlier, P. Parnaudeau, D. Heitz, and E. Lamballais, "Étude numérique et expérimentale de l'écoulement autour d'un cylindre circulaire à ReD = 3900," *17 ème Congrès Français de Mécanique - CFM 2005, 29 août-2 septembre, Troyes*, p. 6, 2005.

[70] P. Parnaudeau, D. Heitz, E. Lamballais, and J.-H. Silvestrini, "Direct numerical simulations of vortex shedding behind cylinders with spanwise linear nonuniformity," *Journal of Turbulence*, vol. 8, p. N13, Jan. 2007. [Online]. Available: https://www.tandfonline.com/doi/full/10.1080/14685240600767706

[71] W. J. Gonçalves da Silva Pinto and F. Margnat, "A shape optimization procedure for cylinders aeolian tone," *Computers & Fluids*, vol. 182, pp. 37–51, Mar. 2019. [Online]. Available: https://linkinghub.elsevier.com/retrieve/pii/S0045793019300283

[72] ——, "Shape optimization for the noise induced by the flow over compact bluff bodies," *Computers & Fluids*, vol. 198, p. 104400, Feb. 2020. [Online]. Available: https://linkinghub.elsevier.com/retrieve/pii/S0045793019303585

[73] ——, "Influence of cylinder breadth and shape on the onset of flow unsteadiness and the aeolian tone level," *Computers & Fluids*, vol. 228, p. 105067, Oct. 2021. [Online]. Available: https://linkinghub.elsevier.com/retrieve/pii/S0045793021002280

[74] G. Narváez, "Fluid-solid thermal coupling in pipe and channel turbulent flows via a dual immersed boundary method," Ph.D. dissertation, Universidade Federal do Rio Grande do Sul, 2019. [Online]. Available: https://lume.ufrgs.br/handle/10183/197867

[75] E. Lamballais and R. Vicente Cruz, "From Explicit to Implicit Subgrid-Scale and Wall Modelling in Large-Eddy Simulation," in *Bjørn Skallerud and Helge I. Andersson (eds)*, 2019, pp. 1–24.

[76] R. Vicente Cruz, E. Lamballais, and R. Perrin, "Implicit Wall-Layer Modelling in Turbulent Pipe Flow," in *Direct and Large Eddy Simulation XII*, M. García-Villalba, H. Kuerten, and M. V. Salvetti, Eds. Cham: Springer International Publishing, 2020, vol. 27, pp. 425–431, series Title: ERCOFTAC Series. [Online]. Available: http://link.springer.com/10.1007/978-3-030-42822-8_56

[77] R. Vicente Cruz, E. Lamballais, and G. F. N. Campo, "High-fidelity simulation of heat transfer in turbulent pipe flow," *International Topical Meeting on Advances in Thermal Hydraulics ATH20*, pp. 337–348, 2020.

[78] E. Lamballais, R. Vicente Cruz, and R. Perrin, "Viscous and hyperviscous filtering for direct and large-eddy simulation," *Journal of Computational Physics*, vol. 431, p. 110115, Apr. 2021. [Online]. Available: https://linkinghub.elsevier.com/retrieve/pii/S0021999121000073

[79] R. Vicente Cruz, E. Lamballais, and R. Perrin, "Towards high-fidelity simulation of wall turbulence subjected to conjugate heat transfer in complex geometry," *Proceedings ETMM13, Rhodes, Greece*, pp. 415–420, 2021.

[80] S. K. Lele, "Compact finite difference schemes with spectral-like resolution," *Journal of Computational Physics*, vol. 103, no. 1, pp. 16–42, Nov. 1992. [Online]. Available: https://linkinghub.elsevier.com/retrieve/pii/002199919290324R

[81] E. Lamballais, V. Fortuné, and S. Laizet, "Straightforward high-order numerical dissipation via the viscous term for direct and large eddy simulation," *Journal of Computational Physics*, vol. 230, no. 9, pp. 3270–3275, May 2011. [Online]. Available: https://linkinghub.elsevier.com/retrieve/pii/S0021999111000659

[82] R. Vichnevetsky and J. B. Bowles, *Fourier Analysis of Numerical Approximations of Hyperbolic Equations*. SIAM, Jan. 1982, google-Books-ID: GXeXTVGlR7YC.

[83] K. V. Roberts and N. O. Weiss, "Convective Difference Schemes," *Mathematics of Computation*, p. 28, 1966.

[84] H.-O. Kreiss and J. Oliger, "Comparison of accurate methods for the integration of hyperbolic equations," *Tellus*, vol. 24, no. 3, pp. 199–215, Jun. 1972. [Online]. Available: http://tellusa.net/index.php/tellusa/article/view/10634

[85] B. Swartz and B. Wendroff, "The Relative Efficiency of Finite Difference and Finite Element Methods. I: Hyperbolic Problems and Splines," *SIAM J. Numer. Anal.*, vol. 11, no. 5, pp. 979–993, Oct. 1974. [Online]. Available: http://epubs.siam.org/doi/10.1137/0711076

[86] E. Tadmor, "Convergence of Spectral Methods for Nonlinear Conservation Laws," *SIAM Journal on Numerical Analysis*, vol. 26, no. 1, pp. 30–44, 1989, publisher: Society for Industrial and Applied Mathematics. [Online]. Available: http://www.jstor.org/stable/2157705

[87] G.-S. Karamanos and G. Karniadakis, "A Spectral Vanishing Viscosity Method for Large-Eddy Simulations," *Journal of Computational Physics*, vol. 163, no. 1, pp. 22–50, Sep. 2000. [Online]. Available: https://linkinghub.elsevier.com/retrieve/pii/S0021999100965525

[88] R. Pasquetti, "Spectral Vanishing Viscosity Method for Large-Eddy Simulation of Turbulent Flows," *J Sci Comput*, vol. 27, no. 1-3, pp. 365–375, Jun. 2006. [Online]. Available: http://link.springer.com/10.1007/s10915-005-9029-9

[89] V. Borue and S. A. Orszag, "Local energy flux and subgrid-scale statistics in three-dimensional turbulence," *J. Fluid Mech.*, vol. 366, pp. 1–31, Jul. 1998. [Online]. Available: https://www.cambridge.org/core/product/identifier/S0022112097008306/type/journal_article

[90] T. Dairay, V. Fortuné, E. Lamballais, and L. Brizzi, "LES of a turbulent jet impinging on a heated wall using high-order numerical schemes," *International Journal of Heat and Fluid Flow*, vol. 50, pp. 177–187, Dec. 2014. [Online]. Available: https://linkinghub.elsevier.com/retrieve/pii/S0142727X14000940

[91] G. Narváez, E. Lamballais, and E. Schettini, "Simulation of turbulent flow subjected to conjugate heat transfer via a dual immersed boundary method," *Computers & Fluids*, vol. 229, p. 105101, Oct. 2021. [Online]. Available: https://linkinghub.elsevier.com/retrieve/pii/S0045793021002528

[92] S. Goto and J. C. Vassilicos, "Local equilibrium hypothesis and Taylor's dissipation law," *Fluid Dyn. Res.*, vol. 48, no. 2, p. 021402, Apr. 2016. [Online]. Available: https://iopscience.iop.org/article/10.1088/0169-5983/48/2/021402

[93] J. Kim and P. Moin, "Application of a fractional-step method to incompressible Navier-Stokes equations," *Journal of Computational Physics*, vol. 59, no. 2, pp. 308–323, Jun. 1985. [Online]. Available: https://linkinghub.elsevier.com/retrieve/pii/0021999185901482

[94] H. Choi and P. Moin, "Effects of the Computational Time Step on Numerical Solutions of Turbulent Flow," *Journal of Computational Physics*, vol. 113, no. 1, pp. 1–4, Jul. 1994. [Online]. Available: https://linkinghub.elsevier.com/retrieve/pii/S0021999184711120

[95] M. Quadrio, B. Frohnapfel, and Y. Hasegawa, "Does the choice of the forcing term affect flow statistics in DNS of turbulent channel flow?" *European Journal of Mechanics - B/Fluids*, vol. 55, pp. 286–293, Jan. 2016, arXiv: 1509.04877. [Online]. Available: http://arxiv.org/abs/1509.04877

[96] A. Bejan, *Convection Heat Transfer: Bejan/Convection Heat Transfer 4e*. Hoboken, NJ, USA: John Wiley & Sons, Inc., Apr. 2013. [Online]. Available: http://doi.wiley.com/10.1002/9781118671627

[97] B. Kader, "Temperature and concentration profiles in fully turbulent boundary layers," *International Journal of Heat and Mass Transfer*, vol. 24, no. 9, pp. 1541–1544, Sep. 1981. [Online]. Available: https://linkinghub.elsevier.com/retrieve/pii/0017931081902209

[98] H. Kawamura, H. Abe, and Y. Matsuo, "DNS of turbulent heat transfer in channel flow with respect to Reynolds and Prandtl number effects," *International Journal of Heat and Fluid Flow*, vol. 20, no. 3, pp. 196–207, Jun. 1999. [Online]. Available: https://linkinghub.elsevier.com/retrieve/pii/S0142727X99000144

[99] S.-i. Satake, T. Kunugi, and R. Himeno, "High Reynolds Number Computation for Turbulent Heat Transfer in a Pipe Flow," in *High Performance Computing*, G. Goos, J. Hartmanis, J. van Leeuwen, M. Valero, K. Joe, M. Kitsuregawa, and H. Tanaka, Eds. Berlin, Heidelberg: Springer Berlin Heidelberg, 2000, vol. 1940, pp. 514–523, series Title: Lecture Notes in Computer Science. [Online]. Available: http://link.springer.com/10.1007/3-540-39999-2_49

[100] L. Redjem-Saad, M. Ould-Rouiss, and G. Lauriat, "Direct numerical simulation of turbulent heat transfer in pipe flows: Effect of Prandtl number," *International Journal of Heat and Fluid Flow*, vol. 28, no. 5, pp. 847–861, Oct. 2007. [Online]. Available: https://linkinghub.elsevier.com/retrieve/pii/S0142727X07000239

[101] I. Tiselj, E. Pogrebnyak, C. Li, A. Mosyak, and G. Hetsroni, "Effect of wall boundary condition on scalar transfer in a fully developed turbulent flume," *Physics of Fluids*, vol. 13, no. 4, pp. 1028–1039, Apr. 2001. [Online]. Available: http://aip.scitation.org/doi/10.1063/1.1350899

[102] I. Tiselj and L. Cizelj, "DNS of turbulent channel flow with conjugate heat transfer at Prandtl number 0.01," *Nuclear Engineering and Design*, vol. 253, pp. 153–160, Dec. 2012. [Online]. Available: https://linkinghub.elsevier.com/retrieve/pii/S0029549312004396

[103] T. Dairay, "Simulation haute fidélité de l'aérothermique d'un jet en impact," Ph.D. dissertation, Universite de Poitiers, Poitiers, 2013. [Online]. Available: https://tel.archives-ouvertes.fr/tel-01101235/

[104] F. Aulery, A. Toutant, R. Monod, G. Brillant, and F. Bataille, "Numerical simulations of sodium mixing in a T-junction," *Applied Thermal Engineering*, vol. 37, pp. 38–43, May 2012. [Online]. Available: https://linkinghub.elsevier.com/retrieve/pii/S1359431111007411

[105] S. Jaure, F. Duchaine, G. Staffelbach, and L. Y. M. Gicquel, "Massively parallel conjugate heat transfer methods relying on large eddy simulation applied to an aeronautical combustor," *Comput. Sci. Disc.*, vol. 6, no. 1, p. 015008, Oct. 2013. [Online]. Available: https://iopscience.iop.org/article/10.1088/1749-4699/6/1/015008

[106] N. Kasagi, A. Kuroda, and M. Hirata, "Numerical Investigation of Near-Wall Turbulent Heat Transfer Taking Into Account the Unsteady Heat Conduction in the Solid Wall," *Journal of Heat Transfer*, vol. 111, no. 2, pp. 385–392, May 1989. [Online]. Available: https://asmedigitalcollection.asme.org/heattransfer/article/111/2/385/414102/Numerical-Investigation-of-NearWall-Turbulent-Heat

[107] G. Iaccarino and S. Moreau, "Natural and Forced Conjugate Heat Transfer in Complex Geometries on Cartesian Adapted Grids," *Journal of Fluids Engineering*, vol. 128, no. 4, pp. 838–846, Jul. 2006. [Online]. Available: https://asmedigitalcollection.asme.org/fluidsengineering/article/128/4/838/466716/Natural-and-Forced-Conjugate-Heat-Transfer-in

[108] D. De Marinis, M. D. de Tullio, M. Napolitano, and G. Pascazio, "Improving a conjugate-heat-transfer immersed-boundary method," *International Journal of Numerical Methods for Heat & Fluid Flow*, vol. 26, no. 3/4, pp. 1272–1288, May 2016. [Online]. Available: https://www.emerald.com/insight/content/doi/10.1108/HFF-11-2015-0473/full/html

[109] A. F. Polyakov, "Wall effect on temperature fluctuations in the viscous sublayer," *Teplofizika Vysokikh Temperatur, vol. 12, Mar.-Apr. 1974, p. 328-337. High Temperature Science, vol. 12, no. 2, Nov. 1974, p. 286-293.*, 1974.

[110] C. Flageul, S. Benhamadouche, É. Lamballais, and D. Laurence, "On the discontinuity of the dissipation rate associated with the temperature variance at the fluid-solid interface for cases with conjugate heat transfer," *International Journal of Heat and Mass Transfer*, vol. 111, pp. 321–328, Aug. 2017. [Online]. Available: https://linkinghub.elsevier.com/retrieve/pii/S0017931016331945

[111] M. Schäfer, S. Yigit, and M. Heck, "Implicit Partitioned Fluid-Structure Interaction Coupling," in *Volume 4: Fluid Structure Interaction, Parts A and B*. Vancouver, BC, Canada: ASMEDC, Jan. 2006, pp. 105–114. [Online]. Available: https://asmedigitalcollection.asme.org/PVP/proceedings/PVP2006-ICPVT-11/47551/105/319159

[112] F. Duchaine, A. Corpron, L. Pons, V. Moureau, F. Nicoud, and T. Poinsot, "Development and assessment of a coupled strategy for conjugate heat transfer with Large Eddy Simulation: Application to a cooled turbine blade," *International Journal of Heat and Fluid Flow*, vol. 30, no. 6, pp. 1129–1141, Dec. 2009. [Online]. Available: https://linkinghub.elsevier.com/retrieve/pii/S0142727X09001180

[113] M. B. Giles, "Stability analysis of numerical interface conditions in fluid–structure thermal analysis," *International Journal for Numerical Methods in Fluids*, vol. 25, p. 16, 1997.

[114] A. E. Giannenas and S. Laizet, "A simple and scalable immersed boundary method for high-fidelity simulations of fixed and moving objects on a Cartesian mesh," *Applied Mathematical Modelling*, vol. 99, pp. 606–627, Nov. 2021. [Online]. Available: https://linkinghub.elsevier.com/retrieve/pii/S0307904X21003103

[115] E. Lamballais, "Direct numerical simulation of a turbulent flow in a rotating channel with a sudden expansion," *J. Fluid Mech.*, vol. 745, pp. 92–131, Apr. 2014. [Online]. Available: https://www.cambridge.org/core/product/identifier/S0022112014000305/type/journal_article